

## Deliverable 5.5

### Development of a ground motion model and probabilistic seismic hazard analysis for the North Sea



|                     |  |
|---------------------|--|
| Organisation(s)     | NORSAR, NGI, University of Oxford, GEUS, Equinor     |
| Author(s)           | Chen Huang, Brian Carlton, Tom Kettlety, Tine Larsen |
| Reviewer            | Elin Skurtveit, Peter Voss, Zoya Zarifi, Eirik Tvedt |
| Type of deliverable | Report   |
| Dissemination level | Public   |
| WP                  | 5  |
| Issue date          | June 2024  |
| Document version    | 1  |

Keywords: seismic hazard, ground motion, earthquake risk, seismology.

Summary: A report summarising North Sea ground motion model development, near surface attenuation, and probabilistic seismic hazard analysis conducted within WP5 (Risk Quantification) of the SHARP project.

## Executive Summary

This SHARP report presents the findings of the seismic hazard task within work package 5 (WP5: Risk Quantification) of the project. In this task, several activities were conducted: a ground motion model calibration; near surface attenuation quantification; and a revised probabilistic seismic hazard analysis (PSHA). These analyses were each conducted using the SHARP North Sea earthquake catalogue and waveform database, as produced by the project's WP2 (Seismology). The catalogue was enlarged to cover the area 300 km around the North Sea for the PSHA. This report starts with an introduction and review of the many seismic hazard analyses that have been conducted in the North Sea region. Their methodology, scope, and input data are compared, chiefly to frame the new analysis that has been conducted within this study.

Firstly, this study focussed on the calibration of a bespoke ground-motion model (GMM) for the North Sea region using the new SHARP dataset. The collected waveform data underwent a sophisticated three-stage processing scheme to compute the ground-motion intensity measures (IMs) (e.g., spectral accelerations). The processed waveform included the three-component ground motion recordings from  $M \geq 3.5$  events, distances within 10 degrees or 1100 km epicentre distance recorded between 1990 to 2022. It is worth noting that the waveform database is much more limited than the earthquake catalogue. The earthquake catalogue is a list of earthquake magnitudes and their dates and locations. The waveform database is a database of recorded earthquake ground motions. Thus, the waveform database only includes relatively recent earthquakes that were digitally recorded. In addition, through the waveform processing scheme, the earthquake recording might be missing a component, or be too noisy to use in the development of the GMM. The IMs and the metadata of the events and stations (e.g., magnitude, source-to-site distance and site conditions) were compiled into a "flatfile". Based on the characteristics in North Sea data, a simple but effective functional form was proposed to capture the first-order positive linear magnitude scaling, negative linear distance scaling, and general response for rock conditions. The model parameters for the mixed-effect GMM (i.e., coefficients, inter- and intra-event standard deviation as well as spatial correlation range parameters) were estimated through the advanced one-stage algorithm (Ming et al, 2019). The derived GMM was applicable for magnitude range 3.5 to 5.5, epicentral distance range 72 km to 1000 km, and period range 0.03 to 2.6 s. This distance range come primarily from the fact that there are no offshore recordings of earthquakes in this study. The nearest applicable distance of 72 km is considered too far for CO<sub>2</sub> storage sites. However, this could be addressed in the future by incorporating sufficient quality offshore recordings, where they may exist. Compared to the global and regional GMMs that have been applied to the North Sea regions in previous studies, the predictive performance of the North Sea was better in capturing the features in North Sea data.

This was followed by an analysis of near surface attenuation for seismic stations around the North Sea. In this study the ground motion model was largely developed for rock site conditions. To estimate the shaking at the ground surface, we planned to develop site amplification functions based on site response analyses, like Carlton (2014) and Harmon et al. (2019). We developed site profiles using a database of site investigations from the North Sea including geological, geophysical, and geotechnical data. However, due to the lack of strong ground motion data, we were unable to perform traditional site response analyses using acceleration time series as input. As a result, a future study should include the development of site amplification factors based on site response analyses using random vibration theory (RVT) (Rathje and Ozbey, 2006), which uses the Fourier amplitude spectrum (FAS) as input.

One of the main input parameters to constrain a site-specific FAS is kappa ( $\kappa$ ), which is a measure of the high-frequency energy attenuation of ground motions. To estimate  $\kappa$  we used a subset of the earthquake waveform database that included only earthquakes with  $M_w > 3.5$  and records with an epicentral distance ( $R_{epi}$ ) less than 300 km. We estimated  $\kappa$  using the method proposed by Anderson and Hough (1984) and following the recommendations of Ktenidou et al. (2016). We calculated average horizontal-to-vertical spectral ratios (HVSr) for each site (Lermo and Chavez-Garcia, 1993) and removed sites with a clear indication of soil amplification. The estimated values of  $\kappa$  between 0.005 and 0.085 are reasonable and correspond to shear wave velocities over the top 30 meters ( $V_{s30}$ ) of 2000 m/s to 200 m/s (Van Houtte et al., 2011). However, the estimated values of  $\kappa$  do not increase with distance as expected, or they increase at a smaller rate, implying anelastic attenuation ( $Q$ ) several times larger than measured by other researchers using tomography techniques. We conclude that more work is needed to ensure robust estimates of kappa using this North Sea data.

The study concluded with a probabilistic seismic hazard analysis (PSHA). The PSHA included three areal seismic source models based on previous regional studies for Norway (NORSAR, 2019), Germany (Grünthal et al., 2018), France (Drouet et al., 2020), the UK (EQE, 2002; Mosca et al. 2020, 2024), and Europe (Danciu et al., 2021), as well as one zoneless model (smoothed seismicity) based on the updated North Sea earthquake catalogue from WP2. The four different models were combined using a logic tree. For all models we used a truncated exponential model for the magnitude recurrence relation and minimum magnitude of  $M_w = 4.0$ . We use the Akkar et al. (2014), Cauzzi et al. (2015), and Reitbrock and Edwards (2019) ground motion models, in addition to the North Sea specific model. These three models best match earthquakes recorded in and around the North Sea. The PSHA results show that the highest PGA values occur off the west coast of Norway in the Tampen Area (62°N, 4°E), between Norway and Denmark SE of the Tornquist Zone (57.5°N, 7.5°E), and at the Dover Strait (51°N, 1.5°E). The PGA values for 475-year return period on rock predicted along the coasts are all like the values predicted along the coast in the corresponding national studies, and generally smaller in the offshore regions compared to the only previous PSHA conducted for the North Sea (Bungum et al., 2000).

This study has also shown the difficulties in applying the newly combined SHARP earthquake data to make a region-specific GMM and PSHA for the North Sea, giving recommendations for future monitoring and site characterisation efforts. The lack of events with high-quality nearfield (i.e., offshore) recordings, especially those with larger magnitudes, make robust constraint of ground motions more limited. This further highlights that offshore recordings of earthquakes are needed to constrain several aspects of CO<sub>2</sub> storage monitoring. There is also a need to improve the quality of older data. For example, a M 4.5 event in 1980, which occurred near the EOS injector, was included in the earthquake catalogue but the corresponding waveform was not included for GMM development due to data quality. This could be improved in the future with the use of data from permanent offshore nodal seismic systems. However, there are difficulties in applying these kinds of recordings to hazard analysis that would require dedicated research, including a limited instrument response and dynamic range, as well as a complex conversion of the waveform data into physical units (i.e., acceleration or displacement). A challenge of the PSHA was highlighted in the lack of data for small events in the area outside of the strict boundary of the North Sea study region defined by WP2. This could be tackled in an expansion to this study by the additional collection of data in a similar manner as was conducted by WP2, but in wider area outside of the North Sea.

|  |    |
|--|----|
| Executive Summary .....                                | 2  |
| 1 Introduction.....                                    | 6  |
| 1.1 Previous seismic hazard studies .....              | 6  |
| 1.1.1 Grünthal et al (1999) (GSHAP).....               | 6  |
| 1.1.2 Bungum et al. (2000) .....                       | 8  |
| 1.1.3 Woessner et al. (2015) (SHARE) .....             | 9  |
| 1.1.4 Grünthal et al. (2018) (Germany).....            | 11 |
| 1.1.5 NORSAR (2019) (Norway).....                      | 13 |
| 1.1.6 Voss et al. (2015) (Denmark).....                | 15 |
| 1.1.7 Drouet et al. (2020) (France).....               | 16 |
| 1.1.8 Mosca et al. (2020) (UK).....                    | 17 |
| 1.1.9 Danciu et al. (2021) (ESHM20) .....              | 18 |
| 1.1.10 Offshore wind farms .....                       | 20 |
| 1.2 CO <sub>2</sub> storage case studies.....          | 21 |
| 1.3 Ground motion limits.....                          | 22 |
| 2 Methods .....  | 24 |
| 2.1 Probabilistic seismic hazard analysis (PSHA) ..... | 24 |
| 2.2 Ground motion models.....                          | 26 |
| 2.3 High frequency attenuation.....                    | 29 |
| 3 SHARP Seismicity Catalogue.....                      | 33 |
| 3.1 North Sea catalogue .....                          | 33 |
| 3.2 Waveform database .....                            | 36 |
| 4 Ground motion model development .....                | 37 |
| 4.1 Data quality control .....                         | 37 |
| 4.1.1 Waveform processing.....                         | 37 |
| Download waveform .....                                | 38 |
| Initial processing .....                               | 38 |
| Preliminary processing for individual waveform .....   | 38 |
| Refined processing for multi-component waveforms ..... | 38 |
| 4.1.2 North Sea waveform database.....                 | 40 |
| 4.1.3 Discussion .....                                 | 44 |
| Data selection criteria .....                          | 44 |
| Uncertainty in event magnitude and location .....      | 44 |
| 4.2 Flat file construction .....                       | 44 |
| 4.2.1 Event metadata .....                             | 44 |

|       |  |     |
|-------|--|-----|
| 4.2.2 | Station metadata .....                             | 44  |
| 4.2.3 | Time-domain amplitude-based IMs .....              | 48  |
| 4.2.4 | Frequency-domain amplitude-based IMs .....         | 49  |
| 4.2.5 | Energy-related Integral IMs.....                   | 50  |
| 4.2.6 | Discussion .....                                   | 51  |
| 4.3   | GMM estimation and evaluation.....                 | 51  |
| 4.3.1 | Scaling in observations .....                      | 51  |
| 4.3.2 | Functional form .....                              | 53  |
| 4.3.3 | GMM results.....                                   | 56  |
| 4.3.4 | Comparison with previous models.....               | 57  |
| 4.3.5 | Discussion .....                                   | 59  |
| 5     | Near surface attenuation .....                     | 60  |
| 5.1   | Site amplification .....                           | 60  |
| 5.1.1 | Geologic setting.....                              | 60  |
| 5.1.2 | Representative base case profiles.....             | 61  |
| 5.1.3 | Modified profiles .....                            | 65  |
| 5.1.4 | Future work .....                                  | 66  |
| 5.2   | Kappa .....  | 67  |
| 5.2.1 | Overview.....                                      | 67  |
| 5.2.2 | Preliminary Analysis .....                         | 68  |
| 5.2.3 | Additional Work .....                              | 75  |
| 6     | Probabilistic seismic hazard analysis.....         | 81  |
| 6.1   | Sources.....                                       | 81  |
| 6.1.1 | Models 1, 2 and 3 .....                            | 82  |
| 6.1.2 | Model 4.....                                       | 91  |
| 6.2   | GMM integration .....                              | 98  |
| 6.2.1 | GMMs used in nearby national studies.....          | 98  |
| 6.2.2 | Selected GMMs .....                                | 100 |
| 6.3   | PSHA results .....                                 | 101 |
| 6.4   | Comparison of PSHA results with other studies..... | 105 |
| 7     | Discussion and conclusions .....                   | 105 |
| 8     | References.....                                    | 108 |

## 1 Introduction

The key objective of the SHARP project was to better quantify risks to CO<sub>2</sub> storage integrity in the North Sea. Central to this activity is the assessment of risk that earthquakes (i.e., seismicity) could impose on storage operations. This report details the methodology and results of a task conducting a new assessment of seismic hazard in the North Sea region. This new assessment has two main parts: the derivation of a regional ground motion model (GMM), and an updated probabilistic seismic hazard analysis (PSHA). The GMMs, also known as Ground-motion prediction equations (GMPEs), relate a ground-motion parameter (e.g., peak ground acceleration, PGA) to a set of explanatory variables describing the earthquake source, wave propagation path and local site conditions (e.g., Douglas, 2003; Stewart et al., 2015), which is elaborated in Section 2.2. These are being conducted using data that is newly created as a part of the SHARP project in its second work package, which explicitly focussed on seismology data.

This report will first introduce the previous seismic hazard studies which have been conducted in the region and frame this new analysis in terms of both the nearby CO<sub>2</sub> storage projects and the ground motion limits given by the various regulatory jurisdictions in the region. It then describes the methodology for the GMM derivation, the quantification of near surface attenuation effects, and the PSHA. The seismicity datasets used here will then be described, before moving onto the results and discussion of the GMM, surface attenuation, and PSHA studies.

### 1.1 Previous seismic hazard studies

#### 1.1.1 Grünthal et al (1999) (GSHAP)

The Global Seismic Hazard Assessment Program (GSHAP) was an international project that ran from 1992 until 1998. It aimed to develop regionally coordinated and homogeneous seismic hazard maps for all onshore locations world-wide. Grünthal et al (1999) presents the results for GSHAP region 3, which includes most of central and northern Europe. The Grünthal et al. (1999) study is based on a catalogue of merged national earthquake databases and 196 seismic source zones merged from different national studies (Figure 1-1). Grünthal et al. (1999) used three different sets of ground motion models, one for the Fennoscandian Shield, one for the Vrancea area in Romania, and one set of ground motion models for the rest of the study area. Figure 1-2 shows the seismic hazard map for rock calculated by Grünthal et al. (1999) for a 475-year return period.

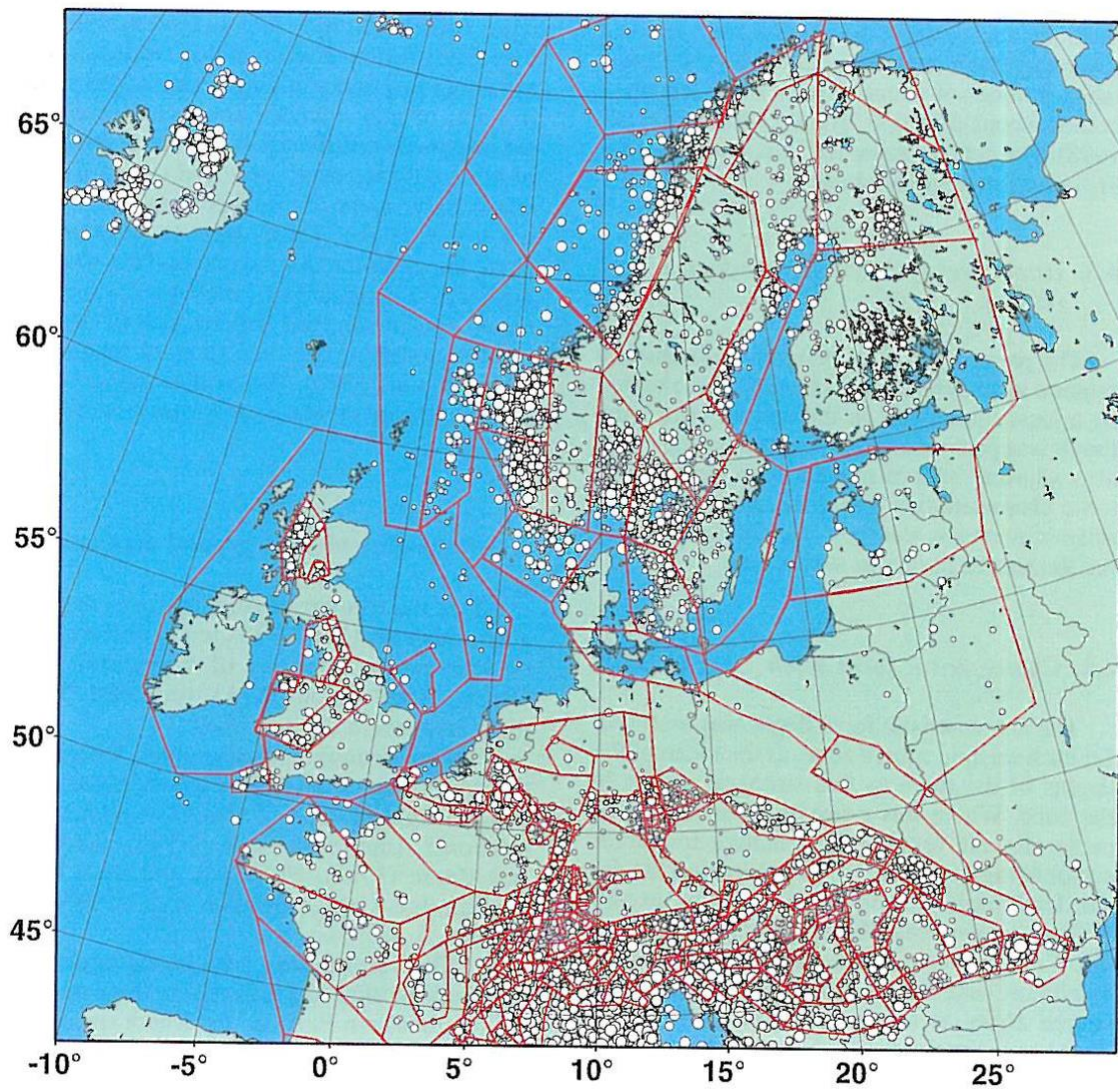
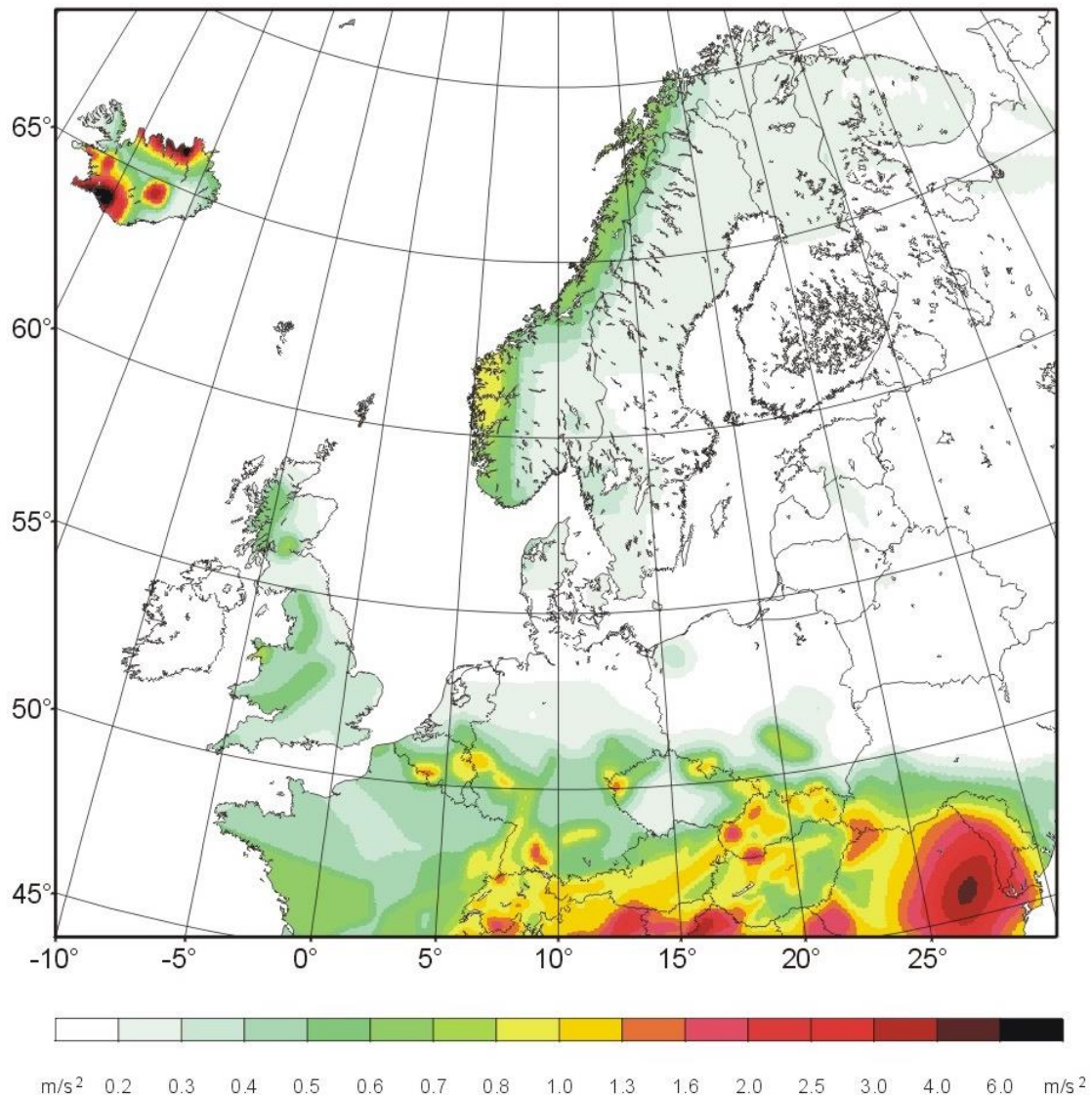


Figure 1-1 Seismic source model used in GSHAP region 3 (Grünthal et al., 1999).



*Figure 1-2 Seismic hazard map for peak ground acceleration (PGA) with return period of 475-years on rock according to GSHAP (Grünthal et al., 1999).*

### 1.1.2 Bungum et al. (2000)

Bungum et al. (2000) developed a unified seismic hazard map for Norway, the North Sea and the U.K. Bungum et al. (1998) describe the model for the Norwegian sector of the North Sea and the report by EQE (2002) describes the model for the UK and UK sector of the North Sea. Bungum et al. (2000) used a coarse seismic source characterisation model and a fine seismic source characterisation model. All source zones have three sets of activity rate and b-value pairs, with different weights implemented in a logic tree. Figure 1-3 shows the fine seismic source characterization model used in Bungum et al. (2000) and the PGA values for 475-year return period on rock.

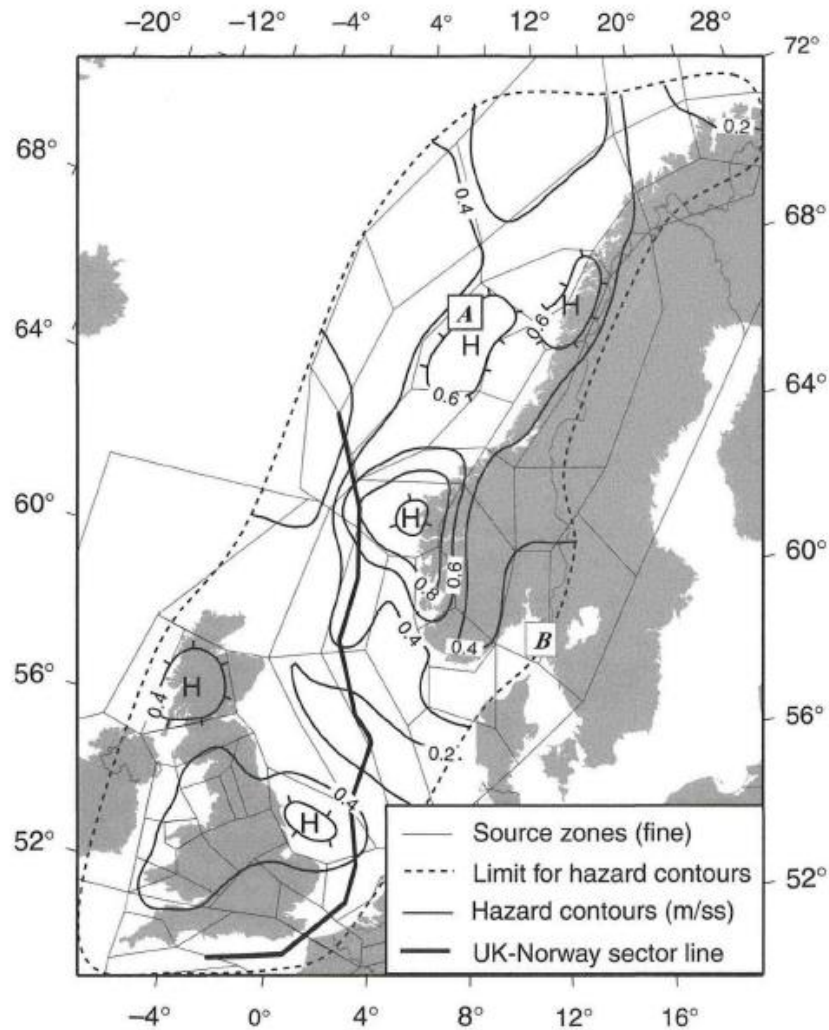


Figure 1-3 Fine seismic source model and resulting PGA ( $m/s^2$ ) for 475-year return period on rock (Bungum et al., 2000).

### 1.1.3 Woessner et al. (2015) (SHARE)

The Seismic Hazard Harmonization in Europe (SHARE) project (Woessner et al., 2015) conducted a seismic hazard analysis for all of Europe. It was the first completed regional contribution to the Global Earthquake Model initiative. Woessner et al. (2015) used three different seismic source models; an areal source model (Figure 1-4), a fault source model with background seismicity, and an area-smoothed model based on fault slip rate and past seismic activity. The areal seismic source zonation for the UK is based mainly on Musson and Sergeant (2007), and the North Sea is mainly based on Bungum et al. (2000), with some adjustments. The SHARE project used four ground motion models for active shallow and oceanic crust, five for stable continental regions, two for deep seismicity in the Vrancea region, and one for volcanic and swarm type earthquakes. Figure 1-5 shows the PGA on rock for 475-year return period according to the SHARE project.

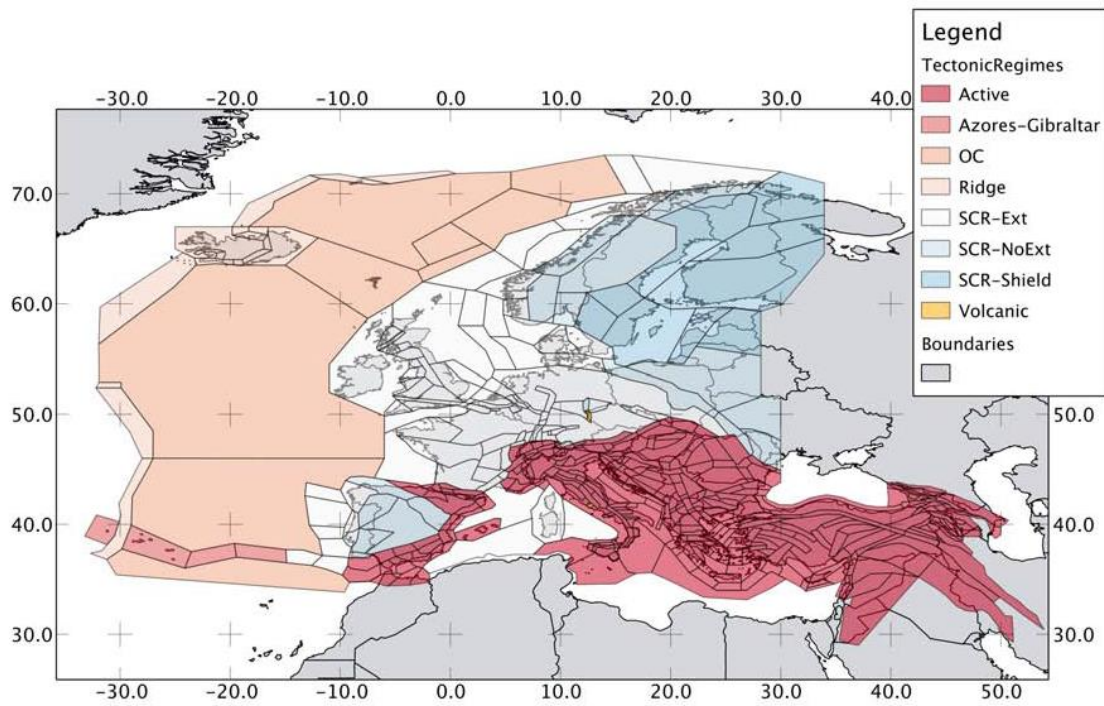


Figure 1-4 Areal source model used in the SHARP project (Woessner et al., 2015), showing the tectonic regimes of each of the areal sources.

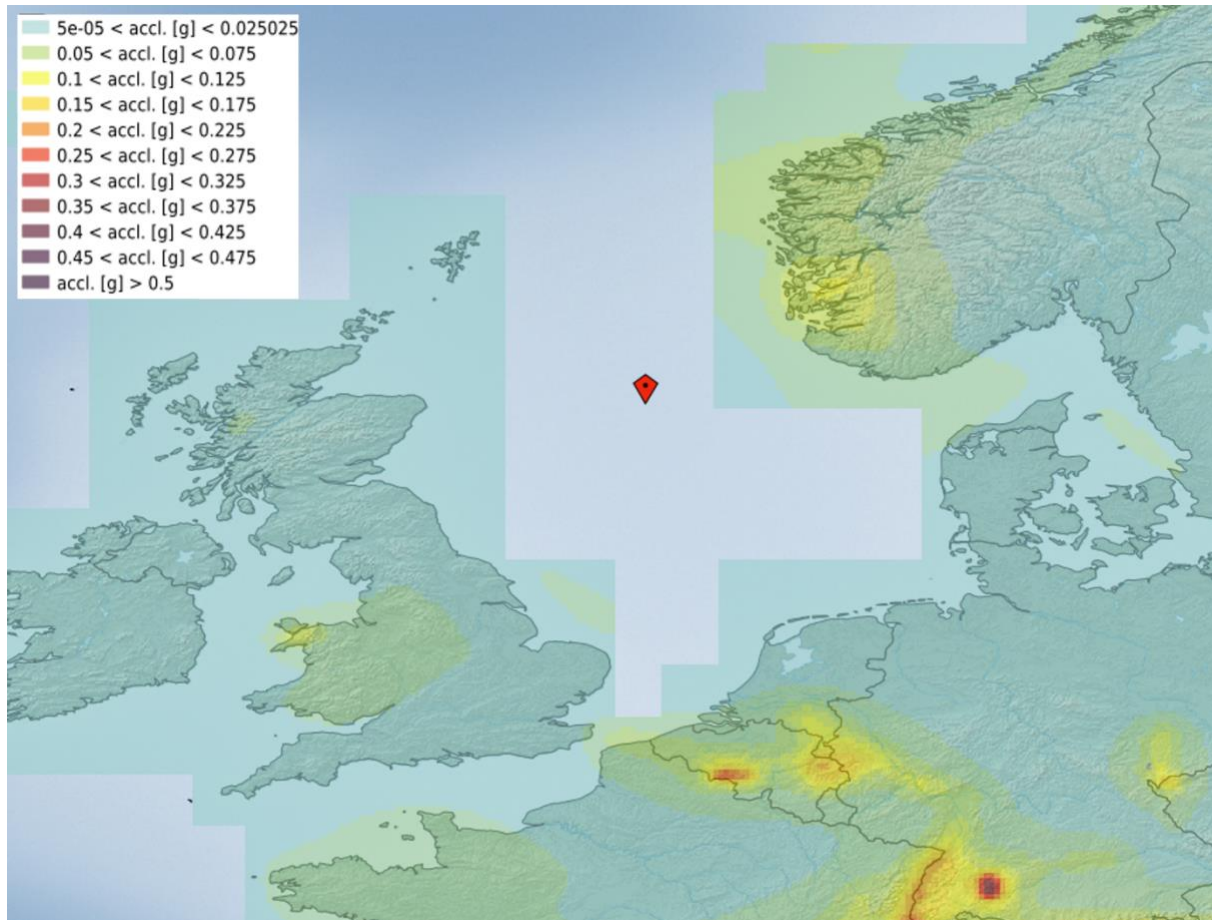


Figure 1-5 PGA on rock for 475-year return period from the SHARE project (Woessner et al., 2015).

#### 1.1.4 Grünthal et al. (2018) (Germany)

Grünthal et al. (2018) performed a PSHA for Germany that was then used as the official seismic hazard maps for use with EN 1998-1. They used seven different seismic source models. Two large scale areal source zones (A and B), three smaller scale areal source zones (C, D, and E), and two zoneless models (smoothed seismicity models). They used five different ground motion models in a logic tree framework. Model A is based on tectonics and model B is a slight modification of model A. Models C, D and E are based more on the fault lineations as well as historical seismicity. Model C was used by the SHARE project. Figure 1-6 shows model D. Grünthal et al. (2018) used five ground motion models in a logic tree framework. Figure 1-7 shows the PGA for a 475-year return period and  $V_{s30} = 800 \text{ m/s}^2$ . The lowest seismic hazard in Germany is in the north, closest to the North Sea.

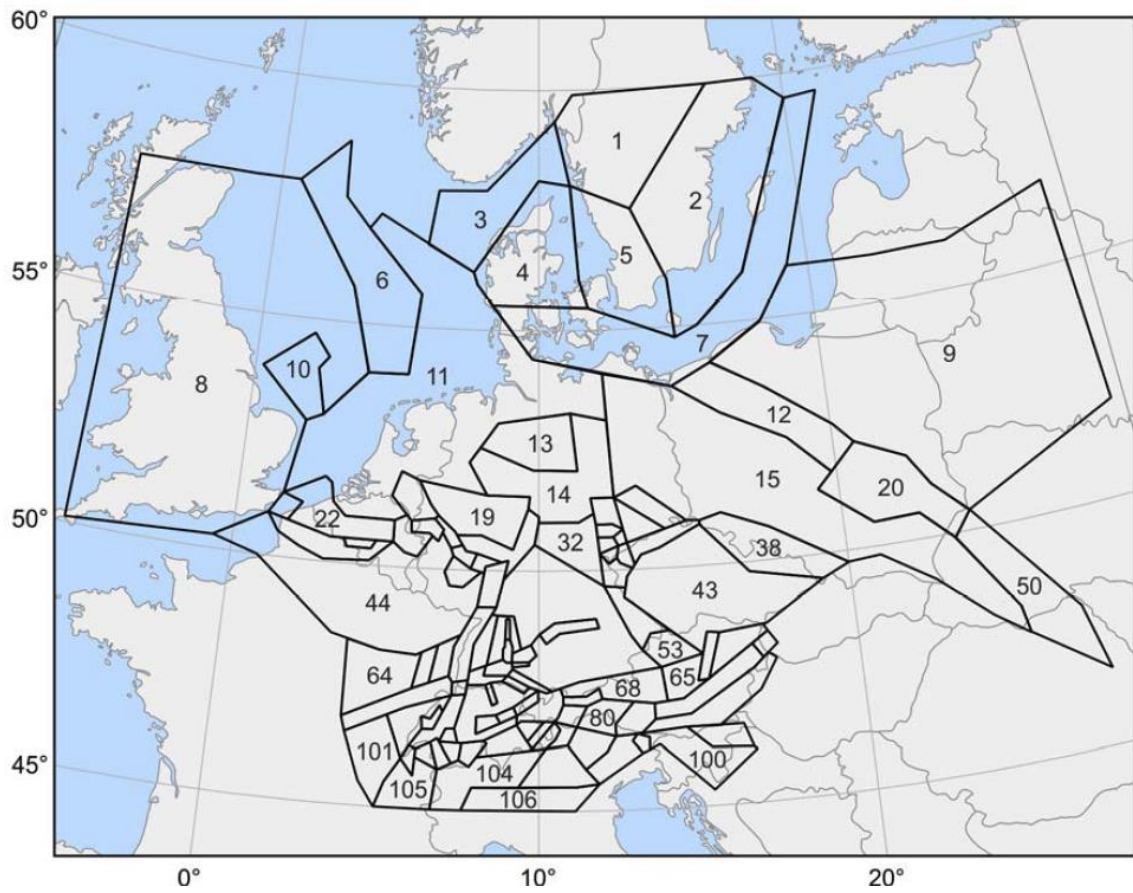


Figure 1-6 Seismic source model D from Grünthal et al (2018).

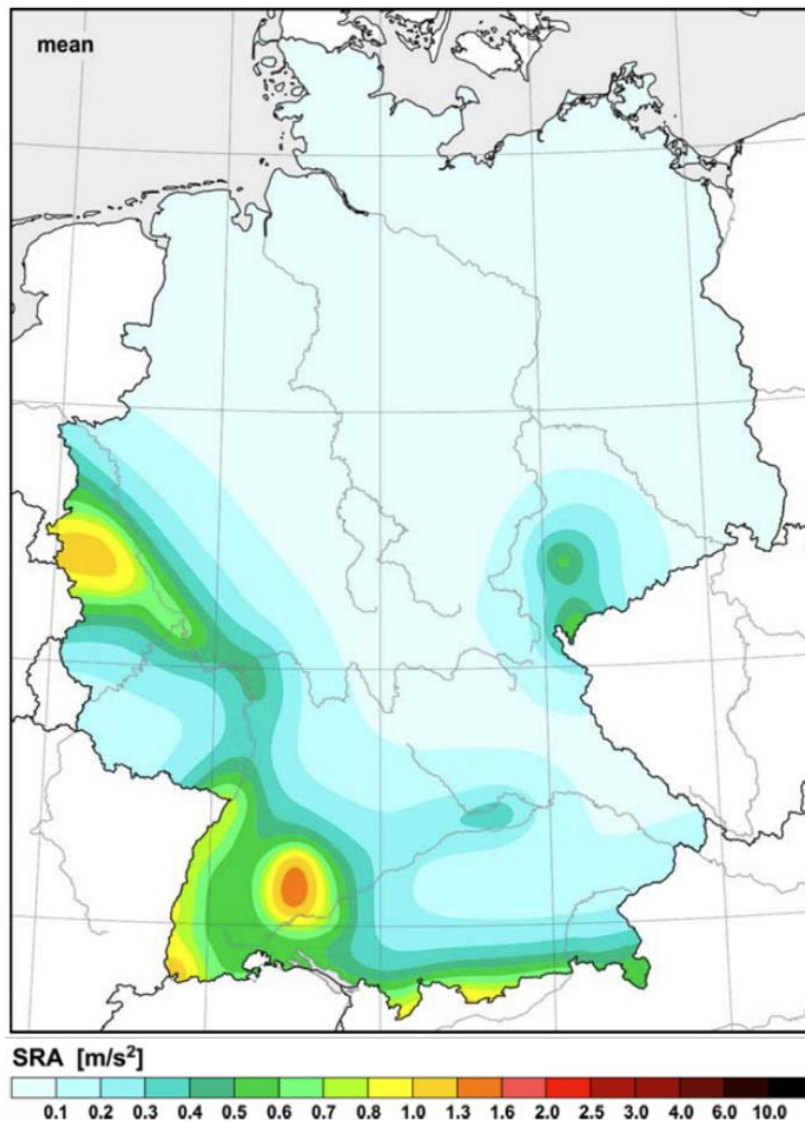


Figure 1-7 PGA for 475-year return period for  $V_{s30} = 800 \text{ m/s}^2$  (Grünthal et al., 2018)

#### 1.1.5 NORSAR (2019) (Norway)

NORSAR (2019) performed a PSHA for Norway using two different areal source models and one zonation-free model (Figure 1-8), as well as four ground motion models in a logic tree framework. The first seismic source model is based mainly on seismicity and the second more on geology and mapped structural elements. The zonation free approach was implemented in a roughly 10 by 10 km grid (0.1 and 0.2 degrees in latitude and longitude, respectively), reflecting the geographical distribution of earthquakes. This study was built on the catalogue developed from an extensive analysis of historical data combined with more recent instrumental data with 33864 reports between 1497 through 2018 with magnitudes up to Mw 6.7. The final seismic hazard maps are for peak ground acceleration (PGA) and spectral acceleration (Sa) at 0.1 s and 1.0 s for 5% damping with the 10% exceedance in 475 years, covering mainland Norway and the Svalbard archipelago for the reference velocity of 1200 m/s. Offshore Norwegian waters were not considered in this study, as shown in Figure 1-9.

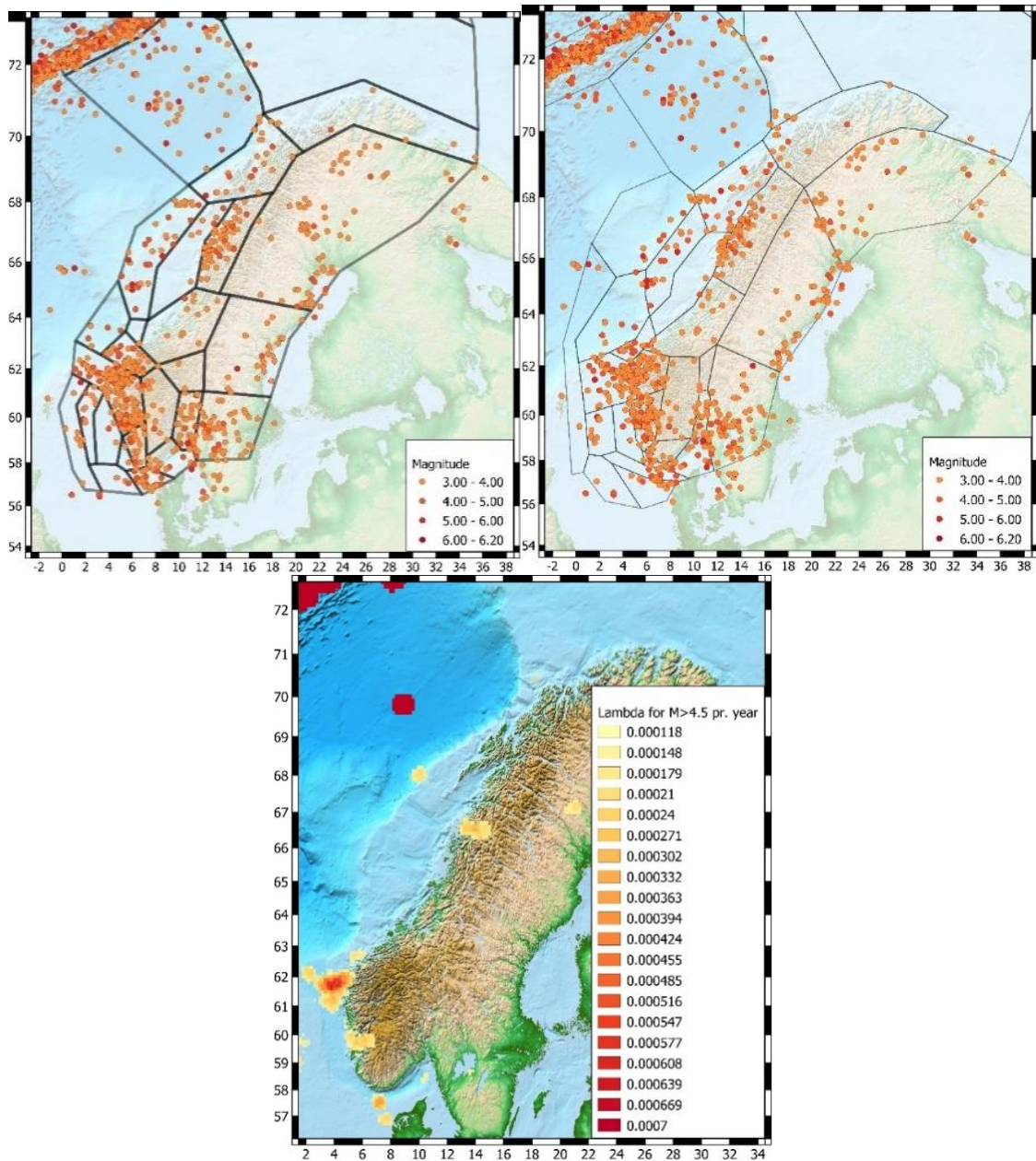


Figure 1-8 The two zonation applied for mainland Norway. Zonation 1 (top left) was based mainly on seismicity patterns. Zonation 2 (top right) was based mainly with reference to mapped structures (Norwegian Geological Survey). Only  $M \geq 3.0$  included. Note that also for Svalbard two zonation were defined but shown only in the Supplementary Information. The zonation-free model (bottom left) with lambda values obtained for the zonation-free model for mainland Norway.

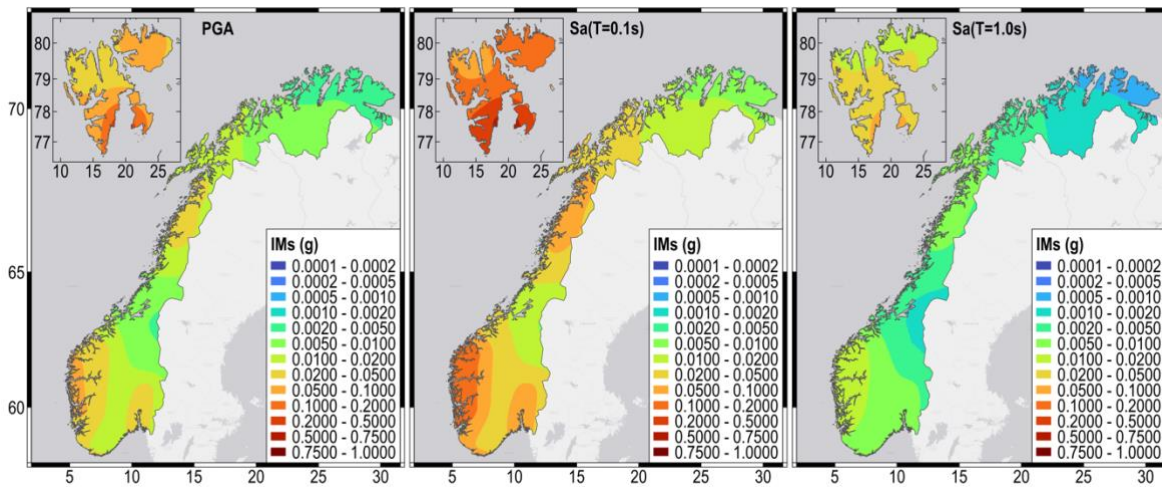


Figure 1-9 10% exceedance probability in 50 years (PGA at 475 years return period). Left: PGA; Middle: T=0.1 seconds. Right: T=1 second.

#### 1.1.6 Voss et al. (2015) (Denmark)

Voss et al. (2015) carried out the first national PSHA for Denmark for the purpose of obtaining seismic zoning input to the Danish National Annexes to Eurocode 8. The PSHA was applied to the 8 source areas in Figure 1-10 using the CRISIS software (Ordaz et al., 2007). The zonation was chosen based on observed seismicity and geology, and the calculations are only valid for onshore areas. Lacking information on attenuation of earthquake signals in Denmark, the hazard map was calculated assuming Ground type A (rock). The magnitude of completeness since 1960 was estimated to  $M_L$  3.0 yielding a Gutenberg-Richter b-value of  $0.96 \pm 0.1$ . Historical accounts of earthquakes in Denmark were used together with the instrumentally recorded earthquake database to estimate that the expected maximum magnitude for an earthquake in Denmark within a return period of 475 years is  $M_L$  5.3  $\pm$  0.1. A total of 119 instrumentally recorded earthquakes went into the calculation of the seismic hazard map for peak ground acceleration (PGA) with a return period of 475 years shown in Figure 1-10. The highest levels are found in NW Jutland and NE Zealand reflecting that the highest levels of seismicity are observed in Skagerrak and Kattegat. For Denmark the PGA ranges from  $6 \text{ cm/s}^2$  to  $30 \text{ cm/s}^2$ .

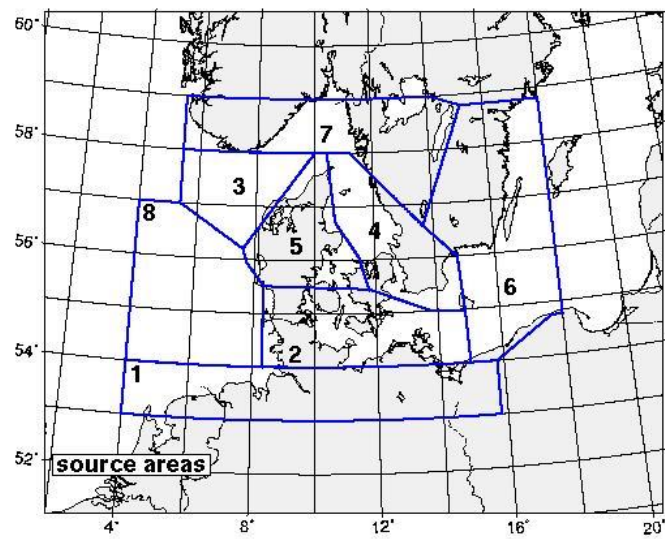


Figure 1-10 source areas in Denmark (from Voss et al, 2015).

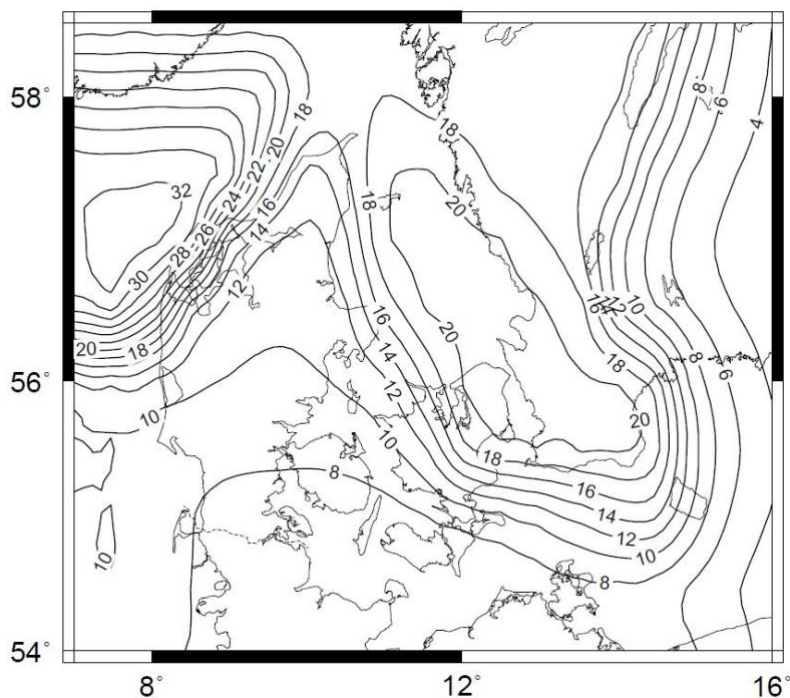


Figure 1-11 Estimated PGA for Ground type A in  $\text{cm/s}^2$  for a return period of 475. From Voss et al., 2015.

#### 1.1.7 Drouet et al. (2020) (France)

Drouet et al (2020) performed a PSHA for France using three areal source models termed GEOTER, EDF, and IRSN. The GEOTER model was developed by Le Dortz et al. (2019) based on the geology and neotectonics of France. The EDF model is an update of the model employed for seismic hazard assessments of nuclear power plants owned by EDF-TEGG in France. The IRSN model was developed by the French Institute for Radioprotection and Nuclear Safety and considers geology as well as seismotectonic activity. Figure 1-12 shows the PGA values for a 475-year return period for  $V_{s30} = 800 \text{ m/s}^2$ .

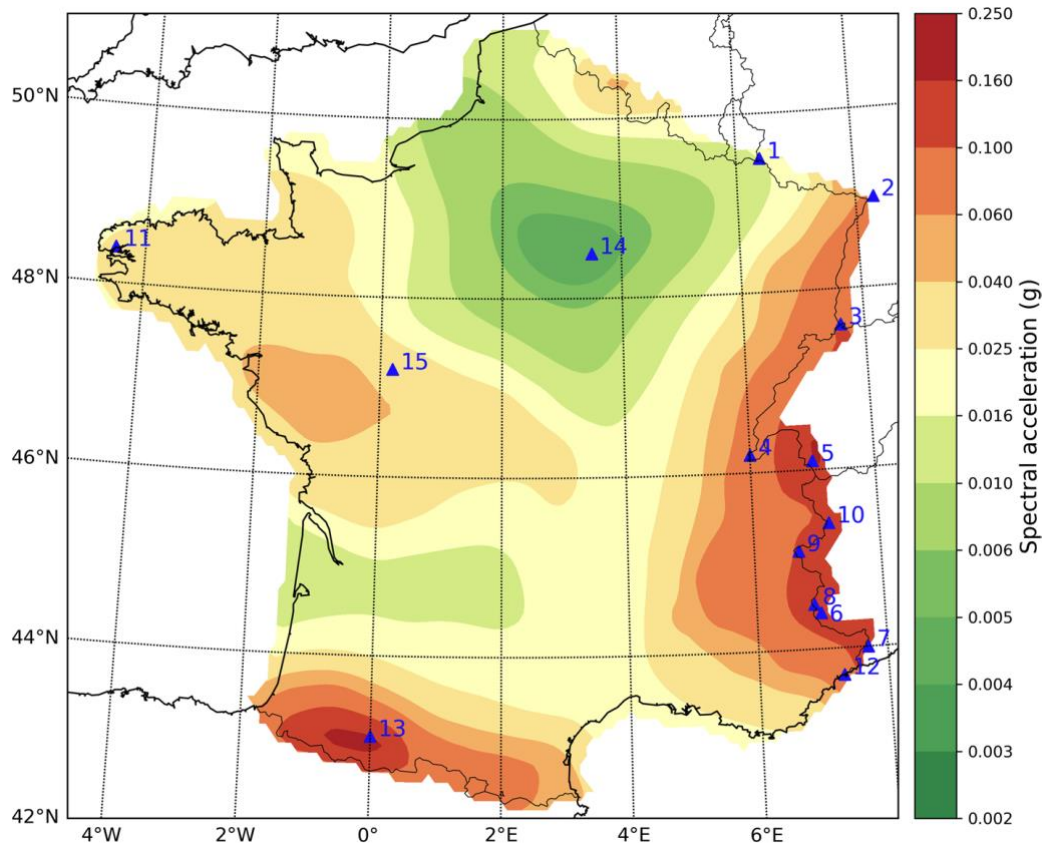


Figure 1-12 PGA for 475-year return period for  $V_{s30} = 800 \text{ m/s}^2$  (Drouet et al. 2020). The blue triangles are points where Drouet et al. (2020) compared their model with other PSHA studies.

#### 1.1.8 Mosca et al. (2020) (UK)

Mosca et al. (2020) is an update of the onshore UK national seismic hazard maps conducted by Musson and Sargeant (2007). They used a Monte Carlo-based approach like Musson and Sargeant (2007). The results represent the official seismic hazard maps for use with EN 1998-1. Mosca et al (2020) developed an earthquake catalogue based on the BGS catalogue, the International Seismological Centre (ISC) online database and the earthquake catalogue of Manchuel et al. (2018) for France. The catalogue includes earthquakes up to 31 August 2018. The seismic source characterisation is based on the areal source model used by Woessner et al. (2015) for the SHARE project with some modifications (Figure 1-13). Mosca et al (2020) used the same ground motion models and weights as Tromans et al. (2019) for their PSHA of the nuclear power plant at Hinkley Point, in Somerset, southwest England. Figure 1-13 also shows the PGA on rock for 475-year return period.

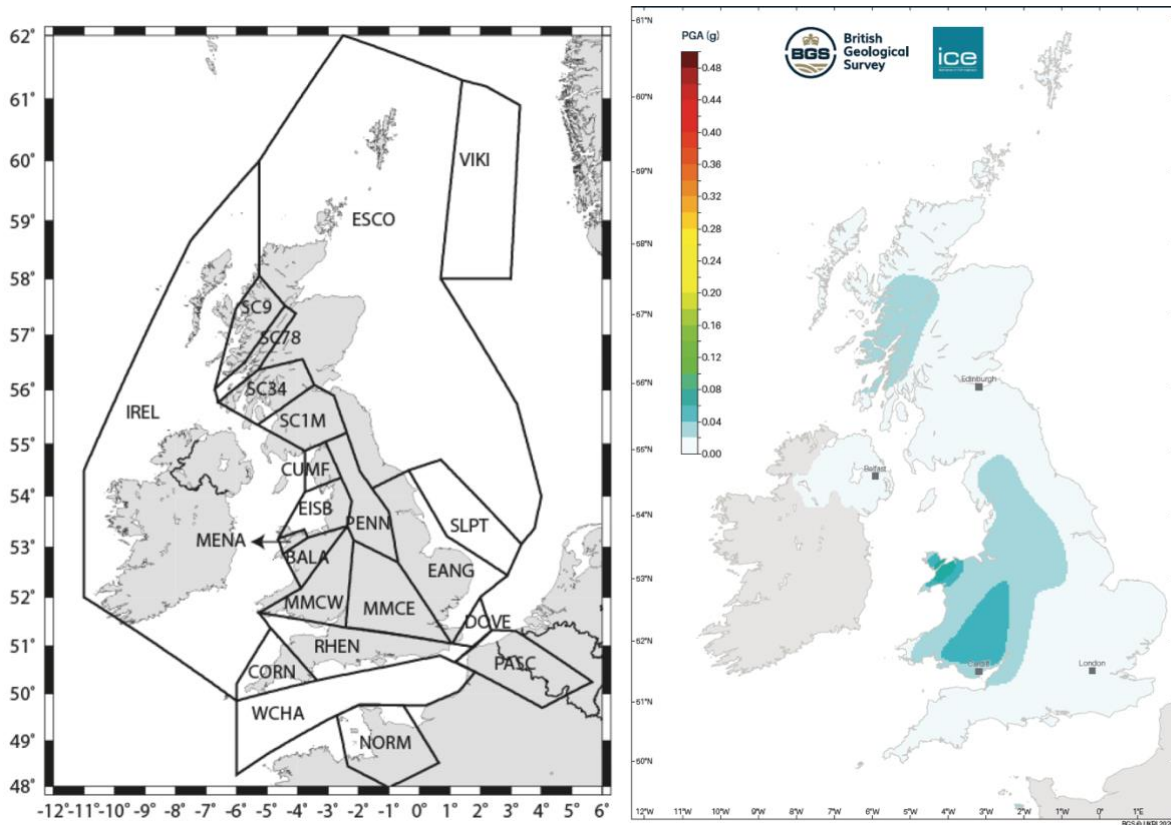


Figure 1-13 Left: Seismic source model used in Mosca et al. (2020). Right: PGA on rock for 475-year return period.

#### 1.1.9 Danciu et al. (2021) (ESHM20)

The 2020 European Seismic Hazard Model (ESHM20) (Danciu et al., 2021) is an update of the SHARE project and follows the same principles and methodology. Danciu et al. (2021) used an areal source model (Figure 1-14) and a fault source model with smoothed background seismicity. The areal seismic source zonation is the same as Mosca et al. (2020) for the UK, Bungum et al. (2000) for Norway, Model C from Grünthal et al. (2018) for Germany and the IRSN model described in Drouet et al. (2020) for France. To model earthquake shaking a scaled backbone approach was used. This method uses a single ground motion model scaled up and down with adjustment factors that consider the epistemic uncertainty. Figure 1-15 shows the PGA on rock for 475-year return period.

**ESHM20: Area Sources Model**

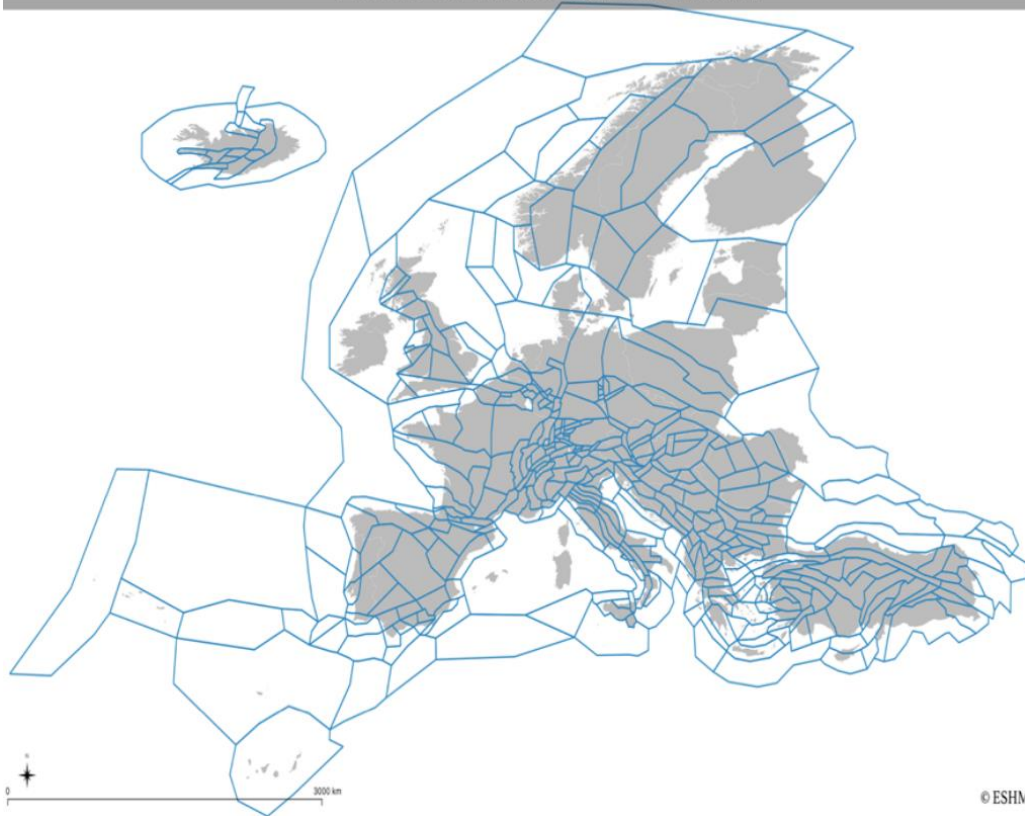


Figure 1-14 Areal source model used in the ESHM20 project (Danciu et al., 2021).

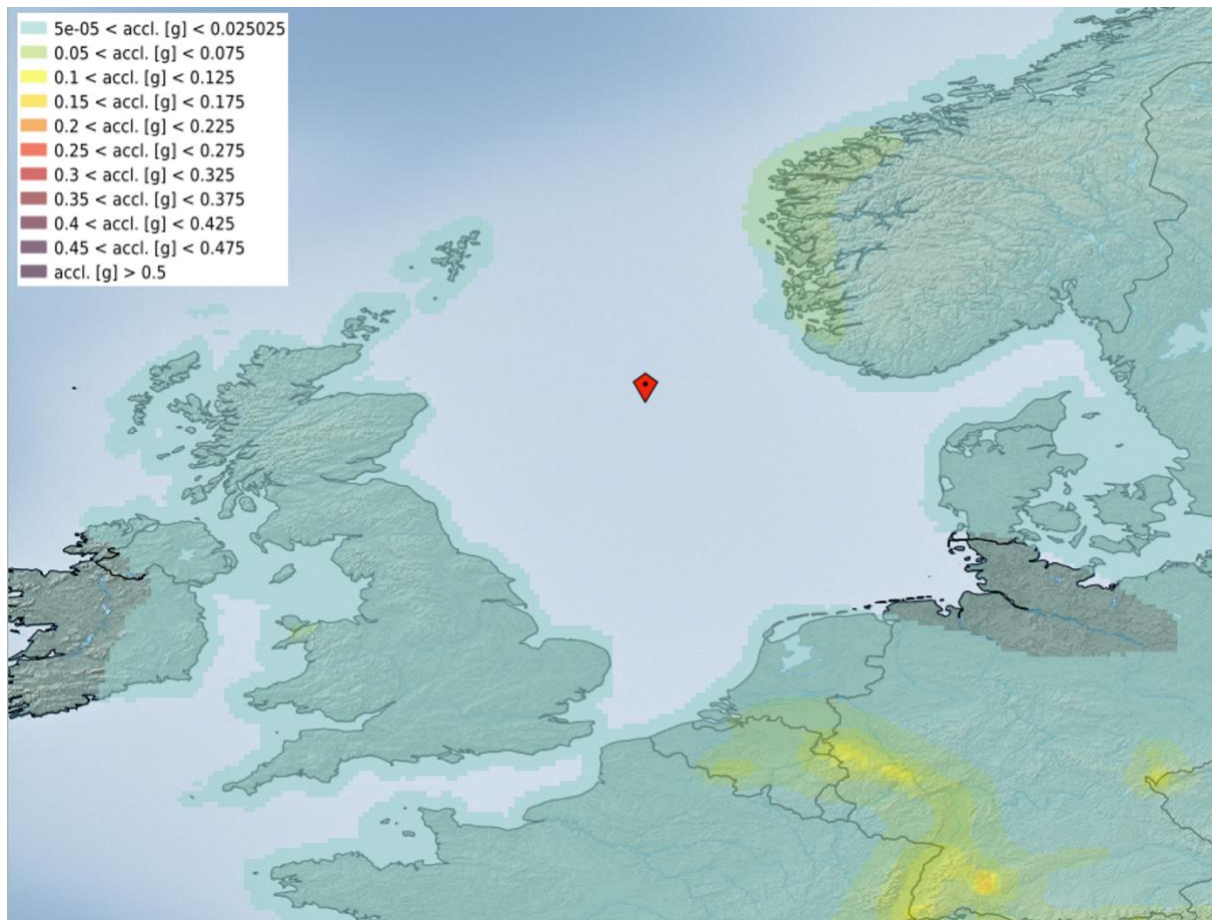


Figure 1-15 PGA on rock for 475-year return period from the ESHM project (Danciu et al., 2021).

-

#### 1.1.10 Offshore wind farms

Several PSHA conducted for offshore wind farms in the North Sea are publicly available. In the Dutch sector, site investigation and PSHA are collected by the Netherlands Enterprise Agency (RVO) and stored on their website (<https://offshorwind.rvo.nl/>). PSHA reports for at least four windfarm zones are currently available to the public. All four reports use similar seismic source models consisting of three different areal source models and five ground motion models. Seismic source Model 1 is based mainly on the GEOTER model for France described in Le Dortz et al. (2019) and Drouet et al. (2020) as well as Grünthal et al. (2018) for Germany. Model 2 is based on the seismic hazard assessment of Belgium by Verbeek et al. (2009) and model D from Grünthal et al (2018) for Germany. Model 3 is based on model C from Grünthal et al (2018) for Germany.

Carlton et al. (2022) performed a PSHA for the Sofia offshore windfarm, which is located about 200 km off the east coast of England on the Dogger Bank. They used one areal source model based on Bungum et al. (2000) with additions from Musson and Sergeant (2007) and one areal source model based on the SHARP project (2015), as well as four smooth gridded seismicity models based on different magnitude conversion and declustering techniques.

Finally, Carlton et al. (2019) present a simplified PSHA for a potential CO<sub>2</sub> storage site at Smeaheia, 60 km off the west coast of Norway. They used one areal source model and one smoothed gridded seismicity model along with the NGA East ground motion models (Goulet et al., 2018).

## 1.2 CO<sub>2</sub> storage case studies

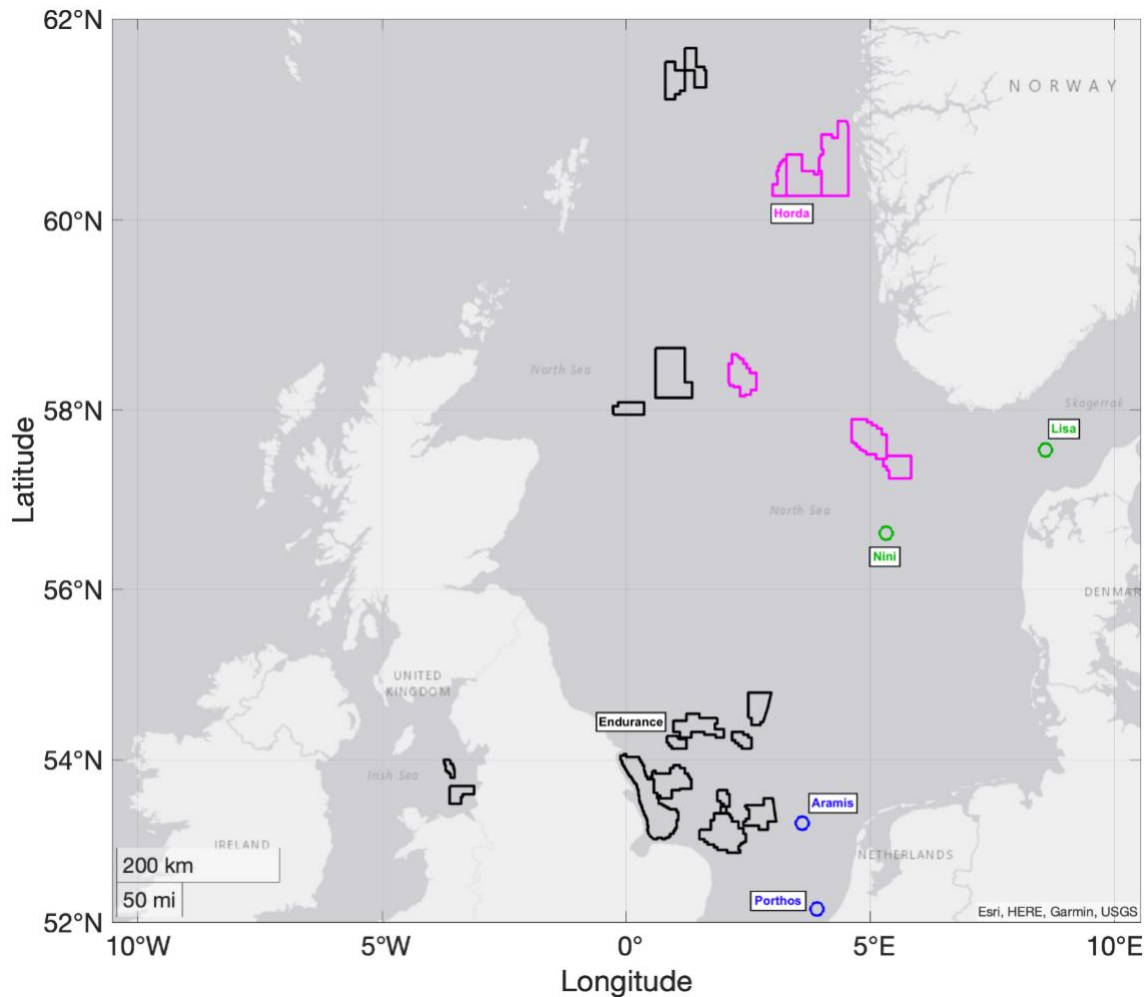


Figure 1-16 Map showing the locations of the case study areas of the SHARP project. Polygons show the carbon storage licence blocks for both the UK (black) and Norway (magenta). Circles show the approximate locations of the Dutch (blue) and Danish (green) case study projects. Project names are annotated.

The SHARP project focusses on several case study projects in the North Sea. Their locations are shown in Figure 1-16. For the UK, this is the Greater Bunter Sandstone area, east of central England. Chiefly, this focusses on the Endurance project, located around 60 km east of Flamborough Head. In Norway, this is the Horda platform region, chiefly the Eos well, a part of the Northern Lights project. In the Netherlands, it is the Aramis project located around 120 km northwest of Amsterdam, as well as the Porthos site, near to the Port of Rotterdam. In Denmark, there is the Greensand project in the Nini West field, located around 170 km west of the Danish coast, and the Lisa structure, closer to land off the north coast.

Each case study serves to better understand how states of stress can be better underpinned in different storage contexts. Each however also exists in different seismological contexts, with strongly varying activity rates and sizes of nearby historical earthquakes (See Section 3). This means that seismic hazard varies significantly across the region. Thus, there is a clear necessity for hazard to be thoroughly

and accurately quantified using the most appropriate ground motion models and underlying source characterisation data.

### 1.3 Ground motion limits

It is valuable to contextualise the forecasted ground motions from hazard models with the engineering limits that are often given in international engineering standards commonly adopted by regulators. Here, we will briefly summarise some of the relevant regulations in North Sea jurisdictions, and what limits they impose.

The seismic hazard code for onshore buildings and infrastructure in the EU – Eurocode EN.1998.1.2004 – explicitly excludes offshore developments from its remit. It states that: “structures, such as... offshore structures... are beyond the scope of EN 1998.”

The International Standards Organisation’s (ISO) ISO 19901-2:2022 is the key engineering standard for oil and gas offshore infrastructure. It details specific requirements for offshore structures with respect to seismic design procedures and criteria. Whilst it does not explicitly mention CO<sub>2</sub> storage, it is reasonable to assume that this standard may be adopted for the storage industry. It is at least a reasonable analogue for comparison of the procedures and hazard limits imposed.

This standard is adopted in the UK (as BS EN ISO 19901-2:2022), which is the British implementation of the European Union’s EN ISO 19901-2:2022, which is identical to ISO 19901-2:2022. The Norwegian adoption of this standard is listed under NS-EN ISO 19901-2:2022. All the above CO<sub>2</sub> storage case studies thus fall under this same standard. There are some specific national provisions included in ISO 19901-2:2022, with Norway being the one relevant for the SHARP project. This modifies some specific probabilities and definitions around proscribed exposure level of earthquake hazard in Norwegian waters.

ISO 19901-2 contains a procedure to estimate if there is a need for engineering design to take seismic risk into account. Figure 1-17 shows the spectral acceleration at a period of 1.0 seconds for a return period of 1000 years and rock site. In the North Sea, values of peak spectral acceleration range from 0.03 to 0.2 g. This standard gives guidance on whether simple or more complex modifications need to be made to engineering designs due to seismic risk. This is codified in a “seismic risk category” (SRC), also shown in Figure 1-17. The Danish projects and the Dutch Aramis project are in SRC 1 zones, and thus, by this standard, no extra evaluation for seismic hazard needs to be conducted. The UK Endurance, Norwegian Northern Lights, and Dutch Porthos projects are in SRC 2 zones, and thus only a simplified procedure of seismic risk assessment is deemed necessary. No North Sea case studies require the more intensive, site specific, seismic hazard analysis based on this standard. This “detailed seismic action procedure” is required to be conducted only for areas with a SRC of 3 or above, which have a PGA at 1.0 s period in a 1000-year return period of greater than 0.25 g.

However, regulators may still ask operators of CO<sub>2</sub> storage projects for a site-specific seismic hazard analysis due to the specific needs of ensuring containment of CO<sub>2</sub>. This will be in addition to the above requirements laid out in these standards. If any do exist, specific thresholds or criteria for seismic hazard have not been made publicly available by North Sea regulators.

Other engineering standards for seismic hazard exist for the offshore wind industry: Risø Guidelines for Design of Wind Turbines, Guideline for the Certification of Wind Turbines by Germanischer Lloyd, International Electrotechnical Commission's IEC 61400-1: Wind turbines - Part 1: Design requirements, and the DNV standard: Support structures for wind turbines. These generally conclude that return

periods of 475 years are most appropriate for seismic hazard analysis of wind turbine structures. They also detail how hazard analyses need to be modified to suit the torsional stresses that wind farms are more susceptible to, such as treating horizontal and vertical ground motions from earthquakes separately.

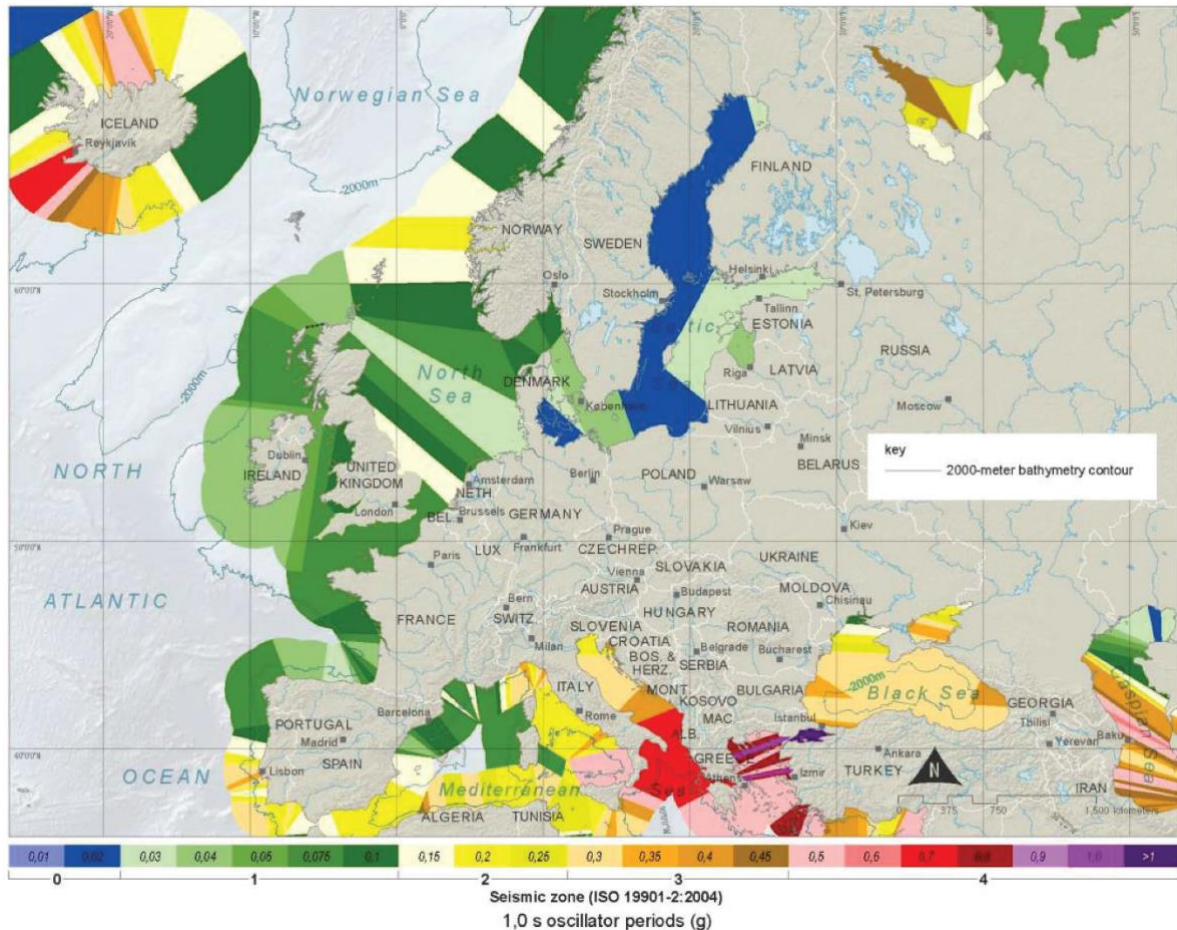


Figure 1-17 5% damped spectral response acceleration map at a period of 1.0 seconds from ISO 19901-2. Colours represent different levels of the response spectral value for a one second oscillator period ( $S_a(T=1)$ ) for a 1000-year return period. Levels of  $S_a(T=1)$  determine the seismic risk category (SRC) zone, shown by the bar under the map. This map is the result of a PSHA analysis conducted by ISO 19901-2 (2022). Depending on which SRC zone a structure falls in determines whether a simple or more detailed action on seismic integrity risk needs to be conducted.

## 2 Methods

### 2.1 Probabilistic seismic hazard analysis (PSHA)

PSHA is a methodology that estimates the probability that an earthquake intensity measure will be exceeded at a given location in a set future time period. The main purpose of a PSHA is to aid in the decision of what level of an intensity measure to use in the design of a structure to ensure a desired performance state, and what magnitude and distance combination are most likely to produce the chosen level of the intensity measure.

We performed the PSHA calculations using the computer program HAZ45.3 developed by Professor Norman Abrahamson (Abrahamson, 2023; Hale et al., 2018). This program implements the PSHA methodology developed principally by Cornell (1968) and refined by McGuire (1974; 1978). This PSHA method has five basic components (Baker, 2008):

1. Identify all relevant earthquake sources.
2. Characterize the rates at which earthquakes of various magnitudes ( $M$ ) are expected to occur for each source.
3. Characterize the distribution of source-to-site distances ( $R$ ) for each source.
4. Predict the chosen intensity measure for all combinations of magnitude, distance and  $\epsilon$  (the number of standard deviations of the ground motion model used to estimate the intensity measure) for each source.
5. Calculate the hazard curve for each intensity measure as follows:
  - a. Combine probabilities of  $M$ ,  $R$  and  $\epsilon$  to calculate the rate that each  $M$ ,  $R$ , and  $\epsilon$  scenario occurs.
  - b. Rank each scenario according to the predicted intensity measure.
  - c. Sum the rates of each scenario from largest intensity measure to smallest intensity measure, so that smallest intensity measure (least damaging) has the greatest rate of exceedance (hazard level).
  - d. Plot the rate of exceedance versus intensity measure to obtain the hazard curve.

Figure 2-1 shows the five components graphically. The design value of the intensity measure is chosen as the value corresponding to the hazard level deemed acceptable based on consequences of failure and societal risk. Acceptable hazard levels are often specified in standards or by local governments.

In PSHA there are two main types of uncertainty: aleatory variability and epistemic uncertainty.

Aleatory variability is the natural randomness in a process. As more data are collected the aleatory variability does not necessarily increase or decrease, it just becomes more accurate and closer to the true randomness of the process. In PSHA, the aleatory variability is characterised by the probability density function for some variables (e.g., for earthquake magnitude or depth), and by first and second moments (mean and standard deviation) for the ground motion models. Aleatory variability controls the shape of the hazard curve.

Epistemic uncertainty is the scientific uncertainty in a model due to imperfect knowledge, which may be due to limited data and/or simplified mathematical idealisation. In theory, as more data are collected, epistemic uncertainty should decrease. Examples of epistemic uncertainty in PSHA are alternate seismic source models and ground motion models, and different maximum magnitudes, widths and faulting types of a given source.

Epistemic uncertainty is considered in PSHA by using a logic tree framework (Kulkarni et al., 1984). Each branch of the logic tree represents an alternative credible model or parameter value and is given

a weight. The weights at each branch tip are mutually exclusive and collectively exhaustive and must sum to one. The weights are based on engineering judgment of how accurate or 'credible' each alternative model is. In this way, the use of a logic tree allows multiple credible models to be included in the PSHA. When using a logic tree, a separate PSHA is conducted for each combination of alternative models (i.e. each final branch of the logic tree). Then, all the different hazard curves are combined using the branch weights to estimate the mean hazard.

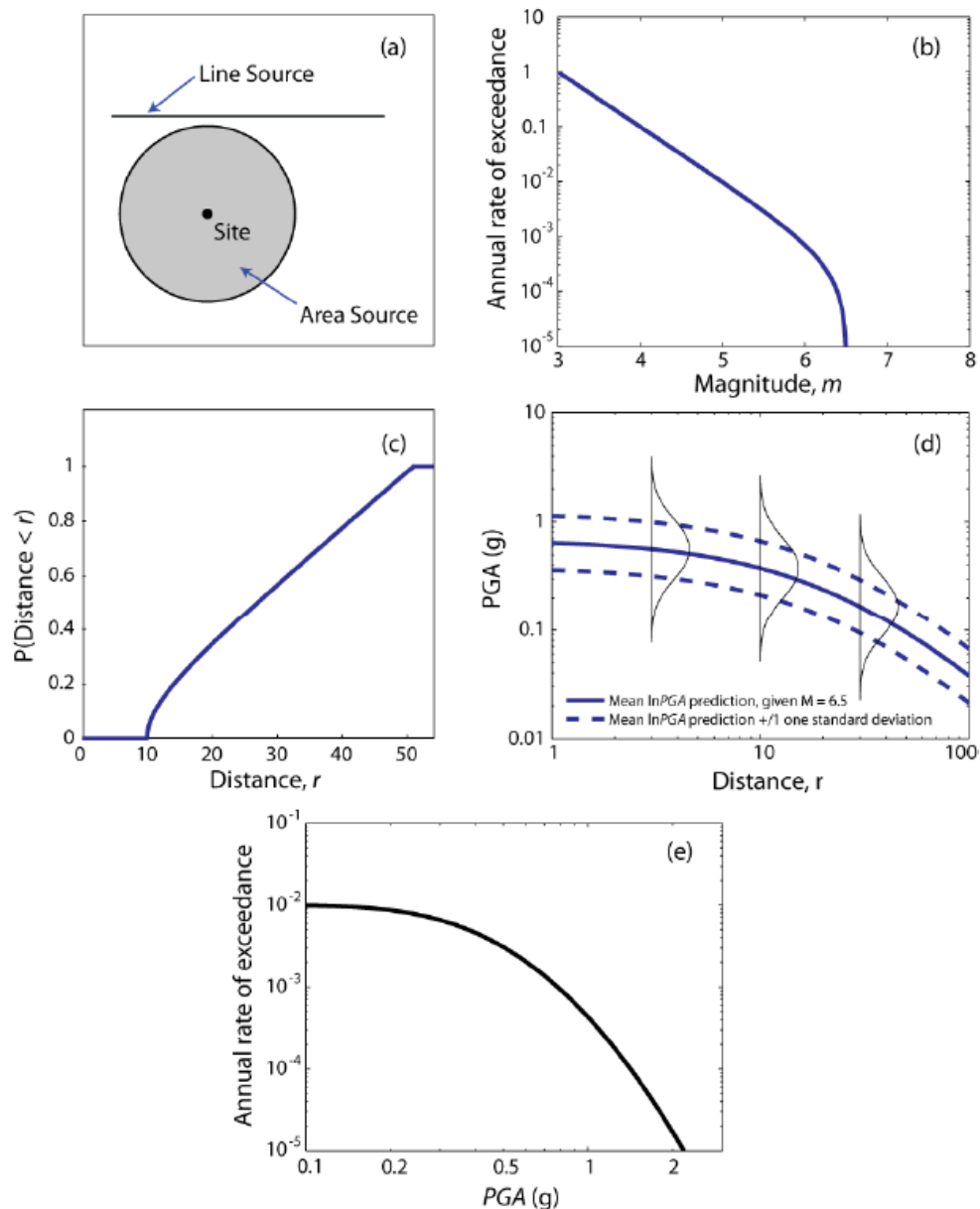


Figure 2-1 Schematic illustration of the five main components of a PSHA. (a) Identify earthquake sources. (b) Characterize the rate of occurrence of earthquake magnitudes for each source. (c) Characterize the distribution of source-to-site distances for each source. (d) Predict the intensity measure for all combinations of magnitude, distance and epsilon. (e) Combine information from parts a-d to compute the annual rate of exceedance for a given intensity measure (Baker, 2008).

## 2.2 Ground motion models

A ground-motion model (GMM), also known as ground motion prediction equation (GMPE), is a statistical model that is calibrated based on observations and/or simulations, which describes the (median) IM estimate and its variabilities as a function of various predictor variables (e.g., magnitude, source-to-site distance). In a broader definition, a GMM also involves the spatial correlation and the cross-IM correlation, which describe the underlying correlation structures in the residuals of the ground-motion prediction function. It is one of the key components in PSHA (i.e., step 4) to predict the distribution of selected intensity measures (IMs). A schematic plot of the GMM and the associated major effects was presented in Figure 2-2.

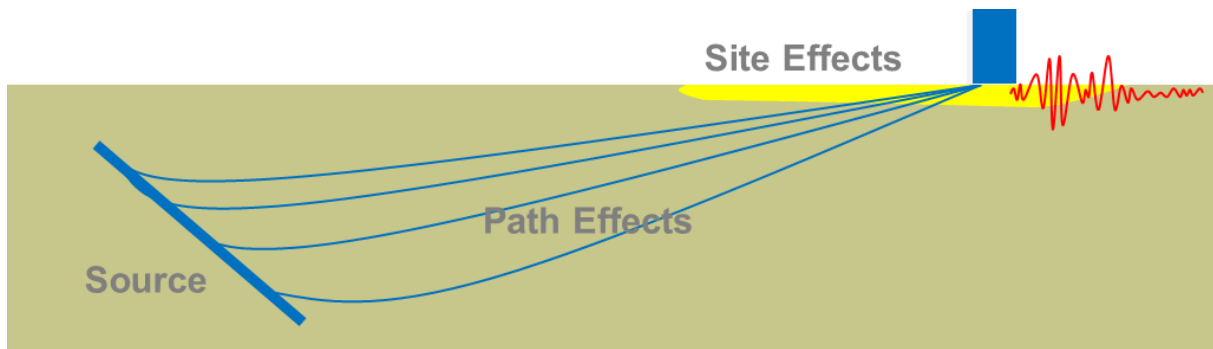


Figure 2-2 A schematic plot of the GMM and the associated major effects.

The state of practice is to treat the GMM as a mixed-effects model with a certain correlation structure (Jayaram and Baker, 2010) as in Equation (1),

$$Y_{ij} = f(\mathbf{X}_{ij}, \mathbf{b}) + \eta_i + \varepsilon_{ij}, i = 1, \dots, N, j = 1, \dots, n_i \quad (1)$$

where  $Y_{ij} = \log_{10} IM_{ij}$  is the logarithm of IM at station  $j$  of earthquake  $i$ ;  $f(\mathbf{X}_{ij}, \mathbf{b})$  is the ground-motion prediction function with a matrix of predictor variables  $\mathbf{X}_{ij}$  for station  $j$  during earthquake  $i$  and a vector of unknown model coefficients  $\mathbf{b}$ ; the total error is decomposed into the interevent error  $\eta_i$  and the intra-event error  $\varepsilon_{ij}$ ;  $\eta_i$  is the interevent error of earthquake  $i$  with zero mean and  $\tau$  standard deviation, accounting for the variability between events at the same site;  $\varepsilon_{ij}$  is the intra-event error at station  $j$  of earthquake  $i$  with zero mean and  $\phi$  standard deviation, accounting for the variability between different sites within the same event;  $N$  is the number of earthquake events;  $n_i$  is the number of recording stations during earthquake  $i$ .

The ground-motion IMs are simplified representations of the complete ground-motion waveforms, capturing various features of the recorded accelerograms. It is commonly assumed that the logarithmic IMs,  $Y_{ij}$ , follow a multivariate normal distribution (Jayaram and Baker, 2008, Foulser-Piggott and Stafford, 2012; Kempton and Stewart, 2006; Stafford et al., 2016), as shown in Equation (2).

$$\mathbf{Y}_i \sim \mathcal{N}[f(\mathbf{X}_{ij}, \mathbf{b}), \tau^2 \mathbf{1}_{n_i \times n_i} + \phi^2 \mathbf{\Omega}_i(\omega)] \quad (2)$$

where  $\mathbf{1}_{n_i \times n_i}$  is an  $n_i \times n_i$  matrix of ones. Let  $\mathbf{\Lambda}_i(\boldsymbol{\lambda}) = \tau^2 \mathbf{1}_{n_i \times n_i} + \phi^2 \mathbf{\Omega}_i(\omega)$  where  $\boldsymbol{\lambda} = (\tau^2, \phi^2, \omega)^T$ , the covariance matrix for the total errors of the considered IM (of all the considered earthquakes),  $\mathbf{\Lambda}(\boldsymbol{\lambda})$ , is the direct sum of  $(\mathbf{\Lambda}_i(\boldsymbol{\lambda}))_{i=1, \dots, N}$ , denoted as  $\mathbf{\Lambda}(\boldsymbol{\lambda}) = \oplus_{i=1}^N \mathbf{\Lambda}_i(\boldsymbol{\lambda})$ . To account for the spatial correlation, the  $jj'$ -th element of  $\mathbf{\Omega}_i(\omega)$  (i.e., i.e., the spatial correlation between site  $j$  and  $j'$  during

earthquake  $i$ ) can be expressed as a function of the inter-station distance under the second-order stationary  $d_{jj'}$ . The exponential spatial correlation function was considered  $k(d_{jj'}) = \exp(-d_{jj'}/h)$ , where the positive range parameter  $h$  represents the characteristic length scale (corresponding to the distance as which the spatial correlation is 0.37 in the exponential case). The effective range  $\tilde{h}$  is the effective range corresponding to 0.05 spatial correlation and  $\tilde{h} = 3h$ .

This study considered three categories of commonly used ground-motion IMs:

- Time-domain amplitude-based IMs associated with the peak ground shaking and elastic structural responses (e.g., peak ground acceleration, spectral ordinates)
- Frequency-domain amplitude-based IMs associated with seismological effects (e.g., effective amplitude spectra)
- Integral IMs related to the cyclic energy dissipation (e.g., arias intensity, significant duration).

The IM of multiple components, particularly the two orthogonal horizontal, was computed following the geometric mean and RotD50 definitions. The geometric mean was preferable in the preliminary analysis due to that the far-field weak-motion data has less noticeable polarise effect. The difference between the geometric mean and RotD50 is insignificant. Future work will compute the RotD50 and compare the ground motion characteristics, leading to an updated GMM.

- Geometric mean:  $\sqrt{IM_x \cdot IM_y}$ . Compared to taking the larger component out of the two horizontal components, the geometric mean leads to lower aleatory uncertainty in GMMs (Beyer and Bommer, 2006, 2007).
- RotD50: the 50th percentile (median) value computed from the time series  $a_{Rot}(t) = x(t) \cdot \cos(\theta) + y(t) \cdot \sin(\theta)$ , where  $\theta$  is the rotation angle ranging from 0 degree to 180 degree. RotD50 is independent of the in situ orientation, which can handle an extreme case of polarised ground motions better than the geometric mean.

The ground-motion prediction function  $f(\mathbf{X}_{ij}, \mathbf{b})$  can be expressed as follows, to account for the dependence of IMs on the source, path, and site effects:

$$f(\mathbf{X}_{ij}, \mathbf{b}) = f(source) + f(path) + f(site) \quad (3)$$

The source function  $f(source)$  includes the magnitude accounting for seismic energy. Bommer et al. (2010) have suggested that the GMM should include the nonlinear magnitude term (e.g., quadratic magnitude function  $M_w^2$ ) to model the magnitude saturation (i.e., the IMs do not increase at a constant rate or without bound with the increasing magnitude). The path function  $f(path)$  includes the source-to-site distance representing the seismic wave propagation and attenuation. Bommer et al. (2010) have suggested the magnitude-dependent distance term (e.g.,  $M_w \log(R)$ ) should be included in GMM to account for the distance saturation (i.e., the distance range within which the IMs saturates (roughly in the near field) is not constant for all sizes of earthquakes), which is because the rupture area increases with increasing earthquake magnitude (Wells and Coppersmith, 1994). The site function  $f(site)$  includes the variables (e.g., site classification or  $V_{s30}$ ) related to near-surface soil conditions. Other predictor variables (e.g., stress drop and hanging wall effect) are included in recent GMMs to further explain the dependence on various effects but are not considered in this study due to the lack of sufficient data to restrain the model parameters.

The spatial correlation and cross-IM correlation influence the inter-event and intra-event variabilities, which can be accounted for through the covariance matrix for the distribution of  $(\mathbf{Y}_i)_{i=1, \dots, N}$  in the considered IMs. A homoscedastic aleatory variability (i.e., the interevent and intra-event standard

deviations,  $\tau^2$  and  $\phi^2$ , are constant across sites and events) is assumed in Equation (2), as the limited data in this study will not be statistically sufficient to model heteroscedasticity (e.g., aleatory uncertainty as a function of magnitude, source-to-site distance, site effects and/or other parameters).

The ergodic assumption, which is commonly considered in the existing GMMs, suggests that the source, path, and site effects estimated, and the variability measured from the recordings of a global database accurately represent those properties expected at a single site (Graves et al., 2011; Stewart et al., 2017). This assumption is commonly considered in regions where ground motion data is sparse and utilizes global data or region with data abundant. Same assumption is pertained in this study, which can be improved in the future if more regional data are available.

The maximum likelihood estimation approaches with the consideration of interevent and intra-event components of ground-motion variability have become the standard to estimate the model parameters (e.g.,  $\mathbf{b}$ ,  $\tau^2$  and  $\phi^2$ ) (Douglas and Edwards, 2016). Abrahamson and Youngs (1992) and Joyner and Boore (1993) have proposed the maximum likelihood-based algorithms to estimate the mixed-effects GMM without correlation structure (i.e.,  $\mathbf{\Omega}_i(\omega) = \mathbf{I}_i$ ). Chen and Tsai (2002) have extended the Joyner and Boore (1993) algorithm by adding an interstation random effect but still without a correlation structure. To incorporate the spatial correlation in the GMM estimation process, Jayaram and Baker (2010) and Hong et al. (2009) have improved the algorithms of Abrahamson and Youngs (1992) and Joyner and Boore (1993), respectively. Although these multi-stage algorithms are feasible in practice and may be numerically stable by estimating the parameters, particularly spatial correlation function in separate steps, it is not optimal in various aspects from a statistical estimation perspective.

To address this issue, Ming et al. (2019) developed a one-stage estimation method based on the method of scoring (Fisher, 1925) under the maximum likelihood estimation framework, as a specialised alternative procedure for fitting GMMs with spatial correlation. The Fisher scoring method is a modified version of the Newton-Raphson algorithm, which is more numerically stable. This classical method that is still widely used in the statistical field and implemented in many R packages, e.g., generalized linear modelling software (GLM). Compared to the multi-stage algorithms, The proposed one-stage estimation approach produces model parameter estimators consistently in a single stage, which admits any parametric class of correlation functions and associated spatial correlation properties. The general procedure is shown in Figure 2-3 and for more mathematical details please refer to Ming et al. (2019).

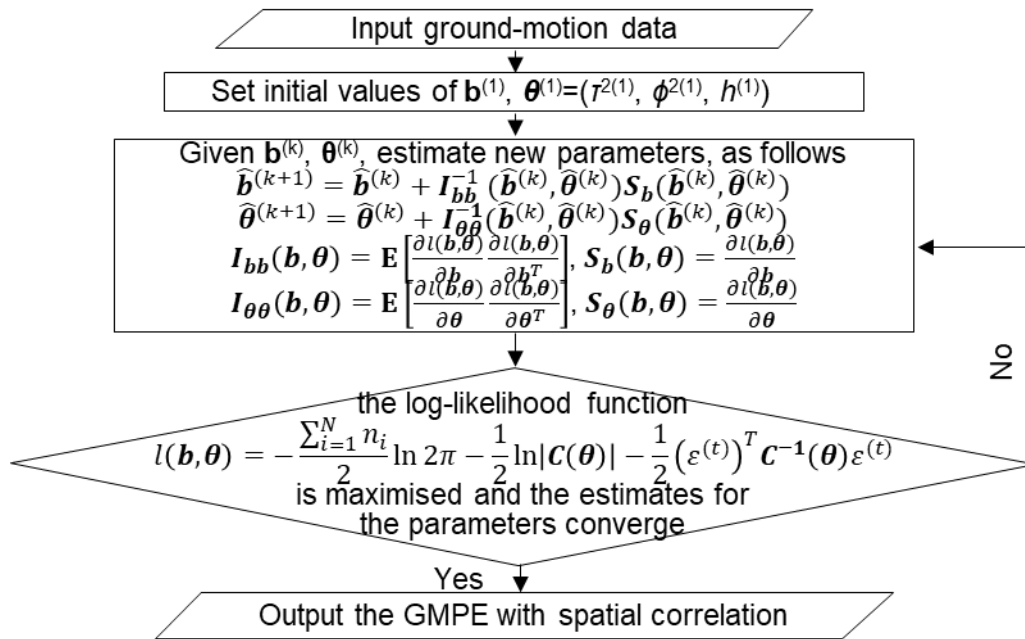


Figure 2-3 The one-stage estimation method based on the method of scoring (Fisher, 1925) under the maximum likelihood estimation framework.  $\mathbf{b}$  is the model coefficients and  $\tau^2$  and  $\phi^2$  are the standard deviations of interevent and interevent errors. If spatial correlation is considered,  $h$  is the interstation distance related to spatial correlation.

This method has been applied to develop a new GMM with spatial correlation using the Italian strong-motion records for a set of IMs, to investigate the correlation properties in ground motions (Huang and Galasso, 2019, Huang et al., 2020).

### 2.3 High frequency attenuation

Kappa ( $\kappa$ ) is a measure of the high-frequency energy attenuation of ground motions (Anderson and Hough, 1984). It is an essential parameter for two tasks related to seismic hazard. The first is to adequately calibrate physical models, which are then used to develop a database of synthetic ground motions. The database of synthetic ground motions can then be used to aid in the development of a region-specific ground motion model. This is especially useful in areas such as the North Sea where the empirical database of ground motions is severely limited in the large magnitude and near distance ranges. The second main use of  $\kappa$  is to aid in the conversion of ground motion models developed for other regions to the target region, called host-to-target conversion method (Cambell, 2003). The host-to-target conversion method requires estimates of shear wave velocity ( $V_s$ ) and  $\kappa$  values of the underlying reference rock from the host and target regions. However, there are no estimates of  $\kappa$  for the North Sea, and assuming  $\kappa$  values from empirical correlations for other regions would add a large amount of uncertainty (Biro and Renault, 2012). Therefore, one of the objectives of this study was to estimate  $\kappa$  for sites in and around the North Sea.

We estimated  $\kappa_{r\_AS}$  using the method proposed by Anderson and Hough (1984). This method is based on the logarithmic decay of the acceleration Fourier amplitude spectrum (Figure 2-4). It is termed  $\kappa_{r\_AS}$  in the taxonomy of Ktenidou et al. (2014) because it is at a certain distance,  $r$ , from the source, and  $\kappa$  is calculated from the acceleration spectrum (AS). This method is viable for earthquakes of magnitude

about three or larger, where the low source corner frequency,  $f_c$ , allows the fitting to be performed above  $f_c$ . In this method,  $\kappa_{r\_AS}$  is calculated as:

$$\kappa_{r\_AS} = -\lambda/\pi \quad (1)$$

$$\lambda = \frac{\ln(A_{f_2}) - \ln(A_{f_1})}{f_2 - f_1} \quad (2)$$

where  $A$  is the Fourier amplitude of the S-wave window of the acceleration time series and  $f_1$  and  $f_2$  are the lower and upper frequency bounds used to calculate  $\kappa_{r\_AS}$ . We calculated the  $\kappa_{r\_AS}$  for both horizontal components and took the average. We only used ground motions with  $f_2 - f_1 > 8$  Hz, to ensure a robust calculation of  $\kappa_{r\_AS}$  (Ktenidou et al., 2013).

We followed the recommendations of Ktenidou et al. (2016) to select  $f_1$  and  $f_2$ . We selected  $f_1$  as the larger of LUF,  $1.5 \cdot f_c$ , or 5 Hz. LUF is the lowest useable frequency and is taken as  $LUF = 1.25 \cdot f_{cHP}$  (Goulet et al., 2014). The  $f_{cHP}$  is the high pass frequency and is the highest frequency from the following two criteria: lowest frequency with signal to noise ratio  $SNR > 3$  or the frequency where the FAS at low frequencies starts to deviate from a line equal to  $f^2$ . The line equal to  $f^2$  is based on the theoretical acceleration decay at low frequencies of the  $f^2$  model (Brune, 1970, 1971). We used the highest selected frequency from all three components as the  $f_{cHP}$  for all three components.

The buffer of 1.5 above the corner frequency ( $f_c$ ) is to avoid trade-offs between the source and the site as well as uncertainty in the estimate of  $f_c$  (Ktenidou et al., 2016). The corner frequency was estimated as (Brune, 1970, 1971):

$$f_c = 4.9 * 10^4 * \beta * \left(\frac{\Delta\sigma}{M_0}\right)^{1/3} \quad (3)$$

$$M_0 = 10^{(1.5 \cdot M_w + 16.05)} \quad (4)$$

where  $f_c$  is in Hz,  $\beta$  is the shear wave velocity at the source in km/s,  $\Delta\sigma$  is the stress drop in MPa, and  $M_0$  is the seismic moment in  $N \cdot m$ . We assumed  $\beta = 3.5$  km/s and  $\Delta\sigma = 10$  MPa (100 bar). These assumptions gave a reasonable fit for most of the ground motions.

The limiting value of 5 Hz was imposed to ensure only high frequencies were used in the calculation of kappa.

The value of  $f_2$  was selected as  $f_2 = HUF$ , where HUF is the highest useable frequency. HUF was calculated as  $HUF = f_{cLP}/1.25$ , where  $f_{cLP}$  is the low pass frequency.  $f_{cLP}$  was calculated as the highest frequency with signal to noise ratio  $SNR > 3$  that was lower than the Nyquist frequency. We used the lowest selected frequencies from all three components (two horizontal and one vertical) as the  $f_{cLP}$  for all three components.  $\kappa_{r\_AS}$  can only be measured in the usable frequency range (LUF to HUF). This is to ensure the ground motion has been corrected for the instrument response and there is an adequate signal to noise ratio (Ktenidou et al., 2016).

Parolai and Bindi (2004) found that soil amplification can affect the measured value of  $\kappa_{r\_AS}$ . For example, a shallow impedance contrast caused by a thin deposit of soft soil over hard rock would cause an amplification peak in the high-frequency range where  $\kappa_{r\_AS}$  is measured (Figure 2-5). If  $\kappa_{r\_AS}$  is measured before the peak this results in an underestimation, and if it is measured after the peak this results in an overestimation (Ktenidou et al., 2016). We calculated average horizontal-to-vertical spectral ratios (HVSr) for each site (Lermo and Chavez-Garcia, 1993). This provides an indication of the frequencies most affected by local site resonance. We either removed sites with a clear indication of

soil amplification, selected  $f_1$  and  $f_2$  to avoid the frequencies affected by amplification, or selected  $f_1$  and  $f_2$  over a wide frequency band to minimize the effect of site amplification (Parolai and Bindj, 2004).

Anderson and Hough (1984) found that  $\kappa_{r_{AS}}$  values for a given station increase with distance. From this observation they hypothesised that  $\kappa_{r_{AS}}$  includes contributions from both the local geology of the top few kilometres of crust beneath the station (site) and the regional geological structure (path). To isolate the value of  $\kappa$  due to just site effects (termed  $\kappa_{0_{AS}}$  by Ktenidou et al., 2014), they suggested to extrapolate values of  $\kappa_{r_{AS}}$  back to  $R_{epi} = 0$ . Ktenidou et al. (2014) found that in most cases a linear or bi-linear model is adequate. This implies a depth and frequency independent value of anelastic attenuation ( $Q$ ) for the frequencies over which  $\kappa_{r_{AS}}$  is measured. The bi-linear model consists of a constant for short distances followed by a linearly increasing line for longer distances. The maximum distance where path affects are apparent (i.e. the distance from zero out to where the bi-linear model remains flat) depends on the region (Ktenidou et al., 2016), with more active regions having smaller values of  $Q$  and as a result the effect of distance becomes noticeable at shorter distances. For example, Kishida et al. (2014) estimated  $\kappa$  for ground motions from southern Arizona and found no dependence on distances out to 60 km, whereas Ktenidou et al. (2014) measured  $\kappa$  for ground motions in Greece and found no dependence on distance only up to 20 km. We fit bi-linear models where the hinge distance was a regression parameter. We performed regression analyses to estimate  $\kappa_{0_{AS}}$  for each station, as well as different regions.

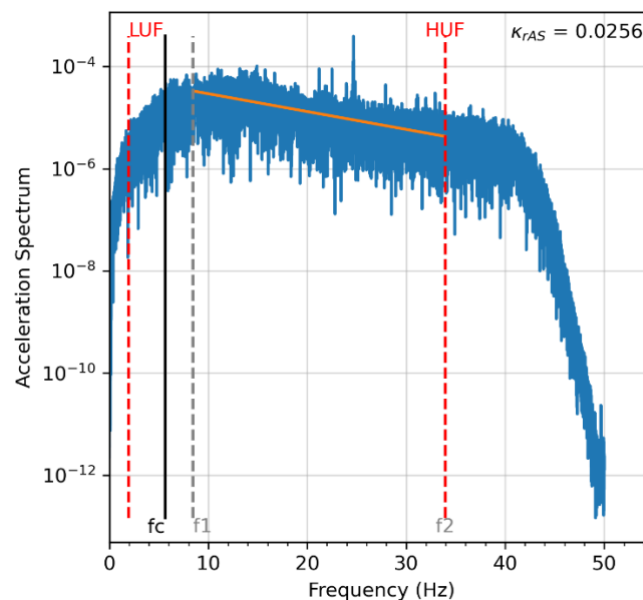


Figure 2-4 Example selection of  $f_1$  and  $f_2$  and calculation of  $\kappa_{r_{AS}}$  (orange line) for a  $M_w = 3.6$  earthquake that occurred on April 1, 2010, recorded at the BER station with  $R_{epi} = 284$  km.

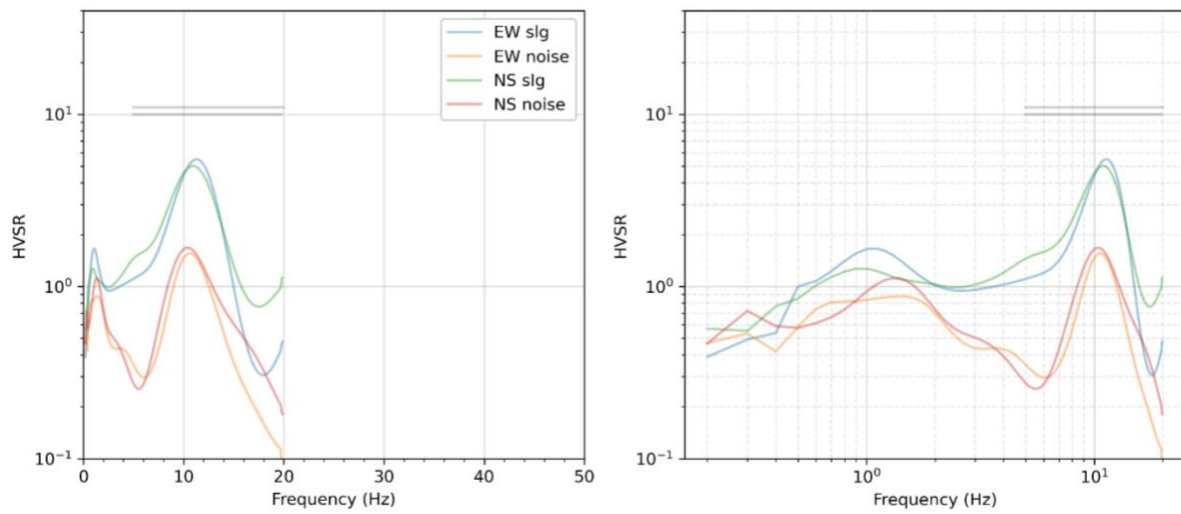


Figure 2-5 Horizontal to vertical spectral ratios (HVSr) for station NGW20. The coloured lines are the average HVSr for the EW and NS components from all records. The grey lines show the ranges of  $f_1$  and  $f_2$  for each of the records.  $S_{lg}$  is the HVSr from the S-wave window of the acceleration time series and noise is from the noise trace.

### 3 SHARP Seismicity Catalogue

This new GMM and PSHA analysis is being supported with data that was produced by the SHARP project in its second work package. This focused on seismological data and methods, and its first deliverable was a large collection of earthquake data from the North Sea. This data forms the most complete and homogeneous record of earthquakes in the region. It is detailed in Deliverable D2.1, and updates to it are given in D2.4. Here, we will briefly summarise the dataset, and how it has been used and adapted for use in the seismic hazard analyses.

#### 3.1 North Sea catalogue

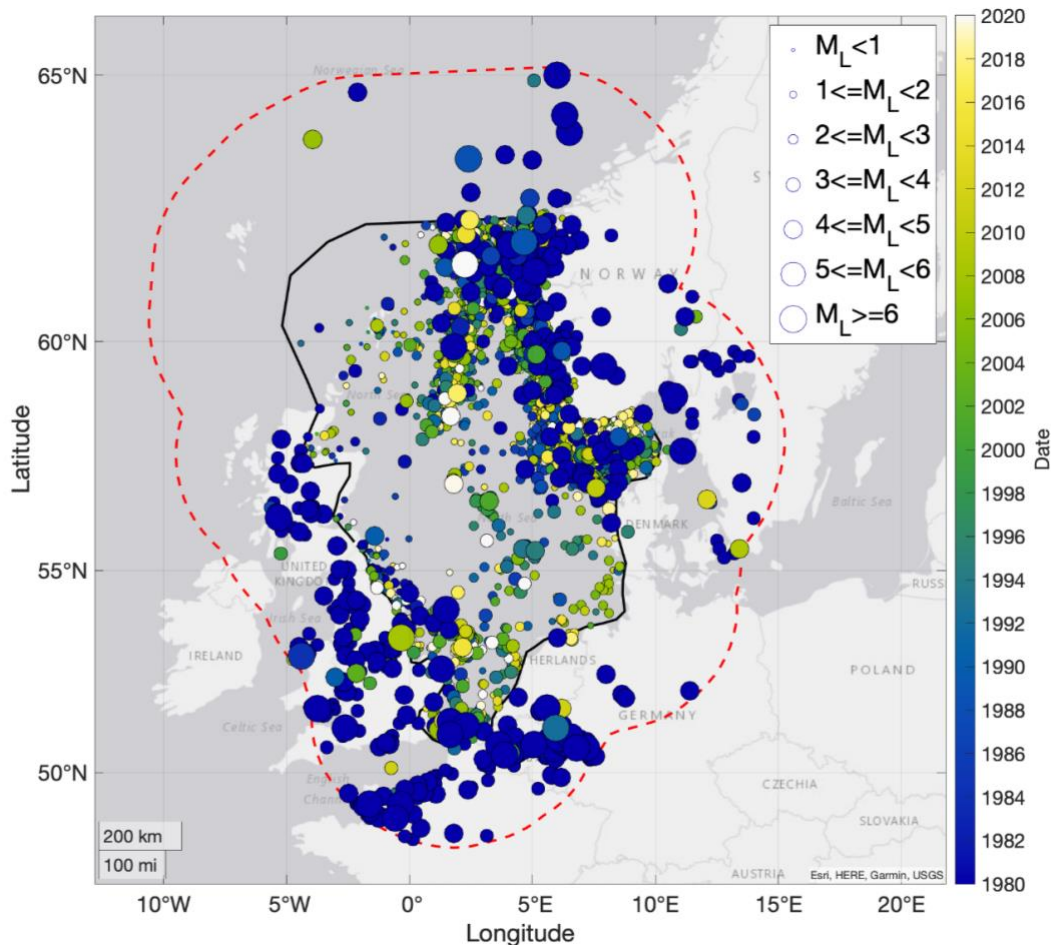
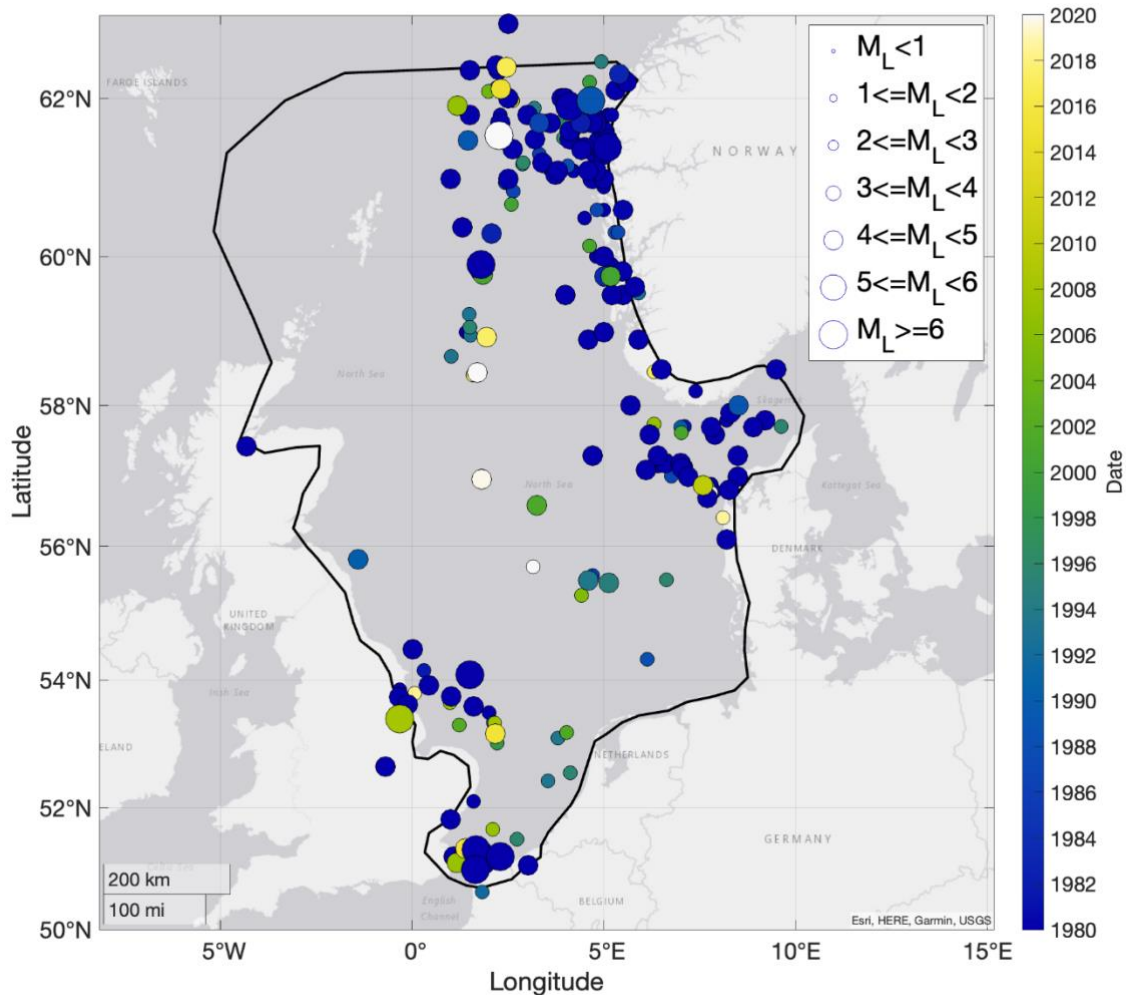


Figure 3-1 Map showing the expanded version of the SHARP North Sea catalogue intended for seismic hazard analysis. Events are sized by magnitude and coloured by occurrence time since 1980. The black solid line shows the original North Sea polygon used for discriminating events that are of primary interest to the SHARP project, while the red dashed line shows the expanded region.

An extensive data collection and amalgamation exercise was conducted within the SHARP project to amass all available records of earthquakes that took place in the North Sea. The merging and cleaning of the data, and subsequent removal of “explosion” signals (as opposed to earthquakes), was a lengthy exercise. This led to the earthquake data shown in Figure 3-1. This data forms the most complete and homogeneous records of earthquakes in the region, as is enabling several ongoing research activities. These include relocation, moment tensor inversion, and stress drop analysis.

The initial region of interest for the data collection exercise was defined by the polygon shown in Figure 3-1 by the black solid line. This rings the North Sea area, extending onshore by around 5 to 10 km, and surrounds the CO<sub>2</sub> storage projects of interest to this project. All follow-on activities thus far have focussed on events just within this area.



*Figure 3-2 Map of events within the SHARP North Sea study area (shown by the black polygon) with local magnitude above 3.5. These are the events which are particularly relevant for seismic hazard analysis. Events shown just outside the polygon region have at least one origin within the polygon, though here the prime origin is shown.*

For seismic hazard analysis, felt earthquake occurrence rates need to be quantified both within and outside the region of interest. The current version of the North Sea earthquake catalogue was formed using a spatial filter, (i.e., the polygon). For the seismic hazard analysis that is being conducted in here, the current catalogue needed to be expanded, including event data for a 300 km area around the polygon. This larger region is shown in Figure 3-1 by the red dashed line.

Figure 3-2 also shows the events which were added in this expansion to the initial SHARP earthquake catalogue. The event data was collected from the [European Seismic Hazard Model 2020](#) (ESHM20), which contains event times, hypocentres, and moment magnitudes. These events included historical

seismicity dating back to 1349 CE within the North Sea study area, and 1000 CE within the expanded region. These historical data are primarily collected from Rovida et al. (2022). Data for 579 events were added to this expanded version of the bulletin from the ESHM20 database. 122 of these events were within the original polygon, and 457 were outside. Where there was already data in the bulletin for a ESHM20 event (i.e., for the 122 events), the origin and magnitudes were folded into the appropriate data blocks. This merging of event data was manually quality-controlled to ensure no false mergers occurred. Earthquakes outside the polygon were added as wholly new events.

It may appear that there are a great number of larger magnitude events in the supplemental region shown in Figure 3-1. This is an effect of selection, completeness, and plotting. The ESHM catalogue provides data for larger events, dating back as far as possible. These larger events naturally only have magnitudes which are relevant to seismic hazard (generally  $M > 3$ ). Equivalently large and historic events that may have occurred in the middle of the North Sea study region likely were undetected, and thus not present in the historical data which makes up most of the ESHM earthquake catalogue. The seismic hazard analysis naturally focusses on the larger events in the catalogue, though smaller are shown in Figure 3-1. Figure 3-2 and Figure 3-3 show the events in the North Sea study area with a magnitude great than 3, that are more relevant for the seismic hazard analysis here.

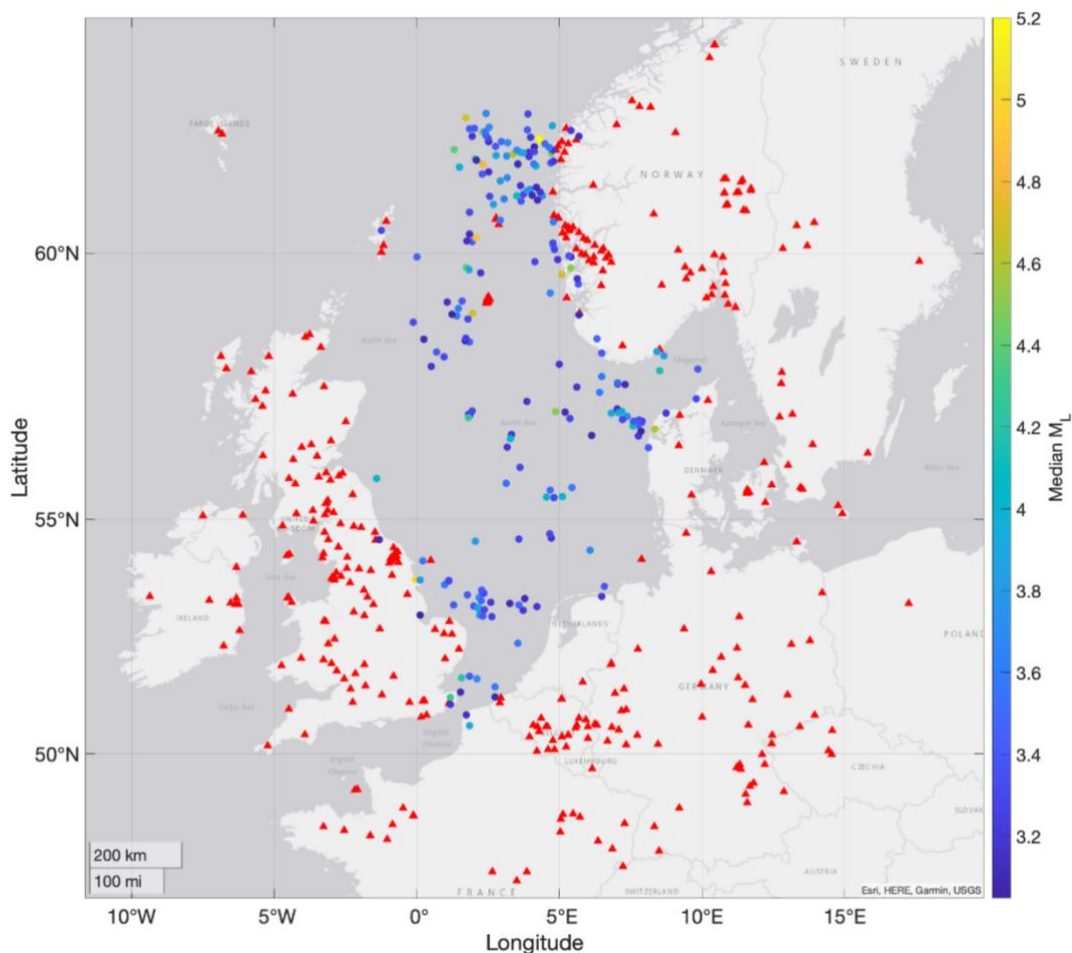


*Figure 3-3* Map showing events (epicentres shown by coloured circles) with a local magnitude above 3. These are coloured by magnitude. Red triangles show the locations of seismic monitoring stations for which data was represented in the full SHARP earthquake bulletin (an expanded catalogue which includes arrival times of events at stations).

### 3.2 Waveform database

In the SHARP project, it became increasingly clear that waveform data for events in the above catalogue would be needed to facilitate much of the future work, including the GMM and near surface attenuation work detailed below. An extensive search of waveform archives was conducted for all events in the catalogue with a magnitude greater than 3.5 which took place after 1990. These data were compiled into a waveform repository that was accessible by all SHARP project partners.

Figure 3-3 shows the location of seismic stations for which waveform data was retrievable for events in the catalogue. Naturally, smaller events are recorded on fewer, closer stations. Few stations in the region can acquire usable data for smaller earthquakes across the North Sea, at larger (>100 km) distances. These large event-station distances of many of the events affects the construction of the GMM significantly, as discussed in Section 4.

## 4 Ground motion model development

### 4.1 Data quality control

The data quality control was primarily focused on the waveform processing, which partially governs the final compilation of the North Sea waveform database. It also includes the verification of the station metadata (e.g., instruments and site conditions).

#### 4.1.1 Waveform processing

Using the SHARP database, we downloaded all available waveforms for records with an epicentral distance  $R_{epi} \leq 100$  degree  $\sim 1000$  km and moment magnitude  $M_w \geq 3.5$ . We then processed the ground motions using the ObsPy package in python (Beyreuther et al, 2010) following a similar methodology to the PEER NGA East project (Goulet et al., 2021). We applied the following three-stage processing scheme to the earthquake waveforms, as shown in Figure 4-1.

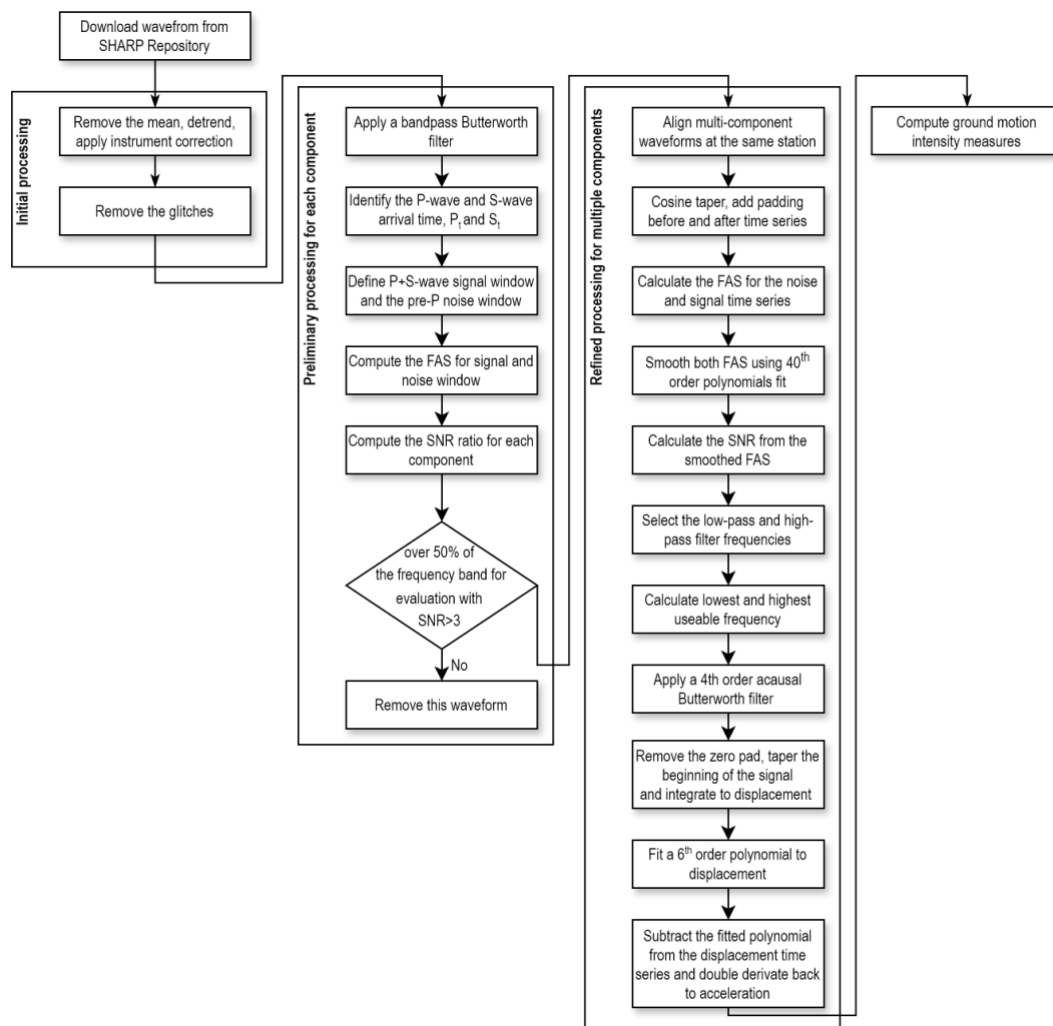


Figure 4-1 The three-stage processing scheme. The initial processing focuses on removing the instrument response. The preliminary processing focuses on selecting each individual component with signal to noise ratio (SNR)  $>3$ . The refined processing focuses on aligning multiple-component waveform and baseline correction.

### *Download waveform*

1. Download each signal 120 seconds before and 360 seconds after the given event time.

### *Initial processing*

2. Remove ground motions with less than three components (two horizontal and one vertical)
3. Remove the mean, detrend, apply instrument correction.
4. Remove glitches, where glitches are defined as absolute values  $1e8$  times larger than the average of the absolute values of the waveform.

### *Preliminary processing for individual waveform*

5. Compute P-wave ( $P_t$ ) and S-wave ( $S_t$ ) arrival times
  - a. Apply a bandpass Butterworth filter at 0.8 Hz and 80% of the Nyquist frequency to help pick P-wave and S-wave arrival times. The median Nyquist frequency is 20 Hz.
  - b. Compute P-wave and S-wave arrival times using the STA/LTA algorithm
  - c. Compute the P-wave and S-wave arrival times based on seismic wave travel times using the iasp91 velocity model (Kennett and Engdahl, 1991).
  - d. before 2000 priority STA/LTA, after 2000 If the P-wave arrival time estimated from the AR-AIC + STA/LTA method occurs before the event time, use the P-wave and S-wave arrival times estimated from this method. Otherwise, use the P-wave and S-wave arrival times estimated from the travel time method.
6. Compute SNR
  - a. Model the noise time series as five seconds after the start of the trace (i.e. 115 seconds before the event start time) to three seconds before the P-wave arrival time (Figure 4-2).
  - b. Define the duration of the signal time series window as  $\max(30, 5*(S_t - P_t))$  seconds
  - c. Model the signal time series as five seconds before the P-wave arrival time plus the duration of the signal time series window (Figure 4-2).
  - d. Compute frequency spectra FAS (using multitaper,  $P = 4$ ,  $k_{spec} = 7$ ) over the P+S-wave window and compare it to the pre-P noise window
  - e. Compute the SNR within the frequency band for evaluation  $[0.1\text{Hz}, 85\% \text{ of } f_N]$
  - f. Select the preliminary high pass frequency ( $f_{c_{HP,0}}$ ) as lowest frequency with  $\text{SNR} > 3$
  - g. Select the preliminary low-pass filter frequency ( $f_{c_{LP,0}}$ ) as the highest frequency with  $\text{SNR} > 3$
7. Keep waveform that over 50% of the frequency band for evaluation with  $\text{SNR} > 3$  for refined processing.

### *Refined processing for multi-component waveforms*

8. Synchronise multi-component P and S picks
  - a. Select between STA/LTA and travel time, scrutinised with visual inspection. If travel time results is similar to STA/LTA results use the travel time results
  - It is worth noting that AR-AIC method was tested but not selected in the end because this method requires three-component waveform, which was not sufficient in the database. We aim to use as many waveforms as possible. Not many has three components, particular for the old records. The resultant records include a set of vertical records and a set of two-component horizontal records
9. Filtering
  - a. Apply a 5% cosine taper to the end of the noise and signal time series. This helps prevent numerical issues when calculating the Fourier amplitude spectra (FAS) (Goulet et al., 2021).
  - b. Add zeros to the end of both the signal and the noise time series until they have a length equal to the next power of two greater than twice either the signal or time series, whichever is larger. This avoids possible wrap-around effects that can occur in the time domain after applying acausal filters (Goulet et al., 2021).
  - c. Calculate the FAS for the noise and signal time series.

- d. Smooth both FAS using 40<sup>th</sup> order polynomials fit in the log-log domain. Bahrampouri et al. (2020) found that using a 40<sup>th</sup> order polynomial to smooth the FAS instead of the Konno-Ohmachi filter (Konno and Ohmachi, 1998) gave more reasonable choices for the filter corners and was much faster computationally.
  - e. Calculate the signal to noise ratio (SNR) from the smoothed FAS.
  - f. Select the low-pass filter frequency ( $f_{CLP}$ ) as the highest frequency with  $SNR > 3$  that is lower than the Nyquist frequency. Use the lowest selected frequencies from all three components (two horizontal and one vertical) as the  $f_{CLP}$  for all three components.
  - g. Select the high pass frequency ( $f_{CHP}$ ) as the highest frequency from the following three criteria: lowest frequency with  $SNR > 3$ , the frequency where the FAS at low frequencies starts to deviate from a line equal to  $f^2$ , or  $f = 0.05$  Hz. The line equal to  $f^2$  is based on the theoretical acceleration decay at low frequencies of the  $f^2$  model (Brune, 1970). The limiting frequency of 0.05 Hz was used to ensure a proper baseline correction (Bahrampouri et al., 2020). Use the highest selected frequency from all three components as the  $f_{CHP}$  for all three components.
  - h. Calculate the highest useable frequency as  $HUF = f_{CLP} / 1.25$  and the lowest useable frequency as  $LUF = f_{CHP} * 1.25$ .
  - i. Apply a 4th order acausal Butterworth filter to the signal at the high and low-pass frequencies.
10. Baseline correction:
- a. Remove the zero pad.
  - b. Taper the beginning of the signal using a 5% cosine taper.
  - c. Double integrate the signal to displacement.
  - d. Fit a 6<sup>th</sup> order polynomial to the displacement time series where the 0<sup>th</sup> and 1<sup>st</sup> order coefficients are forced to be 0.
  - e. Subtract the fitted polynomial from the displacement time series and double derivate back to acceleration.

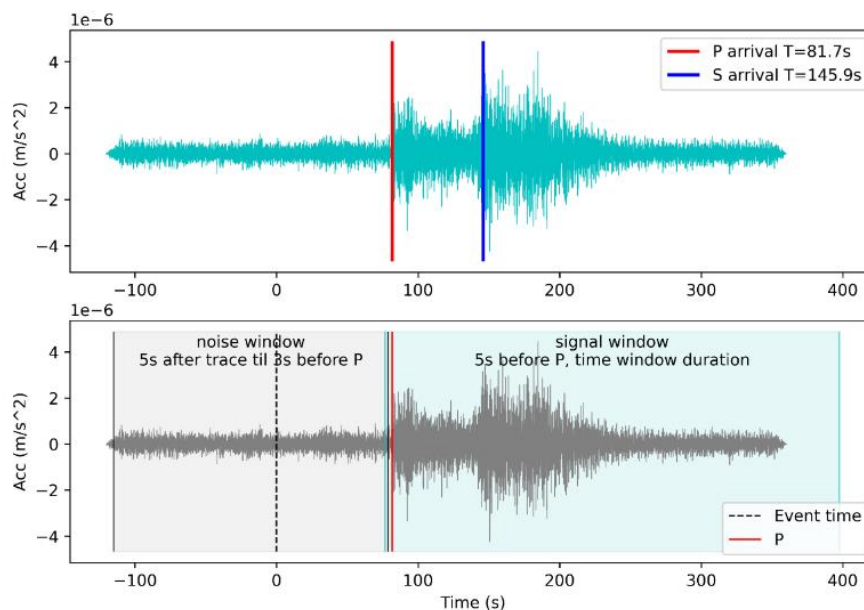


Figure 4-2 Example of preliminary processing.

#### 4.1.2 North Sea waveform database

It is worth pointing out that the North Sea database is under continuous development and maintenance of uniformly processed time series developed for the North Sea. The below results are collected based on the version 1.3 of the SHARP catalogue. The results should be considered as preliminary rather than finalised. The analysis process will be repeated based on the latest catalogue. The prime magnitude identified in the North Sea catalogue, which is usually the maximum of various magnitude scales reported by the agencies, is used for in the following analysis.

The current North Sea waveform database includes the three-component ground motion recordings from several selected events ( $M \geq 3.5$ , distances within 100 degrees or 1100 km epicentre distance) recorded in the North Sea region between 1990 – 2022, as shown in Figure 4-3. Most of the selected events are located on the west coast of Norway, the middle of the North Sea and the east coast of UK. Stations from Norway, Germany and the UK contributed the most recordings. A notable issue is the recording station coverage. Though there were various onshore stations around the North Sea, the scarcity of offshore stations within the North Sea (i.e., within the red North Sea polygon) poses a challenge in ground-motion model development. It is worth noted that offshore data from certain  $CO_2$  sites are collected within the SHARP project, however, due to the challenge in waveform processing (e.g., instrument response removal) they are not considered in the current GMM development.

Compared to the original North Sea catalogue, there are only a limited number of earthquakes selected for the ground motion study, as shown in Figure 4-4, and the reasons are two-fold. Firstly, an earthquake with a magnitude lower than 4 is considered of limited engineering significance and is expected to cause no damage to buildings. However, to balance the number of available data and the engineering significance, we extended the lower magnitude threshold to  $M 3.5$ , which still eliminated about 97% of events in the catalogue. Secondly, earthquakes with no three-component recording that passed the processing scheme (e.g.,  $SNR \geq 3$ ) were eliminated.

As shown in Figure 4-4, three moderate earthquakes with  $M \geq 5$  were selected. The largest earthquake is the  $M 5.2$  Florø earthquake occurred 130 km west of Florø in Bergen, Norway on 21 March 2022 at 06:32:57 am (local Norway time). This earthquake is one of the strongest earthquakes that has been registered in the area offshore Western Norway since instrumental recordings started in Bergen in 1905 (Ottemöller and Sørensen 2022). The  $M 5$  southern Viking graben earthquake on 30 June 2017 was one of the largest seismic events in the Norwegian part of the North Sea during the last century (Jerkins et al. 2020). The  $M 5$  earthquake shook the county of Kent, United Kingdom on 28 April 2007, which was the most damaging event to have occurred in the UK since the 1957 East Midlands earthquake (Rossetto et al. 2012).

The current North Sea database contains over 733 three-component records from 69 earthquake events at 132 recording stations. The magnitude-distance distribution of the North Sea database, as shown in Figure 4-5, showed that the database was dominated by far-field and low-magnitude data, as most of the stations are onshore about 500 km from the epicentres and over half of the data are for  $M 4.25$  and below. Compared to the NGA-East database covering 1 to 1000 km and  $M 2$  to 7 range in Figure 4-6, the North Sea database was narrower in both distance (100 to 1000 km) and magnitude range (3.5 to 5.5). The lack of near-field and large-magnitude data constrains the ground-motion model to a limited applicable range. Synthetic ground motions of near-field large-magnitude event may complement the observed database, if the synthetic ground motions are validated from seismological and engineering perspectives.

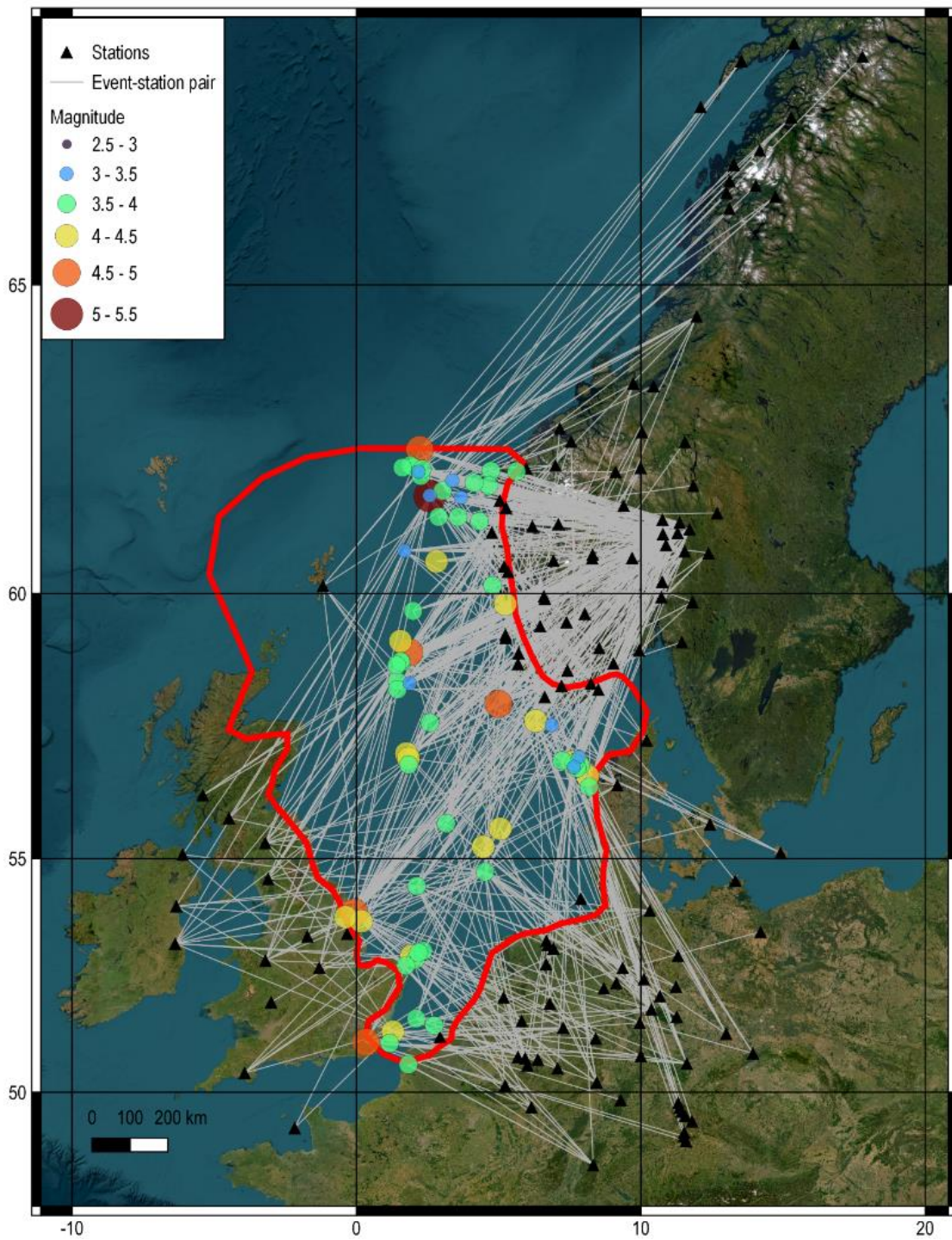


Figure 4-3 Event-station distribution. The red polygon is the North Sea polygon used for catalogue construction.

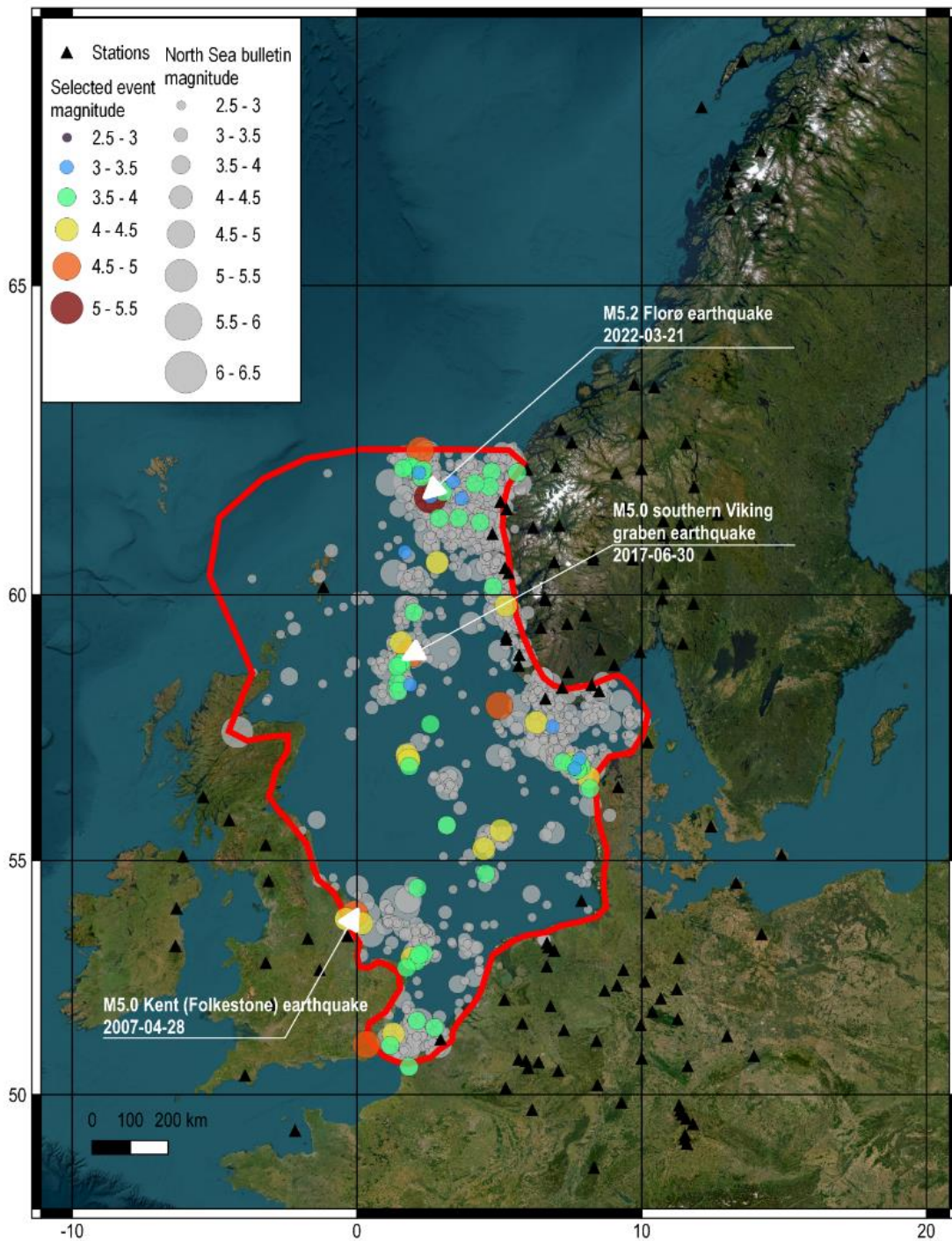


Figure 4-4 Comparison of the selected events (in colours) and events in the North Sea catalogue (in gray), with highlights on the three largest selected events.

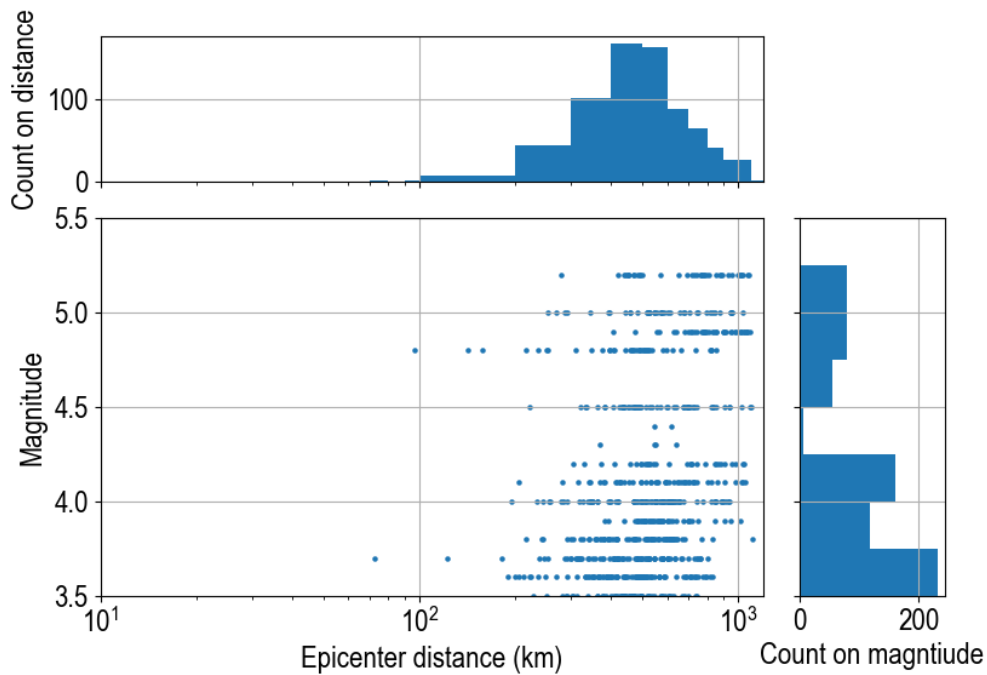


Figure 4-5 Magnitude-distance distribution of the North Sea database, with the corresponding histograms.

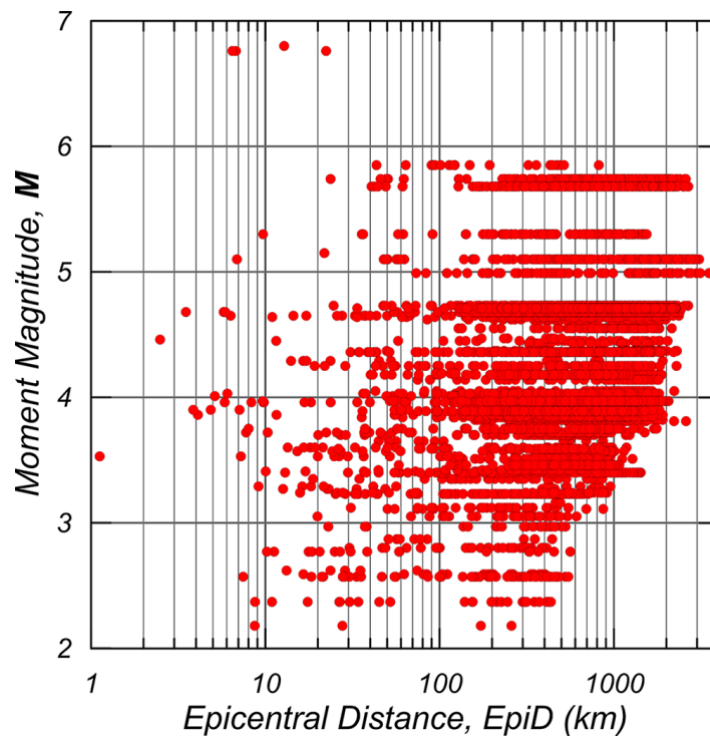


Figure 4-6 Magnitude versus distance coverage of recordings in the NGA-East ground-motion database from (Goulet et al. 2021).

### 4.1.3 Discussion

#### *Data selection criteria*

The data selection criteria were driven by the magnitude threshold  $M > 3.5$  and the processed waveforms, which were slightly different from the NGA-East process. NGA-East selection criteria require that the event catalogue includes all moment magnitude ( $M$ )  $> 4$  and selected well-recorded  $M \geq \sim 2.5$  earthquakes with five or more records within 100 km, to avoid smaller earthquakes with too few records and to focus on selecting earthquakes with more records at distances less than 100 km that can help the characterisation of geometrical spreading and attenuation. (Goulet et al. 2021b). However, due to event-station coverage, the North Sea data was naturally lacking near-field data. This will be addressed in the future by including good-quality waveforms from some events on offshore permanent reservoir monitoring (PRM).

#### *Uncertainty in event magnitude and location*

The prime magnitude used in this study was generally the maximum of the reported magnitude of different magnitude scales (e.g., mostly local magnitude, moment magnitude and surface magnitude). Though it indirectly relates to the total seismic energy released, the prime magnitude may bring in additional uncertainty in characterising the ground motions. This will be addressed using harmonised and unified converted magnitude in future work.

The accuracy of the location of the earthquake (i.e., longitude, latitude and depth) would have a greater impact in characterising the near-field ground-motion characteristics. However, the resultant database was dominated by far-field data, the impact of location on the geometric spreading and attenuation was limited.

## 4.2 Flat file construction

This section presents the overview of the preliminary flatfile, which is the building block for GMM development. The corresponding flatfile contains:

- metadata, if available, from the source and station databases;
- waveform processing information.
- time-domain amplitude-based IMs: the geometric mean of pseudo-spectral acceleration PSA, pseudo-spectral velocity PSV, and spectral displacement SD for 5%-damped elastic oscillators for periods ranging from 0.01 to 10 s;
- frequency-domain amplitude-based IMs: effective amplitude spectra EAS data within useable frequency range;
- energy-related integral IMs: the geometric mean of Arias intensity, cumulative absolute velocity (CAV), 5%-75% significant duration and 5%-95% significant duration;
- the processed and filtered time series.

Future work will compute the RotD50 and compare the ground motion characteristics, leading to an updated GMM.

### 4.2.1 Event metadata

The metadata of events (i.e., epicentre location, magnitude, hypocentre depth, focal mechanism) were collected from the North Sea catalogue and materials from WP2.

### 4.2.2 Station metadata

The metadata of station (i.e., network, instrument, site conditions) were collected from the respective agencies, as well as other openly available database.

All the waveform data was collected from seismometer stations, as limited accelerometer stations were available around the North Sea region. Only either “HH\*” channel (i.e., sampling rate about 80 to 250 Hz) or “BH\*” channel (i.e., sampling rate about 10 to 80 Hz) of the high gain seismometers were selected for further processing, while data from “LH\*” channel (i.e., sampling rate about 1 Hz) was removed due to low sampling rate. The distribution of station channel is shown in Figure 4-7 and about 62% data was collected from “BH\*” channel. Due to the seismometer sampling rate and far-field observations, the available number of recordings was significantly reduced for frequency above 15 Hz. Most of the available data are within the 1-10 Hz frequency range. Compared to the NGA-East database where about 90% of the collected data were recorded by seismographs as shown in Figure 4-9, the North Sea database showed similar distribution across frequency. In particular, the NGA-East database was spared above 14 Hz possibly due to the transportable array (TA) network (~14 Hz) (Goulet et al. 2021b).

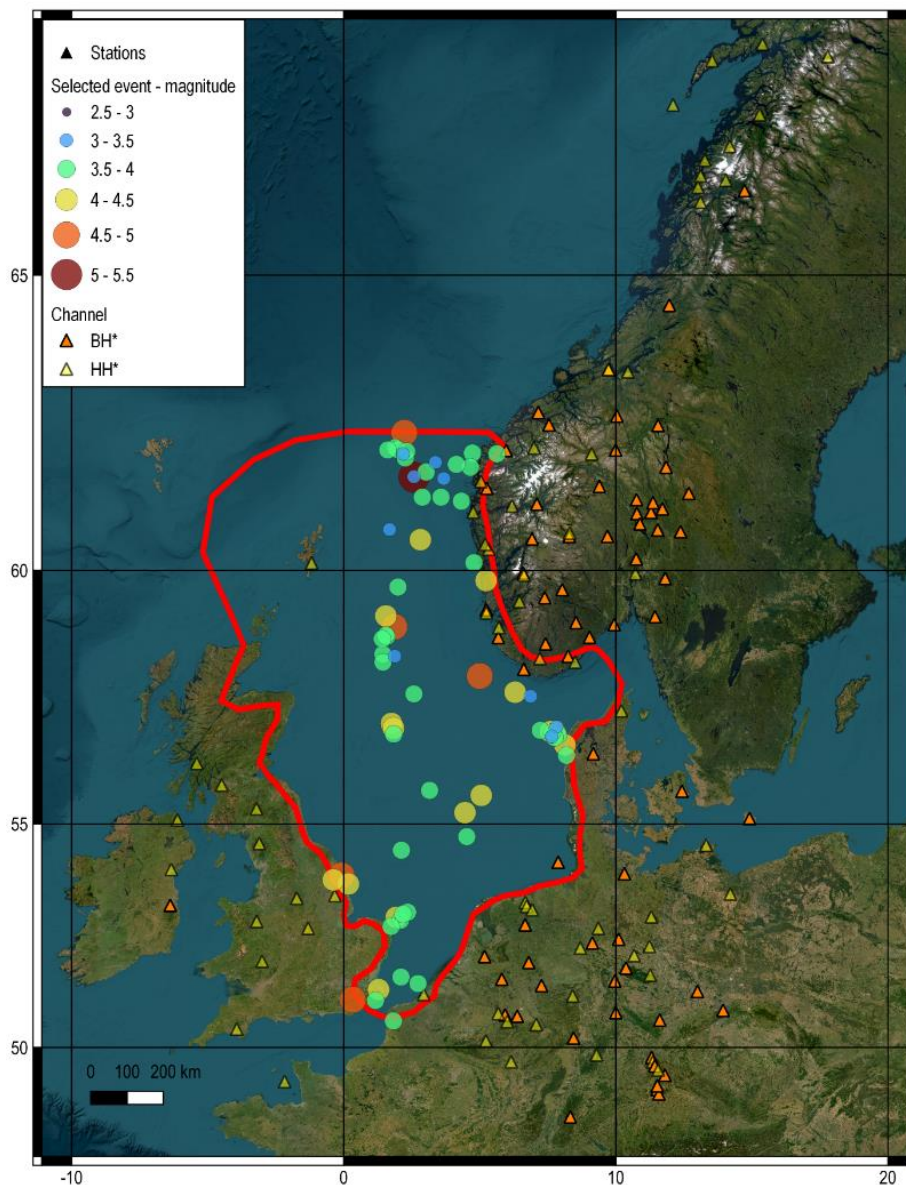


Figure 4-7 Distribution of station channel.

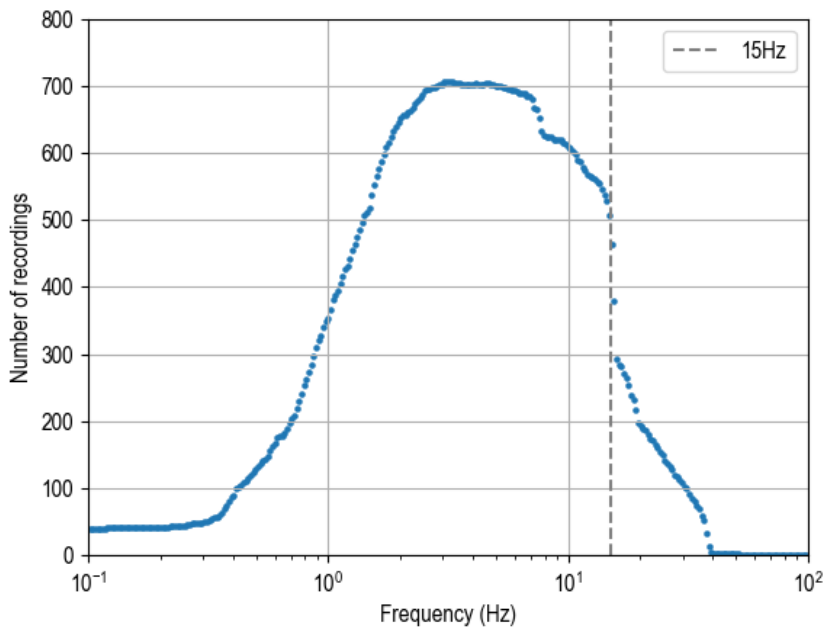


Figure 4-8 Number of recordings versus frequency in the North Sea database.

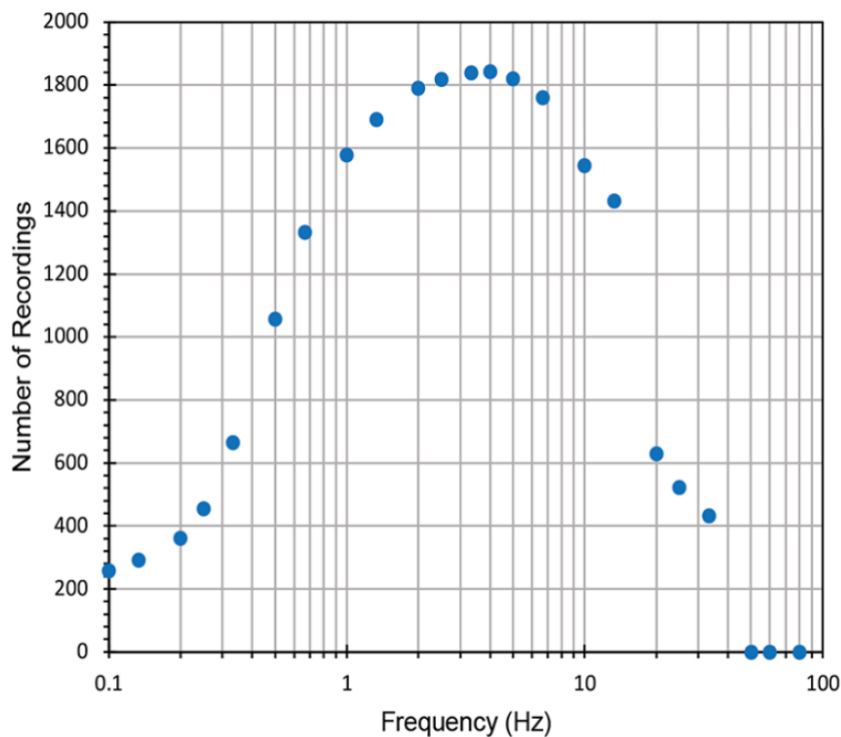


Figure 4-9 Number of recordings versus frequency in the NGA-East database from (Goulet et al. 2021a).

The  $V_{s30}$  at the station was first estimated based on the geology description (about 58% of stations), otherwise was estimated based on the USGS global  $V_{s30}$  model (about 42% of stations). The site condition was later categorised based on the Eurocode 8 site classification, as shown in Table 4-1.

Table 4-1 Eurocode 8 ground types

| Ground type | Description of stratigraphic profile   | $V_{s30}$ (m/s)    |
|-------------|--|--------------------|
| A           | Rock or other rock-like geological formation, including at most 5 m of weaker material at the surface.   | > 800              |
| B           | Deposits of very dense sand, gravel, or very stiff clay, at least several tens of metres in thickness, characterised by a gradual increase of mechanical properties with depth.              | 360 - 800          |
| C           | Deep deposits of dense or medium-dense sand, gravel or stiff clay with thickness from several tens to many hundreds of metres.   | 180 - 360          |
| D           | Deposits of loose-to-medium cohesionless soil (with or without some soft cohesive layers), or of predominantly soft-to-firm cohesive soil.   | < 180              |
| E           | A soil profile consisting of a surface alluvium layer with $V_s$ values of type C or D and thickness varying between about 5 m and 20 m, underlain by stiffer material with $V_s > 800$ m/s. |                    |
| S1          | Deposits consisting, or containing a layer at least 10 m thick, of soft clays/silts with a high plasticity index ( $PI > 40$ ) and high water content  | < 100 (indicative) |
| S2          | Deposits of liquefiable soils, of sensitive clays, or any other soil profile not included in types A - E or S1   |                    |

The spatial distribution of the station grouped by Eurocode 8 site classification was shown in *Figure 4-10*. All stations in Norway are located on the bedrock. Most of the stations in other countries around the North Sea are also located on the rock sites while some are on situated on the sediment. About 80% sites are Class A, 7% Class B and 13% Class C. Due to the lack of detailed site information (e.g., borehole data and in-situ tests) for most stations, the uncertainty in the estimated  $V_{s30}$ , as well as the resultant site classification, was large.

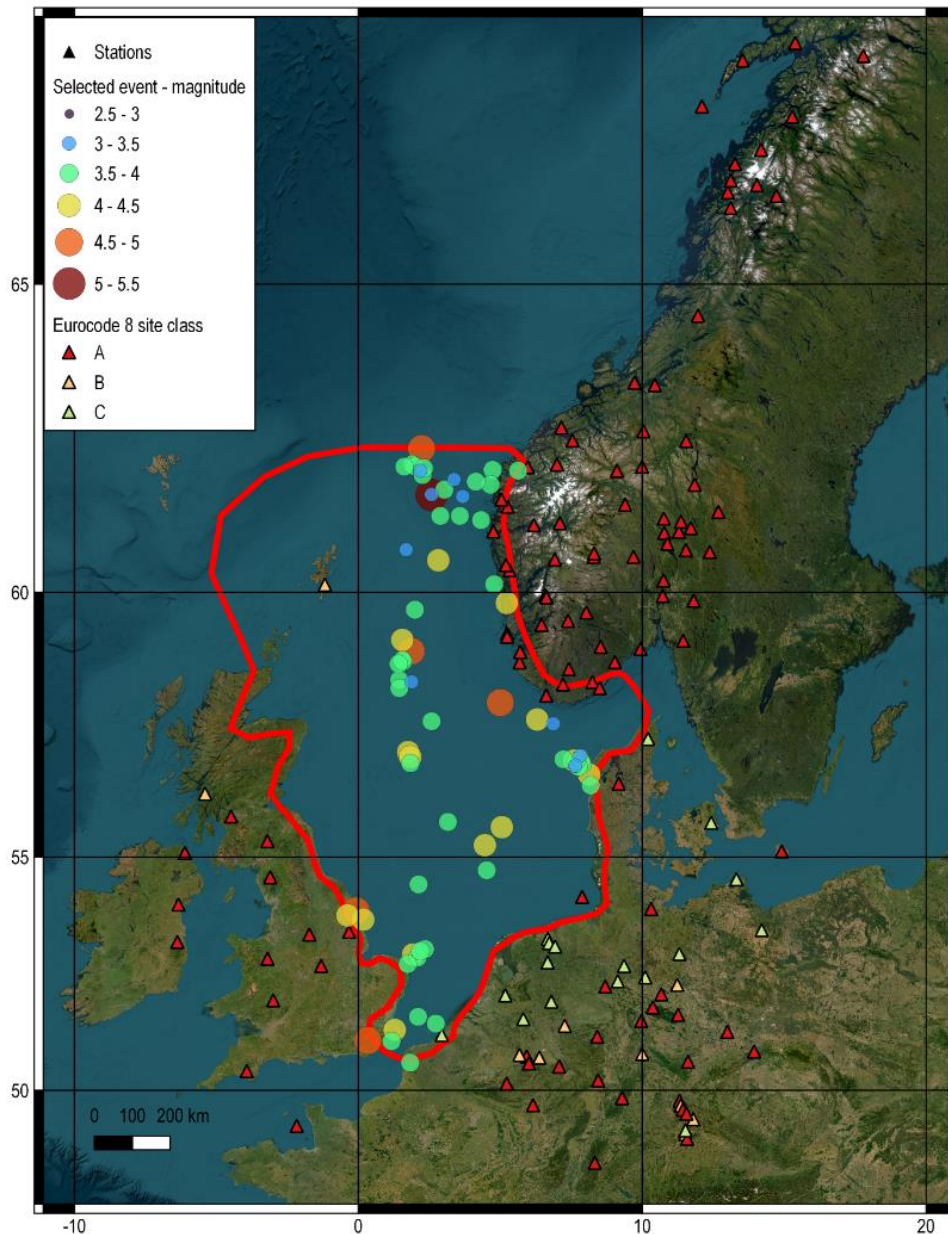


Figure 4-10 Distribution of stations, grouped by site classification in Eurocode 8 (2014).

#### 4.2.3 Time-domain amplitude-based IMs

The computed time-domain amplitude-based IMs is shown in Figure 4-11, grouped by instrument channel. It is shown that the general shapes of the spectral ordinates were like those observed in global and regional datasets (e.g., NGA-West2 and NGA-East). However, the amplitudes of the spectral ordinates were relatively small. This is because most of the data were collected in the far-field stations and for small-magnitude events and thus amplitudes were small as expected. The scatter plot showed the distribution of  $PSA(t=0.1s)$  against distance. The difference between data from different instrument showed that the bandwidth and sampling rate of the instrument limited the usable range of structural periods.

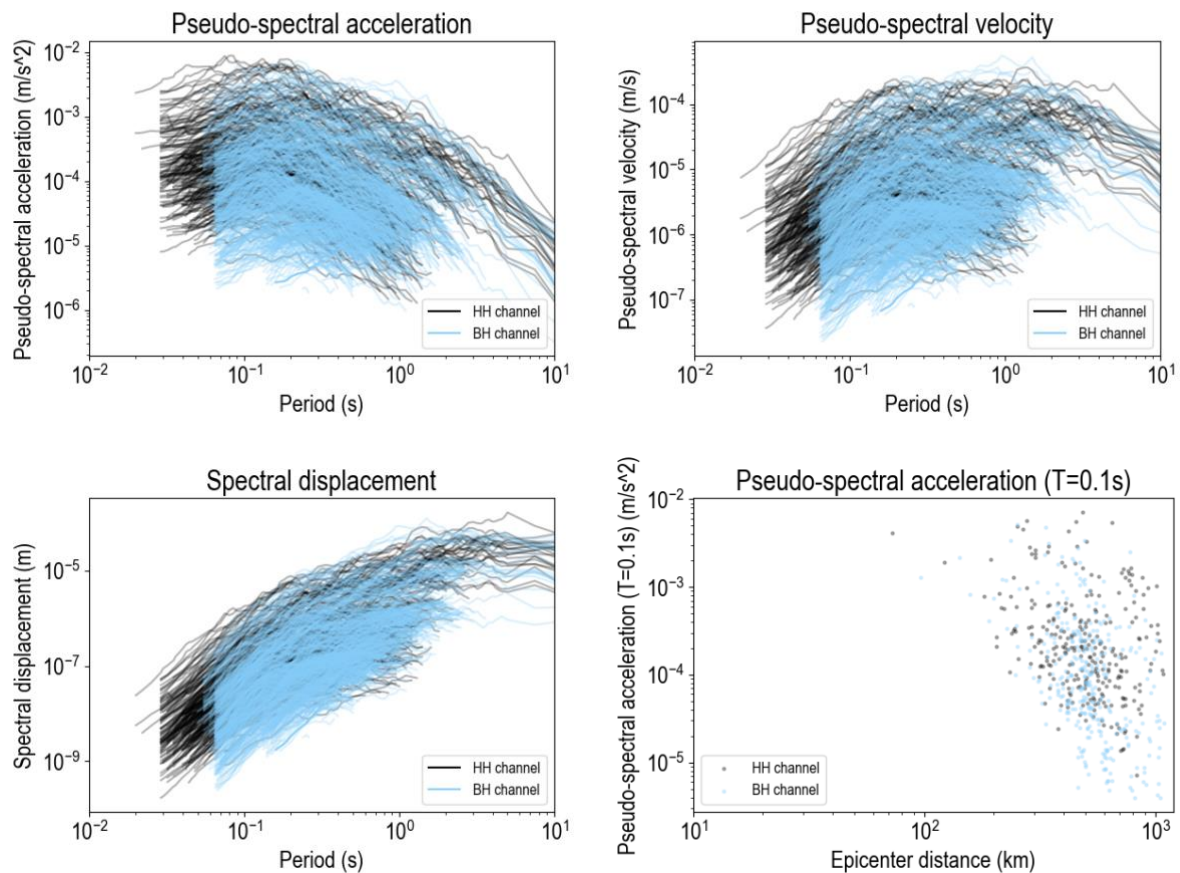


Figure 4-11 Overview of the time-domain amplitude-based IMs: the pseudo-spectral acceleration PSA (upper left), pseudo-spectral velocity PSV (upper right), and spectral displacement SD (lower left) for 5%-damped elastic oscillators for periods ranging from 0.01 to 10 s, and PSA( $T=0.1\text{s}$ ) – distance (lower right). The blue data corresponds to the BH channel (i.e., sampling rate of about 10-80 Hz) and the black data corresponds to the HH channel (i.e., sampling rate of about 80-250 Hz).

#### 4.2.4 Frequency-domain amplitude-based IMs

The effective amplitude spectrum (EAS) is an orientation-independent version of FAS that represents the mean power of two horizontal components of motion in a fashion consistent with RotD50. The EAS is recommended to be smoothed using the Konno-Ohmachi (1998) log-based technique with parameters that minimize the misfit of RVT parameters relevant to PSA computation.

The computed frequency-domain amplitude-based IMs is shown in Figure 4-12, grouped by instrument channel. Like the observations in 4.2.3, the shape of the EAS was like those in global and regional database, but the amplitude was small due to the low-magnitude and far-field observations. The scatter plot showed the distribution of EAS( $f=10.0\text{Hz}$ ) against distance. The difference in instrument resulted in the limited usable frequency range.

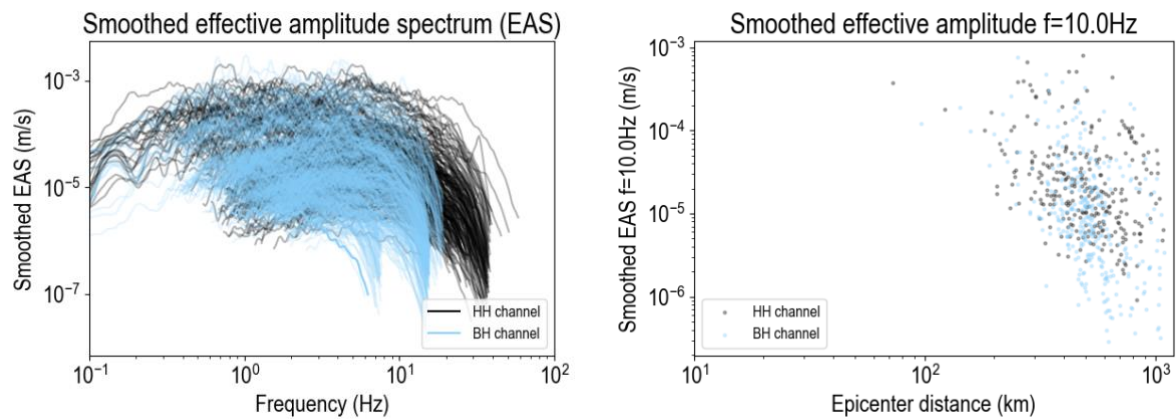


Figure 4-12 Overview of the frequency-domain amplitude-based IMs: smoothed effective amplitude spectrum (left) and EAS (10.0 Hz) – distance (right). The blue data corresponds to the BH channel (i.e., sampling rate of about 10-80 Hz) and the black data corresponds to the HH channel (i.e., sampling rate of about 80-250 Hz).

#### 4.2.5 Energy-related Integral IMs

The computed energy-related integral IMs is shown in Figure 4-13, grouped by instrument channel. The four energy-related IMs were scattered, and they showed certain linear trends with respect to distance. Regarding the Arias intensity and CAV, the values were significantly small, implying limited seismic energy in the recorded waveform. This is due to the weak motion data in the far-field and for low-magnitude earthquakes. Two kinds of significant durations were considered, namely the time intervals between 5–75% and 5–95% of Arias intensity (denoted as D5-75 and D5-95, respectively). The values of significant durations increased as distance increased and the significant duration is about 100s at around 500 km distance, which was like those observed in the global dataset (NGA-West2 in Du and Wang, 2017). There was no systemic difference in the energy-related integral IMs due to the instrument.

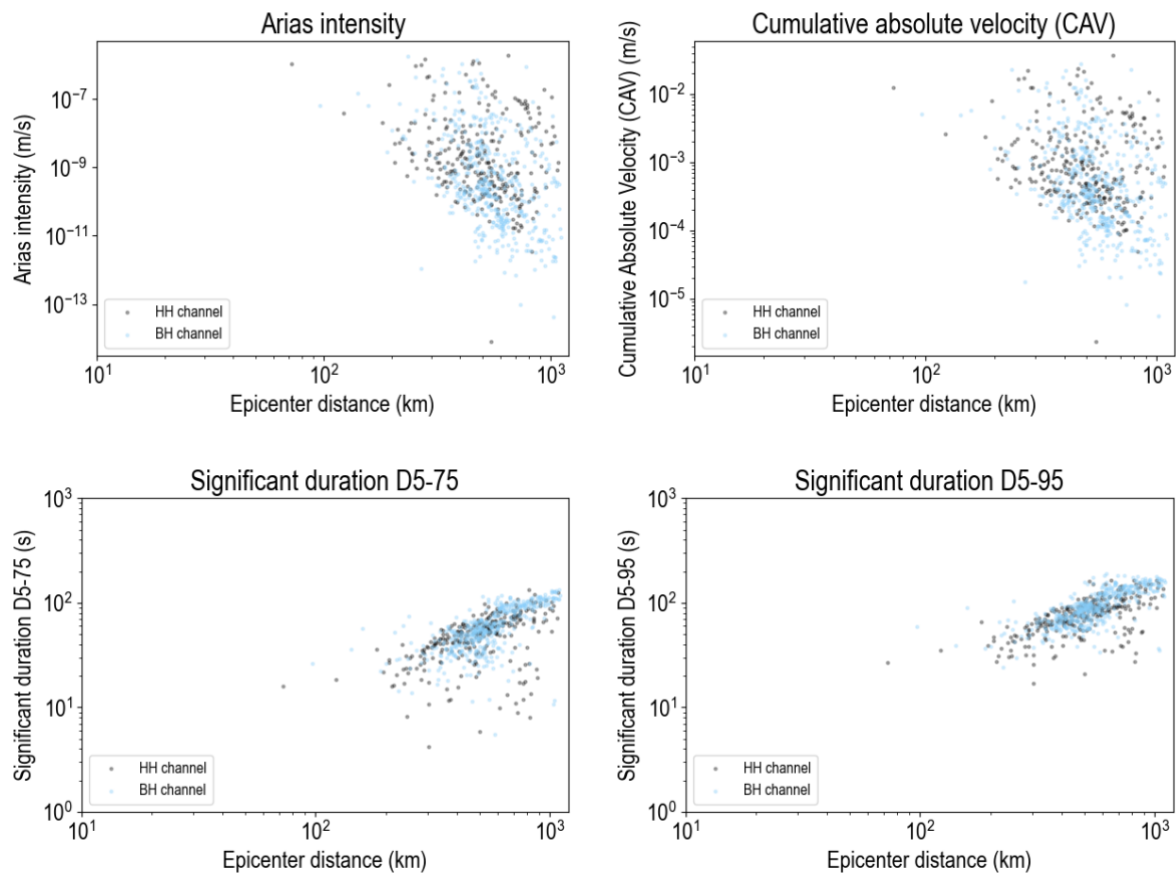


Figure 4-13 Overview of the energy-related Integral IMs. Arias intensity (upper left), cumulative absolute velocity (upper right), 5-75% significant duration (lower left), and 5-95% significant duration (lower right) are shown. The blue data corresponds to the BH channel (i.e., sampling rate of about 10 to 80 Hz) and the black data corresponds to the HH channel (i.e., sampling rate of about 80 to 250 Hz).

#### 4.2.6 Discussion

This section constructed the preliminary flatfile for the North Sea region which will be used as the input for the GMM development. Since the underlying data was dominated by weak motions, the flatfile covered a limited range of magnitude, distance and usable frequency, which was later reflected in the GMM development. The geometric mean was used in this study and future studies would explore the RotD50 definition.

### 4.3 GMM estimation and evaluation

#### 4.3.1 Scaling in observations

This section evaluated the scaling in terms of magnitude, distance and site condition in the observations (hereafter the observations are referred to as observations in a 10-based algorithm), which helps us understand the first-order feature captured by these selected variables.

The magnitude scaling is shown in Figure 4-14. Regarding PSA( $T=0.1s$ ), there were positive linear trends between observations and magnitude across different distance ranges. However, the slopes of magnitude scaling were slightly different in each distance group. Similar patterns were found in PSA( $T=1.0s$ ) but the difference in the slopes was not notable across different distance ranges.

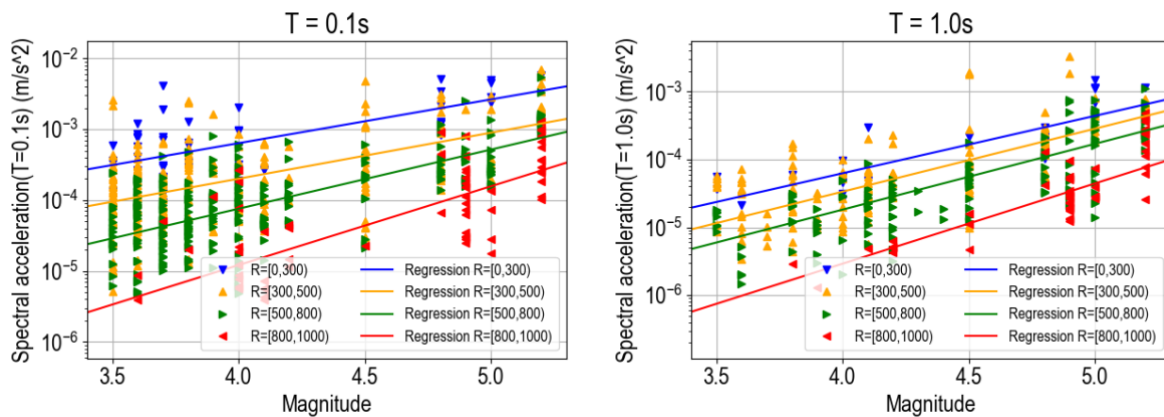


Figure 4-14 Magnitude scaling for PSA(T=0.1s) (left) and PSA(T=1.0s) (right), grouped by distance range.

The distance scaling is shown in Figure 4-15. Regarding PSA(T=0.1s), there were negative linear trends between observations and distance across different magnitude ranges. However, the slopes of distance scaling were notably different in each magnitude group. Similar patterns were found in PSA(T=1.0s) but the difference in the slopes was less notable across different magnitude ranges.

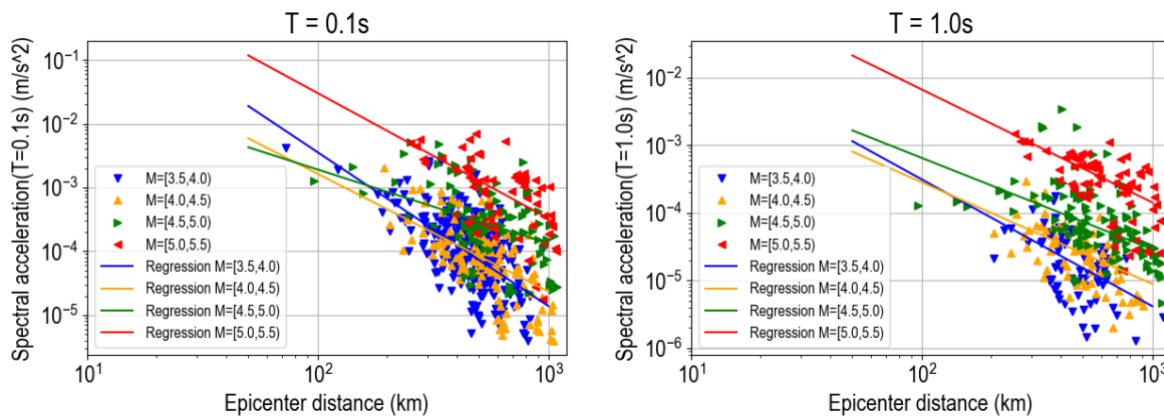


Figure 4-15 Distance scaling for PSA(T=0.1s) (left) and PSA(T=1.0s) (right), grouped by magnitude.

The site condition scaling is shown in Figure 4-14. Regarding PSA(T=0.1s) and PSA(T=1.0s), there was no clear trends between observations and site conditions across different distance ranges. It is worth noting that there was a clear unbalance between observations at the rock site class (class A) and those at soil site class (class B and C).

Though the discussions were concentrated on spectral accelerations, similar observations were also found in frequency-based IMs and energy-related IMs.

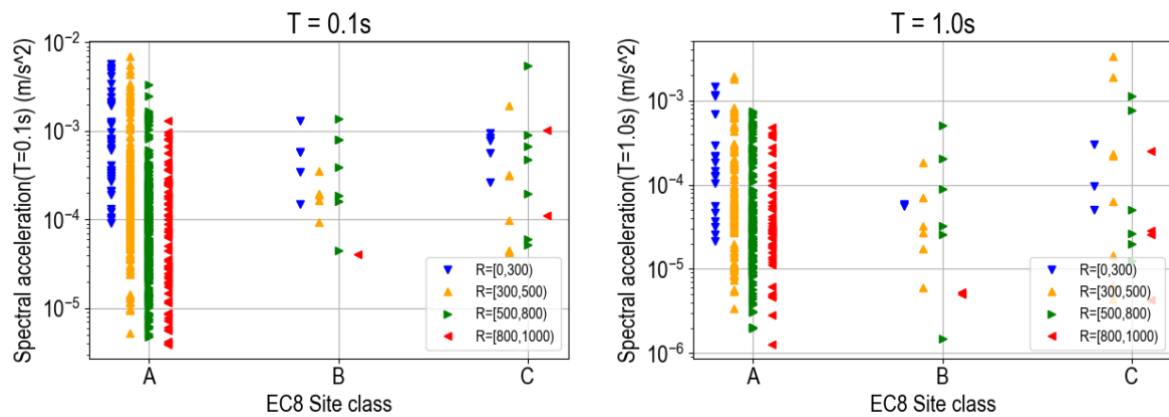


Figure 4-16 Site condition scaling for PSA( $T=0.1s$ ) (left) and PSA( $T=1.0s$ ) (right), grouped by distance range.

#### 4.3.2 Functional form

Section 4.3.1 evaluated the scaling in observations and found the general trends in observations with respect to magnitude and distance. This section evaluated the suitable functional form that can capture the major trend in observations.

First, a linear magnitude functional form was proposed to fit the observations and then a linear distance functional form was proposed to fit the resultant residuals. The final residuals were compared with the site class. The Huber regression, which is a type of robust regression using a loss function instead of traditional least-squares to mitigate the effects of outliers, was used for this section.

Functional form study for PSA( $T=0.1s$ ) is shown in Figure 4-17. First, the first-order positive linear trend between observations and magnitude was captured by the empirical model  $\hat{Y}$ . It is worth noting that there was a large scattering (grey points) lying outside  $\pm 1.35\sigma$  to the model, which implied high-order magnitude dependence was not captured. Then, the first-order negative linear trend between residuals  $Y - \hat{Y}$  and distance was captured by the empirical model  $\hat{Y}'$ . Finally, the violin plots of the remaining residuals  $Y - \hat{Y} - \hat{Y}'$  showed that the median residuals for the rock sites (class A) were about zeros, while the median residuals for soil sites (class B and C) were higher than zeros. This implied that there was systematic difference in observations at soil sites from rock sites. Thus, a dummy variable for soil site class was proposed.

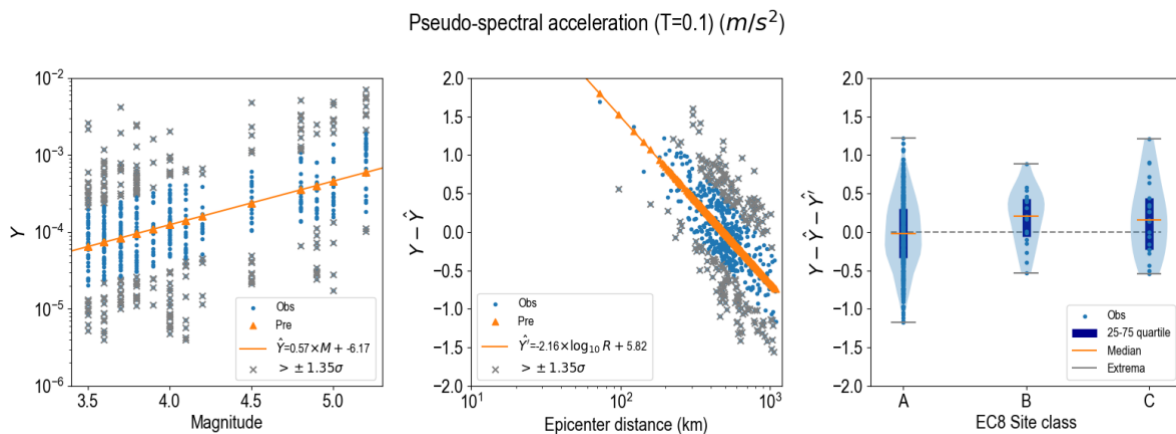


Figure 4-17 Functional form study for PSA( $T=0.1s$ ). (Left) First the observation  $Y$  was used to fit a linear magnitude function  $\hat{Y}$ . (Mid) Then the residuals  $Y - \hat{Y}$  were used to fit a linear distance function  $\hat{Y}'$ . (Right) Finally, the remaining residuals  $Y - \hat{Y} - \hat{Y}'$  were grouped by site conditions to develop the violin plots. The observations outside  $\pm 1.35\sigma$  had limited contribution to regression.

Functional form study for PSA( $T=1.0s$ ) is shown in Figure 4-18. Like the functional form study for PSA( $T=0.1s$ ), first-order positive linear model between observations and magnitude was fitted to the observations. Then, a first-order negative linear trend between residuals  $Y - \hat{Y}$  and distance was fitted. Finally, the violin plots showed that the remaining residuals at rock sites had zero median while the medium residuals at soil sites were generally smaller than those at rock sites and were negative.

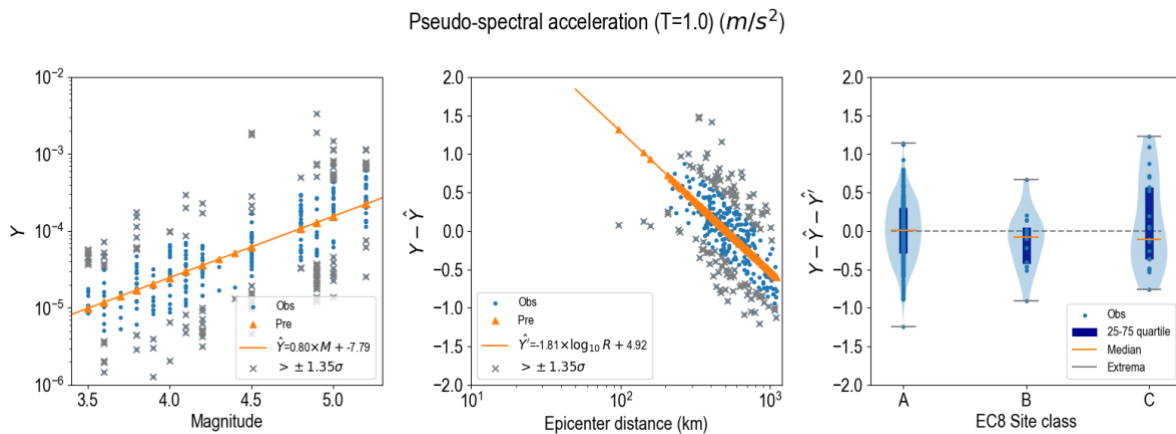


Figure 4-18 Functional form study for PSA( $T=1.0s$ ). (Left) First the observation  $Y$  was used to fit a linear magnitude function  $\hat{Y}$ . (Mid) Then the residuals  $Y - \hat{Y}$  were used to fit a linear distance function  $\hat{Y}'$ . (Right) Finally, the remaining residuals  $Y - \hat{Y} - \hat{Y}'$  were grouped by site conditions to develop the violin plots. The observations outside  $\pm 1.35\sigma$  had limited contribution to regression.

Though the functional forms of other non-spectral IMs are different from those of spectral IMs, the variables included in these GMMs are similar (e.g., magnitude, source-to-site distance, site conditions). Thus, this study considered the same functional forms for all the IMs. The functional form study was also performed for other non-spectral IMs, as shown in Figure 4-19 and Figure 4-20. The results also supported the decision to use the same functional form.

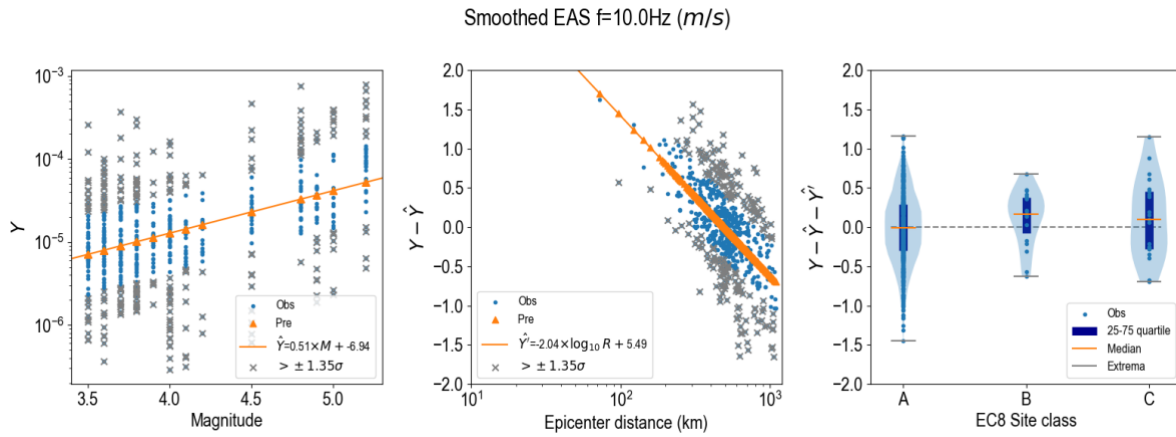


Figure 4-19 Functional form study for EAS( $f=10\text{Hz}$ ). (Left) First the observation  $Y$  was used to fit a linear magnitude function  $\hat{Y}$ . (Mid) Then the residuals  $Y - \hat{Y}$  were used to fit a linear distance function  $\hat{Y}'$ . (Right) Finally, the remaining residuals  $Y - \hat{Y} - \hat{Y}'$  were grouped by site conditions to develop the violin plots. The observations outside  $\pm 1.35\sigma$  had limited contribution to regression.

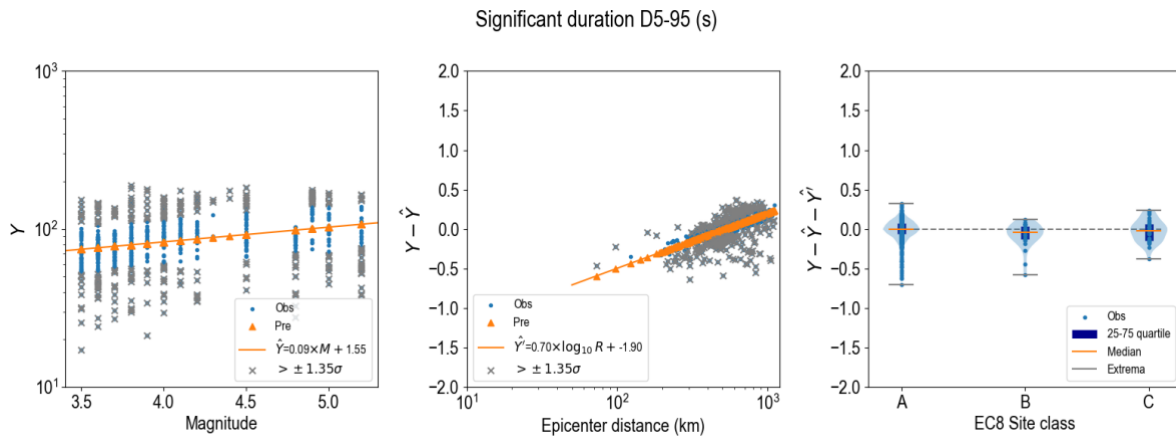


Figure 4-20 Functional form study for significant duration D5-95. (Left) First the observation  $Y$  was used to fit a linear magnitude function  $\hat{Y}$ . (Mid) Then the residuals  $Y - \hat{Y}$  were used to fit a linear distance function  $\hat{Y}'$ . (Right) Finally, the remaining residuals  $Y - \hat{Y} - \hat{Y}'$  were grouped by site conditions to develop the violin plots. The observations outside  $\pm 1.35\sigma$  had limited contribution to regression.

Based on these results, the final functional form was considered as follows

$$Y_{ij} = b_1 + b_2 M_i + b_3 \log_{10}(R_{ij}) + b_4 F_{soil,ij} + \eta_i + \varepsilon_{ij}$$

$$i = 1, \dots, N, j = 1, \dots, n_i$$

Where:

- $Y_{ij} = \log_{10} IM_{ij}$  is the base-10 logarithm of IM at station  $j$  of event  $i$ ;
- $b_{1,\dots,4}$  are the regression coefficients to be estimated;
- $M_i$  is the magnitude (i.e., prime magnitude in North Sea catalogue) of event  $i$ ;
- $R_{ij}$  is the epicentre distance in km of station  $j$  of event  $i$ ;

- $F_{soil,ij}$  is the dummy variable of station  $j$  of event  $i$ , where 1 for soil site and 0 for rock site;
- $\eta_{i=1,\dots,N}$  is the interevent error, which is independent and identically distributed with  $\mathbb{E}(\eta_i) = 0$  and  $\text{var}(\eta_i) = \tau^2$ ;
- $\boldsymbol{\varepsilon}_{i=1,\dots,N}$  is the independent intraevent error vector of size  $n_i \times 1$  with  $\mathbb{E}(\boldsymbol{\varepsilon}_i) = \mathbf{0}$  and  $\text{var}(\boldsymbol{\varepsilon}_i) = \phi^2 \boldsymbol{\Omega}_i(h)$ , where  $\boldsymbol{\Omega}_i(h)$  is the spatial correlation matrix correlation of event  $i$  and  $h$  is the characteristic length scale. The  $jj'$ -th element of the exponential spatial correlation function  $\exp(-d_{jj'}/h)$ , where  $d_{jj'}$  is the inter-station distance. The effective range  $\tilde{h}$  is the effective range corresponding to 0.05 spatial correlation and  $\tilde{h} = 3h$ .
- it is noted that  $\eta_{i=1,\dots,N}$  and  $\boldsymbol{\varepsilon}_{i=1,\dots,N}$  are assumed to be mutually independent; hence, the total standard deviation is calculated as  $\sigma = \sqrt{\tau^2 + \phi^2}$  from interevent ( $\tau$ ) and intraevent (-) standard deviations  $\phi$ ;
- $N$  is the total number of events
- $n_i$  is the number of stations for event  $i$

#### 4.3.3 GMM results

Given the model set-up in Section 4.3.2, the model parameters were estimated by the one-stage scoring estimation algorithm introduced in Section **Error! Reference source not found.**, with and without consideration of spatial correlation. If the number of observations was less than 10% of the total observations due to a limited usable frequency range, it was considered there was no sufficient data for regression and thus no model was developed. The estimated results were presented and discussed in this section.

The estimated parameters of the proposed GMM for PSA(T=0.1s) and PSA(T=1.0s) were shown in Table 4-2. The coefficients corresponding to magnitude scaling and distance scaling (i.e., b2 and b3) derived from the one-stage algorithm were generally consistent (e.g., same sign, similar absolute values) with the results from multi-stage evaluation (i.e., Figure 4-17 and Figure 4-18). The slight difference in the b2 and b3 values was due to the model set-up (e.g., mixed-effect regression vs robust regression) and estimation algorithm. The coefficient corresponding to the site condition scaling (i.e., b4) for PSA(T=0.1s) was as expected positive while that for PSA(T=1.0s) was positive though Figure 4-18 suggesting negative. This may be due to the insufficiency of soil data to constrain the parameters. The medium predictions between the GMM with and without spatial correlation were similar.

Moreover, this study compared the GMM with and without the exponential spatial correlation in Table 4-2. As expected, the inclusion of spatial correlation would slightly change the estimates of coefficients (i.e., b1 to b4) but would significantly change the estimates of the standard deviations of inter- and intra-event errors. The incorporation of spatial correlation, in comparison with the model estimated without spatial correlation, resulted in a reduction of the interevent variance and an increase of the interevent variance. However, the values of standard deviations (i.e.,  $\tau$ ,  $\phi$  and  $\sigma$ ) were generally larger than global models (e.g., Cauzi 2014  $\tau \sim 0.22 - 0.24$ ,  $\phi \sim 0.33 - 0.37$ , RietbrockEdwards2019Mean  $\tau \sim 0.19 - 0.29$ ,  $\phi \sim 0.14 - 0.21$ , Akkar 2014  $\tau \sim 0.22 - 0.24$ ,  $\phi \sim 0.35 - 0.42$  in the natural log). This was due to the limited data.

The characteristic length scale  $h$  and the corresponding effective range  $\tilde{h}$  were shown in Table 4-2. The effective ranges were larger for PSA at longer periods than those at shorter periods, which was consistent with the trending in the literature. However, the effective ranges were significantly larger than those in the literature (Jayaram and Baker, 2009). This may be due to that the dataset was dominantly observations from small magnitude events and far distance stations and thus the

correlation in these weak motions was stronger than that of global heterogeneous strong motions. It is worth noting that when fitting the model with spatial correlation, the regression may encounter local maximum thus the several initial values should be tested to update estimates.

*Table 4-2 The estimated parameters of the proposed GMM for PSA(T=0.1s) and PSA(T=1.0s).*

| IM               | PSA(T=0.1s) |                     | PSA(T=1.0s) |                     |
|------------------|-------------|---------------------|-------------|---------------------|
|                  | No spatial  | Exponential spatial | No spatial  | Exponential spatial |
| b1               | 0.577       | 0.031               | -2.706      | -3.375              |
| b2               | 0.726       | 0.695               | 0.849       | 0.947               |
| b3               | -2.779      | -2.512              | -1.994      | -1.903              |
| b4               | 0.089       | 0.145               | 0.100       | 0.009               |
| $\tau$           | 0.346       | 0.311               | 0.308       | 0.053               |
| $\phi$           | 0.328       | 0.355               | 0.300       | 0.406               |
| $h$ (km)         | -           | 80.360              | -           | 377.263             |
| $\tilde{h}$ (km) | -           | 214.078             | -           | 1131.789            |

The estimation results for other IMs were summarised in the supplements.

Considering the dataset limitation and numerical stability, the GMM without spatial correlation was considered more reliable than that with spatial correlation. The GMM without spatial correlation was applicable for magnitude range 3.5-5.5, epicentre distance range 72km – 1000km, and period range 0.03s – 2.6s. It is worth noting that the applicable range of the derived GMM was rather limited compared to the global and regional GMMs, any extrapolation of the derived model should be use with caution.

#### 4.3.4 Comparison with previous models

This section compared the predictive performance of the derived GMM with global and regional GMMs applicable to the North Sea regions, which helps better understand the epistemic uncertainty in ground motion prediction.

Three global and regional GMMs were selected, namely Akkar et al. (2014), Cauzzi et al. (2015), and Reitbrock and Edwards (2019) GMM. Further details of these GMMs were introduced in Section **Error! Reference source not found.** The medium predictions for a set of M-R scenarios at a rock site provided by these four GMMs are shown in Figure 4-21, as well as observations within  $\pm 0.5M$  and  $\pm 50km$  of the scenarios.

For close-distance scenarios (beyond the applicable range of the North Sea GMM) in Figure 4-21 (left panels), the predictions from the preliminary North Sea GMM were generally consistent with the other GMMs, as the  $\pm\sigma$  medium prediction covered the range of predictions from other GMMs. However, the decay of amplitude with respect to periods in North Sea GMM was faster than those from other GMMs, implying certain unique features in the North Sea dataset. Moreover, the prediction from the preliminary North Sea GMM was not as smooth as the other GMMs, which may be due to the scattering in the dataset.

For far-distance scenarios (beyond the applicable range of the other GMMs) in Figure 4-21 (mid and right panels), the North Sea GMM was consistent with the observations. However, the other GMMs

were generally overestimated the ground motions, reaching the  $+\sigma$  medium prediction of the North Sea GMM. The decays of amplitude with respect to periods were similar among the four GMMs.

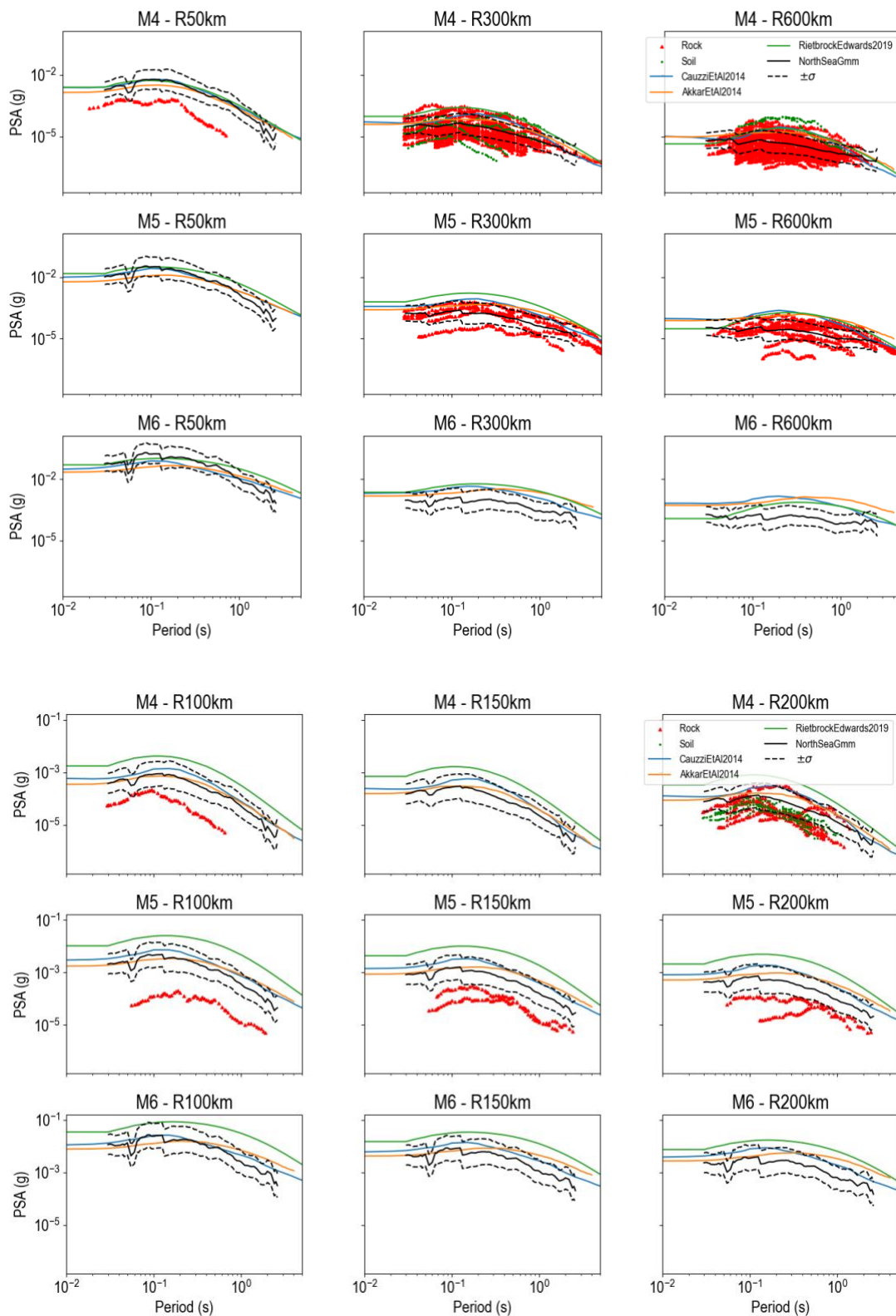


Figure 4-21 The medium predictions for a set of M-R scenarios at a rock site provided by Akkar et al. (2014), Cauzzi et al. (2015), Reitbrock and Edwards (2019), and preliminary North Sea GMM. The dash

*lines were  $\pm\sigma$  of the medium prediction of the preliminary North Sea GMM. The red and green markers represented the observations at rock and soil sites, respectively.*

In general, the preliminary GMM captured the ground-motion characteristics in North Sea data (i.e., weak motion at the far field, faster decay with respect to periods in the near field) while the other GMM were overestimated the North Sea ground motion.

#### 4.3.5 Discussion

This section developed the preliminary GMM for the North Sea based on the flatfile constructed in Section 4.3. Due to the paucity of observations, the derived GMM was only applicable for magnitude range 3.5-5.5, epicentre distance range 72 – 1000 km, and period range 0.03 – 2.6 s. There was a relatively large epistemic and aleatory uncertainty, which can be significantly improved by expanding the database and data quality.

Other parameters related to the earthquake process, such as the focal mechanism and  $V_{s30}$ , were not considered in the preliminary GMM. The reasons were two-fold. First, due to the lack of information and tests, most of those parameters could only be collected based on estimation with large epistemic uncertainty, which would not improve the predictive performance of the derived model. Second, the limited available data for those parameters cannot well-constrain the corresponding regression parameters.

## 5 Near surface attenuation

### 5.1 Site amplification

Near surface soils can have a significant effect on ground shaking due to earthquakes (Seed et al., 1976). Site amplification models are used to modify predicted earthquake shaking from a reference rock condition to the soil surface (e.g. Seyhan and Stewart, 2014). The ground motion model described in the previous section is defined for a reference rock condition. This section describes the amplification factors to estimate the shaking at the soil surface.

This study follows a similar methodology to Carlton (2014) and Harmon et al. (2019), who developed site amplification functions based on 1D site response analyses for deep soft soil deposits and CENA, respectively. We first developed nine base case profiles representative of different locations and soil conditions encountered in the North Sea. Then, we modified the nine base case profiles to explore the effects of elastic site period (also called the initial fundamental period,  $T_s$ ) and profile depth. The nine base case profiles and 27 modified profiles are based on geological, geophysical, and geotechnical data from projects performed by the Norwegian Geotechnical Institute (NGI) in the North Sea.

Then, we planned to perform 1D total stress analyses in DEEPSOIL V7.0 (Hashash et al., 2020) using acceleration time series from earthquakes occurring and recorded in the study area. However, as shown in Figure 4-11, the maximum spectral acceleration in the waveform database is only 0.001 g. This occurs at a spectral period of 0.1 seconds. These values are too low for any engineering significance. As a result, we were unable to develop a model to predict site specific amplification factors for the North Sea. To overcome this obstacle, in the future, we will use random vibration theory (RVT) (Rathje and Ozbey, 2006) to estimate amplification factors based on design Fourier amplitude spectra based on seismological parameters calibrated to the North Sea.

The following section describes the geologic setting of the North Sea to provide insight into the origin and formation of the various site profiles. Next, the base case profiles and modified soil profiles are described. Finally, we outline the future work that is planned.

#### 5.1.1 Geologic setting

The tectonic and geological development of the North Sea is complex, involving several orogenic phases. The development can be divided into several geological provinces or terranes (Ziegler, 1975; Gregersen et al., 1989). Volcanic activity during the Triassic and Jurassic (roughly 250 Ma to 150 Ma) created a system of horsts and grabens in the North Sea, which are highs and lows separated by normal faults. This was followed by thermal subsidence, which created an intracratonic sedimentary basin (Glennie and Underhill, 1998). In the Palaeocene to Eocene (65.5 to 34 Ma), seafloor spreading began in the North Atlantic and mountain building in the Alps, and basin margins were uplifted due to inversion, producing a series of submarine fans (NPD, 2021). Over the last 2.6 million years large volumes of sediment were eroded from Scandinavia and the UK and deposited in the North Sea by the movement of ice sheets during at least three different glacial periods (Cameron et al., 1987; Ottesen et al., 2018). Uplift and subsidence rates are suggested to be much higher immediately after deglaciation, decelerating until the present day to rates comparable with modern-day tide-gauge data (Shennan, 1989). The changes in climate also resulted in regional-scale oscillations in sea level and major changes in river drainage configurations (Lee et al., 2006; Cohen et al., 2014).

Sediments in the North Sea have been deposited and reworked by several different environments ranging from arctic (including tundra, permafrost, sub-glacial (i.e. under ice) and pro-glacial (i.e. in front of ice)), temperate (including lacustrine, fluvial and estuarine or lagoonal), as well as terrestrial

(exposed to wind and weather) and have undergone desiccation due to drying, evapotranspiration and freezing. However, glacial activity is the main factor in the formation of near surface soils in the North Sea (Ottesen et al., 2018; Bellwald et al., 2022). Many locations are a complex of highly deformed glacial till, created as the ice sheets oscillated back and forth, bringing eroded soils with them that were often left in ridges (terminal moraines) at the front of the ice (Morén et al., 2018). As the ice moved backwards and forwards push-moraines were formed, which were then overridden and eroded by later glacial advances. Between these ridges shallow lakes developed. The soils are often folded, disturbed and sometimes faulted following their original horizontal deposition (Cotterill et al, 2017a,b). As a result of the many different environments that helped to form it, the North Sea has a complex geology, both vertically and laterally (Bellwald et al., 2022; Petrie et al., 2022).

### 5.1.2 Representative base case profiles

We selected nine base case soil profiles to represent the different types of sediments encountered in the North Sea. Each base case profile is derived from cone penetration test, borehole, and laboratory test data, as well as geological and geophysical interpretations of soil layering.

For 1D nonlinear site response analyses, the required input parameters are the shear wave velocity, unit weight, shear strength, and shear modulus reduction and damping curves of the soil profile with depth, as well as the shear wave velocity, unit weight and damping of the underlying elastic half-space. Section 3.2 describes the shear wave velocity, unit weight and shear strength of the base case profiles, and section 3.3 describes the target shear modulus reduction and damping curves used.

Figure 5-1 and Figure 5-2 present the shear wave velocity, shear strength and soil type with depth for the base case profiles. The blue shaded areas are modelled as coarse grained soils (gravels and sands) and the orange shaded areas are modelled as fine grained soils (silts and clays). These figures show the wide variety of soil profiles, with some mainly clay profiles, some mainly sand profiles, and several highly interlayered profiles. Many of the profiles also have shear wave velocity reversals, where the shear wave velocity of a layer above is higher than the layer below. This is caused by the high level of geologic variability of the soils, as explained in Section 6.1.1. Some layers may have been exposed to weather, while others were reworked by glaciers. The soil unit weights range from 18 kN/m<sup>3</sup> to 21.5 kN/m<sup>3</sup>.

Table 5-1 lists the depth, elastic site period ( $T_s$ ), time averaged shear wave velocity over the top 30 meters ( $V_{s30}$ ) and site class according to ISO 19901-2 for each of the profiles. The depths of the base case profiles range from 15 m to 62 m. Each of the profiles ends in either weathered rock or hard glacial till with shear wave velocities greater than 750 m/s (not shown in Figure 5-1 and Figure 5-2). The elastic site period is the period most likely to experience the highest amplifications due to resonance. The elastic site periods range from 0.18 s to 1.0 s. The  $V_{s30}$  values range from 177 m/s to 460 m/s, with two of the sites classified as E sites, five as D, and two as C. According to ISO 19901-2, E sites have  $120 \text{ m/s} < V_{s30} \leq 180 \text{ m/s}$ , D sites have  $180 \text{ m/s} < V_{s30} \leq 350 \text{ m/s}$ , and C sites have  $350 \text{ m/s} < V_{s30} \leq 750 \text{ m/s}$ . We selected more D sites than E or C because this is the main type of soil class in the database.

The shear modulus reduction and damping curves describe the change in stiffness (shear modulus) and damping with shear strain. For fine grained soil layers, we used the model of Darendeli (2001) and for coarse grained soil layers we used the model of Menq (2003).

The Darendeli (2001) model requires the mean effective confining pressure (which is dependent on the unit weight and coefficient of lateral earth pressure,  $K_0$ ), overconsolidation ratio (OCR), plasticity index ( $I_p$ ), the loading frequency ( $f$ ) and the number of loading cycles ( $N$ ). The loading frequency and

N are difficult to estimate and do not have a great effect on the model within the ranges applied in earthquake applications, therefore, we use  $f = 1$  and  $N = 10$ , as recommended by Darendeli (2001). The Menq (2003) model is also dependent on the mean effective stress and number of loading cycles, as well as the coefficient of uniformity ( $C_u$ ) and median grain size ( $D_{50}$ ).

Table 5-2 lists the minimum and maximum values used to define the shear modulus reduction and damping curves using the Darendeli (2001) and Menq (2003) models. The coarse grained soils modelled in this study range from well graded to poorly graded fine to coarse sand. The fine grained soils range from silts to clays with plasticity indexes of 8 to 40 and OCR from 1 to 20. The large OCR values are due to the long history of glacial activity. Figure 5-3 show the bounds of the shear modulus reduction and damping curves used to describe the nonlinear behavior of the soil, respectively. The coarse grained soils generally predict a more linear behavior than the fine grained soils, with lower damping and larger normalized shear modulus for the same shear strain. Small strain damping ranges from 0.5% to 3.7%.

The maximum frequency ( $f_{\max}$ ) that can be propagated in a non-linear time domain analysis is given by  $f_{\max} = V_s / (4 \cdot H)$ , where  $V_s$  is the shear wave velocity of the soil layer and  $H$  is the soil layer thickness. For frequencies above  $f_{\max}$ , 1D non-linear site response analyses under-predict the response spectral values and give values that are flat and equal to the peak ground acceleration (Stewart et al., 2008). We therefore modified the thicknesses of the soil layers so that  $f_{\max}$  exceeds 50 Hz for all soil layers.

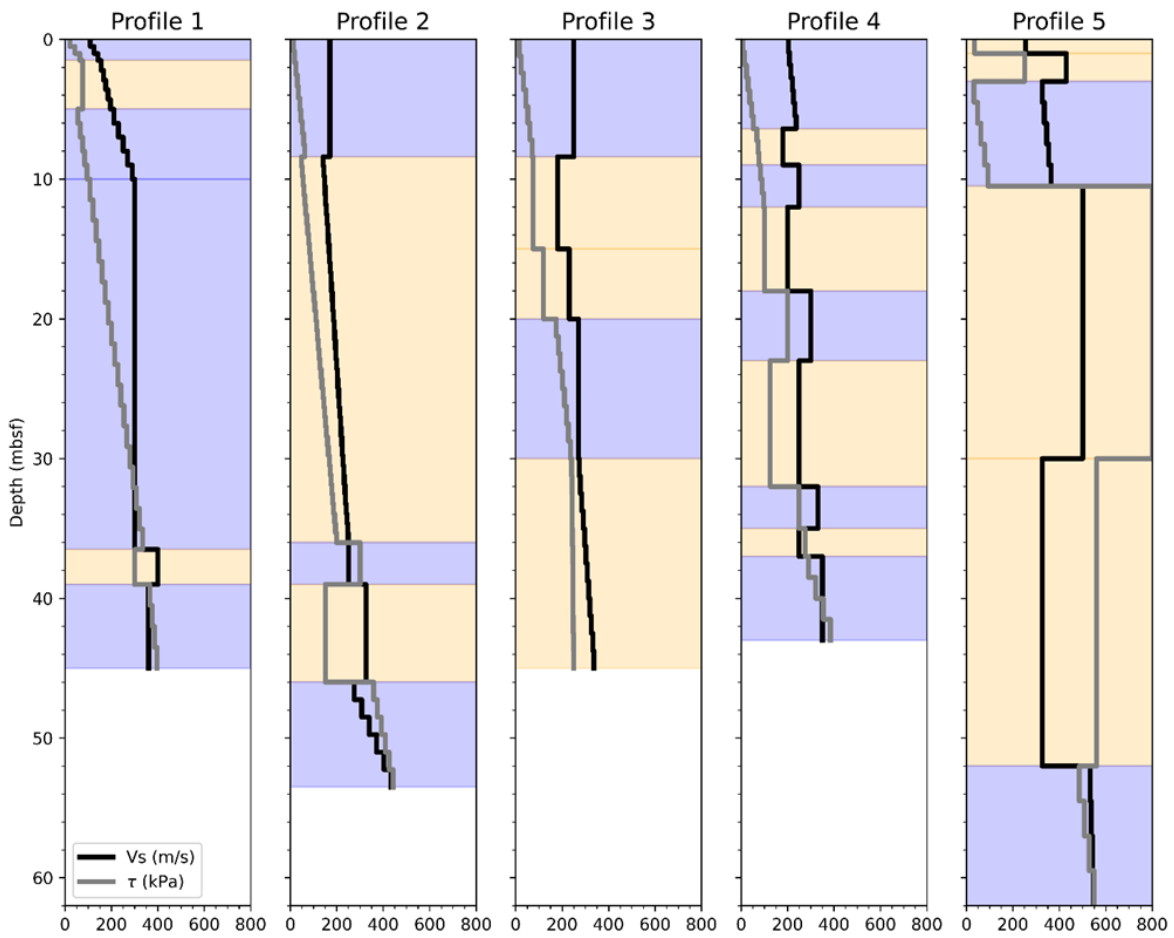


Figure 5-1 Shear wave velocity ( $V_s$ ), shear strength ( $\tau$ ), and soil type with depth for base case profiles 1-5. Blue shaded areas are modelled as coarse grained material, and orange shaded areas as fine grained material.

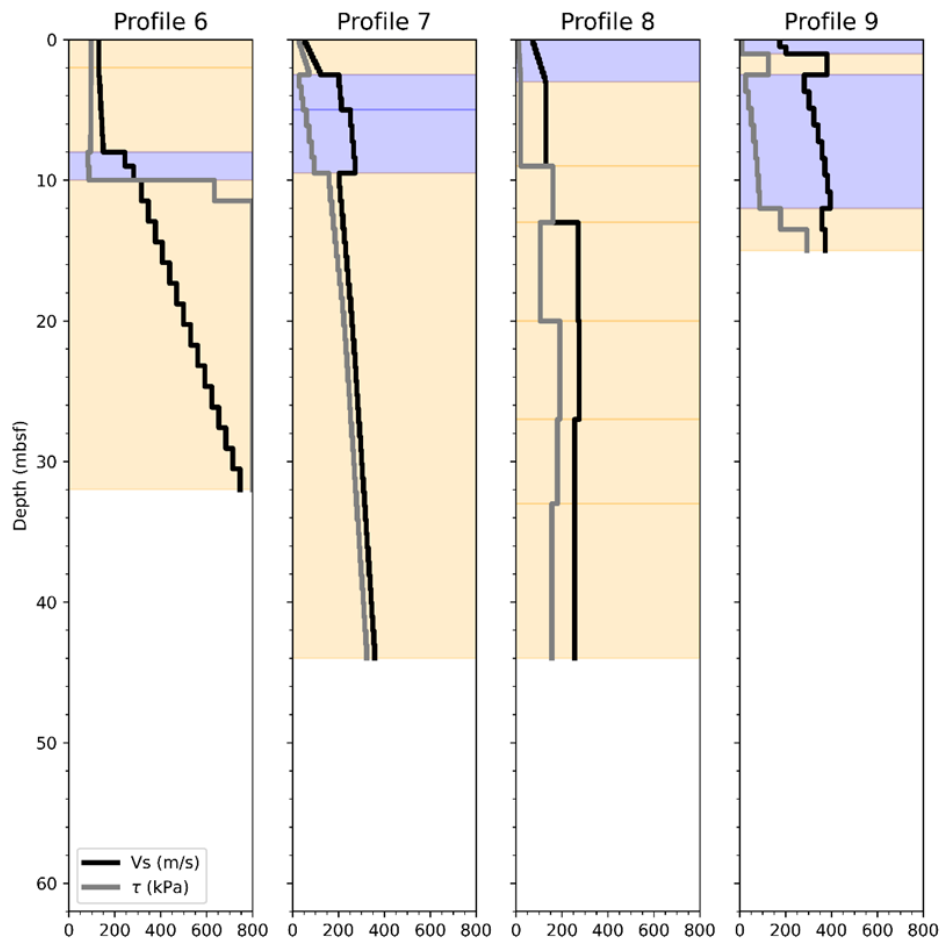


Figure 5-2 Shear wave velocity ( $V_s$ ), shear strength ( $\tau$ ), and soil type with depth for base case profiles 6-9. Blue shaded areas are modelled as coarse grained material, and orange shaded areas as fine grained material.

Table 5-1 Characteristics of the base case profiles (ISO Class is the ISO 19901-2 site class according to  $V_{s30}$ ).

| Profile | Depth (m) | $T_s$ (s) | $V_{s30}$ (m/s) | ISO Class |
|---------|-----------|-----------|-----------------|-----------|
| 1       | 45        | 0.66      | 252             | D         |
| 2       | 53.5      | 1         | 177             | E         |
| 3       | 45        | 0.71      | 234             | D         |
| 4       | 43        | 0.69      | 231             | D         |
| 5       | 62        | 0.62      | 433             | C         |
| 6       | 32        | 0.44      | 282             | D         |
| 7       | 44        | 0.73      | 213             | D         |
| 8       | 44        | 0.88      | 180             | E         |
| 9       | 15        | 0.18      | 460             | C         |

Table 5-2 Minimum and maximum soil parameters used to define the shear modulus reduction and damping curves.

| Parameter | Cu  | D <sub>50</sub> (mm) | I <sub>p</sub> | OCR | K <sub>0</sub> |
|-----------|-----|----------------------|----------------|-----|----------------|
| Minimum   | 1.3 | 0.1                  | 8              | 1   | 0.3            |
| Maximum   | 8   | 2                    | 40             | 20  | 1.8            |

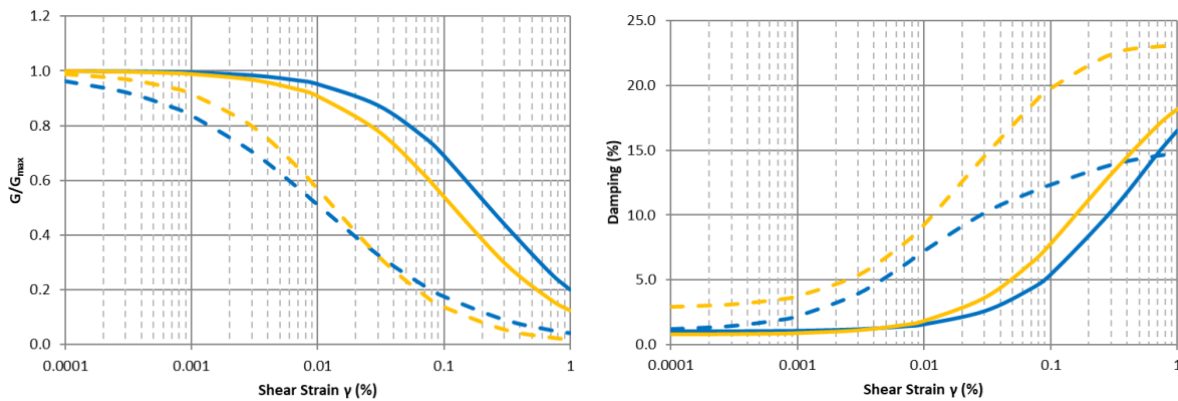


Figure 5-3 Upper (solid) and lower (dashed) bound shear modulus reduction curves (left) and damping curves (right) used for coarse grained soils (blue) and fine grained soils (orange).

### 5.1.3 Modified profiles

The base case scenarios only have elastic site periods between 0.2 and 1.0 seconds. However, many offshore structures such as wind turbines have elastic periods around 2 to 4 seconds, and some machinery used for substations has elastic periods as low as 0.1 seconds. In addition, geophysical data from the North Sea shows that some sites contain more than 100 m deposits of sediment (Ottesen et al., 2018; Bellwald et al., 2022). Therefore, we shortened the base case profiles by roughly half, and extended the profiles by about two and four times, to capture the effect of different elastic site periods on the amplification factors. To shorten the base case sites, we simply truncated them. To extend the base case sites, we fit the following equation to the base case shear wave velocity profiles (Carlton and Tokimatsu, 2014):

$$\ln(V_s) = c_1 + c_2 * \ln(z) \tag{1}$$

where  $z$  is the depth below seafloor in meters, and  $V_s$  is in m/s. For properties other than the shear wave velocity, we extended the last layer. Table 5-3 lists the best fit of coefficients  $c_1$  and  $c_2$  for each base case profile. The values of  $c_1$  are like those derived by Carlton and Tokimatsu (2014) but the values of  $c_2$  are lower. In other words, the increase of  $V_s$  with depth is smaller in the North Sea than predicted by the equations of Carlton and Tokimatsu (2014), which were derived from onshore sites in California and Japan.

Figure 5-4 shows the elastic site periods and depths of each of the 36 sites. The nine base case sites are in orange and the 27 modified sites are in blue. Figure 5-4 shows that the 36 sites cover elastic site periods from 0.1 to 4 seconds and depths from 7 m to 300 m.

Table 5-3 Coefficients for equation 2 to extend the base case shear wave velocity profiles.

| Profile | $c_1$ | $c_2$ |
|---------|-------|-------|
| 1       | 4.9   | 0.264 |
| 2       | 4.4   | 0.366 |
| 3       | 4.4   | 0.366 |
| 4       | 5     | 0.18  |
| 5       | 5.5   | 0.203 |
| 6       | 4.7   | 0.401 |
| 7       | 4.5   | 0.389 |
| 8       | 4.9   | 0.140 |
| 9       | 5.4   | 0.250 |

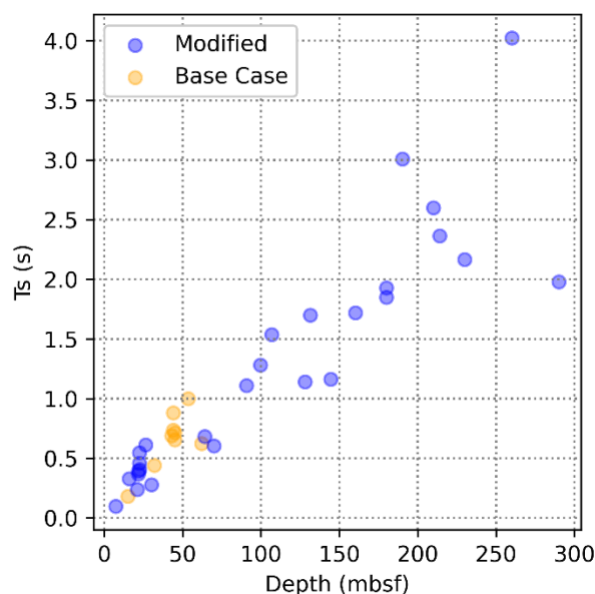


Figure 5-4 Elastic site period ( $T_s$ ) vs. depth for all site profiles.

#### 5.1.4 Future work

Due to the lack of strong ground motion data, we will estimate site amplification factors based on site response analyses using random vibration theory (RVT) (Rathje and Ozbey, 2006) and the profiles described above. We will use the computer program STRATA (Kottke et al., 2019), which is specifically designed to perform equivalent linear site response analyses using RVT and can also vary soil properties to evaluate uncertainty in soil parameters. The procedure for equivalent linear site response analyses using RVT is the same as a traditional equivalent linear site response except instead of using an acceleration time series as input, a Fourier amplitude spectrum (FAS) is used. The input FAS can be estimated using the Brune spectrum (Brune, 1970, 1971) calibrated with site specific seismological parameters. The Brune spectrum is the simplest and most common theoretical representation of an FAS due to an earthquake. The most important input parameters are the earthquake magnitude, the source to site distance, the stress drop ( $\Delta\sigma$ ), high frequency attenuation ( $\kappa$ ), and the anelastic attenuation ( $Q$ ). Like a traditional equivalent linear analysis, transfer functions are then used to propagate the FAS through the soil column to obtain the FAS at the soil surface. The transfer function

is calculated using the one-dimensional wave equation and is based on the stiffness, damping and thickness of the soil layers. Finally, RVT is used to calculate the response spectrum at the soil surface from the FAS at the soil surface. Figure 5-5 shows this workflow schematically.

Once the site response analyses are completed, we will perform regression analyses to develop a model to account for site effects.

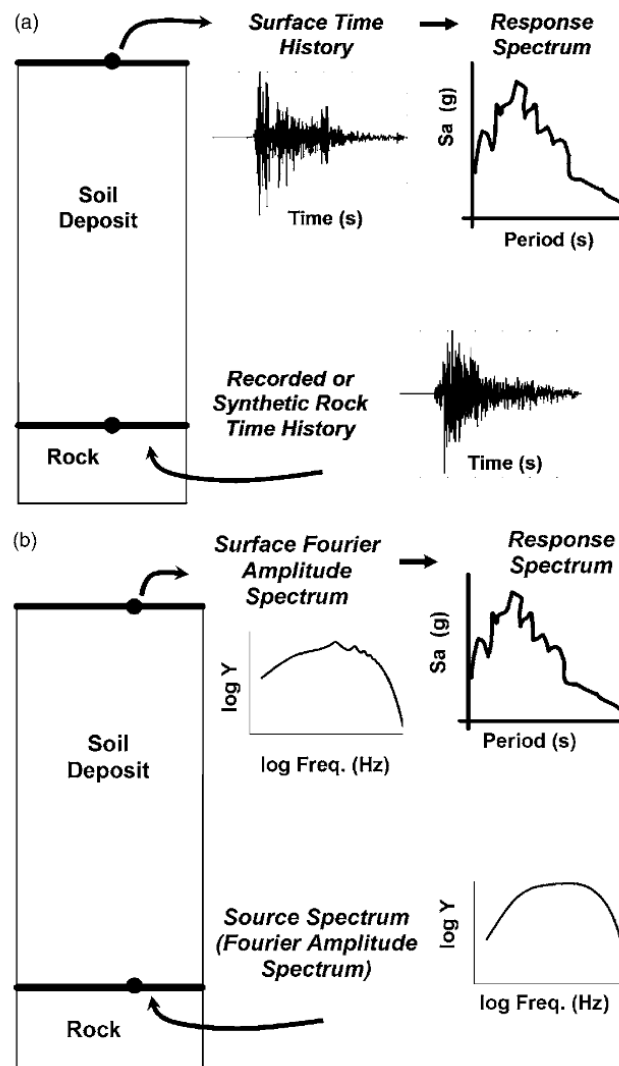


Figure 5-5 a) traditional equivalent linear site response analysis using an acceleration time series as input; b) site response analysis using random vibration theory (Rathje and Ozbey, 2006).

## 5.2 Kappa

### 5.2.1 Overview

This section describes the results of the kappa analyses. We first tried to estimate  $\kappa_0$  for as many stations as possible around the North Sea. This is documented in section 5.2.2. However, due to limited data and inconsistent results, in section 5.2.3 we focus on a subset of stations in Western Norway.

### 5.2.2 Preliminary Analysis

#### **Database**

To estimate  $\kappa_{r,AS}$  we used a subset of the earthquake waveform database (section 3.2) that included only earthquakes with  $M_w > 3.5$  and records with an epicentral distance ( $R_{epi}$ ) less than 300 km. In addition, as described in section 2.3, we only used ground motions with  $f_2 - f_1 > 8$  Hz (Ktenidou et al., 2013) and we removed records from stations that were affected by soil amplification in the high frequency range (Lermo and Chavez-Garcia, 1993) to ensure a robust calculation of  $\kappa_{r,AS}$ . The resulting database contained 230 three-component records from 54 earthquakes and 60 stations recorded from 1995 to 2022. Figure 5-6 shows the locations of the earthquake epicentres, stations, and travel paths of the recorded earthquake records. Figure 5-7 shows the number of earthquake recordings per station in the kappa database. There are only seven stations with 10 or more recordings, all of which are in western Norway except station LRW, which is located on the Shetland Islands. Only two stations have 20 or more recordings. Figure 5-8 shows the cumulative number of ground motions with  $f_1$  equal to or lower than the given frequency, and the cumulative number of ground motions with  $f_2$  equal to or higher than the given frequency for the database used in this study. About half of the ground motions have  $f_1$  less than 15 Hz and  $f_2$  greater than or equal to 35 Hz.

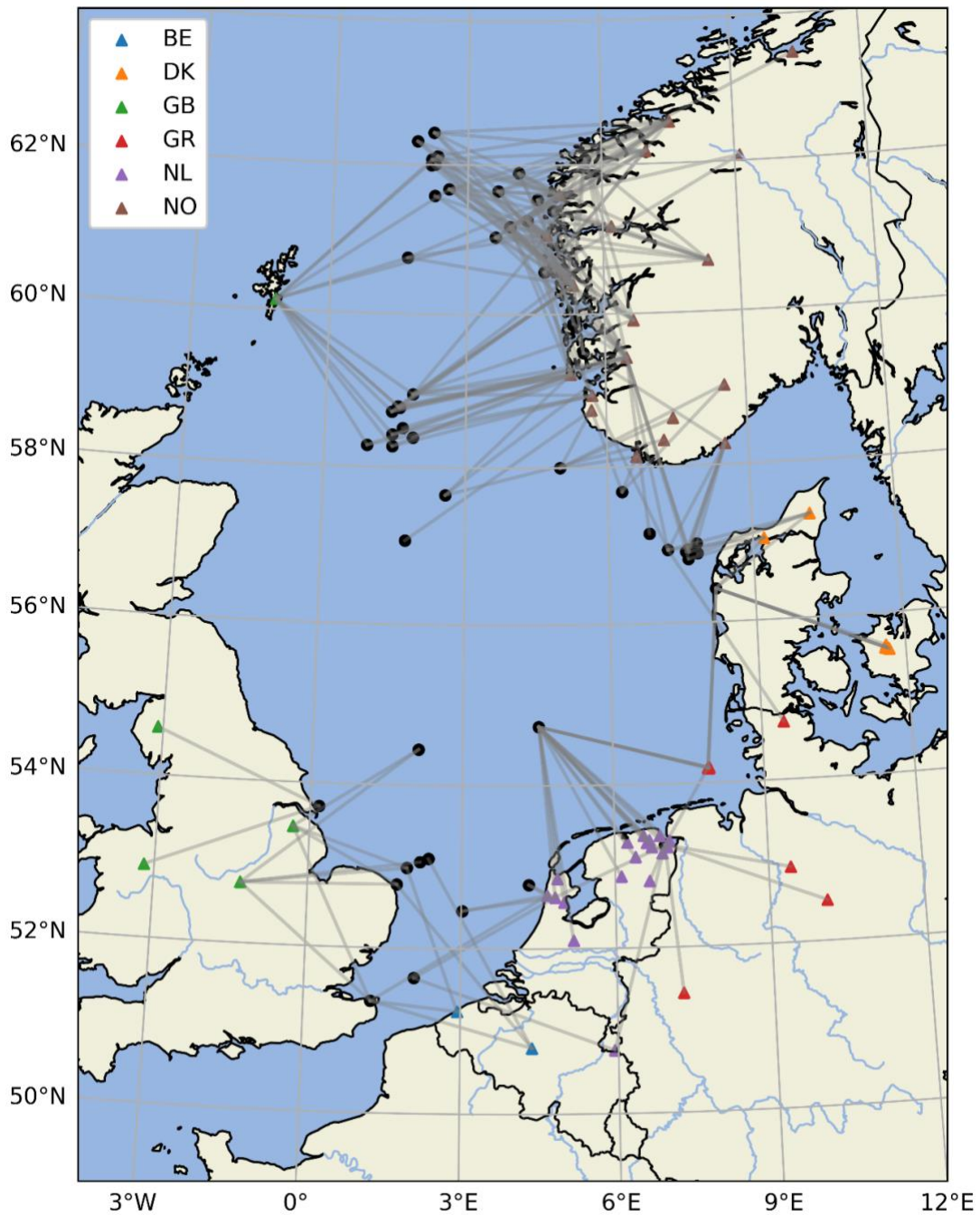


Figure 5-6. Locations of earthquake epicentres (black circles) and stations (triangles coloured based on network) used to evaluate kappa in the North Sea. Grey lines are travel paths between recorded earthquakes and stations.

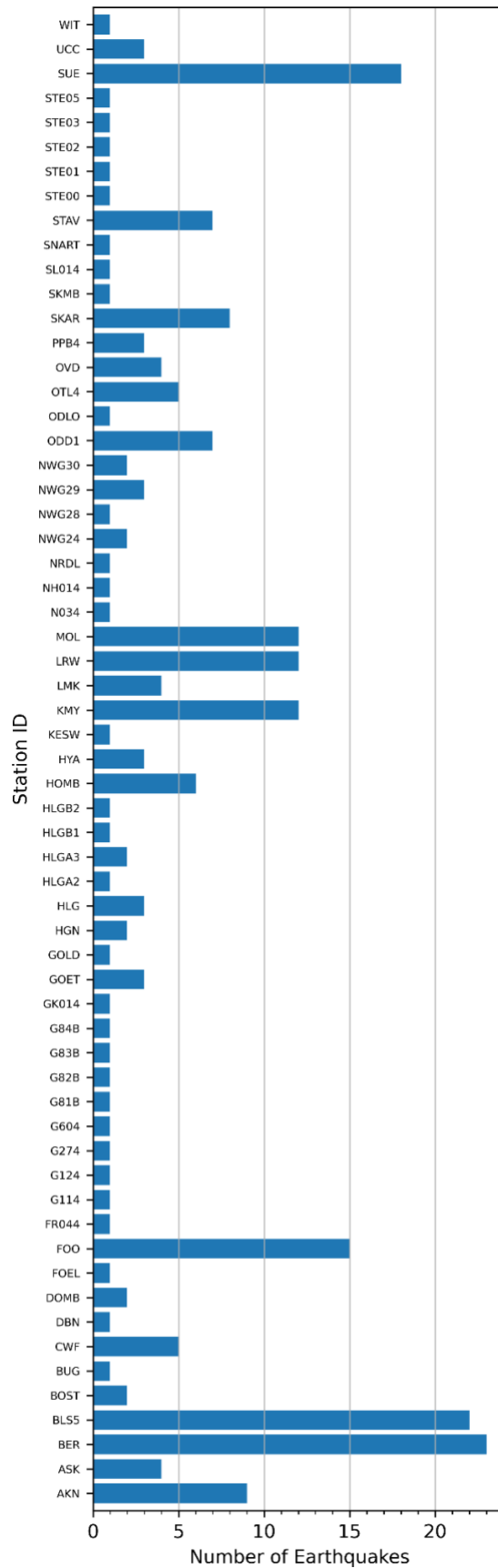


Figure 5-7 Number of earthquake recordings per station in the kappa database.

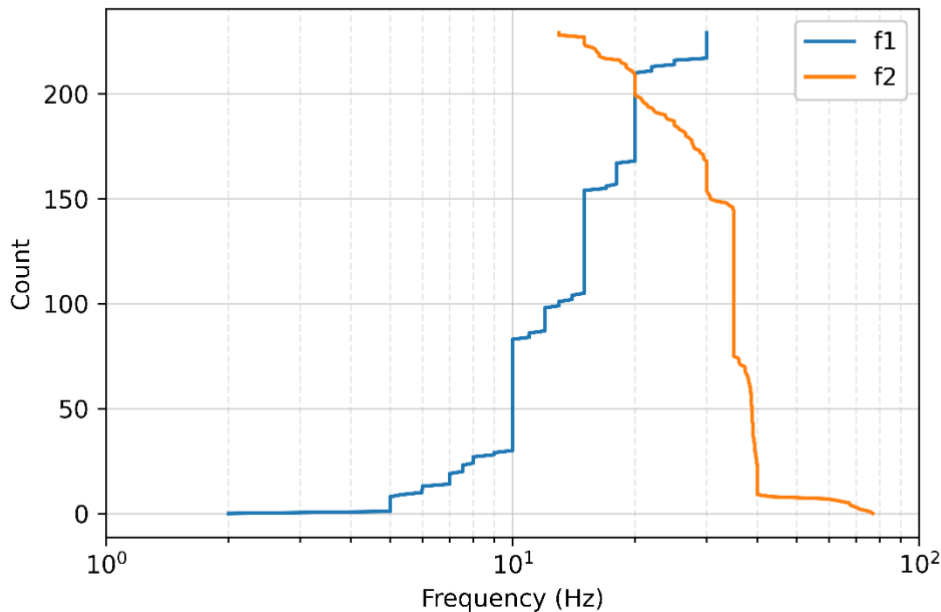


Figure 5-8 The cumulative number of ground motions with  $f_1$  equal to or lower than the given frequency, and the cumulative number of ground motions with  $f_2$  equal to or higher than the given frequency for the kappa database.

### Results and Discussion

Figure 5-9 shows results for  $\kappa_{r\_AS}$  and  $\kappa_0$  by network. The estimated values of  $\kappa_{r\_AS}$  between 0.005 and 0.085 are reasonable and correspond to shear wave velocities over the top 30 meters ( $V_{s30}$ ) of 2000 m/s to 200 m/s (Van Houtte et al., 2011). However, for all networks except the Norwegian network (NO), the  $\kappa_{r\_AS}$  trend with distance is either flat or decreasing, which is contrary to what is expected. The  $\kappa_{r\_AS}$  trend with distance for the Norwegian network is increasing, but much more gradual than expected. The slope of the trend line ( $\kappa_R$ ) can be related to the anelastic attenuation parameter  $Q$  as (Ktenidou et al., 2015):

$$Q = 1/(\beta * \kappa_R) \quad (2)$$

where  $\beta$  is the shear wave velocity at the source in km/s and assumed to be 3.5 km/s. The equivalent  $Q$  value estimated from  $\kappa_R$  for the Norwegian network is around 8000. This is much higher than the values estimated by Demuth (2019) who found  $Q$  values for Norway ranging from 1400 to 2500 for frequencies of 10 – 40 Hz using tomography techniques. The reason for this discrepancy could be that by comparing by networks, different path and site effects obscure the results (i.e. soft soil sites with high  $\kappa_{r\_AS}$  are being mixed with hard rock sites with low  $\kappa_{r\_AS}$ ). However, the results for individual stations and path azimuths are not much better.

Figure 5-10 shows the results for  $\kappa_{r\_AS}$  and  $\kappa_0$  for station BER located in Bergen, Norway. This station has the most recordings (23) of all the available stations. Figure 5-10 shows that the estimated value of  $\kappa_{r\_AS}$  is fairly constant with distance all the way out to 300 km. This is much further than previous studies, which found a constant value of  $\kappa_{r\_AS}$  only out to 20 km (Ktenidou et al., 2014) in Greece or 60

km in Arizona (Kishida et al., 2014). There does not seem to be any difference due to path effects either. The results in Figure 5-10 are colour coded by azimuth of the incoming seismic wave. Different azimuths do not seem to show a consistent trend in  $\kappa_{r\_AS}$  with distance.

The noise windows and S-wave windows used to calculate  $\kappa_{r\_AS}$  were all manually reevaluated to see if the poor correlation with distance was due to incorrect P and S wave arrival time picks. In addition, all values of  $f_1$  and  $f_2$  were also manually evaluated to ensure that the calculation of  $\kappa_{r\_AS}$  occurred for the correct frequency band. This did not substantially change the results. We next tried to fix the values of  $f_1$  and  $f_2$  for each station, to ensure that  $\kappa_{r\_AS}$  was calculated over the same frequency range. The idea behind this is that Q is frequency dependent, therefore  $\kappa_{r\_AS}$  should be calculated over the same frequency range to obtain a more robust estimate of Q and the slope of the trend line ( $\kappa_R$ ). Finally, we fixed the value of  $f_1$  and  $f_2$  to 10 Hz and 30 Hz for all recordings. These changes also did not substantially change the results.

We also tried grouping data from different stations with assumed similar site properties and recordings from similar travel paths. Figure 5-11 shows one example of stations and earthquake travel paths selected for western Norway. All the selected stations are most likely on rock or equivalent stiff site, and the earthquake travel paths cross a similar area. However, Figure 5-11 shows less change in the calculated value of  $\kappa_{r\_AS}$  with distance than expected.

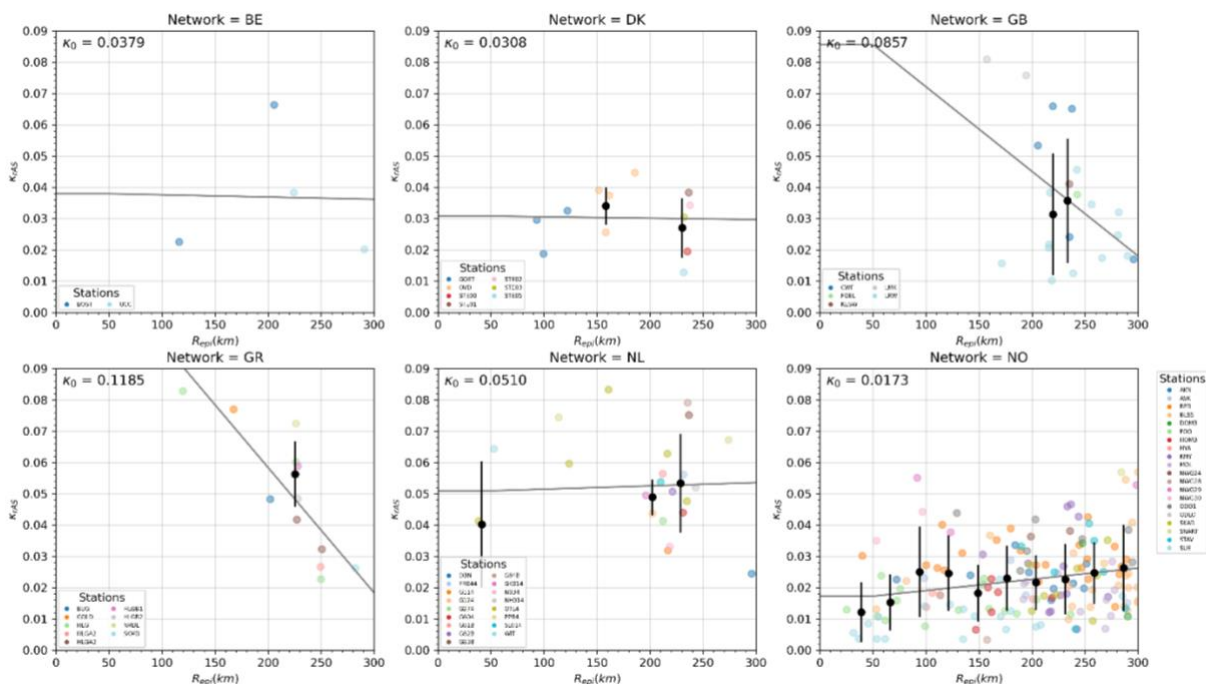


Figure 5-9 Calculated  $\kappa_{r\_AS}$  values and estimated  $\kappa_0$  by network. Black dots and error bars are the average and standard deviation for different distance bins. The grey line is the best fit trend.

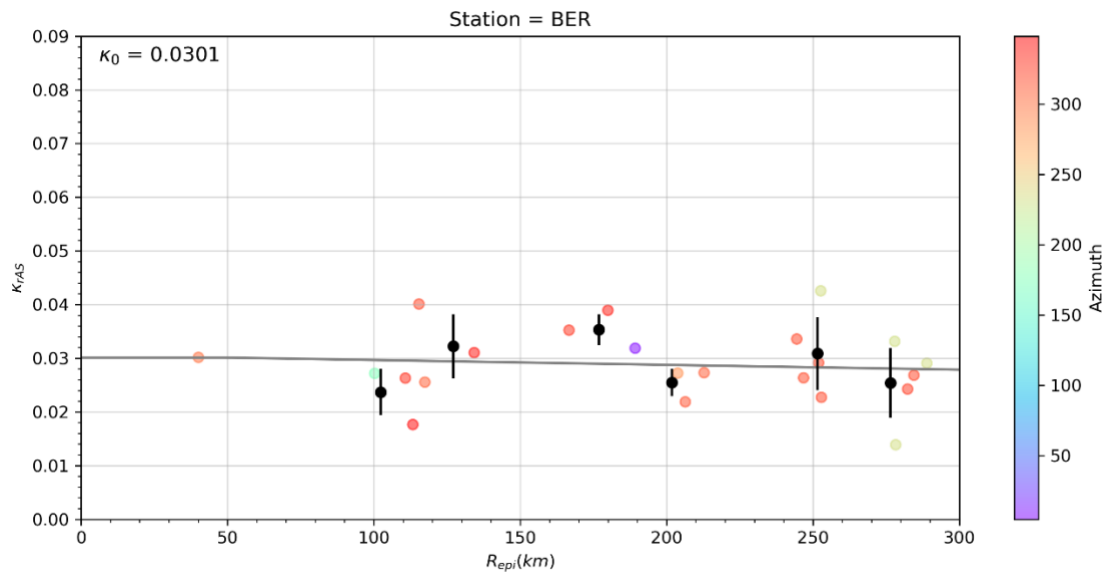


Figure 5-10 Calculated  $\kappa_{r_{AS}}$  values and estimated  $\kappa_0$  for station BER, located near Bergen, Norway. The azimuth is the azimuth of the incoming earthquake wave. Black dots and error bars are the average and standard deviation for different distance bins. The grey line is the best fit trend.

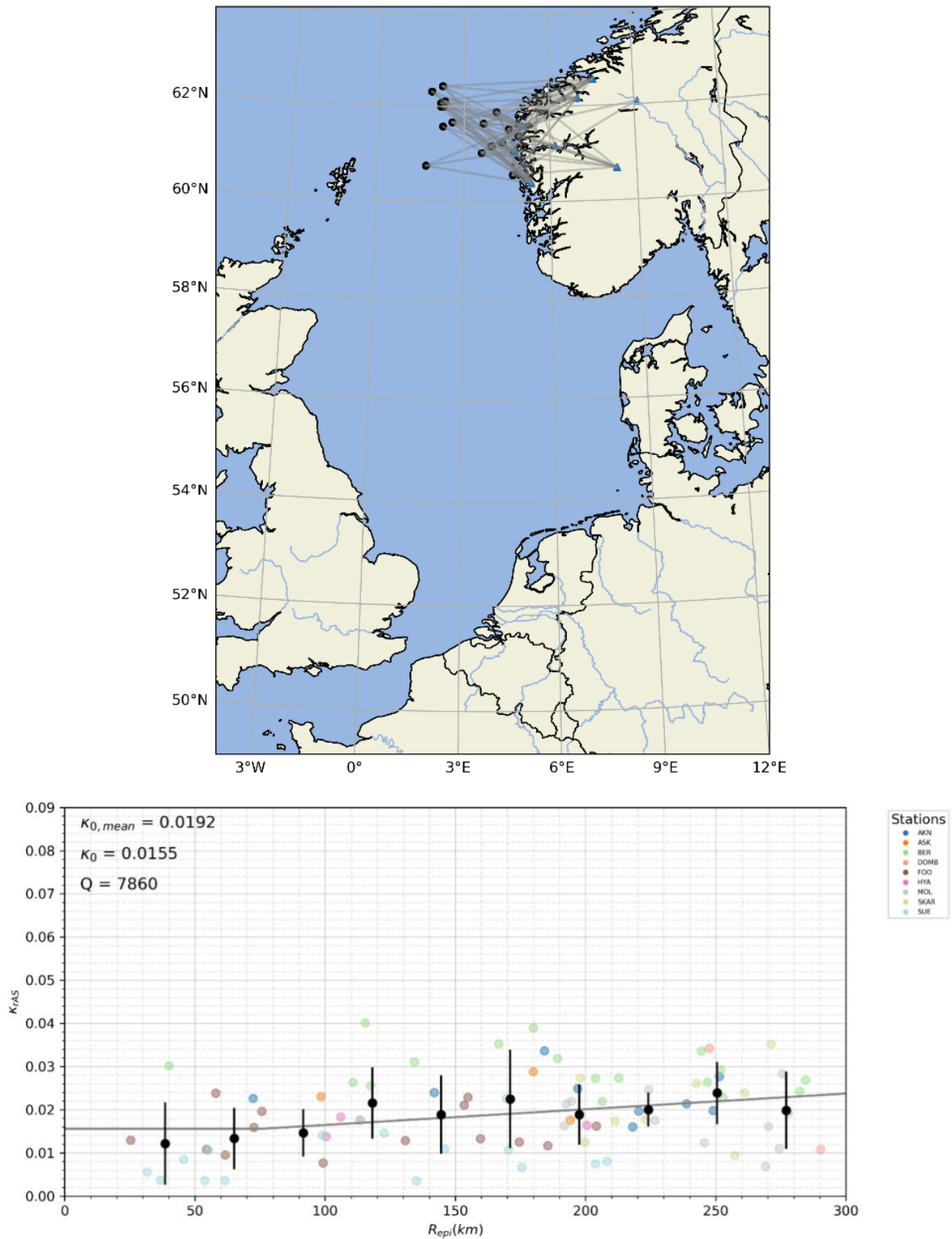
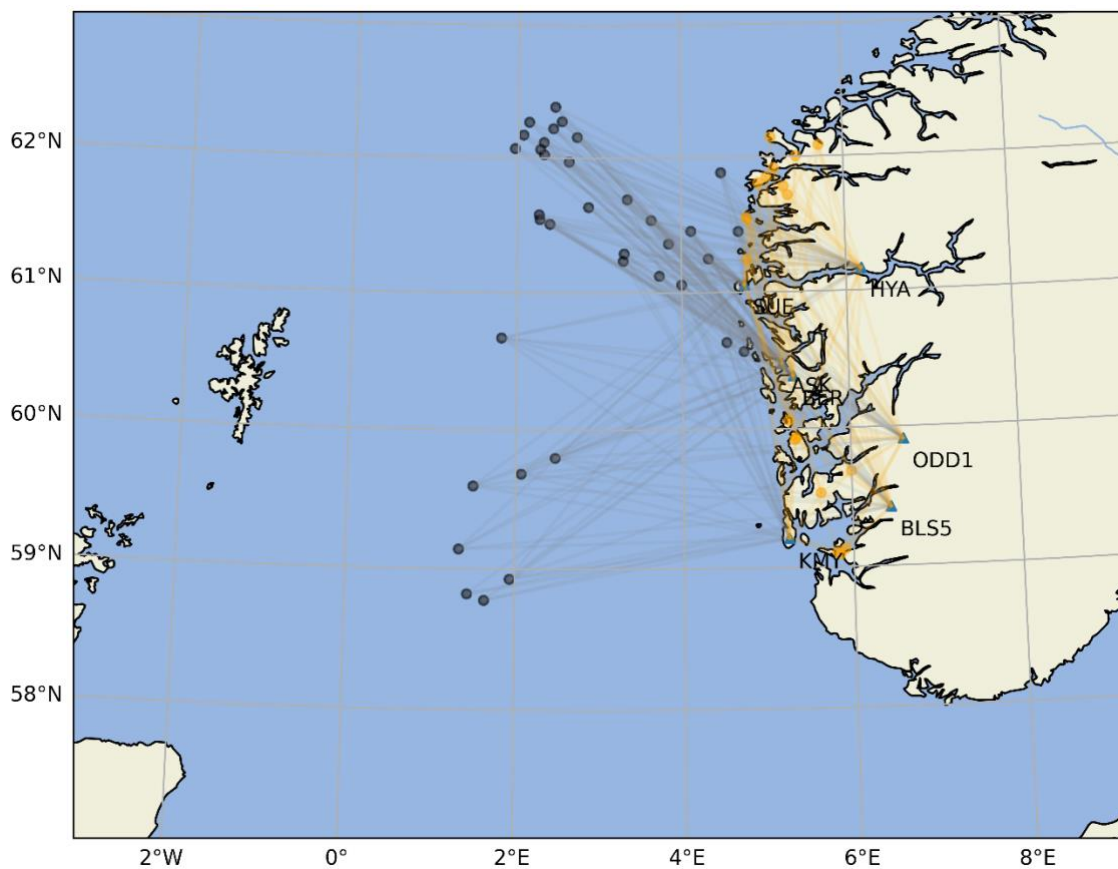


Figure 5-11. Top: map of selected stations, earthquakes, and travel paths. Bottom: calculated  $K_{r,AS}$  values and estimated  $k_0$  for selected stations and travel paths in western Norway. Black dots and error bars are the average and standard deviation for different distance bins. The grey line is the best fit trend.

### 5.2.3 Additional Work

#### **Database**

To investigate the inconclusive results from the previous section, we focused on a subset of stations in Western Norway. Each of these stations is on rock, with no amplification at high frequencies based on the HVSR, has at least one recording with  $R_{epi} < 50$  km, five recordings with  $R_{epi} < 100$  km, and at least 30 recordings total. We decreased the magnitude threshold down to  $M = 3$ . The resulting database contained 290 three-component records from 55 earthquakes and 7 stations recorded from 2009 to 2022. Figure 5-12 shows the locations of the earthquake epicentres, stations, and travel paths of the recorded earthquake records. Figure 5-13 shows the number of earthquake recordings per station in the kappa database.



*Figure 5-12 Locations of offshore earthquake epicentres (black circles), onshore earthquake epicentres (orange circles) and stations (blue triangles) used to evaluate kappa in the additional analyses. Grey and orange lines are travel paths between offshore earthquakes and stations and between onshore earthquakes and stations, respectively.*

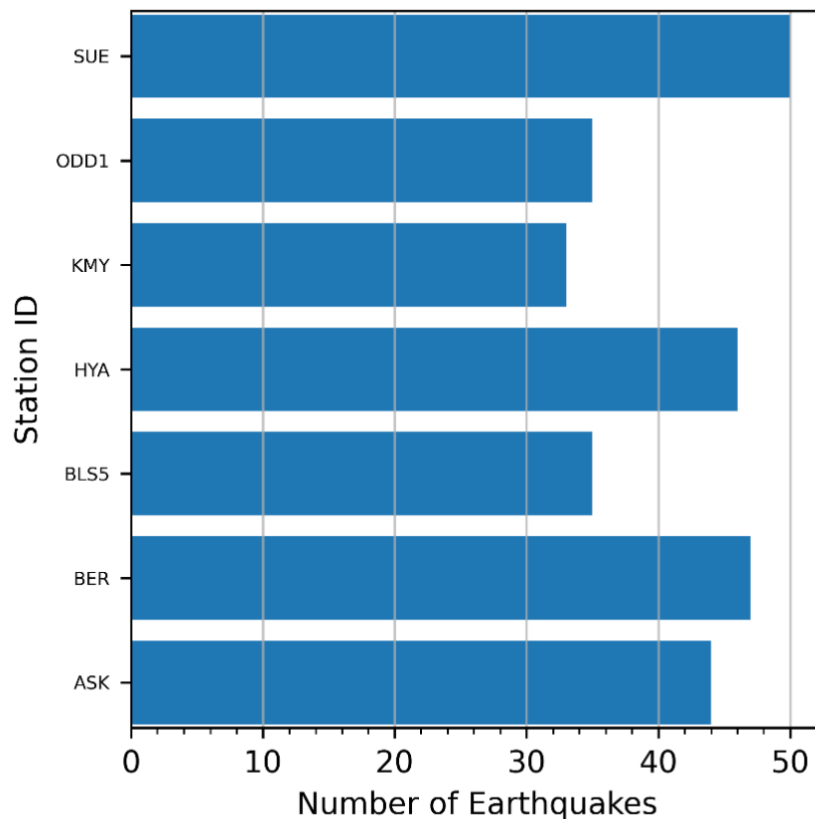


Figure 5-13 Number of earthquake recordings per station in the additional kappa database.

### Results and Discussion

At first the additional analyses produced similar results to the preliminary analyses. The  $\kappa_{r\_AS}$  values did not increase with distance as expected, or they increased but at a much slower rate. However, when we plotted  $\kappa_{r\_AS}$  versus distance for only earthquakes occurring onshore, then the results predicted  $\kappa_0$  and Q values consistent with other studies. Figure 5-12 shows which earthquakes are considered offshore (black circles) and which onshore (orange circles). Figure 5-14 through Figure 5-17 show the results by station. We fit a bi-linear line to the  $\kappa_{r\_AS}$  results to estimate  $\kappa_0$  and Q. The initial flat part of the line ranges between 40 – 60 km, which is like past studies (e.g. Ktenidou et al. 2014 found constant values of  $\kappa_{r\_AS}$  out to 20 km for data from Greece and Kishida et al. 2014 found constant values of  $\kappa_{r\_AS}$  out to 60 km for data from Arizona). Table 5-4 lists the estimated  $\kappa_0$  and Q values for results from onshore earthquakes only. Values of  $\kappa_0$  range from 0.0023 to 0.0227, which are equivalent to  $V_s/30$  values of 1000 – 3000 m/s (Van Houtte et al., 2011). This agrees with the information that these seven sites are on rock. The Q values range from 1600 to 5100, which is within the range of previous studies. Kvamme et al. (1995) found Q values from 2200 – 4750 and Demuth et al (2019) from 1400 – 2200 for frequencies of 10-30 Hz and onshore Norway.

However, the predicted Q values from station HYA and KMY are still not as expected. Station HYA could be since there are no recordings onshore less than 70 km (there were initially recordings less than 50 km away, however  $f_2 - f_1 < 8$  Hz so they were later discarded). However, station KMY has 4 recordings less than 50 km away. One possible explanation could be that these two sit on a different type of

geologic base structure. Figure 5-18 shows a simplified geologic map of Scandinavia. Stations HYA and KMY lie in the Caledonides province while the other stations are on the SW Scandinavian Domain.

The reason for the lack of increase in estimated  $\kappa_{r_{AS}}$  values with distance for offshore earthquakes is still unknown. The most likely reason may be that seismic Lg waves are strongly attenuated in oceanic-continental transition zones (Zhang and Lay, 1995). This transition may act as a filter that masks the distance dependence of  $\kappa_{r_{AS}}$  for seismic waves coming from offshore earthquakes. Future work could investigate this further. Another explanation could be something to do with the geologic structure of the earthquake locations themselves. Figure 5-18 shows that most of the offshore earthquakes come from the Viking Graben or the Møre Margin. Kennett et al. (1985) found that seismic waves passing through the grabens in the central North Sea had very weak Lg waves. What affect this has on  $\kappa_{r_{AS}}$  needs to be studied further.

Table 5-4 Kappa results for onshore earthquakes only.

| Station | $\kappa_0$ | Q    |
|---------|------------|------|
| ASK     | 0.0023     | 1600 |
| BER     | 0.0227     | 3400 |
| BLS5    | 0.0069     | 5100 |
| HYA     | 0.0140     |      |
| KMY     | 0.0100     |      |
| ODD1    | 0.0093     | 1900 |
| SUE     | 0.0037     | 2500 |

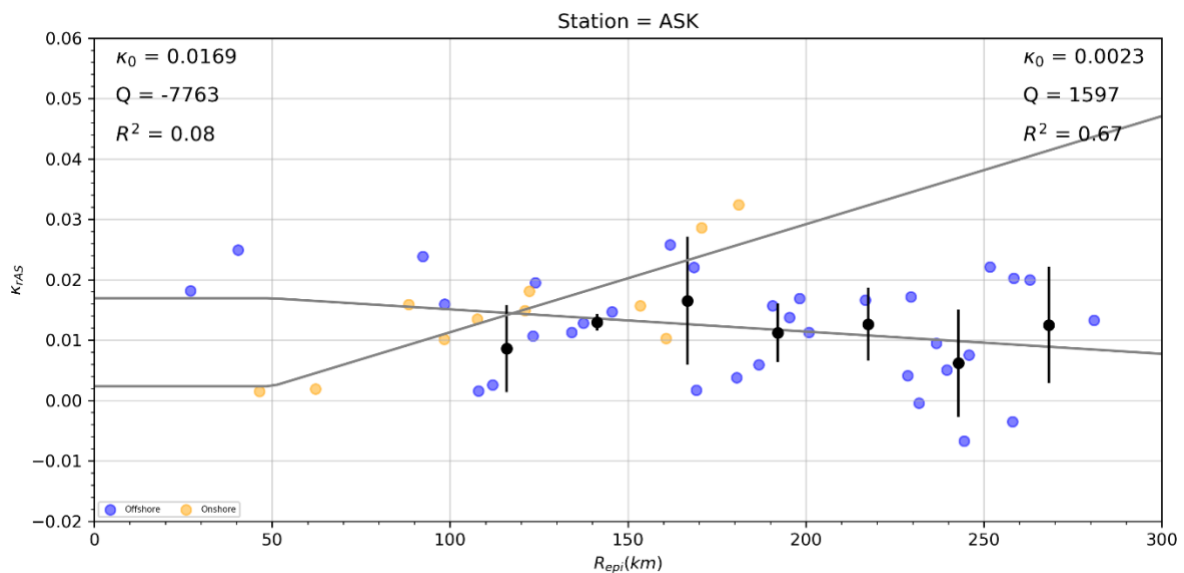


Figure 5-14  $\kappa_{r_{AS}}$  and estimated  $\kappa_0$  and Q for offshore (blue) and onshore (orange) earthquakes. Black dots and error bars are the average and standard deviation for different distance bins. The grey lines are the best fit trend lines. Top left values are for offshore, top right are for onshore.

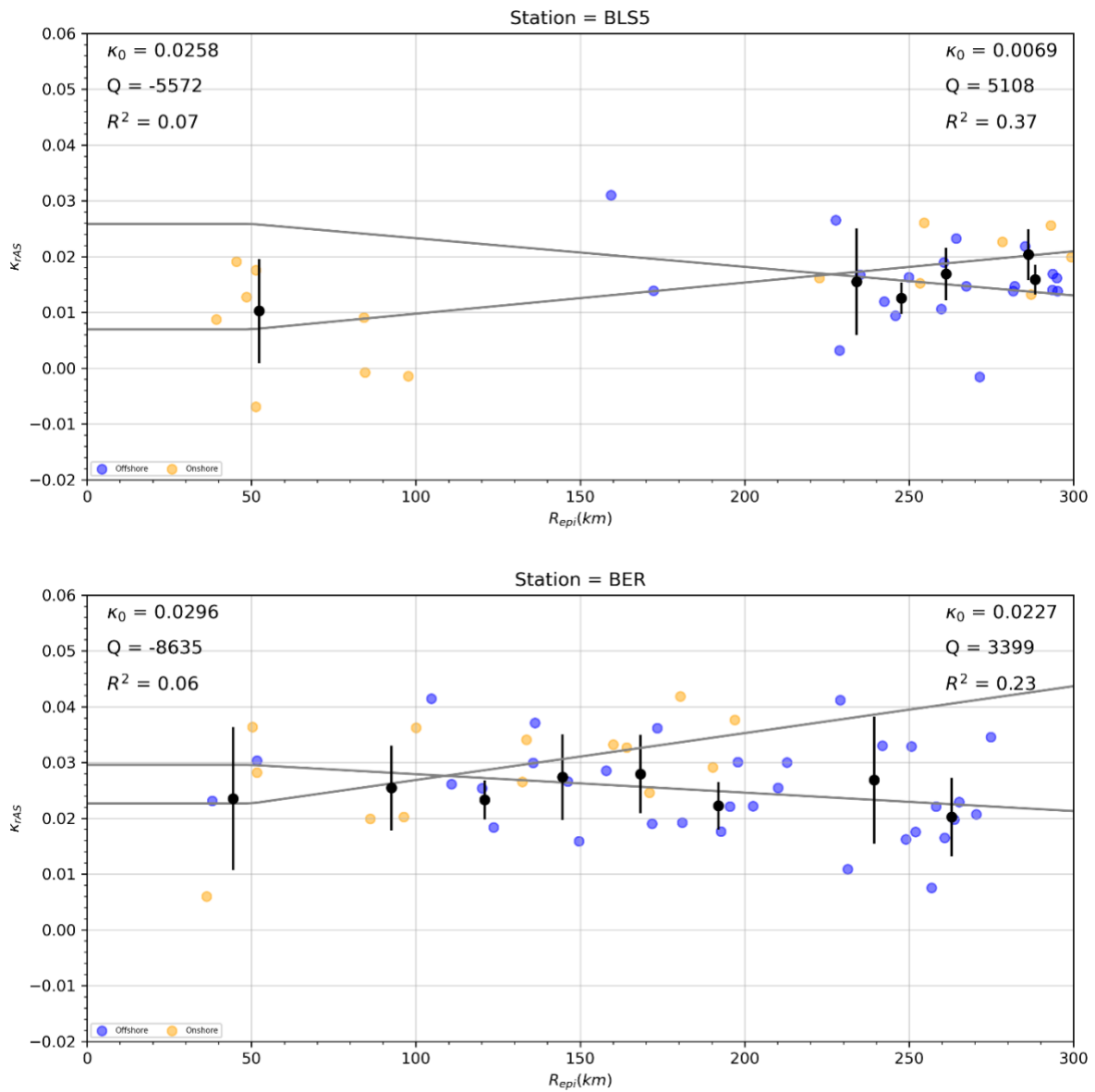


Figure 5-15  $\kappa_{r,AS}$  and estimated  $\kappa_0$  and Q for offshore (blue) and onshore (orange) earthquakes. Black dots and error bars are the average and standard deviation for different distance bins. The grey lines are the best fit trend lines. Top left values are for offshore, top right are for onshore.

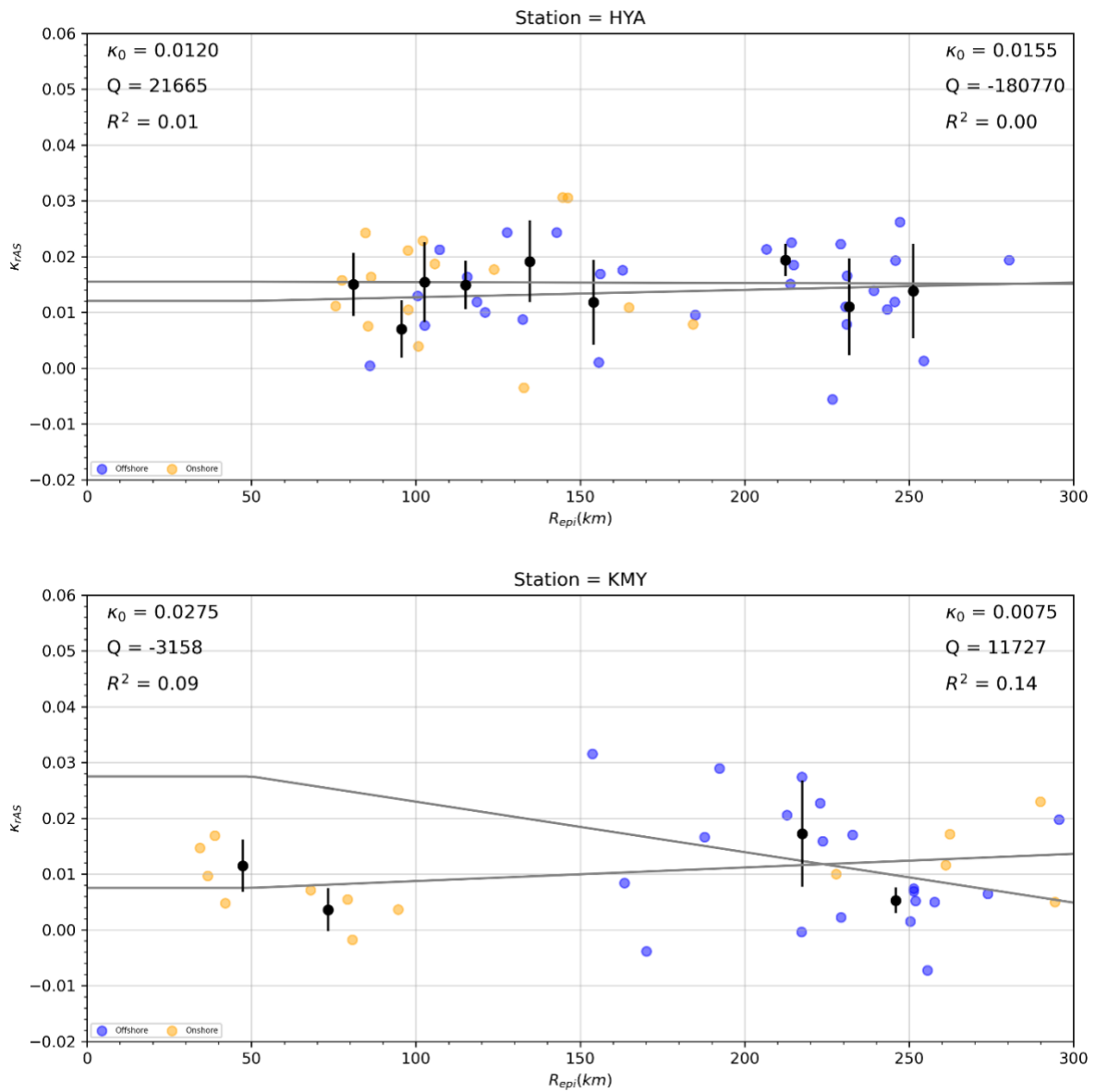


Figure 5-16  $\kappa_{r\_AS}$  and estimated  $\kappa_0$  and Q for offshore (blue) and onshore (orange) earthquakes. Black dots and error bars are the average and standard deviation for different distance bins. The grey lines are the best fit trend lines. Top left values are for offshore, top right are for onshore.

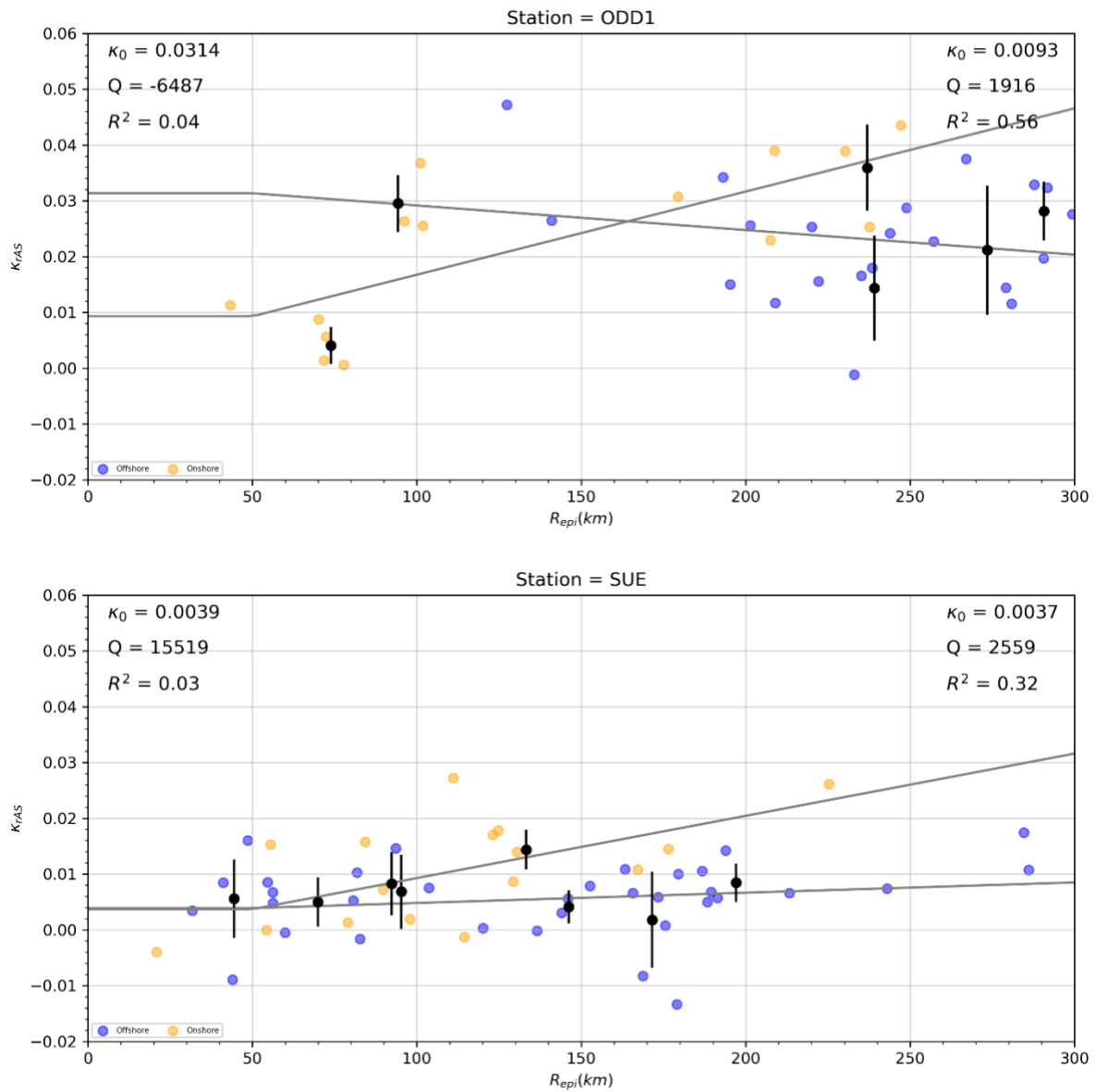


Figure 5-17  $\kappa_{r,AS}$  and estimated  $\kappa_0$  and Q for offshore (blue) and onshore (orange) earthquakes. Black dots and error bars are the average and standard deviation for different distance bins. The grey lines are the best fit trend lines. Top left values are for offshore, top right are for onshore.

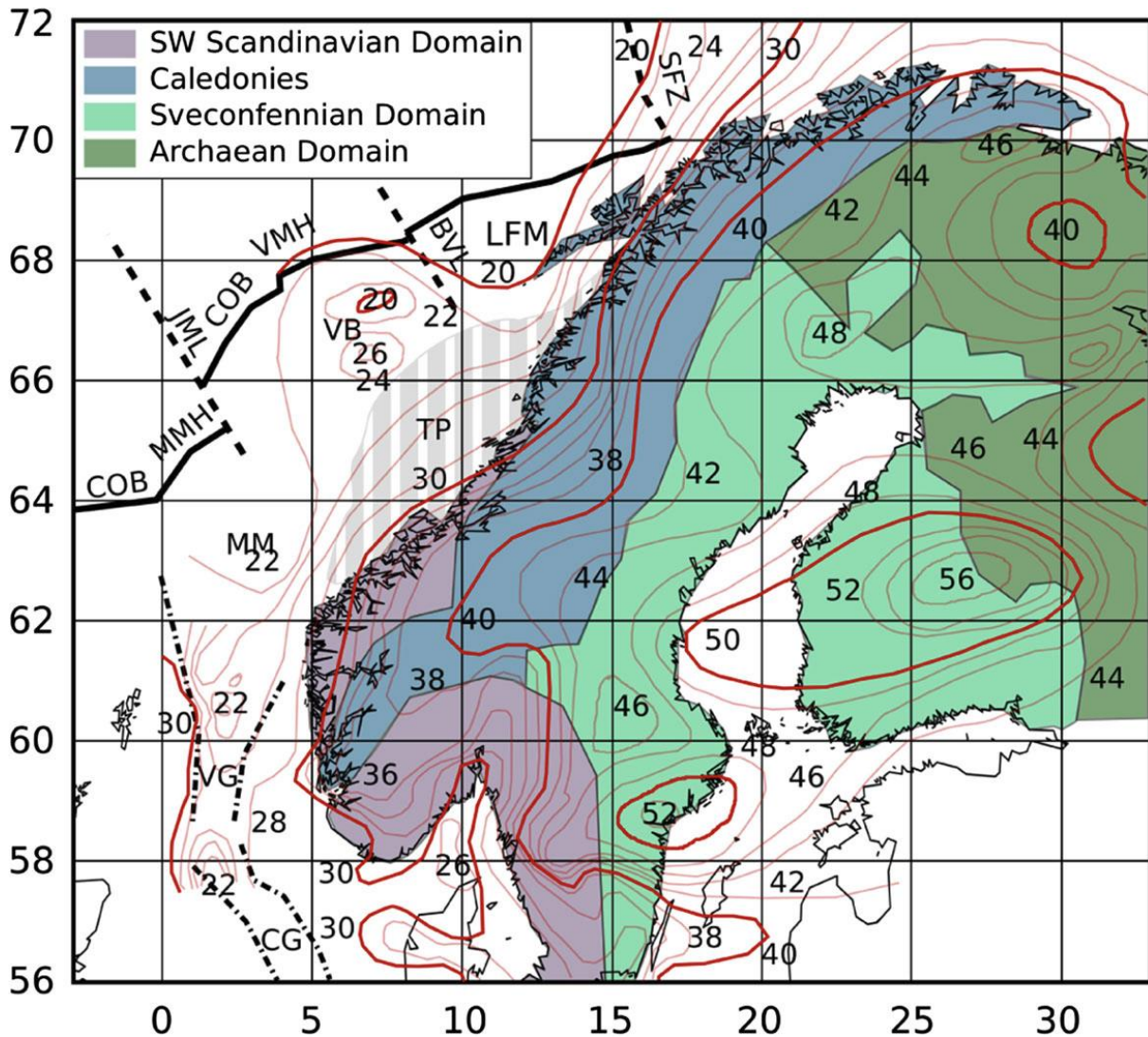


Figure 5-18 Simplified geology of Scandinavia. The red contours are the Moho depth. CG = Central Graben; VG = Viking Graben; MM = Møre Margin. From Demuth et al (2019).

## 6 Probabilistic seismic hazard analysis

### 6.1 Sources

The seismic source model defines the earthquake sources, their geometry, and the rate that earthquakes of various magnitudes are expected to occur on each source (magnitude recurrence relation). We developed three areal seismic source models based on previous regional studies, and one zoneless model (smoothed seismicity) based on the updated North Sea earthquake catalogue. The four different models were combined using a logic tree. For all models we used a truncated exponential model for the magnitude recurrence relation and minimum magnitude of  $M_w = 4.0$ . We set the minimum magnitude at 4.0 because this is likely the minimum magnitude to cause damage (Bommer and Crowley, 2017). Table 6-1 lists the different models and their weights. The following sections describe each seismic source model in more detail.

Table 6-1 Selected seismic source models and weights used in PSHA.

| Seismic Source Model | Weight |
|----------------------|--------|
| Model 1              | 0.25   |
| Model 2              | 0.25   |
| Model 3              | 0.35   |
| Model 4              | 0.15   |

#### 6.1.1 Models 1, 2 and 3

Models 1 and 2 are based on seismic hazard analyses for Norway (NORSAR, 2019), Germany (Grünthal et al., 2018), France (Drouet et al., 2020), and the UK (EQE, 2002; Mosca et al. 2020, 2024). We combined areal sources from each of these national studies to cover an area 300 km around the North Sea study area. For Model 1, we used Zonation 1 from NORSAR (2019), Model D from Grünthal et al. (2018), the EDF model described in Drouet et al. (2020), and a mixture of model A and B from EQE (2002). The source boundaries for these models are mainly based on seismicity patterns. Figure 6-1 shows the areal source zones for Model 1 and Table 6-2 lists the source parameters. Because the activity rates for the different areal sources were not available for the EQE models, we estimated activity rates based on the SHARP catalogue. For Model 2 we used Zonation 2 from NORSAR (2019), model E from Grünthal et al. (2018), the GEOTER model from Drouet et al. (2020), and SZM2 from Mosca et al. (2024). The source boundaries from these models are mainly based on geology and neotectonics. Figure 6-2 shows the areal source zones for Model 2 and Table 6-3 lists the source parameters.

For Model 3 we used the areal source model of the 2020 European Seismic Hazard Model (ESHM20) (Danciu et al., 2021). The areal source boundaries used in ESHM20 are like the areal sources used in Bungum et al. (2000) for Norway, Model C from Grünthal et al. (2018) for Germany, the IRSN model described in Drouet et al. (2020) for France, and SZM1 from Mosca et al. (2024) for the UK. Because these national models are already represented by the ESHM20 model, we did not include them in a separate seismic source model. Figure 6-3 shows the areal source zones for Model 3 and Table 6-4 lists the source parameters.

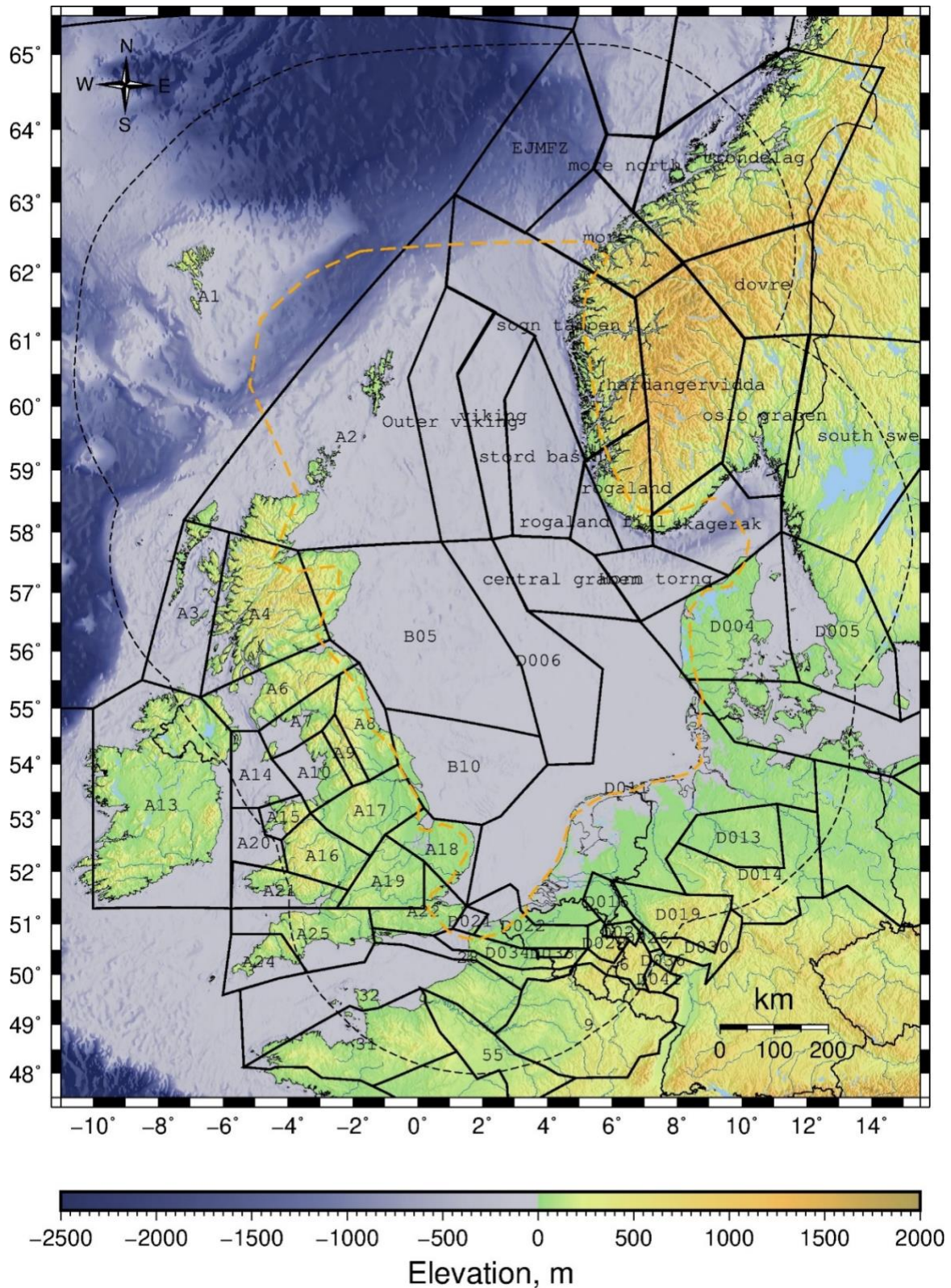


Figure 6-1 Areal source zones for Model 1. The orange dashed line is the area of interest and the black dashed line is 300 km around the area of interest.

Table 6-2 Source characteristics for Model 1. Ref corresponds to N19 = NORSAR (2019), D20 = Drouet et al (2020), G18 = Grünthal et al. (2018) and E02 = EQE (2002). For the depth pdf  $U$  = uniform distribution with top and bottom, and  $T$  = triangle distribution with three points of the triangle. Mech Weights refers to the fault mechanism weights, in the order of strike slip, normal, reverse.

| ID             | Ref | $N(M_{\min}=4)$ | b-value | $M_{\max}$                 | $M_{\max}$ Weights    | Depth pdf          | Mech Weights        |
|----------------|-----|-----------------|---------|----------------------------|-----------------------|--------------------|---------------------|
| central graben | N19 | 0.0073          | 0.920   | [6.6,6.9,7.2]              | [0.165,0.67,0.165]    | $U[5,20]$          | [0.34,0.33,0.33]    |
| dovre          | N19 | 0.0008          | 0.920   | [6.6,6.9,7.2]              | [0.165,0.67,0.165]    | $U[5,20]$          | [0.34,0.33,0.33]    |
| EJMFZ          | N19 | 0.0234          | 0.920   | [6.6,6.9,7.2]              | [0.165,0.67,0.165]    | $U[5,20]$          | [0.34,0.33,0.33]    |
| hardangervidda | N19 | 0.0134          | 0.920   | [6.6,6.9,7.2]              | [0.165,0.67,0.165]    | $U[5,20]$          | [0.34,0.33,0.33]    |
| Horn tornq     | N19 | 0.0670          | 0.920   | [6.6,6.9,7.2]              | [0.165,0.67,0.165]    | $U[5,20]$          | [0.34,0.33,0.33]    |
| mid norw basin | N19 | 0.0226          | 1.063   | [6.6,6.9,7.2]              | [0.165,0.67,0.165]    | $U[5,20]$          | [0.34,0.33,0.33]    |
| mid norw shelf | N19 | 0.0939          | 1.063   | [6.6,6.9,7.2]              | [0.165,0.67,0.165]    | $U[5,20]$          | [0.34,0.33,0.33]    |
| more           | N19 | 0.0755          | 0.920   | [6.6,6.9,7.2]              | [0.165,0.67,0.165]    | $U[5,20]$          | [0.34,0.33,0.33]    |
| more north     | N19 | 0.0035          | 0.920   | [6.6,6.9,7.2]              | [0.165,0.67,0.165]    | $U[5,20]$          | [0.34,0.33,0.33]    |
| oslo graben    | N19 | 0.0792          | 0.920   | [6.6,6.9,7.2]              | [0.165,0.67,0.165]    | $U[5,20]$          | [0.34,0.33,0.33]    |
| Outer viking   | N19 | 0.0139          | 0.920   | [6.6,6.9,7.2]              | [0.165,0.67,0.165]    | $U[5,20]$          | [0.34,0.33,0.33]    |
| rogaland       | N19 | 0.0206          | 0.920   | [6.6,6.9,7.2]              | [0.165,0.67,0.165]    | $U[5,20]$          | [0.34,0.33,0.33]    |
| rogaland fill  | N19 | 0.0059          | 0.920   | [6.6,6.9,7.2]              | [0.165,0.67,0.165]    | $U[5,20]$          | [0.34,0.33,0.33]    |
| skagerak       | N19 | 0.0157          | 0.920   | [6.6,6.9,7.2]              | [0.165,0.67,0.165]    | $U[5,20]$          | [0.34,0.33,0.33]    |
| sogn tampen    | N19 | 0.3137          | 0.920   | [6.6,6.9,7.2]              | [0.165,0.67,0.165]    | $U[5,20]$          | [0.34,0.33,0.33]    |
| south swe      | N19 | 0.0158          | 0.930   | [6.6,6.9,7.2]              | [0.165,0.67,0.165]    | $U[5,20]$          | [0.34,0.33,0.33]    |
| stord basin    | N19 | 0.0171          | 0.920   | [6.6,6.9,7.2]              | [0.165,0.67,0.165]    | $U[5,20]$          | [0.34,0.33,0.33]    |
| trondelag      | N19 | 0.0118          | 0.920   | [6.6,6.9,7.2]              | [0.165,0.67,0.165]    | $U[5,20]$          | [0.34,0.33,0.33]    |
| viking         | N19 | 0.0327          | 0.920   | [6.6,6.9,7.2]              | [0.165,0.67,0.165]    | $U[5,20]$          | [0.34,0.33,0.33]    |
| 6              | D20 | 2.4189          | 0.798   | [6.3,6.5,7.1]              | [0.6,0.3,0.1]         | $T[10,14,20]$      | [0.34,0.33,0.33]    |
| 9              | D20 | 0.1787          | 1.050   | [5.7,6.0,6.6,7.1]          | [0.35,0.35,0.20,0.1]  | $T[8,14,20]$       | [0.34,0.33,0.33]    |
| 28             | D20 | 3.3791          | 0.992   | [6.3,6.5,7.1]              | [0.6,0.3,0.1]         | $T[10,14,20]$      | [0.34,0.33,0.33]    |
| 31             | D20 | 1.8289          | 0.948   | [6.3,6.5,7.1]              | [0.6,0.3,0.1]         | $T[10,14,20]$      | [0.34,0.33,0.33]    |
| 32             | D20 | 0.2822          | 1.032   | [5.7,6.0,6.6,7.1]          | [0.35,0.35,0.20,0.1]  | $T[8,14,20]$       | [0.34,0.33,0.33]    |
| 55             | D20 | 0.1773          | 0.969   | [5.7,6.0,6.6,7.1]          | [0.35,0.35,0.20,0.1]  | $T[8,14,20]$       | [0.34,0.33,0.33]    |
| D002           | G18 | 0.0141          | 1.027   | [5.82,6.04,6.38,6.38,6.82] | [0.2,0.2,0.2,0.2,0.2] | $T[9.6,19.5,32]$   | [0.632,0.263,0.105] |
| D004           | G18 | 0.0108          | 1.110   | [5.7,6.18,6.18,6.48,6.83]  | [0.2,0.2,0.2,0.2,0.2] | $T[9.6,19.5,32]$   | [0.632,0.263,0.105] |
| D005           | G18 | 0.0248          | 1.027   | [5.82,6.04,6.38,6.38,6.82] | [0.2,0.2,0.2,0.2,0.2] | $T[9.6,19.5,32]$   | [0.632,0.263,0.105] |
| D006           | G18 | 0.0087          | 1.110   | [5.69,6.14,6.46,6.68,7.19] | [0.2,0.2,0.2,0.2,0.2] | $T[9.6,19.5,32]$   | [0.632,0.263,0.105] |
| D007           | G18 | 0.0046          | 1.027   | [5.82,6.04,6.38,6.38,6.82] | [0.2,0.2,0.2,0.2,0.2] | $T[9.6,19.5,32]$   | [0.632,0.263,0.105] |
| D011           | G18 | 0.0089          | 1.110   | [5.7,6.18,6.18,6.48,6.83]  | [0.2,0.2,0.2,0.2,0.2] | $T[9.6,19.5,32]$   | [0.632,0.263,0.105] |
| D013           | G18 | 0.0001          | 1.110   | [5.7,6.18,6.18,6.48,6.83]  | [0.2,0.2,0.2,0.2,0.2] | $T[9.6,19.5,32]$   | [0.632,0.263,0.105] |
| D014           | G18 | 0.0028          | 0.864   | [5.7,6.18,6.18,6.48,6.83]  | [0.2,0.2,0.2,0.2,0.2] | $T[8,16.4,32.7]$   | [0.727,0.258,0.015] |
| D015           | G18 | 0.0316          | 1.110   | [5.7,6.18,6.18,6.48,6.83]  | [0.2,0.2,0.2,0.2,0.2] | $T[9.6,19.5,32]$   | [0.632,0.263,0.105] |
| D016           | G18 | 0.0399          | 0.774   | [6.74,6.84,7.03,7.08,7.32] | [0.2,0.2,0.2,0.2,0.2] | $T[7.7,13.7,20.9]$ | [0.267,0.733,0]     |
| D019           | G18 | 0.0044          | 1.110   | [5.69,6.14,6.21,6.47,6.83] | [0.2,0.2,0.2,0.2,0.2] | $T[9.6,19.5,32]$   | [0.632,0.263,0.105] |
| D021           | G18 | 0.0038          | 0.753   | [5.67,6.06,6.25,6.43,6.82] | [0.2,0.2,0.2,0.2,0.2] | $T[5.2,13.4,23.1]$ | [0.571,0.215,0.214] |
| D022           | G18 | 0.0276          | 0.753   | [5.67,6.06,6.25,6.43,6.82] | [0.2,0.2,0.2,0.2,0.2] | $T[5.2,13.4,23.1]$ | [0.571,0.215,0.214] |
| D024           | G18 | 0.0532          | 0.781   | [6.74,6.84,7.03,7.08,7.32] | [0.2,0.2,0.2,0.2,0.2] | $T[7.7,13.7,20.9]$ | [0.267,0.733,0]     |

|      |     |        |       |                            |                       |                  |                     |
|------|-----|--------|-------|----------------------------|-----------------------|------------------|---------------------|
| D026 | G18 | 0.0095 | 0.949 | [6.74,6.84,7.03,7.08,7.32] | [0.2,0.2,0.2,0.2,0.2] | T[7.7,13.7,20.9] | [0,0.75,0.25]       |
| D028 | G18 | 0.0514 | 0.788 | [6.74,6.84,7.03,7.08,7.32] | [0.2,0.2,0.2,0.2,0.2] | T[7.7,13.7,20.9] | [0.267,0.733,0]     |
| D030 | G18 | 0.0167 | 0.864 | [5.69,6.14,6.21,6.47,6.83] | [0.2,0.2,0.2,0.2,0.2] | T[8,16.4,32.7]   | [0.727,0.258,0.015] |
| D033 | G18 | 0.0338 | 0.753 | [5.67,6.06,6.25,6.43,6.82] | [0.2,0.2,0.2,0.2,0.2] | T[5.2,13.4,23.1] | [0.571,0.215,0.214] |
| D034 | G18 | 0.0154 | 0.845 | [5.67,6.06,6.25,6.43,6.82] | [0.2,0.2,0.2,0.2,0.2] | T[5.2,13.4,23.1] | [0.571,0.215,0.214] |
| D036 | G18 | 0.0356 | 0.991 | [5.66,6.04,6.47,6.59,7.18] | [0.2,0.2,0.2,0.2,0.2] | T[7.7,13.7,20.9] | [0,0.75,0.25]       |
| D041 | G18 | 0.0173 | 0.845 | [5.66,6.04,6.47,6.59,7.18] | [0.2,0.2,0.2,0.2,0.2] | T[5.2,13.4,23.1] | [0.571,0.215,0.214] |
| A1   | E02 | 0.0130 | 1.150 | [6.0,6.5,7.0]              | [0.4,0.4,0.2]         | T[0,10,30]       | [0.34,0.33,0.33]    |
| A2   | E02 | 0.0033 | 1.150 | [6.0,6.5,7.0]              | [0.4,0.4,0.2]         | T[0,10,30]       | [0.34,0.33,0.33]    |
| A3   | E02 | 0.0008 | 1.150 | [6.0,6.5,7.0]              | [0.4,0.4,0.2]         | T[0,10,30]       | [0.34,0.33,0.33]    |
| A4   | E02 | 0.0267 | 1.280 | [6.0,6.5,7.0]              | [0.4,0.4,0.2]         | T[0,10,30]       | [0.34,0.33,0.33]    |
| A6   | E02 | 0.0006 | 1.280 | [6.0,6.5,7.0]              | [0.4,0.4,0.2]         | T[0,10,30]       | [0.34,0.33,0.33]    |
| A7   | E02 | 0.0067 | 1.280 | [6.0,6.5,7.0]              | [0.4,0.4,0.2]         | T[0,10,30]       | [0.34,0.33,0.33]    |
| A8   | E02 | 0.0004 | 1.280 | [6.0,6.5,7.0]              | [0.4,0.4,0.2]         | T[0,10,30]       | [0.34,0.33,0.33]    |
| A9   | E02 | 0.0133 | 1.280 | [6.0,6.5,7.0]              | [0.4,0.4,0.2]         | T[0,10,30]       | [0.34,0.33,0.33]    |
| A10  | E02 | 0.0100 | 1.280 | [6.0,6.5,7.0]              | [0.4,0.4,0.2]         | T[0,10,30]       | [0.34,0.33,0.33]    |
| A13  | E02 | 0.0031 | 1.150 | [6.0,6.5,7.0]              | [0.4,0.4,0.2]         | T[0,10,30]       | [0.34,0.33,0.33]    |
| A14  | E02 | 0.0004 | 1.150 | [6.0,6.5,7.0]              | [0.4,0.4,0.2]         | T[0,10,30]       | [0.34,0.33,0.33]    |
| A15  | E02 | 0.0133 | 1.280 | [6.0,6.5,7.0]              | [0.4,0.4,0.2]         | T[0,10,30]       | [0.34,0.33,0.33]    |
| A16  | E02 | 0.0067 | 1.280 | [6.0,6.5,7.0]              | [0.4,0.4,0.2]         | T[0,10,30]       | [0.34,0.33,0.33]    |
| A17  | E02 | 0.0233 | 1.280 | [6.0,6.5,7.0]              | [0.4,0.4,0.2]         | T[0,10,30]       | [0.34,0.33,0.33]    |
| A18  | E02 | 0.0100 | 1.280 | [6.0,6.5,7.0]              | [0.4,0.4,0.2]         | T[0,10,30]       | [0.34,0.33,0.33]    |
| A19  | E02 | 0.0005 | 1.280 | [6.0,6.5,7.0]              | [0.4,0.4,0.2]         | T[0,10,30]       | [0.34,0.33,0.33]    |
| A20  | E02 | 0.0003 | 1.150 | [6.0,6.5,7.0]              | [0.4,0.4,0.2]         | T[0,10,30]       | [0.34,0.33,0.33]    |
| A21  | E02 | 0.0167 | 1.280 | [6.0,6.5,7.0]              | [0.4,0.4,0.2]         | T[0,10,30]       | [0.34,0.33,0.33]    |
| A22  | E02 | 0.0100 | 1.280 | [6.0,6.5,7.0]              | [0.4,0.4,0.2]         | T[0,10,30]       | [0.34,0.33,0.33]    |
| A24  | E02 | 0.0004 | 1.280 | [6.0,6.5,7.0]              | [0.4,0.4,0.2]         | T[0,10,30]       | [0.34,0.33,0.33]    |
| A25  | E02 | 0.0033 | 1.280 | [6.0,6.5,7.0]              | [0.4,0.4,0.2]         | T[0,10,30]       | [0.34,0.33,0.33]    |
| B05  | E02 | 0.0026 | 1.150 | [6.0,6.5,7.0]              | [0.4,0.4,0.2]         | T[0,10,30]       | [0.34,0.33,0.33]    |
| B10  | E02 | 0.0100 | 1.150 | [6.0,6.5,7.0]              | [0.4,0.4,0.2]         | T[0,10,30]       | [0.34,0.33,0.33]    |

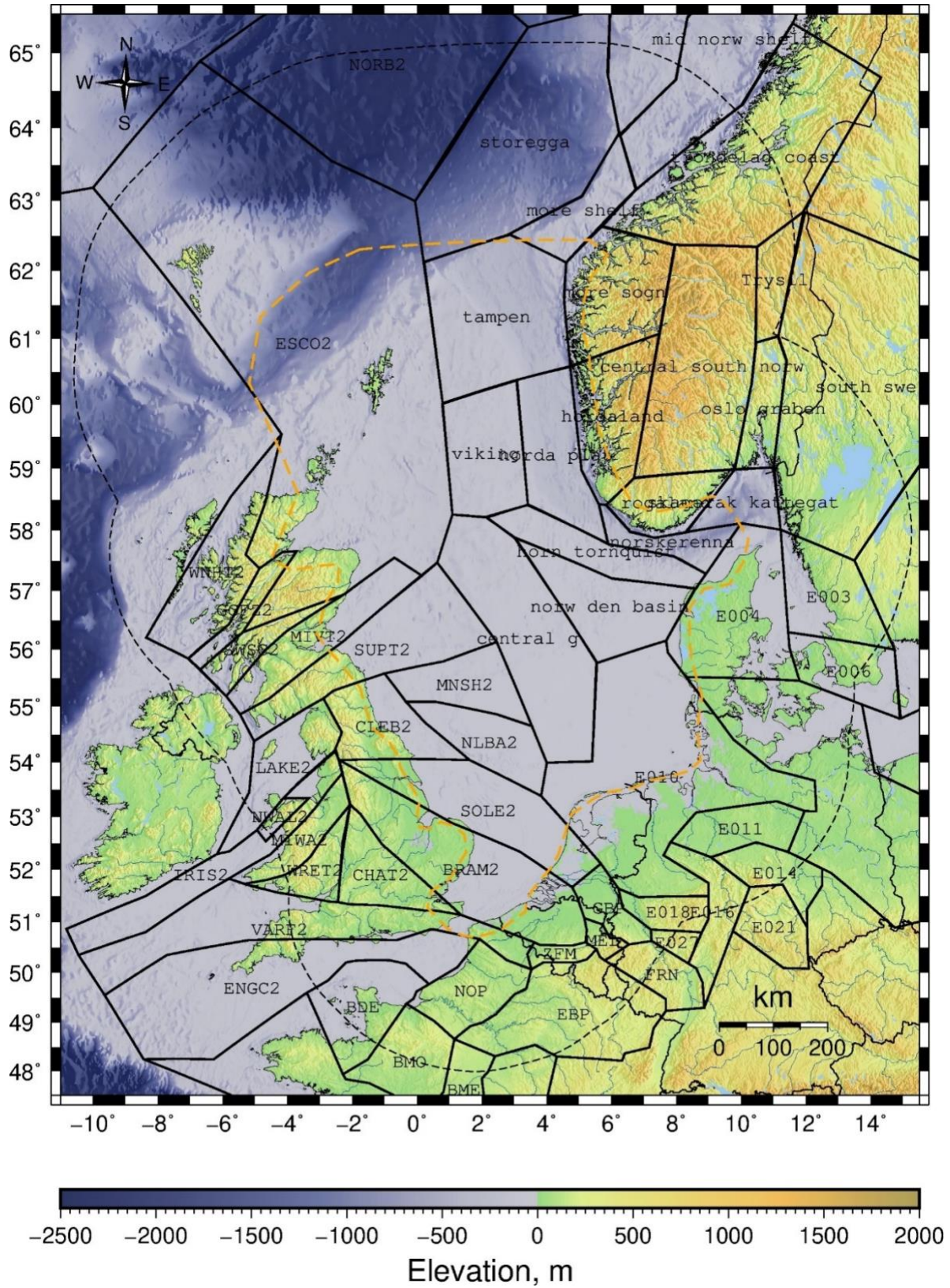


Figure 6-2 Areal source zones for Model 2. The orange dashed line is the area of interest and the black dashed line is 300 km around the area of interest.

Table 6-3 Source characteristics for Model 2. Ref corresponds to N19 = NORSAR (2019), D20 = Drouet et al (2020), G18 = Grünthal et al. (2018) and M24 = Mosca et al. (2024). For the depth pdf  $U$  = uniform distribution with top and bottom, and  $T$  = triangle distribution with three points of the triangle. Mech Weights refers to the fault mechanism weights, in the order of strike slip, normal, reverse.

| ID                 | Ref | $N(M_{\min}=4)$ | b-value | $M_{\max}$                 | $M_{\max}$ Weights    | Depth pdf      | Mech Weights        |
|--------------------|-----|-----------------|---------|----------------------------|-----------------------|----------------|---------------------|
| central g          | N19 | 0.0247          | 0.920   | [6.6,6.9,7.2]              | [0.165,0.67,0.165]    | U[5,20]        | [0.34,0.33,0.33]    |
| central south norw | N19 | 0.0122          | 0.920   | [6.6,6.9,7.2]              | [0.165,0.67,0.165]    | U[5,20]        | [0.34,0.33,0.33]    |
| horda plat         | N19 | 0.0242          | 0.920   | [6.6,6.9,7.2]              | [0.165,0.67,0.165]    | U[5,20]        | [0.34,0.33,0.33]    |
| hordaland          | N19 | 0.0974          | 0.920   | [6.6,6.9,7.2]              | [0.165,0.67,0.165]    | U[5,20]        | [0.34,0.33,0.33]    |
| horn tornquist     | N19 | 0.0547          | 0.920   | [6.6,6.9,7.2]              | [0.165,0.67,0.165]    | U[5,20]        | [0.34,0.33,0.33]    |
| mid norw shelf     | N19 | 0.0055          | 0.920   | [6.6,6.9,7.2]              | [0.165,0.67,0.165]    | U[5,20]        | [0.34,0.33,0.33]    |
| more shelf         | N19 | 0.0363          | 0.920   | [6.6,6.9,7.2]              | [0.165,0.67,0.165]    | U[5,20]        | [0.34,0.33,0.33]    |
| more sogn          | N19 | 0.1078          | 0.920   | [6.6,6.9,7.2]              | [0.165,0.67,0.165]    | U[5,20]        | [0.34,0.33,0.33]    |
| norskerenna        | N19 | 0.0124          | 0.920   | [6.6,6.9,7.2]              | [0.165,0.67,0.165]    | U[5,20]        | [0.34,0.33,0.33]    |
| norw den basin     | N19 | 0.0183          | 0.920   | [6.6,6.9,7.2]              | [0.165,0.67,0.165]    | U[5,20]        | [0.34,0.33,0.33]    |
| oslo graben        | N19 | 0.0207          | 0.920   | [6.6,6.9,7.2]              | [0.165,0.67,0.165]    | U[5,20]        | [0.34,0.33,0.33]    |
| rogaland           | N19 | 0.0027          | 0.920   | [6.6,6.9,7.2]              | [0.165,0.67,0.165]    | U[5,20]        | [0.34,0.33,0.33]    |
| shelf domes        | N19 | 0.0544          | 0.920   | [6.6,6.9,7.2]              | [0.165,0.67,0.165]    | U[5,20]        | [0.34,0.33,0.33]    |
| skagerak kattedgat | N19 | 0.0165          | 0.920   | [6.6,6.9,7.2]              | [0.165,0.67,0.165]    | U[5,20]        | [0.34,0.33,0.33]    |
| south swe          | N19 | 0.0479          | 0.930   | [6.6,6.9,7.2]              | [0.165,0.67,0.165]    | U[5,20]        | [0.34,0.33,0.33]    |
| storegga           | N19 | 0.0316          | 0.920   | [6.6,6.9,7.2]              | [0.165,0.67,0.165]    | U[5,20]        | [0.34,0.33,0.33]    |
| tampen             | N19 | 0.1408          | 0.920   | [6.6,6.9,7.2]              | [0.165,0.67,0.165]    | U[5,20]        | [0.34,0.33,0.33]    |
| trondelag coast    | N19 | 0.0104          | 0.920   | [6.6,6.9,7.2]              | [0.165,0.67,0.165]    | U[5,20]        | [0.34,0.33,0.33]    |
| Trysil             | N19 | 0.0007          | 0.920   | [6.6,6.9,7.2]              | [0.165,0.67,0.165]    | U[5,20]        | [0.34,0.33,0.33]    |
| viking             | N19 | 0.0258          | 0.920   | [6.6,6.9,7.2]              | [0.165,0.67,0.165]    | U[5,20]        | [0.34,0.33,0.33]    |
| E001               | G18 | 0.0141          | 1.069   | [5.82,6.04,6.38,6.38,6.82] | [0.2,0.2,0.2,0.2,0.2] | T[9.6,19.5,32] | [0.632,0.263,0.105] |
| E003               | G18 | 0.0147          | 1.069   | [5.7,6.18,6.18,6.48,6.83]  | [0.2,0.2,0.2,0.2,0.2] | T[9.6,19.5,32] | [0.632,0.263,0.105] |
| E004               | G18 | 0.0122          | 1.085   | [5.82,6.04,6.38,6.38,6.82] | [0.2,0.2,0.2,0.2,0.2] | T[9.6,19.5,32] | [0.632,0.263,0.105] |
| E006               | G18 | 0.0071          | 1.069   | [5.69,6.14,6.46,6.68,7.19] | [0.2,0.2,0.2,0.2,0.2] | T[9.6,19.5,32] | [0.632,0.263,0.105] |
| E010               | G18 | 0.0064          | 1.085   | [5.82,6.04,6.38,6.38,6.82] | [0.2,0.2,0.2,0.2,0.2] | T[9.6,19.5,32] | [0.632,0.263,0.105] |
| E011               | G18 | 0.0004          | 1.085   | [5.7,6.18,6.18,6.48,6.83]  | [0.2,0.2,0.2,0.2,0.2] | T[9.6,19.5,32] | [0.632,0.263,0.105] |
| E013               | G18 | 0.0155          | 1.085   | [5.7,6.18,6.18,6.48,6.83]  | [0.2,0.2,0.2,0.2,0.2] | T[9.6,19.5,32] | [0.632,0.263,0.105] |
| E014               | G18 | 0.0006          | 1.085   | [5.7,6.18,6.18,6.48,6.83]  | [0.2,0.2,0.2,0.2,0.2] | T[9.6,19.5,32] | [0.632,0.263,0.105] |
| E016               | G18 | 0.0156          | 0.902   | [5.7,6.18,6.18,6.48,6.83]  | [0.2,0.2,0.2,0.2,0.2] | T[8,16.4,32.7] | [0.727,0.258,0.015] |
| E018               | G18 | 0.0029          | 1.085   | [6.74,6.84,7.03,7.08,7.32] | [0.2,0.2,0.2,0.2,0.2] | T[9.6,19.5,32] | [0.632,0.263,0.105] |
| E021               | G18 | 0.0070          | 0.902   | [5.69,6.14,6.21,6.47,6.83] | [0.2,0.2,0.2,0.2,0.2] | T[8,16.4,32.7] | [0.727,0.258,0.015] |
| E027               | G18 | 0.0061          | 1.085   | [5.67,6.06,6.25,6.43,6.82] | [0.2,0.2,0.2,0.2,0.2] | T[9.6,19.5,32] | [0.632,0.263,0.105] |
| GBP                | D20 | 4.5132          | 0.778   | [5.7,6.0,6.6,7.1]          | [0.35,0.35,0.20,0.1]  | T[2,11,19]     | [0.34,0.33,0.33]    |
| BDE                | D20 | 1.4863          | 0.955   | [6.3,6.5,7.1]              | [0.6,0.3,0.1]         | T[10,14,20]    | [0.34,0.33,0.33]    |
| BME                | D20 | 0.1731          | 0.981   | [5.7,6.0,6.6,7.1]          | [0.35,0.35,0.20,0.1]  | T[8,14,20]     | [0.34,0.33,0.33]    |
| BMO                | D20 | 1.6897          | 0.966   | [6.3,6.5,7.1]              | [0.6,0.3,0.1]         | T[10,14,20]    | [0.34,0.33,0.33]    |
| EBP                | D20 | 0.0853          | 1.061   | [5.7,6.0,6.6,7.1]          | [0.35,0.35,0.20,0.1]  | T[8,14,20]     | [0.34,0.33,0.33]    |
| FRN                | D20 | 4.1257          | 0.778   | [5.7,6.0,6.6,7.1]          | [0.35,0.35,0.20,0.1]  | T[2,11,19]     | [0.34,0.33,0.33]    |
| LBO                | D20 | 0.1077          | 1.055   | [5.7,6.0,6.6,7.1]          | [0.35,0.35,0.20,0.1]  | T[8,14,20]     | [0.34,0.33,0.33]    |

|       |     |         |       |                   |                      |             |                  |
|-------|-----|---------|-------|-------------------|----------------------|-------------|------------------|
| MEL   | D20 | 10.0786 | 0.962 | [6.3,6.5,7.1]     | [0.6,0.3,0.1]        | T[10,14,20] | [0.34,0.33,0.33] |
| NOP   | D20 | 0.1731  | 0.981 | [5.7,6.0,6.6,7.1] | [0.35,0.35,0.20,0.1] | T[8,14,20]  | [0.34,0.33,0.33] |
| ZFM   | D20 | 7.5544  | 1.003 | [6.3,6.5,7.1]     | [0.6,0.3,0.1]        | T[10,14,20] | [0.34,0.33,0.33] |
| BACK2 | M24 | 0.1923  | 1.012 | [6.5,6.7,6.9,7.1] | [0.5,0.2,0.2,0.1]    | T[5,15,20]  | [1,0,0]          |
| BRAM2 | M24 | 0.0013  | 0.830 | [6.5,6.7,6.9,7.1] | [0.5,0.2,0.2,0.1]    | T[5,15,20]  | [1,0,0]          |
| CHAT2 | M24 | 0.0001  | 0.989 | [6.5,6.7,6.9,7.1] | [0.5,0.2,0.2,0.1]    | T[5,15,20]  | [1,0,0]          |
| CLEB2 | M24 | 0.0002  | 0.923 | [6.5,6.7,6.9,7.1] | [0.5,0.2,0.2,0.1]    | T[5,15,20]  | [1,0,0]          |
| ENGC2 | M24 | 0.0001  | 1.003 | [6.5,6.7,6.9,7.1] | [0.5,0.2,0.2,0.1]    | T[5,15,20]  | [1,0,0]          |
| ESCO2 | M24 | 0.0006  | 1.012 | [6.5,6.7,6.9,7.1] | [0.5,0.2,0.2,0.1]    | T[5,15,20]  | [1,0,0]          |
| GGFZ2 | M24 | 0.0002  | 0.970 | [6.5,6.7,6.9,7.1] | [0.5,0.2,0.2,0.1]    | T[5,15,20]  | [1,0,0]          |
| IRIS2 | M24 | 0.0001  | 0.988 | [6.5,6.7,6.9,7.1] | [0.5,0.2,0.2,0.1]    | T[5,15,20]  | [1,0,0]          |
| LAKE2 | M24 | 0.0001  | 1.007 | [6.5,6.7,6.9,7.1] | [0.5,0.2,0.2,0.1]    | T[5,15,20]  | [1,0,0]          |
| MIVT2 | M24 | 0.0001  | 1.019 | [6.5,6.7,6.9,7.1] | [0.5,0.2,0.2,0.1]    | T[5,15,20]  | [1,0,0]          |
| MIWA2 | M24 | 0.0001  | 1.022 | [6.5,6.7,6.9,7.1] | [0.5,0.2,0.2,0.1]    | T[5,15,20]  | [1,0,0]          |
| MNSH2 | M24 | 0.0001  | 1.012 | [6.5,6.7,6.9,7.1] | [0.5,0.2,0.2,0.1]    | T[5,15,20]  | [1,0,0]          |
| NLBA2 | M24 | 0.0001  | 1.012 | [6.5,6.7,6.9,7.1] | [0.5,0.2,0.2,0.1]    | T[5,15,20]  | [1,0,0]          |
| NORB2 | M24 | 0.0002  | 1.012 | [6.5,6.7,6.9,7.1] | [0.5,0.2,0.2,0.1]    | T[5,15,20]  | [1,0,0]          |
| NWAL2 | M24 | 0.0002  | 1.005 | [6.5,6.7,6.9,7.1] | [0.5,0.2,0.2,0.1]    | T[5,15,20]  | [1,0,0]          |
| SOLE2 | M24 | 0.0039  | 0.997 | [6.5,6.7,6.9,7.1] | [0.5,0.2,0.2,0.1]    | T[5,15,20]  | [1,0,0]          |
| SUPT2 | M24 | 0.0001  | 1.011 | [6.5,6.7,6.9,7.1] | [0.5,0.2,0.2,0.1]    | T[5,15,20]  | [1,0,0]          |
| SWSC2 | M24 | 0.0002  | 0.979 | [6.5,6.7,6.9,7.1] | [0.5,0.2,0.2,0.1]    | T[5,15,20]  | [1,0,0]          |
| VARF2 | M24 | 0.0001  | 0.975 | [6.5,6.7,6.9,7.1] | [0.5,0.2,0.2,0.1]    | T[5,15,20]  | [1,0,0]          |
| WNHT2 | M24 | 0.0001  | 1.056 | [6.5,6.7,6.9,7.1] | [0.5,0.2,0.2,0.1]    | T[5,15,20]  | [1,0,0]          |
| WRET2 | M24 | 0.0007  | 0.825 | [6.5,6.7,6.9,7.1] | [0.5,0.2,0.2,0.1]    | T[5,15,20]  | [1,0,0]          |

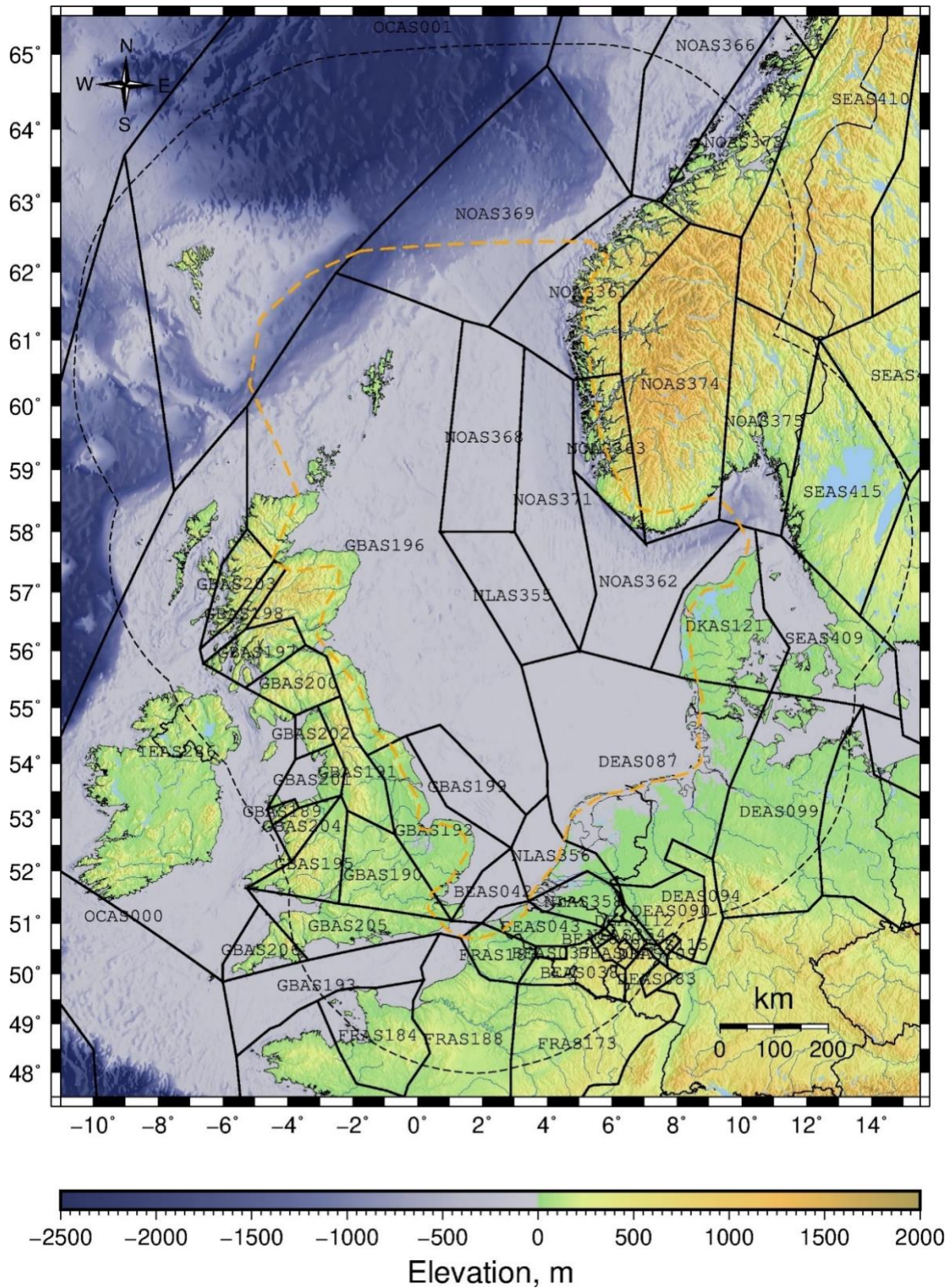


Figure 6-3 Areal source zones for Model 3. The orange dashed line is the area of interest and the black dashed line is 300 km around the area of interest.

Table 6-4 Source characteristics for Model 3 (ESHM20). For the depth pdf  $T$  = triangle distribution with three points of the triangle. Mech Weights refers to the fault mechanism weights, in the order of strike slip, normal, reverse.

| ID      | $N(M_{min}=4)$ | b-value | $M_{max}$       | $M_{max}$ Weights | Depth pdf          | Mech Weights       |
|---------|----------------|---------|-----------------|-------------------|--------------------|--------------------|
| BEAS037 | 0.0871         | 1.000   | [6.3, 6.6, 6.9] | [0.5, 0.4, 0.1]   | T[8.0, 10.0, 15.0] | [0.33, 0.34, 0.33] |
| BEAS038 | 0.0110         | 1.000   | [6.3, 6.6, 6.9] | [0.5, 0.4, 0.1]   | T[8.0, 10.0, 15.0] | [0.33, 0.34, 0.33] |
| BEAS040 | 0.0271         | 1.000   | [6.3, 6.6, 6.9] | [0.5, 0.4, 0.1]   | T[8.0, 10.0, 15.0] | [0.35, 0.15, 0.5]  |
| BEAS041 | 0.0398         | 1.000   | [6.3, 6.6, 6.9] | [0.5, 0.4, 0.1]   | T[8.0, 10.0, 15.0] | [0.35, 0.15, 0.5]  |
| BEAS042 | 0.0203         | 1.000   | [6.3, 6.6, 6.9] | [0.5, 0.4, 0.1]   | T[8.0, 9.0, 13.0]  | [0.35, 0.15, 0.5]  |
| BEAS043 | 0.0203         | 1.000   | [6.3, 6.6, 6.9] | [0.5, 0.4, 0.1]   | T[8.0, 9.0, 13.0]  | [0.35, 0.15, 0.5]  |
| DEAS083 | 0.0044         | 0.911   | [6.3, 6.6, 6.9] | [0.5, 0.4, 0.1]   | T[8.0, 10.0, 15.0] | [0.35, 0.15, 0.5]  |
| DEAS087 | 0.0037         | 1.047   | [6.3, 6.6, 6.9] | [0.5, 0.4, 0.1]   | T[8.0, 10.0, 15.0] | [0.33, 0.34, 0.33] |
| DEAS090 | 0.0037         | 1.047   | [6.3, 6.6, 6.9] | [0.5, 0.4, 0.1]   | T[8.0, 10.0, 15.0] | [0.33, 0.34, 0.33] |
| DEAS094 | 0.0059         | 1.050   | [6.3, 6.6, 6.9] | [0.5, 0.4, 0.1]   | T[8.0, 10.0, 15.0] | [0.35, 0.15, 0.5]  |
| DEAS099 | 0.0037         | 1.047   | [6.3, 6.6, 6.9] | [0.5, 0.4, 0.1]   | T[8.0, 10.0, 15.0] | [0.33, 0.34, 0.33] |
| DEAS103 | 0.0074         | 1.047   | [6.3, 6.6, 6.9] | [0.5, 0.4, 0.1]   | T[8.0, 10.0, 15.0] | [0.33, 0.34, 0.33] |
| DEAS109 | 0.1023         | 0.910   | [6.6, 6.9, 7.2] | [0.5, 0.4, 0.1]   | T[8.0, 10.0, 15.0] | [0.35, 0.15, 0.5]  |
| DEAS112 | 0.0251         | 1.050   | [6.6, 6.9, 7.2] | [0.5, 0.4, 0.1]   | T[8.0, 10.0, 15.0] | [0.9, 0.0, 0.1]    |
| DEAS115 | 0.0072         | 0.910   | [6.3, 6.6, 6.9] | [0.5, 0.4, 0.1]   | T[8.0, 10.0, 15.0] | [0.33, 0.34, 0.33] |
| DKAS121 | 0.0065         | 1.040   | [6.3, 6.6, 6.9] | [0.5, 0.4, 0.1]   | T[8.0, 10.0, 15.0] | [0.5, 0.1, 0.4]    |
| FRAS173 | 0.0162         | 1.060   | [6.3, 6.6, 6.9] | [0.5, 0.4, 0.1]   | T[8.0, 12.0, 18.0] | [0.35, 0.15, 0.5]  |
| FRAS183 | 0.0068         | 1.000   | [6.3, 6.6, 6.9] | [0.5, 0.4, 0.1]   | T[8.0, 10.0, 15.0] | [0.33, 0.34, 0.33] |
| FRAS184 | 0.0742         | 0.861   | [6.3, 6.6, 6.9] | [0.5, 0.4, 0.1]   | T[8.0, 12.0, 18.0] | [0.4, 0.2, 0.4]    |
| FRAS188 | 0.0302         | 1.060   | [6.3, 6.6, 6.9] | [0.5, 0.4, 0.1]   | T[8.0, 12.0, 18.0] | [0.35, 0.15, 0.5]  |
| GBAS189 | 0.0316         | 1.000   | [6.3, 6.6, 6.9] | [0.5, 0.4, 0.1]   | T[8.0, 10.0, 15.0] | [0.33, 0.34, 0.33] |
| GBAS190 | 0.0132         | 1.070   | [6.3, 6.6, 6.9] | [0.5, 0.4, 0.1]   | T[8.0, 10.0, 15.0] | [0.33, 0.34, 0.33] |
| GBAS191 | 0.0262         | 1.072   | [6.3, 6.6, 6.9] | [0.5, 0.4, 0.1]   | T[8.0, 10.0, 15.0] | [0.33, 0.34, 0.33] |
| GBAS192 | 0.0105         | 1.070   | [6.3, 6.6, 6.9] | [0.5, 0.4, 0.1]   | T[8.0, 10.0, 15.0] | [0.33, 0.34, 0.33] |
| GBAS193 | 0.0089         | 1.000   | [6.3, 6.6, 6.9] | [0.5, 0.4, 0.1]   | T[8.0, 12.0, 18.0] | [0.33, 0.34, 0.33] |
| GBAS195 | 0.0825         | 1.000   | [6.3, 6.6, 6.9] | [0.5, 0.4, 0.1]   | T[8.0, 10.0, 15.0] | [0.33, 0.34, 0.33] |
| GBAS196 | 0.0145         | 1.000   | [6.3, 6.6, 6.9] | [0.5, 0.4, 0.1]   | T[8.0, 10.0, 15.0] | [0.33, 0.34, 0.33] |
| GBAS197 | 0.0200         | 0.940   | [6.3, 6.6, 6.9] | [0.5, 0.4, 0.1]   | T[8.0, 10.0, 15.0] | [0.33, 0.34, 0.33] |
| GBAS198 | 0.0219         | 0.940   | [6.3, 6.6, 6.9] | [0.5, 0.4, 0.1]   | T[8.0, 10.0, 15.0] | [0.33, 0.34, 0.33] |
| GBAS199 | 0.0132         | 1.070   | [6.3, 6.6, 6.9] | [0.5, 0.4, 0.1]   | T[8.0, 10.0, 15.0] | [0.33, 0.34, 0.33] |
| GBAS200 | 0.0021         | 0.939   | [6.3, 6.6, 6.9] | [0.5, 0.4, 0.1]   | T[8.0, 10.0, 15.0] | [0.33, 0.34, 0.33] |
| GBAS201 | 0.0174         | 1.000   | [6.3, 6.6, 6.9] | [0.5, 0.4, 0.1]   | T[8.0, 10.0, 15.0] | [0.33, 0.34, 0.33] |
| GBAS202 | 0.0087         | 1.000   | [6.3, 6.6, 6.9] | [0.5, 0.4, 0.1]   | T[8.0, 10.0, 15.0] | [0.33, 0.34, 0.33] |
| GBAS203 | 0.0081         | 0.940   | [6.3, 6.6, 6.9] | [0.5, 0.4, 0.1]   | T[8.0, 10.0, 15.0] | [0.33, 0.34, 0.33] |
| GBAS204 | 0.0043         | 1.000   | [6.3, 6.6, 6.9] | [0.5, 0.4, 0.1]   | T[8.0, 10.0, 15.0] | [0.33, 0.34, 0.33] |
| GBAS205 | 0.0141         | 1.000   | [6.3, 6.6, 6.9] | [0.5, 0.4, 0.1]   | T[8.0, 10.0, 15.0] | [0.33, 0.34, 0.33] |
| GBAS206 | 0.0070         | 1.000   | [6.3, 6.6, 6.9] | [0.5, 0.4, 0.1]   | T[8.0, 10.0, 15.0] | [0.33, 0.34, 0.33] |
| IEAS286 | 0.0054         | 0.995   | [6.3, 6.6, 6.9] | [0.5, 0.4, 0.1]   | T[8.0, 10.0, 15.0] | [0.33, 0.34, 0.33] |
| NLAS354 | 0.1995         | 1.050   | [6.6, 6.9, 7.2] | [0.5, 0.4, 0.1]   | T[9.0, 10.0, 15.0] | [0.35, 0.15, 0.5]  |

|         |        |       |                 |                 |                    |                    |
|---------|--------|-------|-----------------|-----------------|--------------------|--------------------|
| NLAS355 | 0.0040 | 1.050 | [6.3, 6.6, 6.9] | [0.5, 0.4, 0.1] | T[8.0, 10.0, 15.0] | [0.9, 0.0, 0.1]    |
| NLAS356 | 0.0067 | 1.050 | [6.6, 6.9, 7.2] | [0.5, 0.4, 0.1] | T[8.0, 9.0, 13.0]  | [0.9, 0.0, 0.1]    |
| NLAS358 | 0.0891 | 1.050 | [6.6, 6.9, 7.2] | [0.5, 0.4, 0.1] | T[9.0, 10.0, 15.0] | [0.35, 0.15, 0.5]  |
| NOAS361 | 0.2229 | 0.834 | [6.3, 6.6, 6.9] | [0.5, 0.4, 0.1] | T[8.0, 10.0, 15.0] | [0.2, 0.55, 0.25]  |
| NOAS362 | 0.0762 | 1.040 | [6.3, 6.6, 6.9] | [0.5, 0.4, 0.1] | T[8.0, 10.0, 15.0] | [0.5, 0.1, 0.4]    |
| NOAS363 | 0.1096 | 0.840 | [6.3, 6.6, 6.9] | [0.5, 0.4, 0.1] | T[8.0, 10.0, 15.0] | [0.2, 0.55, 0.25]  |
| NOAS366 | 0.0017 | 1.040 | [6.3, 6.6, 6.9] | [0.5, 0.4, 0.1] | T[8.0, 10.0, 15.0] | [0.2, 0.55, 0.25]  |
| NOAS368 | 0.0275 | 1.040 | [6.3, 6.6, 6.9] | [0.5, 0.4, 0.1] | T[8.0, 10.0, 15.0] | [0.33, 0.34, 0.33] |
| NOAS369 | 0.0708 | 1.040 | [6.3, 6.6, 6.9] | [0.5, 0.4, 0.1] | T[8.0, 10.0, 15.0] | [0.2, 0.55, 0.25]  |
| NOAS370 | 0.0871 | 1.040 | [6.3, 6.6, 6.9] | [0.5, 0.4, 0.1] | T[8.0, 10.0, 15.0] | [0.2, 0.55, 0.25]  |
| NOAS371 | 0.0069 | 1.040 | [6.3, 6.6, 6.9] | [0.5, 0.4, 0.1] | T[8.0, 10.0, 15.0] | [0.5, 0.1, 0.4]    |
| NOAS373 | 0.0275 | 1.040 | [6.3, 6.6, 6.9] | [0.5, 0.4, 0.1] | T[8.0, 10.0, 15.0] | [0.2, 0.55, 0.25]  |
| NOAS374 | 0.0219 | 1.040 | [6.3, 6.6, 6.9] | [0.5, 0.4, 0.1] | T[8.0, 10.0, 15.0] | [0.2, 0.55, 0.25]  |
| NOAS375 | 0.0719 | 1.040 | [6.3, 6.6, 6.9] | [0.5, 0.4, 0.1] | T[8.0, 10.0, 15.0] | [0.2, 0.55, 0.25]  |
| OCAS000 | 0.0408 | 0.907 | [6.3, 6.6, 6.9] | [0.5, 0.4, 0.1] | T[2.0, 10.0, 18.0] | [0.3, 0.1, 0.6]    |
| OCAS001 | 0.1632 | 0.907 | [6.3, 6.6, 6.9] | [0.5, 0.4, 0.1] | T[2.0, 10.0, 18.0] | [0.3, 0.1, 0.6]    |
| SEAS409 | 0.0195 | 0.840 | [6.3, 6.6, 6.9] | [0.5, 0.4, 0.1] | T[8.0, 10.0, 15.0] | [0.5, 0.1, 0.4]    |
| SEAS410 | 0.0056 | 1.040 | [6.3, 6.6, 6.9] | [0.5, 0.4, 0.1] | T[8.0, 10.0, 15.0] | [0.2, 0.55, 0.25]  |
| SEAS413 | 0.0107 | 0.910 | [6.3, 6.6, 6.9] | [0.5, 0.4, 0.1] | T[8.0, 10.0, 15.0] | [0.5, 0.1, 0.4]    |
| SEAS414 | 0.0324 | 1.000 | [6.3, 6.6, 6.9] | [0.5, 0.4, 0.1] | T[8.0, 10.0, 15.0] | [0.5, 0.1, 0.4]    |
| SEAS415 | 0.0112 | 0.910 | [6.3, 6.6, 6.9] | [0.5, 0.4, 0.1] | T[8.0, 10.0, 15.0] | [0.5, 0.1, 0.4]    |

#### 6.1.2 Model 4

The fourth and final model was a smoothed gridded seismicity model based on the earthquake catalogue compiled by SHARP. The SHARP catalogue includes all known earthquakes that have occurred within 300 km of the area of interest. To use the catalogue for the PSHA, we converted all magnitudes to moment magnitude, removed dependent events (declustering) and checked for completeness.

There are many different types of magnitude scales and different agencies calculate the same magnitude scale differently. Therefore, when compiling an earthquake catalogue from multiple sources, it is important to convert the magnitudes to the same scale. Because almost all ground motion models use moment magnitude ( $M_w$ ) in their calculations, it is standard practice to convert to moment magnitude. We converted the magnitudes to  $M_w$  using the magnitude conversion equations proposed by Grünthal et al. (2009) for central, northern and north-western Europe. These are the same equations used by Mosca et al. (2020) for the UK, Grünthal et al. (2018) for Germany, and NORSAR (2019) for Norway. Figure 6-4 shows the magnitude converted catalogue.

PSHA assumes that all earthquake events are independent, therefore, dependent events such as foreshocks and aftershocks must be removed. This procedure is called declustering. We used the declustering model of Burkhard and Grünthal (2009), which is an update of the Grünthal (1985) method and uses a magnitude dependent space and time window to define foreshocks and aftershocks. This is the same method used by Mosca et al. (2020) for the UK and Grünthal et al. (2018) for Germany. Figure 6-5 shows the magnitude converted and declustered catalogue.

The third step in preparing an earthquake catalogue is ensuring completeness. All earthquakes above a minimum magnitude ( $M_{\min}$ ) that occurred in each area and time period must be included in an earthquake catalogue to accurately predict the magnitude recurrence parameters. If all earthquakes are not included, then the catalogue is incomplete. Normally, most catalogues are incomplete for smaller magnitude earthquakes because they are harder to detect without a strong ground motion station nearby. We used the method of Stepp (1972) to evaluate the earthquake catalogue for completeness for individual magnitude bins. This allows information for larger earthquakes from historical records to be used with information from instrument records that cover a much shorter time period. To evaluate completeness, we used superzones like the superzones used in ESHM20 (Figure 6-6). We defined three zones roughly approximating the UK (SZ06), Norway (SZ49), and continental Europe (SZ04).

After the earthquake catalogue was corrected for earthquake magnitude, dependent events and completeness, we calculated the overall activity rate, b-value and uncertainty bounds for each superzone using the maximum likelihood method of Weichert (1980). We then used smoothed gridded seismicity to estimate relative activity rates across each of the superzones. Smoothed gridded seismicity is a grid of very small sub-sources with different activity rates but the same magnitude probability density function and Gutenberg-Richter b-value. The different activity rates represent the spatial variability of earthquake occurrence. The relative rates of each cell are based not just on the earthquakes that occurred in that cell, but a weighted average of the rates of the cell and the cells around it. We used a Gaussian distribution with a 60 kilometre radius and 0.1 by 0.1 degree grid cells to calculate the smoothed gridded seismicity. Figure 6-8 shows the smoothed gridded seismicity source model, and Table 6-5 lists the source parameters for each superzone.

The depth pdf was developed based on histograms of depth from the declustered and complete catalogue for each superzone. The weights for each source mechanism are based on the focal mechanism catalogue for each superzone. The maximum magnitude model is the same as used by the SHARE project for stable continental regions and is a little larger than the models used by ESHM20 for the same region.

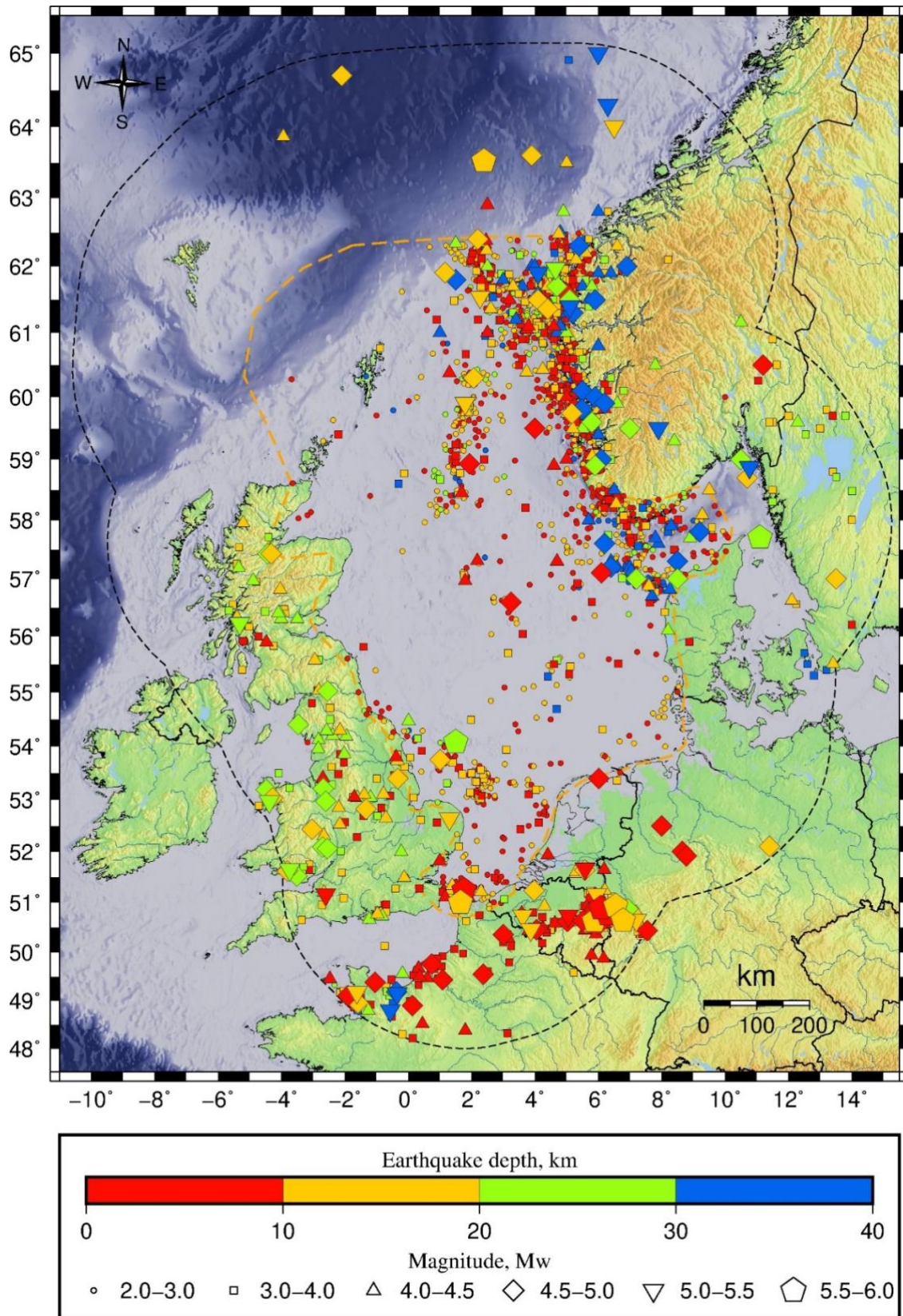


Figure 6-4 Earthquake catalogue before declustering and completeness check. The orange dashed line is the area of interest and the black dashed line is 300 km around the area of interest.

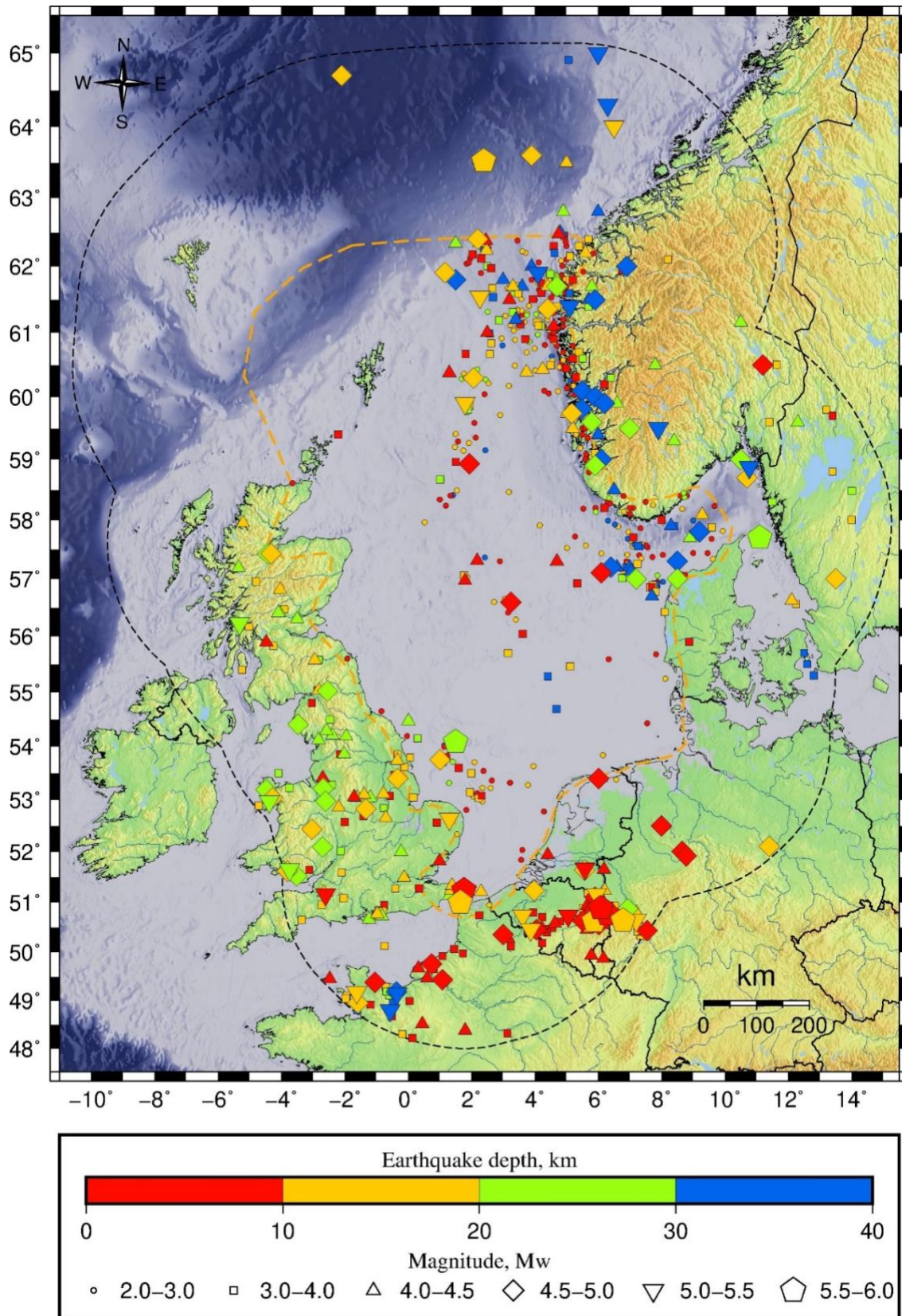


Figure 6-5 Earthquake catalogue after declustering. The orange dashed line is the area of interest and the black dashed line is 300 km around the area of interest.

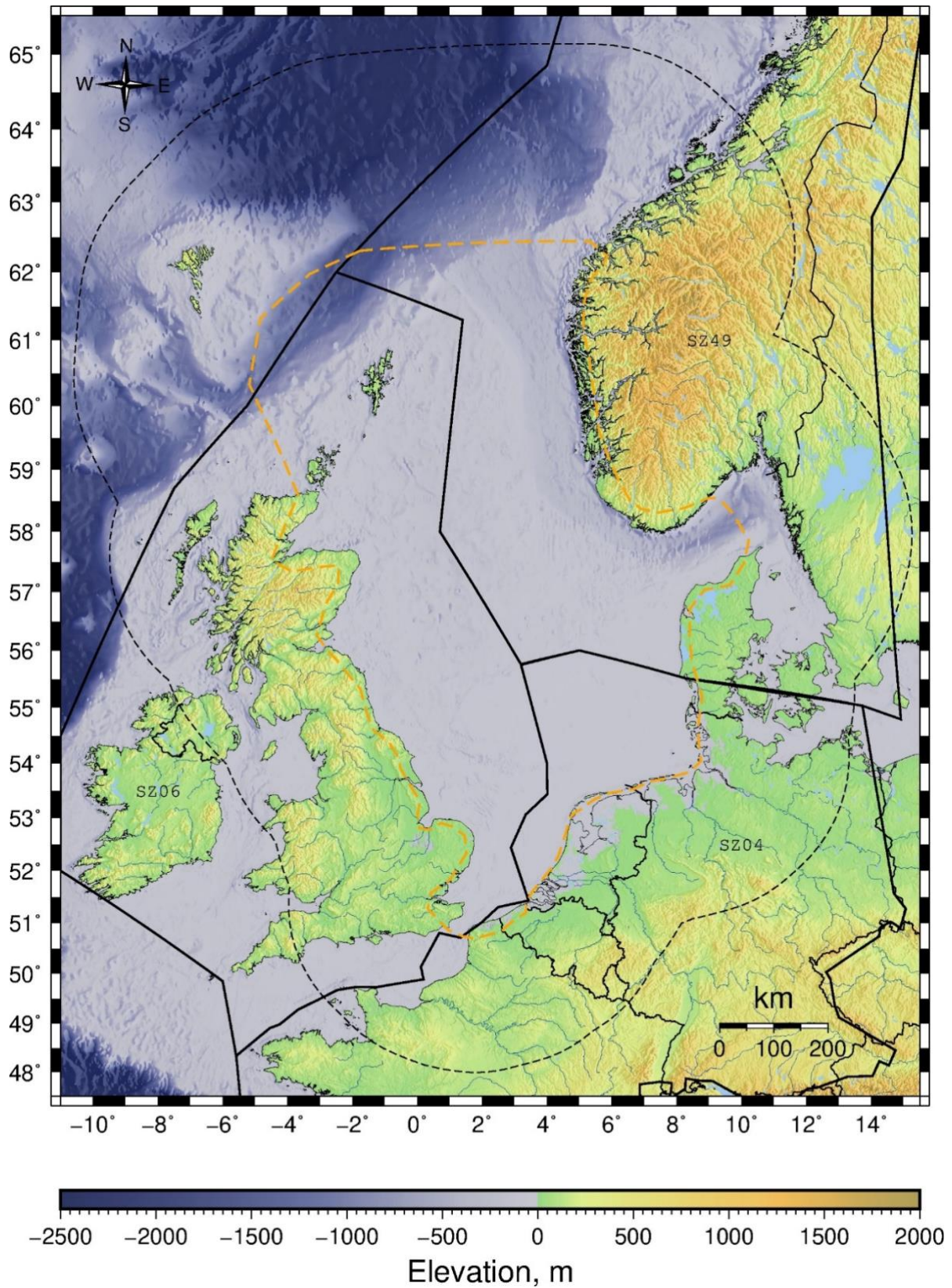


Figure 6-6 Superzones used to estimate completeness and b-values for the smooth seismicity model.

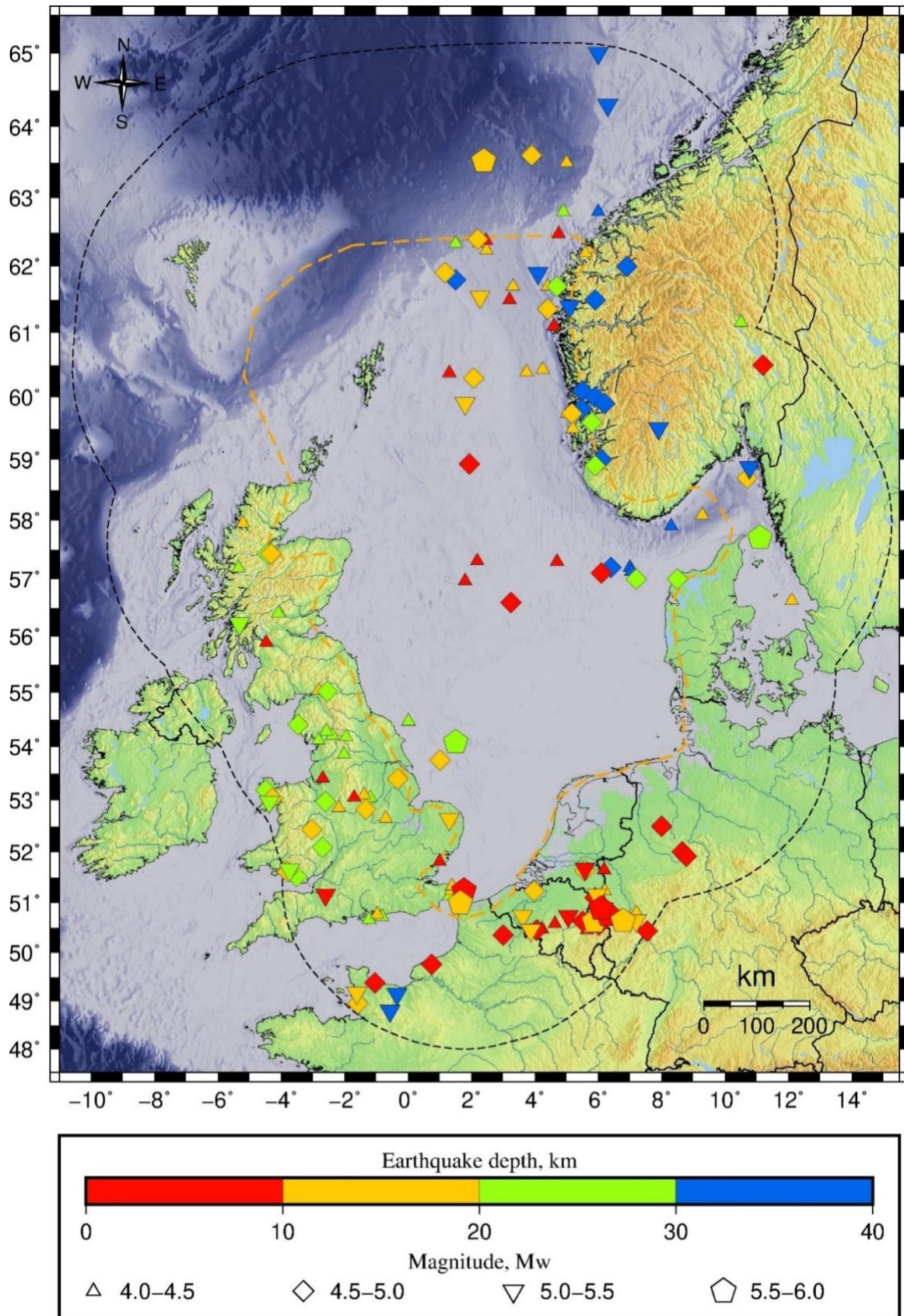


Figure 6-7 Declustered and complete earthquake catalogue for  $M_w > 4.0$ . The orange dashed line is the area of interest and the black dashed line is 300 km around the area of interest.

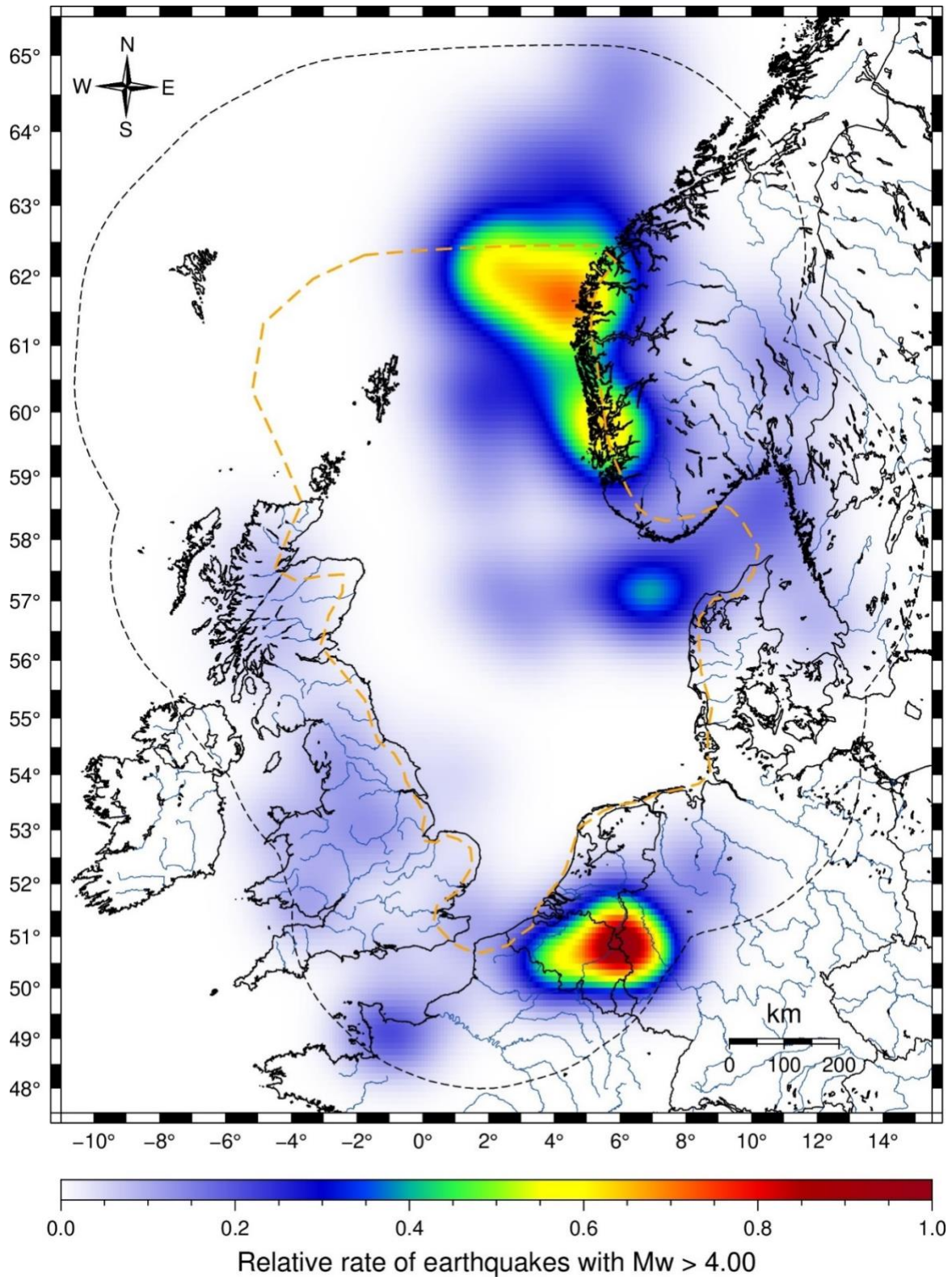


Figure 6-8 Smoothed gridded seismicity heat map for  $M_w > 4.0$  showing the relative activity rate. The orange dashed line is the area of interest and the black dashed line is 300 km around the area of interest.

Table 6-5 Source characteristics for Model 4. For the depth pdf  $T$  = triangle distribution with three points of the triangle. Mech Weights refers to the fault mechanism weights, in the order of strike slip, normal, reverse.  $N(M_{min}=4)$  is the overall activity rate for the entire superzone.

| ID   | $N(M_{min}=4)$ | b-value | $M_{max}$         | $M_{max}$ Weights | Depth pdf  | Mech Weights     |
|------|----------------|---------|-------------------|-------------------|------------|------------------|
| SZ04 | 0.146          | 0.83    | [6.5,6.7,6.9,7.1] | [0.5,0.2,0.2,0.1] | T[0,5,25]  | [0.65,0.25,0.10] |
| SZ06 | 0.145          | 0.96    | [6.5,6.7,6.9,7.1] | [0.5,0.2,0.2,0.1] | T[0,15,25] | [0.6,0.2,0.2]    |
| SZ49 | 0.626          | 1.01    | [6.5,6.7,6.9,7.1] | [0.5,0.2,0.2,0.1] | T[0,5,40]  | [0.25,0.25,0.5]  |

## 6.2 GMM integration

### 6.2.1 GMMs used in nearby national studies

Grünthal et al. (2018) argue that Germany has attenuation properties like that of active crustal regions, and tests by other authors against datasets of small to moderate magnitude earthquakes confirms this. They therefore choose GMMs based on datasets of earthquakes from active tectonic regions. To capture epistemic uncertainty, they chose GMMs developed from different databases and using different functional forms. The models used in Grünthal et al (2018) are Akkar et al. (2014), Bindi et al. (2014) and Derras et al. (2014) to capture the RESORCE database (Akkar et al., 2013), Bindi et al. (2017) to capture the NGA West 2 database (Ancheta et al., 2014), and Cauzzi et al. (2015) to capture Japanese earthquake data, with weights of 0.167, 0.167, 0.167, 0.25, and 0.25, respectively. In addition, Grünthal et al (2018) highlight that stress drops for some recent earthquakes from central Europe were larger than those from more active regions, and therefore stress drops from future earthquakes could also be higher than more active regions. To model this uncertainty in stress drop, Grünthal et al (2018) scaled each GMM by 0.75, 1, 1.25 and 2.0, with weights of 0.14, 0.36, 0.36, 0.14, respectively.

NORSAR (2019) selected 18 GMMs for use in Norway based on the selection criteria of Cotton et al. (2006) and Bommer et al. (2010). They then reduced this to four by keeping only GMM based on different databases and that used different modelling techniques to try and best capture the epistemic uncertainty with the fewest amount of GMMs, like Grünthal et al. (2018). In addition, they selected only GMM valid for  $V_{S30} = 1200$  m/s, since this was the reference rock condition used in the analyses. NORSAR (2019) used the GMMs of Akkar et al. (2014), Bindi et al (2017), Cauzzi et al (2015), and Yenier and Atkinson (2015), with weights of 2/9, 2/9, 2/9, and 1/3, respectively. The weights were chosen based on the method of Scherbaum and Keuhn (2011) considering the amount of overlap in the databases used by the different GMMs chosen.

Villani et al. (2019) evaluated GMMs for use in the UK. They first used the criteria of Bommer et al. (2010) to select an initial eight GMMs from a list of 290. They did not consider GMMs developed for shield regions or eastern North America due to the different geological processes and attenuation of seismic waves from these regions compared to the UK. Villani et al. (2019a) then compared these eight GMMs to recorded data and macroseismic data in the UK. The recorded dataset consisted of 83 records from 12 earthquakes that occurred between 1996 to 2018 with  $M_w$  between 3.2 and 4.5 (Figure 6-9). Villani et al (2019a) recommend using Bindi et al. (2014), Cauzzi et al. (2015), Rietbrock and Edwards (2019), and one of Abrahamson et al. (2014), Chiou and Youngs (2014) or Boore et al. (2014) for PSHA in the UK. Villani et al. (2020) conducted a PSHA for a new nuclear power plant at Wylfa Newydd in North Wales. They used the GMMs of Boore et al. (2014), Chiou and Youngs (2014), Bindi et al. (2014), Cauzzi et al. (2015) and Rietbrock and Edwards (2019) with weights of 0.15, 0.15, 0.20, 0.15, and 0.35, respectively.

Tromans et al. (2019) performed a PSHA for a proposed nuclear power plant at Hinkley Point, in Somerset, southwest England. They used a similar approach to Villani et al. (2019) to select GMMs. They started with a large list of 400 GMMs that they reduced to 12 based on the selection criteria of Cotton et al. (2006) and Bommer et al. (2010). They then compared the 12 GMMs with ground motion instrumental and intensity data retrieved as part of the project. Finally, an expert panel decided on the GMMs of Atkinson and Boore (2006, 2011), Bindi et al. (2014), Boore et al. (2014), Cauzzi et al. (2015) and Rietbrock et al. (2013), with weights of 0.10, 0.30, 0.30, 0.20 and 0.10, respectively. For their update of the UK seismic hazard maps, Mosca et al. (2020) used the same GMMs and weights as Tromans et al. (2019).

Brooks et al. (2020) evaluated the fit of 16 ground motion models to recorded earthquakes from the northern North Sea region (Figure 6-10). They found that the model of Akkar et al. (2014) had the best fit to the data for PGA and most spectral periods, with the models of Akkar and Çağnan (2010), Rietbrock et al. (2013), Abrahamson et al. (2014) and Cauzzi et al. (2015) providing moderate fits for some but not all spectral periods.

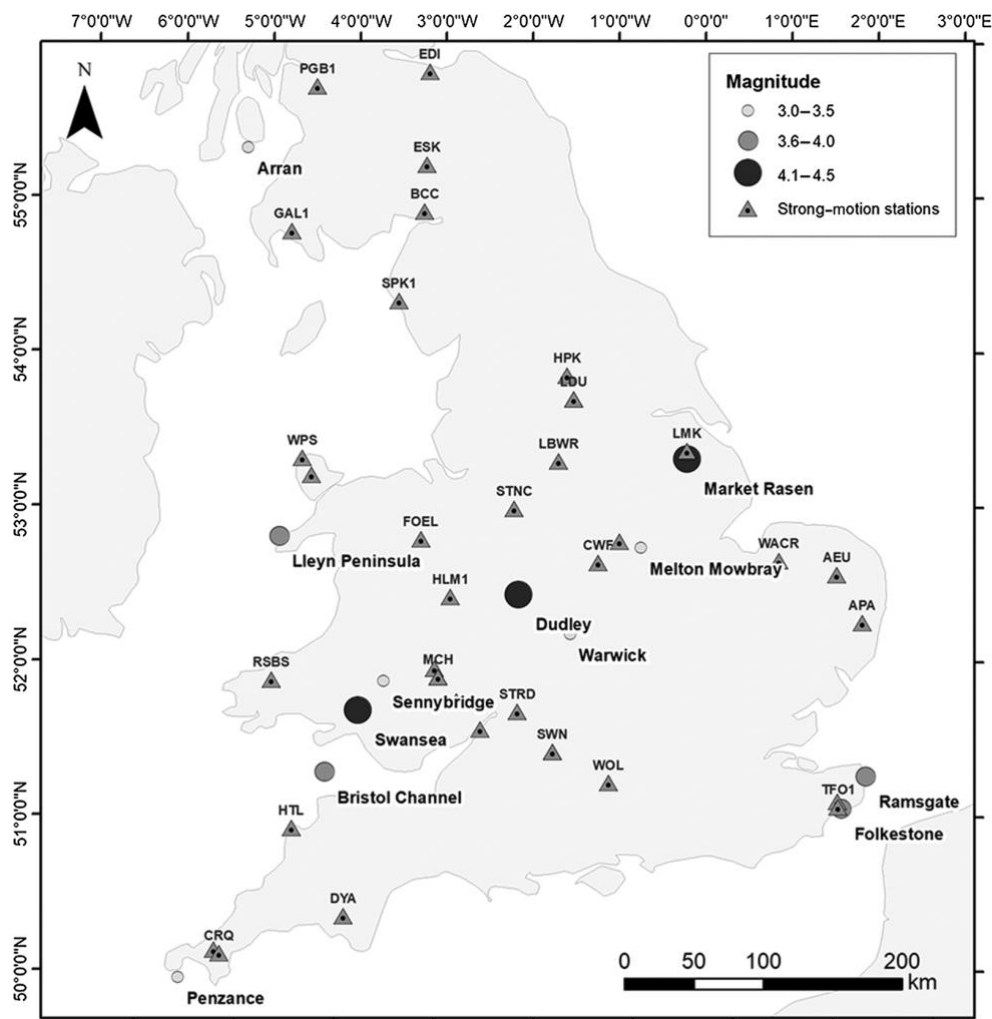


Figure 6-9 Earthquakes (circles) and stations (triangles) of the instrumental dataset used in the GMM evaluation of Villani et al. (2019) for the UK.

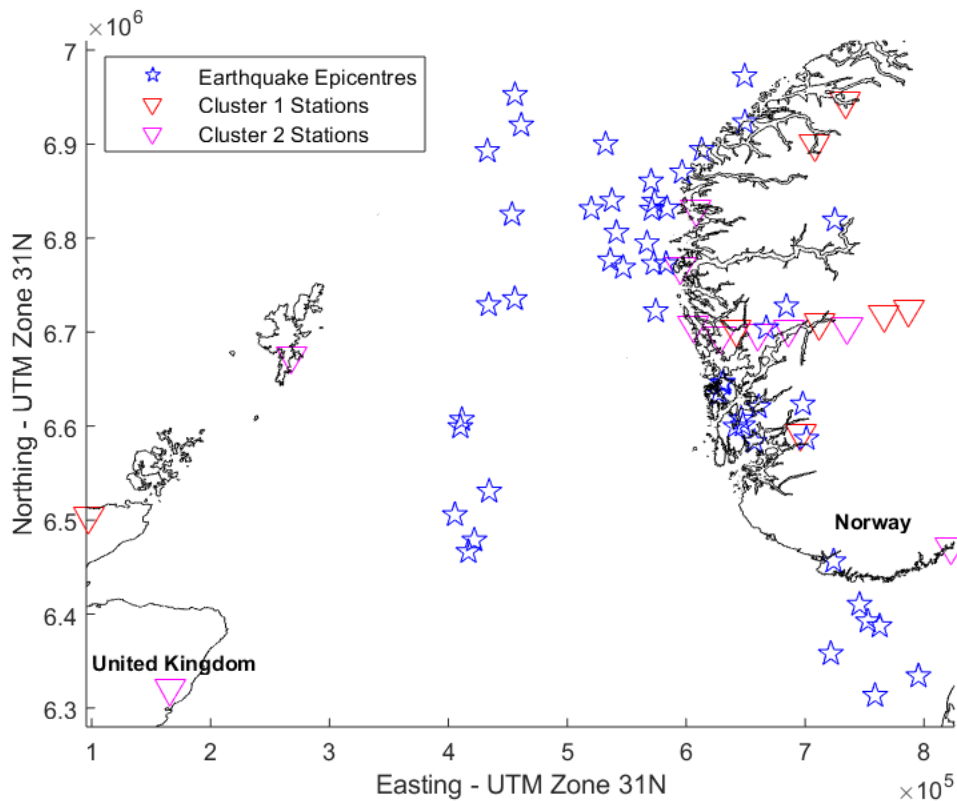


Figure 6-10 Earthquakes (stars) and stations (inverted triangles) used in the GMM evaluation performed by Brooks et al. (2020) for the North Sea.

### 6.2.2 Selected GMMs

Many of the GMMs used in the studies listed above are similar. For example, the Cauzzi et al. (2015) is used by all of them and the Akkar et al. (2014) is used in all the studies except the ones for the UK. In addition, both the UK studies and Brooks et al. (2020) found that Rietbrock et al (2013) performed well for UK and North Sea earthquakes. As a result, we use the Akkar et al. (2014), Cauzzi et al. (2015), and Rietbrock and Edwards (2019) GMMs in addition to the North Sea specific GMM described in section 5. The properties of these models are:

- Akkar et al. (2014): this model was developed for Europe and the Middle East based on a subset of the RESORCE strong ground motion database (Akkar et al. 2013). They developed three different models based on different source to site distance metrics to facilitate hazard calculations using both fault and point sources.
- Cauzzi et al. (2015): This model is an update of the Cauzzi and Faccioli (2008) model. It attempts to develop an empirical ground motion model based on a different dataset than the NGA West 2 database (e.g. Chiou and Youngs, 2014; Boore et al., 2014) and the RESORCE database to capture epistemic uncertainty in PSHA. The database consists of ground motions mostly from Italy, Iceland, Japan, Greece, Turkey and Iran, with a few from California, Alaska, Taiwan and China.
- Rietbrock and Edwards (2019): This is an update to the model of Rietbrock et al. (2013). It is a stochastic finite fault model. The seismological parameters of the stochastic model were based on a database of recorded seismicity in the UK obtained from the BGS. The dataset includes

1187 recordings from 236 events with  $M_L$  between 1.5 and 5.5. It was developed as part of the seismic hazard assessment for the Wylfa Newydd nuclear power plant (Villani et al., 2020).

We used Rietbrock and Edwards (2019) and not Rietbrock et al. (2013), since the former is an update of the latter. To calculate the weights, we used the average weight from the previous studies.

Some of the GMMs use RotD50 spectral acceleration and some the geometric mean. However, Boore and Kishida (2017) show that the difference between these two is less than 7% for all periods. Therefore, we did not adjust any of the GMMs based on spectral acceleration type.

All the selected GMMs except Rietbrock and Edwards (2019) use the time average shear wave velocity over the top 30 metres ( $V_{s30}$ ) to define the site conditions. We used  $V_{s30} = 800$  m/s to represent soft rock conditions, which agrees with the reference rock condition of ISO 19901-2 ( $V_{s30} = 750$  m/s) and Eurocode 8 ( $V_{s30} = 800$  m/s). Rietbrock and Edwards (2019) define spectral accelerations for  $V_{s30} = 2600$  m/s. To convert to  $V_{s30} = 800$  m/s, we used the relations of Stewart et al. (2020).

In this study, the minimum magnitude is  $M_w = 4.0$ , which is lower than the minimum magnitude of the Cauzzi et al. (2015) model, and the maximum magnitude is  $M_w = 7.2$ , which is larger than the maximum magnitude of the Rietbrock and Edwards (2019). In addition, the maximum distance is 300 km, which is larger than the maximum distance of the Cauzzi et al. (2015) and Akkar et al. (2014) models. Therefore, to ensure that these models behave reasonably when extrapolated outside of their intended ranges, we examined the response spectra at upper and lower magnitude and distance bounds. All the models predict reasonable response spectra.

*Table 6-6 Epistemic weights, minimum and maximum magnitude, distance and period ranges of the selected ground motion models*

| Reference                  | Weight | Magnitude ( $M_w$ ) |     | Distance (km) |      | Period (s) |     |
|----------------------------|--------|---------------------|-----|---------------|------|------------|-----|
|                            |        | min                 | max | min           | max  | min        | max |
| Akkar et al. (2014)        | 0.30   | 4.0                 | 8.0 | 0             | 200  | 0.01       | 4   |
| Cauzzi et al. (2015)       | 0.40   | 4.5                 | 7.9 | 0             | 150  | 0.01       | 10  |
| Rietbrock & Edwards (2019) | 0.20   | 3.0                 | 7.0 | 0             | 300  | 0.03       | 5   |
| SHARP                      | 0.10   | 3.5                 | 5.5 | 70            | 1000 | 0.03       | 2.6 |

### 6.3 PSHA results

We performed PSHA calculations for a grid of 412 points equally spaced at 0.5 degrees over the entire area of interest. The analyses were performed for PGA, 0.2, 1 and 4 seconds, and for a  $V_{s30} = 800$  m/s<sup>2</sup>. Figure 6-11, Figure 6-12 and Figure 6-13 show the PGA values for 475-year, 2475-year, and 10000-year return periods, respectively. The highest PGA values occur off the west coast of Norway in the Tampen Area (62°N, 4°E), between Norway and Denmark along the Tornquist Zone (57.5°N, 7.5°E), and at the Dover Strait (51°N, 1.5°E). This follows roughly the same pattern as the observed seismicity (Figure 6-7).

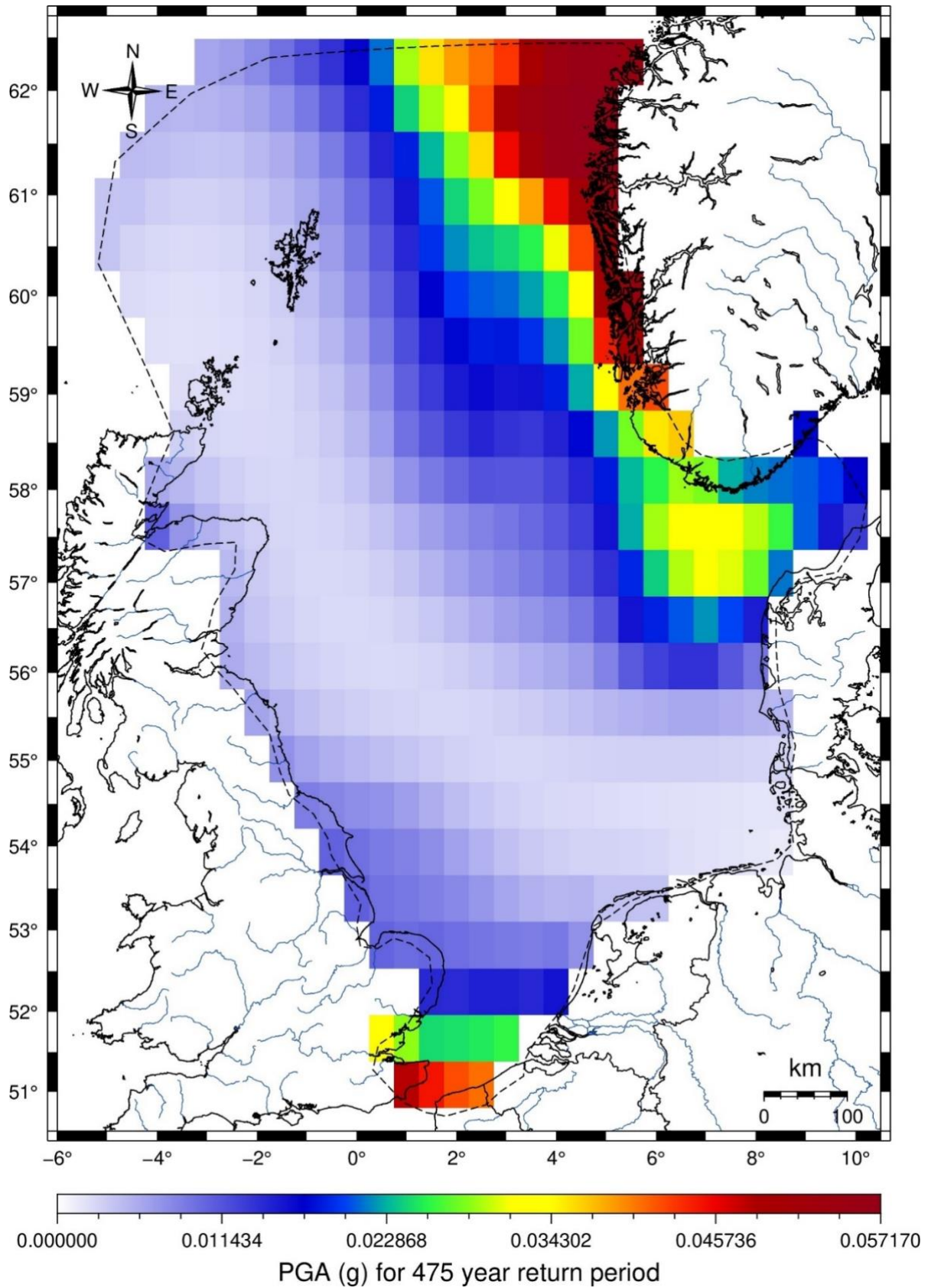


Figure 6-11 PGA for  $V_{s30} = 800$  m/s for a return period of 475 years.

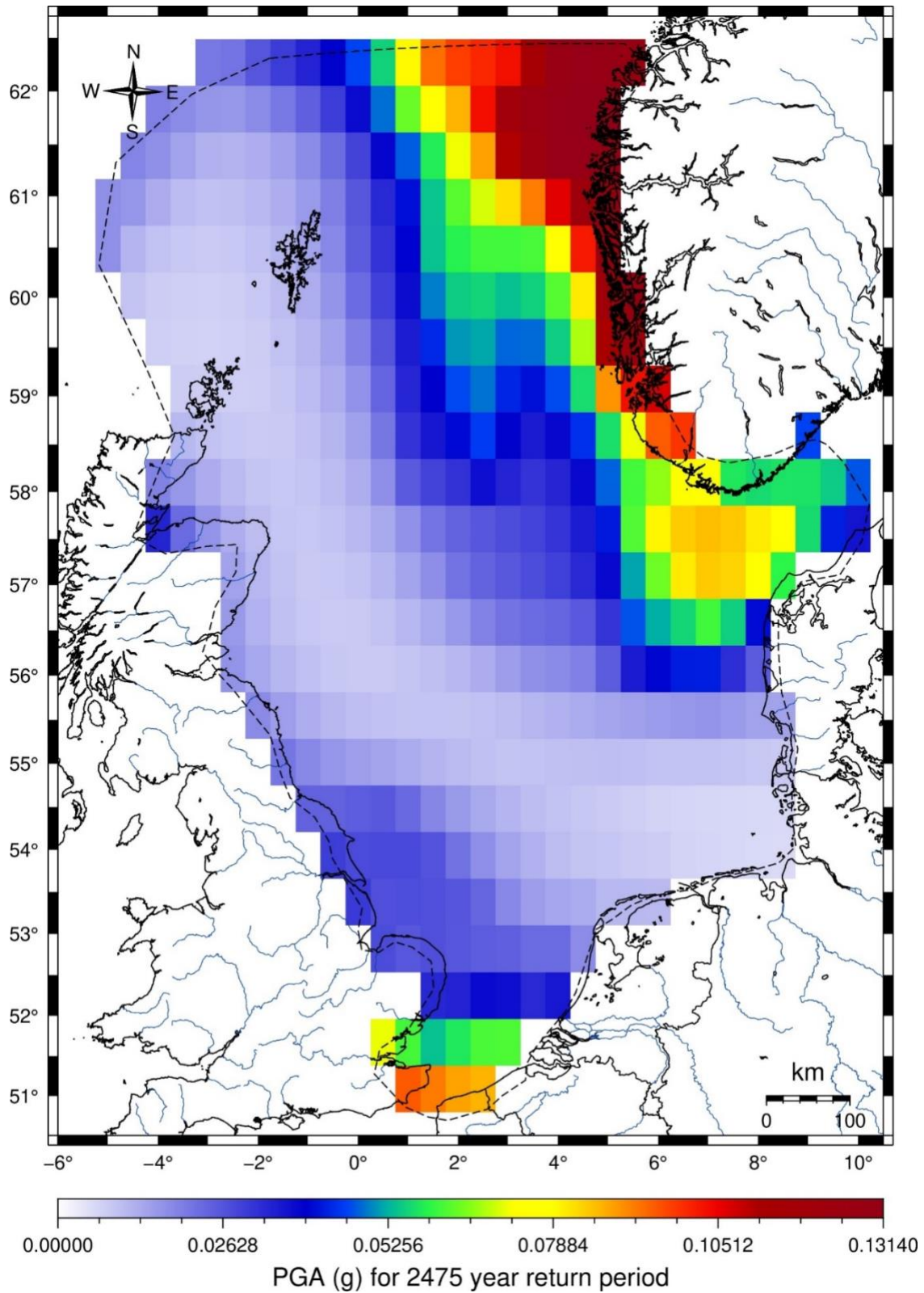


Figure 6-12 PGA for  $V_{s30} = 800$  m/s for a return period of 2475 years.

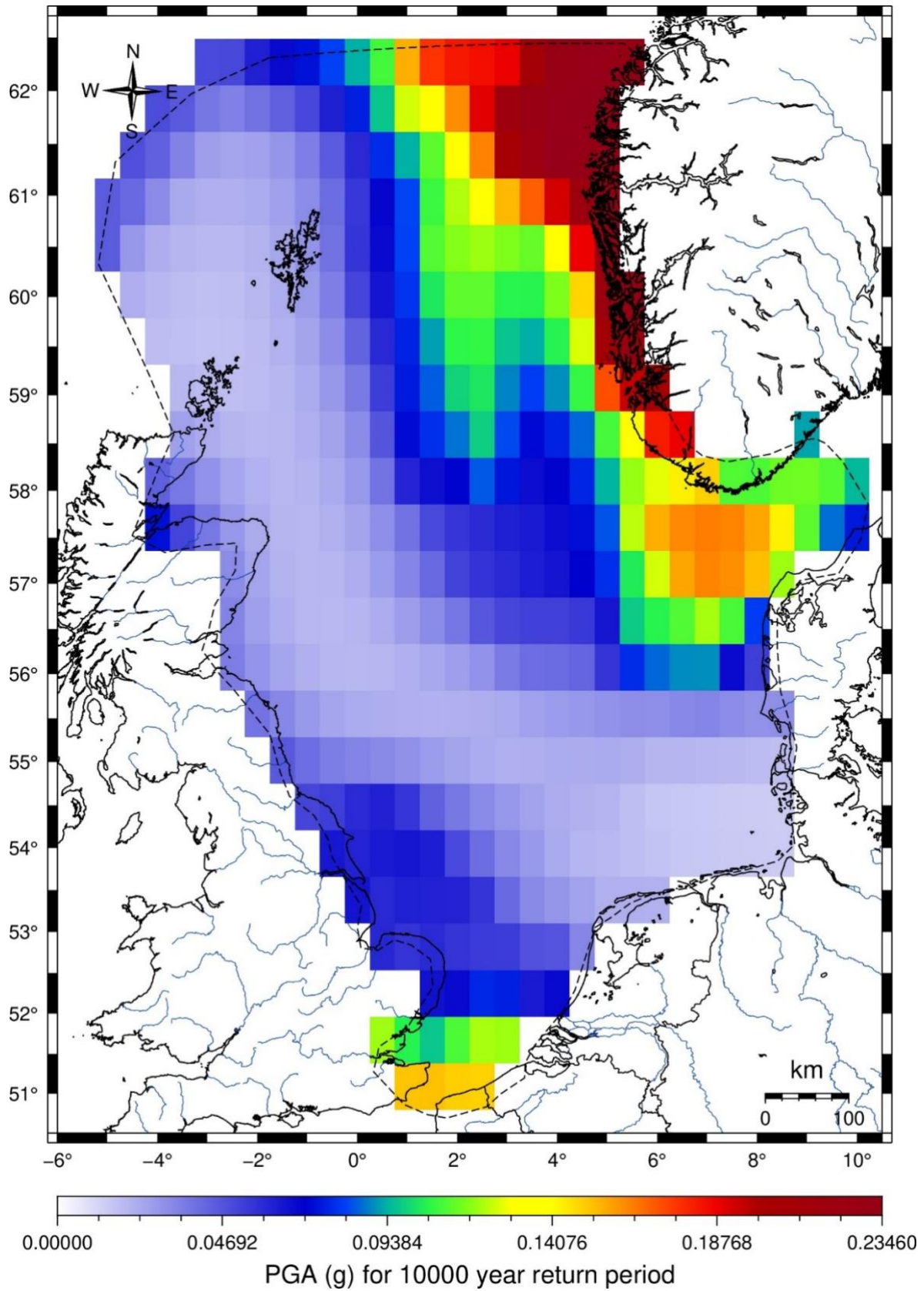


Figure 6-13 PGA for  $V_{s30} = 800$  m/s for a return period of 10000 years.

## 6.4 Comparison of PSHA results with other studies

The PGA values for 475-year return period on rock are generally less than those predicted by the Bungum et al. (2000) study (Figure 1-3), the only publicly available PSHA that includes the entire study area. Table 6-7 lists comparisons for specific regions. The most notable differences are the Dogger Bank area, where the Bungum et al. (2000) model predicts PGA seven times larger than the current PSHA, and the Dover region, which is the only region where the current PSHA predicts larger PGA values than the Bungum et al. (2000) model.

Results from the ESHM study (Figure 1-15, Danciu et al., 2021) are 0-0.025 g for all locations around the study area except for west coast of Norway near the Tampen area, where the values are 0.05-0.075 g, and for the German coast, where the results are 0 g. These results are similar to the current study, however, because the ESHM study was only concerned with onshore results, the local high in the Tornquist area is not reported.

The PGA values for 475-year return period on rock predicted along the coast of the UK, Norway, Denmark, and Germany in this study are all like the values predicted along the coast in the corresponding national studies (Mosca et al., 2020; NORSAR, 2019; Voss et al., 2015; Grünthal et al., 2018). The Danish study (Voss et al., 2015), also predicts similar values for the Tornquist zone off the northwest coast of Denmark.

The one exception is the Dover-Calais region. Mosca et al. (2020) predict PGA values of 0-0.02 g for the UK side (Figure 1-13) and Drouet et al. (2020) predict PGA values of 0.010-0.016 g for the French side (Figure 1-12) for 475 year return period on rock, compared to 0.04-0.05 g from this study. This discrepancy is still being investigated.

*Table 6-7 comparison of the PSHA results for PGA (g) on rock for 475-year return period.*

| Name           | Lat  | Long | SHARP | Bungum et al. (2000) |
|----------------|------|------|-------|----------------------|
| Tampen         | 62   | 4    | 0.057 | 0.100                |
| Tornquist      | 57.5 | 7.5  | 0.033 | 0.040                |
| Dover Strait   | 51   | 1.5  | 0.045 | 0.040                |
| Dogger Bank    | 54   | 1.5  | 0.008 | 0.060                |
| Central Graben | 56   | 3    | 0.005 | 0.020                |

## 7 Discussion and conclusions

### 7.1 Ground motion modelling

This study developed the first ground-motion model for the North Sea based on the earthquake catalogue and waveform data from SHARP WP2, both collected from the regional agency data repositories. The waveform data underwent a sophisticated three-stage processing scheme and then the processed waveforms were used to compute time-domain amplitude-based IMs, frequency-domain amplitude IMs and energy-related integral IMs. The resultant North Sea waveform database includes the three-component ground motion recordings from several selected events ( $M \geq 3.5$ , distances within 10 degrees or 1100 km epicentre distance) recorded in the North Sea region between 1990 – 2022. By evaluating the ground motion characteristics (e.g., scaling with respect to magnitude, source-to-site distance, soil conditions), a simple but effective functional form was proposed. The model parameters were derived using advanced statistical methods. The preliminary GMM for the North Sea, due to the paucity of observations, was only applicable for magnitude range 3.5 – 5.5,

epicentre distance range 72 – 1000 km, and period range 0.03 – 2.6 s. Compared to the global and regional GMMs applicable to the North Sea regions, the predictive performance of the North Sea was better in capturing the feature in North Sea data as expected. The biggest challenge in the GMM development was the lack of large magnitude events and near field data. To address this challenge in the future, offshore waveforms collected from the industrial partners, such as the permanent reservoir monitoring data, would be included. This would lead to another challenge in processing the instrument response. Another approach to address this problem is to perform the ground motion simulation, which should be validated from the engineering perspective.

These underlying difficulties in the input data for the GMM development could be improved through the integration of ocean bottom sensors nearer to the events of interest. Most broadband ocean bottom seismometer deployments are, however, temporary, rarely lasting for more than a year-long period. This naturally limits the applicability of traditional broadband ocean bottom seismometer data. An alternative exists in the form of permanent ocean bottom nodal systems, which are deployed in some areas around the world to monitor oil fields. These are often used as receivers for marine reflection seismic surveys. Passive recordings can be made using these systems and used for nearfield measurements of offshore natural earthquakes. Unfortunately, there can be difficulties in using this nodal data for ground motion calibration. One issue is poorly calibrated instrument responses of the sensors. This is vital to accurately convert recordings into physical units of displacement (this is also critical to use nodal data for determining earthquake magnitude). The variation in coupling of the sensors to the seafloor is also often an unknown, which makes accurate calibration of ground motion recordings challenging. Another issue is the limited sensitivity of these sensors, which are often designed to be sensitive to motions with higher frequencies than are relevant for seismic hazard analysis. In more expansive studies of offshore seismic hazard, it would be ideal to use nodal system data, however this was beyond the scope of this study due to the above challenges. In a future study of North Sea ground motions, nodal system data should be a component. Other novel seismic measurement technologies, such as DAS, could also be integrated into this expansion of the study. However similar significant challenges would have to be overcome, chiefly the lack of a well constrained response and coupling function for typical fibre deployments.

One clear difficulty encountered in the characterisation of earthquakes in the region for hazard analysis is the heterogeneity in the completeness of the data. The magnitude of completeness of the current data is likely around M 4 from around 1980. As the minimum magnitude of hazard events considered was M 4 in this study, this is generally not an issue. However, another key input in the PSHA analysis is the Gutenberg-Richter b-value. Accurate b-values require a completeness magnitude several magnitude units lower than the magnitude of potentially hazardous events. As described in Section 3, the source catalogue was a combination of both the SHARP North Sea catalogue (with no minimum magnitude criteria), and the ESHM earthquake catalogue (with a minimum magnitude of around 3). This difference in the underlying data makes the spatial evaluation of b-value in the areas at the edge of the North Sea region less robust, as there is a difference in the completeness of the underlying event data. This could be combated with the inclusion of the full seismicity catalogue in the 300 km extension region beyond the North Sea study region. This addition is challenging, particularly conducting the same level of scrutiny as was conducted in the seismicity data integration of WP2 of SHARP. Supplementing the catalogue using data from the International Seismological Centre (ISC) could be a means of using quality-controlled earthquake data. Another means of avoiding this issue would be the reduction in scope of the seismic hazard study to purely regions containing data from the SHARP catalogue (i.e., narrow the study to smaller area of the North Sea). This would naturally

have changed the primary objective of this study but could be conducted in a follow-on study of North Sea seismic hazard.

## 7.2 Site amplification

Section 5.1 describes the selection and development of representative site profiles to estimate amplification functions for the North Sea. The sites are selected based on a database of site investigations including geological, geophysical, and geotechnical data. Nine base case sites are selected with 27 modified site profiles to explore the range of elastic site period and profile depth. Due to the lack of strong ground motion data, we were unable to perform traditional site response analyses using acceleration time series as input. As a result, we plan to estimate site amplification factors based on site response analyses using random vibration theory (RVT) (Rathje and Ozbey, 2006). The procedure for equivalent linear site response analyses using RVT is the same as a traditional equivalent linear site response except instead of using an acceleration time series as input, a Fourier amplitude spectrum (FAS) is used. The most important input parameters to constrain the FAS are the earthquake magnitude, the source to site distance, the stress drop ( $\Delta\sigma$ ), high frequency attenuation ( $\kappa$ ), and the anelastic attenuation ( $Q$ ).

In this study we also attempted to estimate  $\kappa$ , which is a measure of the high-frequency energy attenuation of ground motions (Anderson and Hough, 1984). As mentioned above, it is an essential parameter to adequately calibrate physical models, which are necessary to develop a database of synthetic ground motions as well as input FAS for the RVT site response method.  $\kappa$  can also be used to convert ground motion models developed for other regions to the target region, called host-to-target conversion method (Cambell, 2003). The estimated values of  $\kappa_{r\_AS}$  range between 0.005 and 0.085, which are reasonable and correspond to shear wave velocities over the top 30 meters ( $V_{s30}$ ) of 2000 m/s to 200 m/s (Van Houtte et al., 2011). However, the estimated values of  $\kappa_{r\_AS}$  do not increase with distance as expected, or they increase at a smaller rate, implying a  $Q$  value several times larger than those measured by other researchers using tomography techniques. Therefore, more work is needed to ensure robust and credible estimates of  $\kappa$ .

## 7.3 Probabilistic seismic hazard

The PSHA showed that the highest PGA values occur off the west coast of Norway in the Tampen Area (62°N, 4°E), between Norway and Denmark along the Tornquist Zone (57.5°N, 7.5°E), and at the Dover Strait (51°N, 1.5°E). This follows roughly the same pattern as the observed seismicity (Figure 6-7). The PGA values for 475-year return period on rock predicted along the coasts are all similar to the values predicted along the coast in the corresponding national studies and the ESHM study (Danciu et al., 2021). The PGA values in the offshore regions are generally smaller than those predicted by the Bungum et al. (2000) study. Due to the inconclusive  $\kappa$  results, we did not use the host-to-target conversion method (Cambell, 2003). Instead, we used ground motion models that fit well with the empirical data available.

## 7.4 Implications for de-risking and monitoring

This work naturally aids in the assessment of seismic hazard for CO<sub>2</sub> storage projects in the North Sea, and details a methodology which could be applied to other prospective storage areas globally. Despite the difficulties and limitations of the current input data, this study advances the use of PSHA methodology in the North Sea region. Seismic hazard assessments of some form need to be conducted as a part of international standards for offshore industry developments (described in Section 1.3), and this study can inform operators in the North Sea at a regional level if more detailed site-specific

analyses are required. As such, there are several ways in which this study can aid in the other aspects of the SHARP project at large.

This study helps to underpin the seismic hazard and rates of natural seismicity. This will aid in the identification of induced seismicity by providing a statistically robust baseline from which to compare. After injection begins, if activity rates for small to moderate events near to a storage site begin to significantly exceed the rates expected from the recurrence relationships computed in the PSHA, this could provide an indication that seismicity is being induced. If the occurrence of an event or events in the vicinity of a storage project do not exceed the expectations from the PSHA, then this could indicate that a natural sequence is occurring. This discrimination is key to the successful operation and monitoring of storage project, ensuring conformance and public confidence in the project over its lifetime.

The spatial areas of more significant seismic hazard in the region are highlighted through the PSHA analysis. Whilst these areas are known from the prior analyses, described in Section 1.1, this study gives a more accurate regional picture of hazard found using the updated seismicity catalogue, and the partial integration of the North Sea-specific ground motion model. This improvement in the quantification of hazard can be used as an input into several parts of the modelling of risks, and the design of long-term monitoring systems. The way in which PSHA outputs can be used in risk modelling workflows is being detailed in an additional supplemental SHARP deliverable (D5.5b).

The GMM analyses highlight a clear need for offshore measurements of ground motions from earthquakes in the North Sea region. The lack of passive seismic data in the “near-field” event-station distance range limits the calibration of the GMM in those distance ranges, meaning the predicted ground motions in the near field (i.e., in the offshore regions) are less well constrained than the GMMs that have been calibrated using onshore data. This is why an ensemble of GMMs are used in the PSHA, as relying on the offshore data-derived model alone would be insufficient. Improving these offshore ground motion models is key to seismic hazard analyses in the North Sea region, and studies such as Hendriks et al. (2024), which use GMMs to test resilience to induced seismicity offshore.

## 8 References

Abrahamson, N. (2023). HAZ45.3, <https://github.com/abrahamson/HAZ>.

Abrahamson, Norman A. and Robert R. Youngs (1992). A stable algorithm for regression analyses using the random effects model. *Bulletin of the Seismological Society of America* 82(1): 505–510.

Abrahamson, N.A., Silva, W.J., Kamai, R. (2014). Summary of the ASK14 ground motion relation for active crustal regions. *Earthquake Spectra* 301:1025–1055.

Akkar S., Sandikkaya M.A., Senyurt, M., Azari S.A., Ay BÖ (2013). Reference database for seismic ground-motion in Europe (RESORCE). *Bull Earthq. Eng.* 12, 1, 311-339.

Akkar, S., Çağnan, Z. (2010). A local ground-motion predictive model for Turkey and its comparison with other regional and global ground-motion models. *Bull Seismol Soc Am* 100:2978–2995.

Akkar, S., Sandikkaya, M.A., Bommer, J.J. (2014). Empirical ground motion models for point- and extended-source crustal earthquake scenarios in Europe and the Middle East. *Bull Earthq Eng* 12:359–387.

Ancheta, T. D., Darragh, R. B., Stewart, J. P., Seyhan, E., Silva, W. J., Chiou, B. S. J., Wooddell, K. E., Graves, R. W., Kottke, A. R., Boore, D. M., Kishida, T., and Donahue, J. L., (2014). NGA-West2 database, *Earthquake Spectra* 30, 989–1005.

Anderson, J. G., and S. E. Hough (1984). A model for the shape of the Fourier amplitude spectrum of acceleration at high frequencies, *Bull. Seismol. Soc. Am.* 74(5): 1969–1993.

Atkinson, G., and D. Boore (2006). Earthquake ground-motion prediction equations for eastern North America, *Bull. Seismol. Soc. Am.* 96, 2181–2205.

Atkinson, G.M. & Boore, D.M. (2011). Modifications to Existing Ground-Motion Prediction Equations in Light of New Data. *Bulletin of the Seismological Society of America*, 101(3), 1121-1135.

Bahrampouri, M., Rodriguez-Marek, A., Shahi, S., Dawood, H. (2021). An updated database for ground motion parameters for KiK-net records, *Earthquake Spectra*, 37(1): 505-522.

Baker, J. (2008). An introduction to Probabilistic Seismic Hazard Analysis (PSHA). [https://web.stanford.edu/~bakerjw/Publications/Baker \(2008\) Intro to PSHA v1 3.pdf](https://web.stanford.edu/~bakerjw/Publications/Baker%20(2008)%20Intro%20to%20PSHA%20v1%203.pdf).

Bellwald, B., Planke, S., Vadakkepuliambatta, S., Buenz, S., Batchelor, C., Manton, B., ... & Kjølhamar, B. (2022): Quaternary and Neogene Reservoirs of the Norwegian Continental Shelf and the Faroe-Shetland Basin, *First Break*, 40(6): 43-54.

Beyer, Katrin and Julian J. Bommer (2006). Relationships between median values and between aleatory variabilities for different definitions of the horizontal component of motion. *Bulletin of the Seismological Society of America* 96(4A): 1512–1522.

Beyer, Katrin and Julian J. Bommer (2007). Erratum: Relationships between median values and between aleatory variabilities for different definitions of the horizontal component of motion. *Bulletin of the Seismological Society of America* 97(5): 1769.

Beyreuther, M., Barsch, R., Krischer, L., Megies, T., Behr, Y., and Wassermann, J. (2010). ObsPy: A Python Toolbox for Seismology, *Seismological Research Letters*, 81(3): 530-533.

Biasi G.P., Smith K.D. (2001). Site effects for seismic monitoring stations in the vicinity of Yucca Mountain, Nevada, MOL 20011204.0045, A report prepared for the US DOE/University and Community College System of Nevada Cooperative Agreement.

Bindi, D., M. Massa, L. Luzi, G. Ameri, F. Pacor, R. Puglia, P. Augiera (2014). Pan-European ground-motion prediction equations for the average horizontal component of PGA, PGV, and 5%-damped PSA at spectral periods up to 3.0 s using the RESORCE dataset, *Bull Earthq. Eng.* 12, no. 1, 391–430.

Biro, Y., and P. Renault (2012): Importance and impact of host-to-target conversions for ground motion prediction equations in PSHA, in *Proc. 15th World Conference of Earthquake Engineering*, Lisbon, Portugal, 24–28 September, 10 pp.

Bommer, J.J., Crowley, H. (2017). The Purpose and Definition of the Minimum Magnitude Limit in PSHA Calculations. *Seismological Research Letters* 88 (4) 1097–1106.

Bommer, J.J., Douglas, J., Scherbaum, F., Cotton, F., Bungum, H., Fäh, D. (2010). On the selection of ground motion prediction equations for seismic hazard analysis. *Seismol Res Lett* 81(5):783–793.

- Boore, David M. (2010). Orientation-independent, nongeometric-mean measures of seismic intensity from two horizontal components of motion. *Bulletin of the Seismological Society of America* 100(4): 1830–1835.
- Boore D.M., Kishida T. (2017). Relations between some horizontal component ground-motion intensity measures used in practice. *Bull Seismol Soc Am* 107:334–343.
- Boore, D. M., J. P. Stewart, E. Seyhan, and G. M. Atkinson (2014). NGAWest 2 equations for predicting PGA, PGV, and 5%-damped PSA for shallow crustal earthquakes, *Earthq. Spectra* 30, no. 3, 1057–1085.
- Brooks, C., Douglas, J., Shipton, Z., (2020). Improving earthquake ground-motion predictions for the North Sea. *J Seismol* (2020) 24:343–362.
- Brune J. N. (1970). Tectonic stress and the spectra of seismic shear waves from earthquakes, *J. Geophys Res.*, 75: 4997–5002.
- Brune J.N. (1971). Correction: Tectonic stress and the spectra of seismic shear waves from earthquakes, *J. Geophys. Res.*, 76: 5002.
- Bungum, H., Lindholm, C.D., Dahle, A., Hicks, E., Høgdén, S., Nadim, F., Holme, J.K., & Harbitz, C., (1998). Development of Seismic Zonation for Norway: Final Report. Report for the Norwegian Council for Building Standardization (NBR), 187 pp.
- Bungum, H., Lindholm, C.D., Dahle, A., Woo, G., Nadim, F., Holme, J.K., Gudmestad, O.T., Hagberg, T. & Karthigeyan, K. (2000). New seismic zoning maps for Norway, the North Sea, and the United Kingdom. *Seismological research letters*, 71, 687-697.
- Burkhard, M., and Grünthal, G. (2009). Seismic source zone characterization for the seismic hazard assessment project PEGASOS by the Expert Group 2 (EG1b), *Swiss Journal of Geosciences*, Vol. 102, 149–188.
- Cameron, T. D. J., Stoker, M. S., & Long, D. (1987): The history of Quaternary sedimentation in the UK sector of the North Sea Basin, *Journal of the Geological Society*, 144(1), 43-58.
- Carlton B, Barwise A, Kaynia AM (2022). Seismic Hazard Assessment for a Wind Farm Offshore England. *Geotechnics*. 2022; 2(1):14-31.
- Carlton, B.D., Skurtveit, E., Atakan, K., and Kaynia, A.M. (2019). Probabilistic seismic hazard analysis of a CO<sub>2</sub> storage prospect using the NGA East ground motion models. In proceedings of the SECED 2019 Conference, Greenwich, London, 9-10 September.
- Carlton, B. (2014): An Improved Description of the Seismic Response of Sites with High Plasticity Soils, Organic Clays, and Deep Soft Soil Deposits, PhD dissertation, University of California, Berkeley.
- Carlton, B., and Tokimatsu, K., (2014): Statistical Correlation for Shear Wave Velocity of Soils Using Limited Site Data, Proceedings of the 14th Japan Earthquake Engineering Symposium, Tokyo, Japan, December 4-6.
- Cauzzi C., Faccioli E. (2008). Broadband (0.05 to 20 s) prediction of displacement response spectra based on worldwide digital records. *J. Seismol.* 12:453–475.

Cauzzi, C., Faccioli, E., Vanini, M., Bianchini, A. (2015). Updated predictive equations for broadband (0.01–10 s) horizontal response spectra and peak ground motions, based on a global dataset of digital acceleration records. *Bull Earthq Eng* 13: 1587–1612.

Chen, Yi Hau and Chu Chuan Peter Tsai (2002). A new method for estimation of the attenuation relationship with variance components. *Bulletin of the Seismological Society of America* 92(5): 1984–1991.

Chiou, B. S.-J., Youngs, R. R. (2014). Update of the Chiou and Youngs NGA model for the average horizontal component of peak ground motion and response spectra, *Earthq. Spectra* 30, no. 3, 1117–1153.

Cohen, K. M., Gibbard, P. L., & Weerts, H. J. T. (2014): North Sea palaeogeographical reconstructions for the last 1 Ma., *Netherlands Journal of Geosciences*, 93(1-2), 7-29.

Cornell, C.A. (1968). Engineering seismic risk analysis. *Bulletin of the Seismological Society of America*, 58, p. 1583-1606.

Cotterill, C., Phillips, E., James, L., Forsberg, C.F. & Tjelta, T.I. (2017a): How understanding past landscapes might inform present-day site investigations: a case study from Dogger Bank, southern central North Sea, *Near Surface Geophysics*, 2017, 15, 403-413.

Cotterill, C., Phillips, E., James, L., Forsberg, C.F., Tjelta, T.I., Carter, G. & Dove, D. (2017b): The evolution of the Dogger Bank, North Sea: A complex history of terrestrial, glacial and marine environmental change, *Quaternary Science Reviews* 171 (2017), 136-153.

Cotton, F., Scherbaum, F., Bommer, J.J., Bungum, H. (2006). Criteria for selecting and adjusting ground motion models for specific target regions: application to central Europe and rock sites. *J Seismol* 10(2):137–156.

Danciu L., Nandan S., Reyes C., Basili R., Weatherill G., Beauval C., Rovida A., Vilanova S., Sesetyan K., Bard P.-Y., Cotton F., Wiemer S., Giardini D. (2021) - The 2020 update of the European Seismic Hazard Model: Model Overview. *EFEHR Technical Report 001*, v1.0.0.

Darendeli, M. B. (2001): Development of a new family of normalized modulus reduction and material damping curves. PhD dissertation, Univ. of Texas at Austin, Austin, Texas.

Demuth, A. (2019). Ambient noise levels,  $Q_{Lg}$  wave tomography and earthquake source parameters in Norway. PhD dissertation, University of Bergen, Bergen, Norway.

Douglas, J., 2003. Earthquake ground motion estimation using strong-motion records: A review of equations for the estimation of peak ground acceleration and response spectral ordinates. *EarthScience Reviews*, 61:1–2, 43–104.

Douglas, John and Benjamin Edwards (2016). Recent and future developments in earthquake ground motion estimation. *Earth-Science Reviews* 160, 203–219.

Douglas, J., P. Gehl, L. F. Bonilla, and C. Gélis (2010). A  $\kappa$  model for mainland France, *Pure Appl. Geophys.*, 167: 1303–1315.

Du, Wenqi, and Gang Wang. Prediction equations for ground-motion significant durations using the NGA-West2 database. *Bulletin of the Seismological Society of America* 107.1 (2017): 319-333.

- EQE International Ltd. (2002). Seismic hazard - UK continental shelf. Health and Safety Executive Offshore Technology Report 2002/005; 70pp.
- Eurocode 8 (2014) NS-EN 1998-1:2004+A1:2013. Eurocode 8: Design of structures for earthquake resistance - Part 1: General rules, seismic actions and rules for buildings.
- Fisher, Ronald A. (1925). Theory of statistical estimation. *Mathematical Proceedings of the Cambridge Philosophical Society* 22(5): 700–725.
- Foulser-Piggott, Roxane and Peter J. Stafford (2012). A predictive model for Arias intensity at multiple sites and consideration of spatial correlations. *Earthq. Eng. Struct. D.*, 41: 431–451.
- Glennie, K. W., & Underhill, J. R. (1998): Origin, development and evolution of structural styles, *Petroleum geology of the North Sea: Basic concepts and recent advances*, 42-84.
- Goulet C.A., Kishida T. Ancheta T.D., Cramer C.H., Darragh R.B., Silva W.J., Hashash Y.M.A., Harmon J., Stewart J.P., Wooddell K.E., Youngs R.R. (2014). PEER NGA-East database, PEER Report No. 2014/17. Pacific Earthquake Engineering Research Center, Berkeley, CA.
- Goulet, C., Bozorgnia, Y., Abrahamson, N., Kuehn, N., Al Atik, L., Youngs, R., Graves, R., Atkinson, G. (2018). Central and Eastern North America Ground-Motion Characterization: NGA-East Final Report. Pacific Earthquake Engineering Research Center, Berkeley, CA. PEER Report No. 2018/08.
- Goulet C.A., Kishida T. Ancheta T.D., Cramer C.H., Darragh R.B., Silva W.J., Hashash Y.M.A., Harmon J., Parker, G.A., Stewart J.P., Youngs R.R. (2021). PEER NGA-East database, *Earthquake Spectra*, 37(S1): 1331-1353.
- Graves, Robert, Thomas H. Jordan, Scott Callaghan, Ewa Deelman, Edward Field, Gideon Juve, Carl Kesselman, Philip Maechling, Gaurang Mehta, Kevin Milner, David Okaya, Patrick Small and Karan Vahi (2011). CyberShake: A physics-based seismic hazard model for southern California. *Pure and Applied Geophysics* 168(3-4): 367–381.
- Gregersen, S., Basham, P. W., Whittaker, A., Brereton, N. R., Evans, C. J., & Long, R. E. (1989): *Seismotectonics and crustal stress in Great Britain* (pp. 393-411). Springer Netherlands.
- Groholski, D.R., Hashash, Y.M.A., Kim, B., Musgrove, M., Harmon, J. & Stewart, J.P. (2016): Simplified Model for Small-Strain Nonlinearity and Strength in 1D Seismic Site Response Analysis, *Journal of Geotechnical and Geoenvironmental Engineering*, 142(9).
- Grünthal, G. & the GSHAP Region 3 Working Group (1999). Seismic hazard assessment for Central, North and Northwest Europe: GSHAP Region 3. *Annali di Geofisica*, 42(6), p. 999-1011.
- Grünthal, G. (1985). The up-dated earthquake catalogue for the German Democratic Republic and adjacent areas – statistical data characteristics and conclusions for hazard assessment. 3rd International Symposium on the Analysis of Seismicity and Seismic Risk, Liblice, Czechia, 17–22 June.
- Hale, C., Abrahamson, N., Bozorgnia, Y. (2018). Probabilistic Seismic Hazard Analysis Code Verification. Pacific Earthquake Engineering Research Center, PEER Report No. 2018/03.
- Harmon, J., Hashash, Y.M.A., Stewart, J.P., Rathje, E.M., Campbell, K.W., Silva, W.J., Xu, B., Musgrove, M., Ilhan, O. (2019): Site Amplification Functions for Central and Eastern North America – Part 1: Simulation Data Set Development, *Earthquake Spectra*, 35(2), 787-814.

Hashash, Y.M.A., Musgrove, M.I., Harmon, J.A., Ilhan, O., Xing, G., Numanoglu, O., Groholski, D.R., Phillips, C.A., and Park, D. (2020): DEEPSOIL 7.0, User Manual, Urbana, IL, Board of Trustees of University of Illinois at Urbana-Champaign.

Hindriks, K., Oates, S., Kettlety, T., Martuganova, E., Kuehn, D., & Oye, V. (2024). Resilience to Potential CO<sub>2</sub> Injection Induced Seismicity, Estimated from Historic Ground Motion Exposure. 85th EAGE Annual Conference & Exhibition (Including the Workshop Programme), 2024(1), 1–5. <https://doi.org/10.3997/2214-4609.2024101584>

Hong, H. P., Y. Zhang and Katsuichiro Goda (2009). Effect of spatial correlation on estimated ground-motion prediction equations. *Bulletin of the Seismological Society of America* 99(2A): 928–934.

Huang, Chen and Carmine Galasso (2019). Ground-motion intensity measure correlations observed in Italian strong-motion records. *Earthquake Engineering and Structural Dynamics* 48(15): 1634–1660.

Huang, Chen, Karim Tarbali and Carmine Galasso (2020), Correlation properties of integral ground-motion intensity measures from Italian strong-motion records. *Earthquake Engineering Structural Dynamics* 49(15): 1581-1598.

ISO 19901-2 (2022). Petroleum and natural gas industries – Specific requirements for offshore structures – Part 2: Seismic action procedures and criteria. International Organization for Standardization, Geneva, Switzerland.

Jayaram, Nirmal and Jack W. Baker (2008). Statistical tests of the joint distribution of spectral acceleration values. *Bull. Seismol. Soc. Am.* 98(5): 2231–2243.

Jayaram, Nirmal and Jack W. Baker (2009). Correlation model for spatially distributed ground-motion intensities. *Earthquake Engineering and Structural Dynamics* 38(15): 1687–1708.

Jayaram, Nirmal and Jack W. Baker (2010). Considering spatial correlation in mixed-effects regression and the impact on ground-motion models. *Bull. Seismol. Soc. Am.* 100(6): 3295–3303.

Joyner, W B and David M. Boore (1993). Methods for regression analysis of strong-motion data. *Bulletin of the Seismological Society of America* 83(2): 469–487.

Kempton, Justin J. and Jonathan P. Stewart (2006). Prediction equations for significant duration of earthquake ground motions considering site and near-source effects. *Earthquake Spectra*, 22(4): 985–1013.

Kennett B.L.N. and Engdahl E.R., 1991. "Travel times for global earthquake location and phase association." *Geophysical Journal International*, 105:429-465.

Kennett, B.L.N., Gergersen, S., Mykkeltveit, S. and Newmark, R. (1985). Mapping of crustal heterogeneity in the North Sea basin via the propagation of Lg-waves. *Geophys. J.R. astr. Soc.* 83, 299-306.

Kilb, D., G. Biasi, J. G. Anderson, J. Brune, Z. Peng, and F. L. Vernon (2012). A comparison of spectral parameter kappa from small and moderate earthquakes using southern California ANZA seismic network data, *Bull. Seismol. Soc. Am.* 102: 284–300.

Kishida T., Kayen R., Ktenidou O.-J., Silva W.J., Darragh R.B., Watson-Lamprey J. (2014). PEER Arizona strongmotion database and GMPEs evaluation, PEER Report No. 2014/09, Pacific Earthquake Engineering Research Center, Berkeley, CA.

- Konno, K. and Ohmachi, T. (1998) Ground-motion characteristics estimated from spectral ratio between horizontal and vertical components of microtremor, *Bull. Seismol. Soc. Am.*, 88(1): 228–241.
- Kottke, A.R., Wang, X., Rathje, E.M. (2019). *Strata Technical Manual*. <https://github.com/arkottke/strata>.
- Ktenidou O.-J., Abrahamson, N.A., Darragh, R.B., Silva, W.J. (2016). A Methodology for the Estimation of Kappa ( $\kappa$ ) from Large Datasets: Example Application to Rock Sites in the NGA-East Database and Implications on Design Motions. PEER Report No. 2016/01, Pacific Earthquake Engineering Research Center, Berkeley, CA.
- Ktenidou O.-J., Cotton F., Abrahamson N.A., Anderson J.G. (2014). Taxonomy of  $\kappa$ : a review of definitions and estimation approaches targeted to applications, *Seismol. Res. Letts.*, 85 (1): 135–146.
- Ktenidou O.-J., Gélis C., Bonilla L.F. (2013). A study on the variability of  $\kappa$  in a borehole: implications of the computation process, *Bull. Seismol. Soc. Am.*, 103(2A): 1048–1068.
- Kulkarni, R. B., R. R. Youngs, and K. J. Coppersmith (1984). Assessment of confidence intervals for results of seismic hazard analysis, in *Proc. Of the Eighth World Conf. on Earthquake Engineering*, San Francisco, California, Vol. 1, 263–270.
- Lee, J. R., Rose, J., Candy, I. A. N., & Barendregt, R. W. (2006): Sea-level changes, river activity, soil development and glaciation around the western margins of the southern North Sea Basin during the Early and early Middle Pleistocene: evidence from Pakefield, Suffolk, UK, *Journal of Quaternary Science*, 21(2), 155-179.
- Lermo J., Chavez-Garcia F.J. (1993). Site effect evaluation using spectral ratios with only one station, *Bull. Seismol. Soc. Am.*, 83(5): 1574–1594.
- Manchuel, K., Traversa, P., Baumont, D., Cara, M., Nayman, E., and Durouchoux, C., (2018). The French seismic CATalogue (FCAT-17), *Bulletin of Earthquake Engineering*, Vol. 16, 2227-2251.
- McGuire, R.K. (1974). Seismic structural response risk analysis incorporating peak response regressions on earthquake magnitude and distance. Massachusetts Institute of Technology Department of Civil Engineering/Research Report R74-51.
- McGuire, R.K. (1978). FRISK: Computer program for seismic risk analysis using faults as earthquake sources. U.S. Geological Survey Open-File Report 78-1007.
- Menq, F. (2003): Dynamic properties of sandy and gravelly soils. PhD dissertation, Univ. of Texas at Austin, Austin, Texas.
- Ming, Deyu, Chen Huang, Gareth W. Peters and Carmine Galasso (2019). An advanced estimation algorithm for ground-motion models with spatial correlation. *Bulletin of the Seismological Society of America* 109(2): 541–566.
- Morén, B. M., Sejrup, H. P., Hjelstuen, B. O., Borge, M. V., & Schäuble, C. (2018): The last deglaciation of the Norwegian Channel—geomorphology, stratigraphy and radiocarbon dating, *Boreas*, 47(1), 347-366.
- Mosca, I., Sargeant, S., Baptie, B., Musson, R.M.W. and Pharaoh, T (2020). National seismic hazard maps for the UK: 2020 update. British Geological Survey Open Report, OR/20/053. 138pp.

Mosca, I., Baptie, B., Haslam, R., Gafeira, J., Jenkins, G. (2024). Seismic Hazard Assessment for the UK Offshore Exclusive Economic Zone. British Geological Survey Open Report, OR/24/012.

Musson, R.M.W., Sargeant, S.L. (2007). Eurocode 8 seismic hazard zoning maps for the UK. British Geological Survey: Seismology and geomagnetism programme technical report CR/07/125, pp. 70.

NPD (2019): CO2 Atlas for the Norwegian Continental Shelf-Chapter 4.1: Geology of the North Sea. Norwegian Petroleum Directorate.

Ordaz, M., A., A. & Arboleda, J. 2007: CRISIS 2007, Program for Computing Seismic Hazard. <https://ecapra.org/topics/crisis-2007>

Ottesen, D., Batchelor, C. L., Dowdeswell, J. A., & Løseth, H. (2018): Morphology and pattern of Quaternary sedimentation in the North Sea Basin (52–62 N), *Marine and Petroleum Geology*, 98, 836–859.

Parolai S., Bindi D. (2004). Influence of soil-layer properties on k evaluation, *Bull. Seismol. Soc. Am.*, 94: 349–356.

Petrie, H. E., Eide, C. H., Haflidason, H., & Watton, T. (2022): A conceptual geological model for offshore wind sites in former ice stream settings: the Utsira Nord site, North Sea, *Journal of the Geological Society*, 179(5), jgs2021-163.

Phillips, C. & Hashash, Y.M.A. (2009): Damping formulation for nonlinear 1D site response analyses, *Soil Dynamics and Earthquake Engineering*, 29, 1143–1158.

Rathje, E.M., and Ozbey, M.C (2006). Site-specific Validation of Random Vibration Theory-Based Seismic Site Response Analysis. *Journal of Geotechnical and Geoenvironmental Engineering*, 132(7).

Rietbrock, A., Edwards, B. (2019). Update of the UK stochastic ground motion model using a decade of broadband data. International Conference for Society for Earthquake and Civil Engineering Dynamics (SECED), Greenwich, UK, 9-10, September.

Rietbrock, A., Strasser, F., Edwards, B. (2013). A stochastic earthquake ground-motion prediction model for the United Kingdom. *Bull Seismol Soc Am* 103:57–77.

Rovida, A., Antonucci, A., & Locati, M. (2022). The European Preinstrumental Earthquake Catalogue EPICA, the 1000–1899 catalogue for the European Seismic Hazard Model 2020. *Earth System Science Data*, 14(12), 5213–5231. <https://doi.org/10.5194/essd-14-5213-2022>

RVO reports:

TNW: [https://offshorewind.rvo.nl/file/download/629c2998-6429-4f85-86d6-767c680e0ad0/1638781502tnw\\_20211202\\_gm\\_ngi\\_seismic%20hazard%20assessment\\_rev0-f.pdf](https://offshorewind.rvo.nl/file/download/629c2998-6429-4f85-86d6-767c680e0ad0/1638781502tnw_20211202_gm_ngi_seismic%20hazard%20assessment_rev0-f.pdf)

Seed, H. B., Ugas, C., and Lysmer, J. (1976): Site-dependent spectra for earthquake resistant design, *Bulletin of the Seismological Society of America*, Vol. 66(1), 221–244.

Seyhan, E., and Stewart, J.P (2014): Semi-Empirical Nonlinear Site Amplification from NGA-West2 Data and Simulations, *Earthquake Spectra*, 30(3), 1241-1256.

Shennan, I. (1989): Holocene crustal movements and sea-level changes in Great Britain, *Journal of Quaternary Science*, 4(1), 77-89.

- Stafford, Peter J., Timothy J. Sullivan and Domenico Pennucci (2016). Empirical correlation between inelastic and elastic spectral displacement demands. *Earthquake Spectra*, 32(3): 1419–1448.
- Stepp, J.C. (1972). Analysis of completeness of the earthquake sample in the Puget Sound Area and its effect on statistical estimates of earthquake hazard. In proceedings of 1st International Conference on Microzonation, Seattle, USA.
- Stewart, Jonathan P., John Douglas, Mohammad Javanbarg, Yousef Bozorgnia, Norman A. Abrahamson, David M. Boore, Kenneth W. Campbell, Elise Delavaud, Mustafa Erdik, and Peter J. Stafford. "Selection of ground motion prediction equations for the global earthquake model." *Earthquake Spectra* 31, no. 1 (2015): 19-45.
- Stewart J.P, Parker, G.A., Atkinson, G.M., Boore, D.M., Hashash, Y.M.A., Silva, W.J. (2020). Ergodic site amplification model for central and eastern North America, *Earthquake Spectra* 36(1) 42–68.
- Stewart, Jonathan P., Kioumars Afshari and Christine A. Goulet (2017). Non-ergodic site response in seismic hazard analysis. *Earthquake Spectra* 33(4): 1385–1414.
- Stewart, J.P., Kwok, A.O., Hashash, Y.M.A, Matasovic, N., Pyke, R., Wang, Z., Yang, Z. (2008): Benchmarking of Nonlinear Geotechnical Ground Response Analysis Procedures, PEER Research Center Report 2008/04.
- Tromans, I.J., Aldama-Bustos, G., Douglas, J., Lessi-Cheimariou, A., Hunt, S., Daví, M., Musson, R.M.W., Garrard, G., Strasser, F.O., Robertson, C., (2019). Probabilistic seismic hazard assessment for a new-build nuclear power plant site in the UK, *Bulletin of Earthquake Engineering* 17 1–36.
- Van Houtte, C., Drouet, S. and Cotton, F. (2011). Analysis of the origins of  $\kappa$  (kappa) to compute hard rock to rock adjustment factors for GMPEs, *Bull. Seism. Soc. Am.*, 101, 2926–2941.
- Villani, M., Lubkowski, Z., Free, M., Musson, R.M.W., Polidoro, B., McCully, R., Koskosidi, A., Oakman, C., Courtney, T., Walsh, M. (2020). A probabilistic seismic hazard assessment for Wylfa Newydd, a new nuclear site in the United Kingdom. *Bulletin of Earthquake Engineering* 18:4061–4089.
- Villani, M., Polidoro, B., Ader, T., McCully, R., Lubkowski, Z., Courtney, T.J., Walsh, M. (2019). A selection of GMPEs for the UK based on ground motion and macroseismic datasets. *Bull Seismol Soc Am* 109(4):1378–1400.
- Voss, P., Dahl-Jensen, T. & Larsen, T. B. (2015) Earthquake hazard in Denmark, GEUS. Danmarks og Grønlands Geologiske Undersøgelse Rapport Vol. 2015 No. 24 <https://doi.org/10.22008/gpub/30674>
- Weichert, D.H. (1980). Estimation of the earthquake recurrence parameters for unequal observation periods for different magnitudes. *Bulletin of the Seismological Society of America*, 70(4), 1337-1346.
- Wells, Donald L. and Kevin J. Coppersmith (1994). New empirical relationship between magnitude, rupture length, rupture width, rupture area, and surface displacement. *Bulletin of the Seismological Society of America* 84(4): 974–1002.
- Woessner, J., Laurentiu, D., Giardini, D., Crowley, H., Cotton, F., Gruenthal, G., Valensise, G., Arvidsson, R., Basili, R., Demircioglu, M.B., Hiemer, S., Meletti, C., Musson, R.W., Rovida, A.N., Sesetyan, K., Stucchi, M. (2015). The 2013 European Seismic Hazard Model: key components and results. *Bulletin of Earthquake Engineering* 13, p. 3553-3596.



SHARP Storage – Project no 327342



Zhang TR, Lay T (1995). Why Lg phase does not traverse oceanic crust. Bull Seismol Soc Am, 85:1665–1678.

Ziegler, P.A. (1975): Geologic Evolution of North Sea and Its Tectonic Framework, American Association of Petroleum Geologists Bulletin, 59(7), 1073-1097.